UNIVERSITY OF SOUTHAMPTON

The model, design, and management of renewable energy harvesting systems for maritime robots

by

Yu Cao

A thesis submitted for the degree of
Doctor of Philosophy

in the
The Faculty of Engineering and Physical Sciences
School of Engineering

September 2020

UNIVERSITY OF SOUTHAMPTON

ABSTRACT

THE FACULTY OF ENGINEERING AND PHYSICAL SCIENCES
SCHOOL OF ENGINEERING

Doctor of Philosophy

THE MODEL, DESIGN, AND MANAGEMENT OF RENEWABLE ENERGY HARVESTING SYSTEMS FOR MARITIME ROBOTS

by Yu Cao

Renewable energy harvesting systems could provide sustainable power to supply mobile robots for fully autonomous operation. However, the lack of model theory and design technique in current research limit the renewable energy system to the stationary application only. This thesis proposes a methodology to model, design and manage the power system for maritime robots.

A novel non-stationary model including both global and local motion are developed for renewable energy harvesting systems. This offers a new methodology to simulate the power system with a spatial-temporal power generation and demand load model.

The model is utilised by a data-driven approach to design a reliable and economic renewable energy system configuration under the size constraint. This design method is based on the optimisation approach to size the configuration of renewable energy devices.

Furthermore, a learning-based power management strategy was proposed to improve the long term robustness of the power system. Variation and uncertainty in the renewable energy resource are mitigated by learning to plan the power usage from experience.

The non-stationary renewable energy harvesting model shows both global and local motion of the robot influence the power generation and demand load. To match the power generation and demand load of the robot, the size of the renewable energy harvester and storage device has to be optimally designed under strict size constraints. Design optimisation result demonstrated the optimality and feasibility of the proposed renewable energy harvesting system configuration method. For the long-term performance, the learning-based power management strategy outperforms all benchmarking strategies in providing a guaranteed minimum level of power supply.

Research results show the renewable energy could provide sustainable power supply to the robot. These methods and techniques provide a foundation to the model, design and management of renewable energy harvesting systems for mobile maritime robots.

Declaration of Authorship

I, Yu Cao, declare that this thesis entitled The model, design, and management of renewable energy harvesting systems for maritime robots and the work presented in it are my own and has been generated by me as the result of my own original research.

I confirm that:

1. This work was done wholly or mainly while in candidature for a research degree at this University;
2. Where any part of this thesis has previously been submitted for a degree or any other qualification at this University or any other institution, this has been clearly stated;
3. Where I have consulted the published work of others, this is always clearly attributed;
4. Where I have quoted from the work of others, the source is always given. With the exception of such quotations, this thesis is entirely my own work;
5. I have acknowledged all main sources of help;
6. Where the thesis is based on work done by myself jointly with others, I have made clear exactly what was done by others and what I have contributed myself;
7. Either none of this work has been published before submission, or parts of this work have been published as: . Yu Cao, Nicholas Townsend, and Mingyi Tan. "Hybrid renewable energy system for ocean going platforms." OCEANS 2017-Aberdeen. IEEE, 2017.

Signed:

Date:

Contents

List of Figures

List of Tables

List of Algorithms

Nomenclature

Symbol	Meaning	Unit
T_{amb}	Ambient temperature	°C
T_{stc}	Module temperature at STC	°C
ρ_w	Air density	kg/m^3
A_s	Solar panel area	m^2
A_w	Wind turbine swept area	m^2
A_{water}	Water plane area	m^2
A_d	Deck area	m^2
ν	Kinematic viscocity	m^2/s
η	Efficiency of solar panel	1
c_{sl}	Slenderness coefficient	1
Fr	Froude number	1
Re	Reynolds number	1
c_p	Prismatic coefficient	1
c_R	Ship residual coefficient	1
c_A	Ship added resistance	1
C_p	Power coefficient	1
C_t	Thrust coefficient	1
η_{in}	Battery charge efficiency	1
η_{out}	Battery discharge efficiency	1
σ	Battery dischage rate	1
R	Discounted total reward	1
c_d	Deck area coefficient	1
c_T	Ship thrust coefficient	1
k_t	Clearness index	1
K_t	Daily clearness index	1
d_n	Day of the year	1
I_p	Current of solar panel	A
V_p	Voltage of solar panel	V
P_s	Power supply	W
P_p	Power planning	W
P_d	Power demand/Load demand	W
P_g	Power generation	W

Continued on next page

Symbol	Meaning	Unit
G_{stc}	Radiation at STC	W/m^2
G_r	Reflected radiation	W/m^2
G_d	Diffuse radiation	W/m^2
G_b	Beam (direct) radiation	W/m^2
G_g	Global horiontal radiation	W/m^2
E	Energy in the battery	Wh
B_0	Battery inital charge	Wh
B	Battery capacity	Wh
ω_s	Sunrise angle	degrees
δ	Solar declination angle	degrees
β_s	Solar panel horizontal tilt	degrees
α_s	Solar panel surface azimuth	degrees
λ_e	Ecliptic longitude	degrees
θ_a	Apparent wind direction	degrees
θ_t	True wind direction	degrees
θ_s	Ship heading	degrees
ϕ	Latitude	degrees
ϵ	Ecliptic tilt angle	degrees
λ	Longitude	degrees
ω_{ss}	Sunrise angle on inclined surface	degrees
Δ	Displacement	m^3
v_s	Ship speed	m/s
v_t	True wind speed	m/s
v_{in}	Turbine cut in speed	m/s
v_{off}	Turbine cut off speed	m/s
v_{rate}	Turbine rated speed	m/s
v_{si}	Speed of wind at height i	m/s
v_a	Apparent wind speed	m/s
H_i	Height of wind	meters
H	Height of turbine	meters
t	Draught	meters
b	Beam	meters
l	Length	meters
Θ_s	Solar angle on tilt surface	rad
a	action	vector
s	state	vector

Acronyms

Symbol	Meaning
AST	Apparent solar time
DOD	Depth of discharge
DLF	Demand Load Following
$EWMA$	Exponentially Weighted Moving Average
GAF	Generation Absolute Following
GFH	Global Finited Horizon
GHI	Global Horizontal Irradiance
$LPSP$	Lost Power Supply Probability
$REHS$	Renewable Energy Harversting System
RL	Reinforcement Learning
STC	Standard Test Condition
SOC	State of Charge
WSN	Wireless Sensor Netowrk

Acknowledgements

Firstly, I would like to thank my parents for their love and support. Without them, the journey toward a PhD would be impossible.

I would also like to express my gratitude to my supervisors Dr. Nicholas Townsend and Dr. Mingyi Tan. They were always a great listener and advisor in the last few years. At the same time, the financial support from Lloyd's Register Foundation is appreciated.

My sincere thanks also go to members at Fluid Structure Interactions research group. A healthy workplace environment, as well as real friendship, helped me to get through the dissertation period.

Last but not least, I would like to thank Southampton Sailing Robot Team. The adventure with the team inspired my research and encouraged me to explore the future of fully autonomous sustainable maritime robots.

Chapter 1

Introduction

1.1 Motivation and background

Recent advances in computer vision, wireless communication, sensor technology, and artificial intelligence have led to many breakthroughs in robotic systems. The robots' capabilities have evolved rapidly to achieve many challenging tasks such as exploring the unknown area (Figure 1.1a) transporting customer from place to place (Figure 1.1b). The power supply of the robot, however, still relies on finite energy sources such as the battery or fossil fuel. Robots need to stop regularly to charge the battery or refuel the tank that the range and duration is restraint. Due to the nature of finite energy sources, the autonomy of the robot is limited by the capacity of the energy sources. This poses a great challenge to field robot that operated far from the reach of human operators.

The focus has been given to sustainable energy sources to overcome the energy supply issue for long term autonomy. The renewable energy harvesting system (REHS) is a promising solution that could collect the energy from the environment to provide a sustainable power supply. Some of them are shown in Figure 1.1c :The Facebook Aquila drone ([24]) is a long-endurance high latitude unmanned aerial vehicle that using solar power to stay in the air to delivery internet connection to the ground. The Saildrone [63], an autonomous ship (Figure 1.1d) harnessing the wind and solar energy to collect data from the ocean.

The key advantage of using renewable energy harvesting system as the power supply is its sustainability. Energy sustainability ensures the uninterrupted power to the mobile robot and environmental sustainability eliminates greenhouse gas emission. Furthermore, the cost saving in labour cost associated with routine battery exchange or fuel refill could be saved. Ultimately, the renewable energy harvesting system could enable application in sustainable transportation (e.g. in [77, 52]), real-time environmental monitoring (e.g in [59, 43, 15]) and aerial intelligence sensing (e.g in [13, 66]).

While the potential benefits of renewable energy to robots are clear, the scarcity in REHS research for mobile robots limits the wider adoption. Current research on REHS is limited to stationary applications such as off-grid power supply system and wireless sensor network (WSN) that operating at the same location after the deployment. The application-based and domain-specific REHS model theory and design techniques lack the understanding of moving systems.

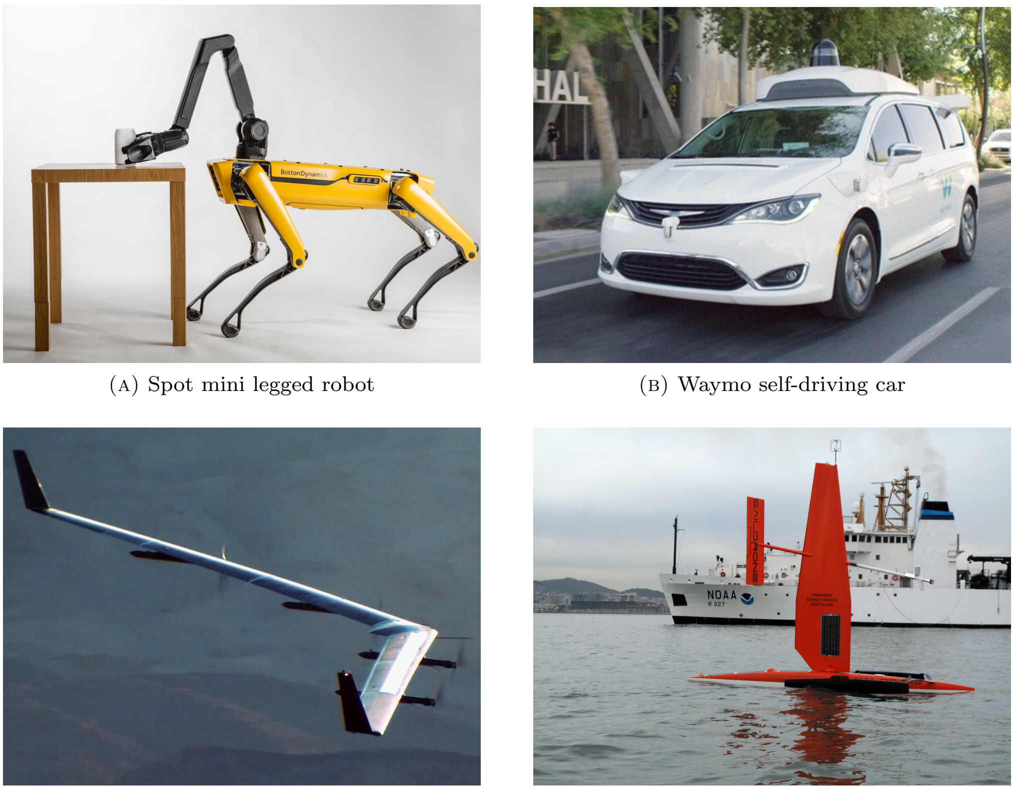

(A) Spot mini legged robot

(B) Waymo self-driving car

(C) Facebook Aquila connectivity drone

(D) Saildrone autonomous sailing boat

Photo credits:
(A) Boston Dynamics, accessed at: bostondynamics.com/spot-mini
(B) Waymo/Beebom, accessed at: beebom.com/uber-alphabet-waymo-cars/
(C) Facebook research/IEEE spectrum, accessed at: spectrum.ieee.org/tech-talk/telecom/internet/facebook-pulls-out-of-secret-spaceport-internet-drone-tests
(D) Saildrone/NOAA, accessed at: pmel.noaa.gov/ocs/saildrone

Figure 1.1: The trends in cleaner and more capable robots

REHS consists of one or more energy harvester(s), storage devices and control unit. Energy harvester(s) harness power from renewable energy resources and the storage devices reserve excessive energy for any future shortage. Power system model including the generation and demand on stationary applications is an established area of research. On the contrary, there is little research on the power system model on a mobile robot. As the robot travels, how the motion in global and local scale would influence the power system is still unknown. The motion of the robot has not to be included in any of the existing stationary models. A moving REHS model is necessary to estimate the power conversion and demand load of the mobile robot.

Off-grid power supply and wireless sensor network (WSN) are the most successful applications in current REHS research. The off-grid power systems harvest renewable energy to supply sustainable energy for the rural area. Off-grid application such as Siddaiah and Saini ([86]) and Singh and Fernandez([88]) match the power conversion and the demand load with an appropriate size of energy harvesters and capacity of storage devices. Mobile robots, on the other hand, have a strict size constraint on the size of energy harvesters and storage devices due to the space limitation. Most common design methods for off-grid application do not apply to the REHS design problem on the mobile robot as space is always limited on board. WSN is low power sensor nodes powered by renewable energy harvesting system. As a miniature sensor node, the WSN is also suffering the limited space issue. Since it is possible to increase the size of energy harvesting devices, the WSN have to dynamically adjust its power consumption level depending on the energy availability. Chauhan and Saini([21]) and Wang et al.([102])'s work on the REHS design for WSN is an example in space-limited design. However, the main challenge of the mobile robot is that the robot has to maintain a minimal level of power supply for the safety-related systems. The requirement on the power system is similar to off-grid application but the constraint is close to WSN. How to deal with this design challenge with conflicting design objectives have to be addressed to plan the REHS configuration for the mobile robot.

REHS reliability is often subject to highly variable renewable energy resources. Conventional REHS has to rely on a dynamic power management strategy for operational reliability. The power management strategies for off-grid power supply such as Riffonneau et al.([81]) and Tazvinga et al.([94]) are developed for system without size constraint. While power management strategies for WSN e.g. Kansal et al. ([44]) and Dargie([26]) allow an adjustable duty cycle as low as zero during the operation. Despite those efforts, the performance of those management strategies cannot guarantee any reliability performance of the mobile robot from their assumptions.

1.2 Research scope

This research focuses on the reliable power supply for fully autonomous maritime robots. To be more specific, the main area of interests is the method and the technique in the model, design and management of power system on maritime robots.

Firstly, the research on the renewable energy system is limited to the energy harvesting in the form of electrical power. There are multiple ways for the mobile robot to harness the energy from renewable resource e.g. directly use mechanical power. However, the robot always requires electricity to control and navigate itself. Regardless of how the energy is used, harvest electricity from renewable resources is necessary for the robot.

Secondly, the hybrid power system is the focus of the research. Maritime robots are limited in space and both wind and solar resources are widely avaliable on the sea. The hybridisation could potentially increase the overall energy density for a higher electrical power generation. Moreover, the complementarity in between multiple resources could also be exploited for a better power supply reliability.

Last but not the least, the life-cycle reliability of hybrid renewable energy system is considered in this study. Power supply reliability are curical to the safe operation of fully autonomous maritime robots. Hence, the power system performance include not only the design of renewable energy harvesting system but also during the operation of maritime robots.

1.3 Aim and objectives

The aim of this research is to develop the methodology to design the renewable energy harversting system for fully autonomous maritime robots.

Despite the benefits in utilising REHS on maritime robots, current research reveals little about the REHS on mobile robots. The research aim above raises the following core research objectives:

- To review the literature concerning the stationary REHS applications and find the gap in conventional model, design and management methods.
- To develop a power system model including both global and local motion of the mobile robot.
- To establish a design method to optimally size the REHS configuration for reliability and economic performance under size constraint.
- To access the power management strategy for a guaranteed minimal level of power supply during the operation.

Each research objective is associated the previous one so they have to be answered in order. Research objectives are intended to contribute the understanding of REHS on mobile system and provide recommendation in the model, design and management of REHS. The result will ultimately improve the power supply quality for the maritime robot.

1.4 Thesis outline

The thesis is organised in seven chapters. Figure 1.2 outlines the general structure of the thesis as a component chart. This chapter overviews the background and objective in the research.

Chapter 2 provides a critical assessment on the current research related to the REHS. The assessment includes both state-of-art model, design and management methods in stationary REHS and the application of renewable energy system on mobile robots.

Based on gap in the research, the method and the technique for the REHS model, design and operation will be presented from Chapter 3 to Chapter 5. Chapter 3 (shown in green) proposed a novel moving REHS model method with both global and local motion of the robot. The power system is numerically simulated by a data-driven approach. With the help of the moving REHS model and simulation approach, the influence of the global and local motion of the mobile robot on the power system is also discussed.

Chapter 4 (shown in blue) presents methods for designing a reliable and cost-effective REHS under the size constraint. Specific design objectives and constraints are first presented in the chapter. This chapter then explains how to form the design challenge as an optimisation problem. The formulation of the optimisation problem as well as the solving algorithm is presented in detail.

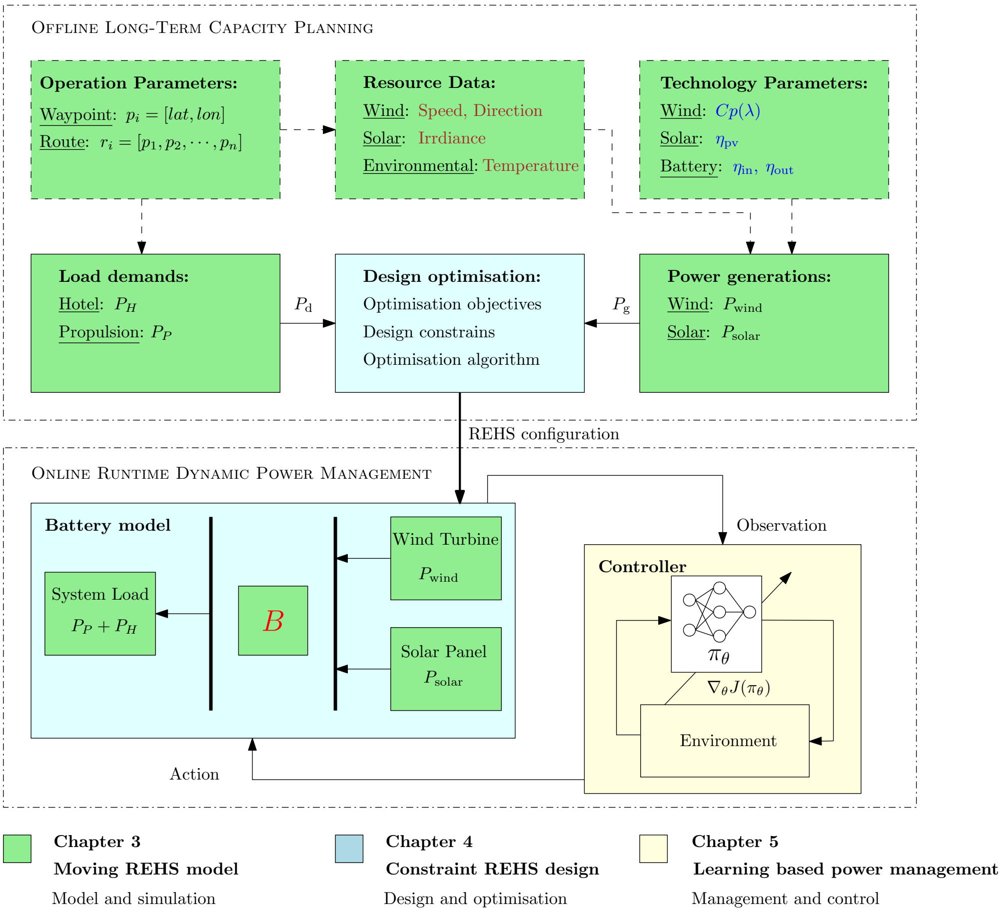

FIGURE 1.2: Outline of the thesis

Chapter 5 (shown in yellow) introduces the power management strategy for operational reliability. The power management strategy employs a learning-based method to plan power usage for mobile robots. In this chapter, the background of the strategy learning method is first introduced. Later on, the power management strategy is compared with benchmarking algorithms. The result is discussed to show the possible benefit of using a learning-based strategy for long term reliability performance.

Chapter 6 demonstrated all proposed methods for reliable REHS in a single case. An autonomous surface vehicle power system design case is studied in this chapter. The case illustrated the challenges in model, design and manage REHS on a mobile robot, and more importantly, showed the improvement with regards to a real-world use case.

Chapter 7 summarised the findings and recommendation in the research. The future work is also recommended at the end of this chapter.

Chapter 2

Literature review

2.1 REHS model

The literature on the modelling of the REHS has paid particular attention to the power generation on stationary off-grid power systems where the system remains at the same location during the operation. A considerable amount of literature on REHS has been published on the off-grid power system (for example [113, 86, 88]), wireless sensor network (for example [72, 95, 96]) and self-powered condition monitoring applications (for example [42, 7, 18, 65]).

There is no consensus on the term to describe the robotics system powered by the renewable energy in the literature. The renewable robot is a well self-explanatory term for the robot. Lamarca et al. ([49]) discussed the potential of using renewable energy directly from the deployment environment. In this study, the author concludes the energy harvesting techniques are only capable of providing power to wireless sensor application. Iqbal and Khan ([40]) reviewed the potential in using renewable energy for the power supply to the mobile robot in Pakistan. The conclusion of this study, however, is that renewable energy can serve as a preferred choice for autonomous robot power.

Those studies have contradicting conclusions but none of them has a quantitative assessment on the actual power generation. Both Lamarca et al. ([49]) and Iqbal and Khan ([40]) estimate the energy generation potential without include the harvesting efficiency and the motion of the robot. What remains unclear is how those factors would impact their conclusion.

Pudney and Howlett ([77])'s work on the solar-powered race car optimised the speed of the vehicle depends on the solar radiation. This work recognises the importance of the global and local motion on the critical speed of the vehicle. However, there is no further discussion on how to model the global and local motion in this work.

Crimmins et al. ([25]) introduce the solar-powered autonomous underwater vehicles for long endurance survey. A solar panel was installed on the vehicle to extend the duration of the robot. The vehicle surface to recharge during the day and submerge to operate during the night. Crimmins et al. conclude the vehicle is suitable for long-term oceanographic survey with a 7.5

hours trial result. The method to estimate the power system model for long-term operation is not clear.

Glykas et al. ([33])'s work on greenhouse emission reduction by integrating renewable energy is focused on ocean surface vehicles. A simplified temperature model is used to evaluate the potential energy-saving based on a rough global region classification. The ocean has been divided as 6 horizontal zones depending on its latitude. This work recognised the difference in solar radiation because of the global motion.

Joshi et al. ([43]) propose another solar-powered autonomous underwater vehicle concept for ocean exploration. In this design, the variation of the solar spectrum and solar cell response is modelled. This result from the model reported the solar incidence angle has an impact on the total harvested energy. The geometry of the solar panel is considered in this model, making it possible to include local motion in the REHS model. Global motion of the vehicle that influences the power generation from resources side is not discussed in this paper.

Bowker et al. ([15]) explore the possibility of harvesting wave energy for the propulsion system. In this work, a pair of wave energy harvesting devices were installed on an autonomous surface vehicle. The wave motion is captured by the flappy foil energy harvesting devices. The wave energy was captured as kinetic energy to directly propel the vehicle in the ocean. This mechanism could potentially be used to generate electricity from the wave, however, the power system model is not provided. Chao ([19]) use the ocean thermal energy to power the underwater float. The principle in ocean thermal energy harvest is to exploit the temperature difference between water columns. Sensors powered by the ocean thermal energy converter is supposed to deploy at a specific site. None of the global and local motion is included in the power generation model.

Colas et al. ([24]) model solar panel local motion when estimating the power generation. The normal vectors of the solar panel are recorded and the solar incidence angle is calculated. Local motion in solar power generation is included in the power system model. However, the aeroplane is not designed for long-distance travel and there is no global motion factor in the model.

Table 2.1 summarised researches on the renewable robots in the source of energy, application and purpose of the power supply. Besides, whether the global or local motion is included in the model is also presented in this table.

Table 2.1: REHS model literature

	Source of energy	Application & Purpose	Global	Local
Pudney and Howlett ([77])	Solar	Land vehicle; propulsion	-	-
Crimmins et al. ([25])	Solar	Underwater vehicle; not specified	-	-
Glykas et al. ([33])	Solar	Ocean vehicle; fuel saving	yes	-
Khare and Singh ([46])	Solar & wave	Ocean vehicle; fuel saving	-	-
Joshi et al. ([43])	Solar	Underwater vehicle; not specified	-	yes
Bowker et al. ([15])	Wave	Ocean vehicle; propulsion	-	-
Lemaire et al. ([51])	Wind	Ocean vehilce; propulsion	-	-
Chao ([19])	Thermal	Underwater float; sensors	-	-
Colas et al. ([24])	Solar	Aerial vehicle; all systems	-	yes

Table 2.2 further summarised REHS models found in those applications. None of them considered both global and local motion when estimating the power generation.

Table 2.2: REHS model literature classification

Global motion Local motion	not considered	considered
not considered	Crimmins et al. ([25]),Khare and Singh ([46]), Pudney and Howlett ([77]), Chao ([19]) Bowker et al. ([15]), Colas et al. ([24])	Glykas et al. ([33])
considered	Joshi et al. ([43])	this work

On the application side, there is no general REHS model established the relationship between the power generation and both motions. A moving REHS model could help to understand the power generation under both global and local motion. Whilst current research on REHS model is missing from the application side, there are many pieces of literature available on the power generation.

RHES models are implemented in software for the design and optimisation. Common software packages are reviewed in Table 2.2. As it is shown in the table, most of the software packages are able to model the hybrid system consists of PV, wind and storage. Different packages are featured in various use cases, e.g. TRNSYS is famous for the trainsit modelling capability. However, all packages are focused on the statinoary applications such as stand alone or small grid.

Table 2.3: REHS software comparison

Software	Models	Feature	Applications	Developer
HOMER	PV, wind, harvesters, biomass, fuel cell, hydro, storage	Easy to use GUI	stand alone, small grid	National Renewable Energy Laboratory
RETScreen	PV, wind, hydro, strorage	Excel based interface	stand alone	Ministry of Natural Resources
iHOGA	PV, wind, hydro, fuel cell, harvester, storage	Hybrid optimisation	stand alone, small grid	University of Zaragoza
TRNSYS	Thermal, PV, wind, storage	Transite state modelling	stand alone, thermal design	University of Wisconsin and University of Colorado
Dymola	PV, wind, harvesters, fuel cells, storage	General purpose simulation	stand alone, small grid	Dassault Systmes

Popular software packages are not applicable to the moving system that the model assumptions are based on the stationary cases that the system stays at the operation site. This motivate us to develop a custom simulation and optimisation package for the mobile robots.

This thesis focus on the wind and solar energy due to its general availability. Wind and solar energy are the most common resources that are accessible to the aerial, maritime and land robots. The domain-specific resource, however, can be integrated into the model given there is a way to estimate the power generation under both global and local motion.

2.1.1 Solar power system

The solar power system for stationary applications is a well-established area of research. The power generation mechanism (e.g [55, 70]), energy harvesting devices modelling (e.g [20, 89, 84]), energy harvesting control strategy (e.g [108, 62, 57, 58]), solar (e.g. [54, 29, 74, 61, 106, 10]) and solar radiation data acquisition (e.g. [2, 34, 80, 50]) can be found in many literatures.

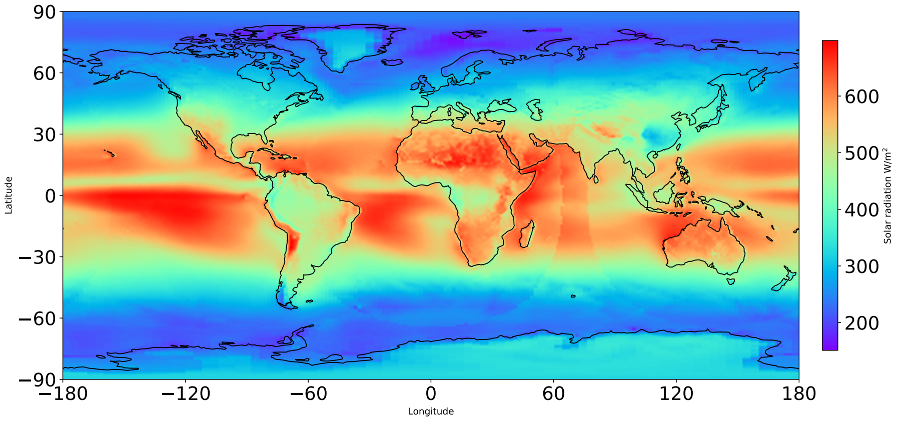

FIGURE 2.1: Global annual averaged solar radiation (data source NASA SSE)

The global solar power resource is unevenly distributed. Figure 2.1 shows the global yearly averaged solar radiation. From the resource side, the global motion would have an impact on power generation. In the literature, global horizontal irradiance (GHI) is the most common used to measure the solar resource. The global horizontal irradiance on a flat surface is:

$$I_g = I_b + I_d \cos(\theta_z) \tag{2.1}$$

where I_g is GHI, I_b is direct normal irradiance (DHI), I_d is the diffused horizontal irradiance (DNI), and θ_z is zenith angle.

When sunlight strikes through the atmosphere of the planet, part of light directly incident on the surface of the earth as direct radiation [shown in Figure 2.2 (A)]. The rest of sunlight scattered by molecules and particles in the atmosphere as diffuse radiation. The direct part is direct normal irradiance (DNI) and the rest is diffused horizontal irradiance (DHI).

The total solar radiation on the panel consists of three parts [shown in Figure 2.2 (B)]. Total solar radiation on the panel depends on the solar irradiance on the earth surface as well as the geometry of the panel. Total solar radiation (also known as POA irradiance) G_g is:

$$G_g = G_b + G_d + G_r \tag{2.2}$$

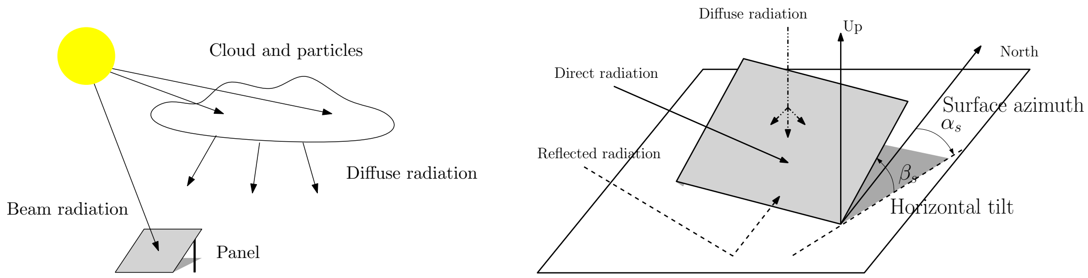

(A) Components of solar radiation (B) Solar radiation on tilt surface

FIGURE 2.2: Different components on tilt solar panel

where G_g is global radiation, G_b is beam radiation, G_d is diffuse radiation, G_r is reflected radiation, all unit in W/m^2.

Beam component depends on the solar angle θ_s between the panel and the Sun:

$$G_b = I_b \cos(\theta_s) \tag{2.3}$$

Diffused radiation on solar panel according to Liu and Jordan ([54]) model is:

$$G_d = I_d \frac{1 + \cos(\beta_s)}{2} \tag{2.4}$$

where β_s is the horizontal tilt shown in Figure 2.2(B).

Reflected radiation on solar panel is:

$$G_r = I_b \rho \cdot \frac{1 - \cos(\beta_s)}{2} \tag{2.5}$$

where ρ is reflectivity index. Values on common surface are shown in Table 2.4.

TABLE 2.4: Typical reflectivity index [98]

Surface	Typical albedo
Fresh asphalt	0.04
Open ocean	0.06
Worn asphalt	0.12
Conifer forest(Summer)	0.08 0.09 to 0.15
Deciduous trees	0.15 to 0.18
Bare soil	0.17
Green grass	0.25
Desert sand	0.40
New concrete	0.55
Ocean ice	0.5 to 0.7
Fresh snow	0.80 to 0.90

The local motion would have an impact on the power generation because of the change in solar panel geometry. Current literature does not include the local motion in the total solar radiation on the solar panel.

The solar power generation model suggested by Huld et al. ([39]) estimate power production from solar panel depends on the intensity of solar radiation, the efficiency of solar panel and the temperature.

$$P(G_g, T) = P_{\text{STC}} \cdot \frac{G_g}{G_{\text{STC}}} \cdot \eta_s(G', T') \tag{2.6}$$

where G_g is global radiation on solar panel, T is module operating temperature of solar panel. $G' \equiv G_g/G_{\text{STC}}$ and $T' \equiv T/T_{\text{STC}}$ are normalized solar radiation and operation temperature, $G_{\text{STC}} = 1000W/m^2$, $T_{\text{STC}} = 25°C$ is solar radiation and module operating temperature under STC (Standard Test Condition), solar module η_s is module efficiency in the model depends both total solar radiation and operating temperature.

Many different solar cells are operating under the same principle – photovoltaic effect. As light from the sun hit the surface of solar panel, it excites an electron into a higher-energy state, an electric potential is then produced by the separation of charges. During the energy conversion, only photons at a suitable energy level can be effectively absorbed and converted into electricity. Not all energy from the light can be fully turned into electrical energy, photons with energy much greater than the bandgap is wasted. Similarly, Photons with energy less than the bandgap energy passing through the semiconductor as if it were transparent.

Typical commercial products have a solar module efficiency around 21.5 % Green et al. ([35]), research solar panel in the laboratory is reportedly as high as 43 %. Those efficiencies are tested under Standard Test Condition (STC): irradiance of $G_{\text{STC}} = 1000W/m^2$, spectral distribution through airmass 1.5 and module temperature at $T_{\text{STC}} = 25°C$. Actual energy conversion of the solar panel is determined by the solar irradiance, spectral distribution, temperature and geometry of solar panel.

Solar irradiance data is often presented as global solar radiation on a flat surface. The solar irradiance components have to be decomposed from GHI to estimate the total radiation on the panel.

In Liu and Jordan ([54])'s early work, the decomposition is based on the clearness index. Clearness index is defined as:

$$k_t = \frac{I_b}{I_0 \cos \Theta_z} \tag{2.7}$$

where I_b is beam radiation, I_0 is extraterrestrial radiation at a constant of 1367 W/m^2, Θ_z is the zenith angle.

Diffuse fraction $k_d = I_d/I_g$ is correlated with k_t using measurements from 98 sites in U.S. and Canada: $k_d = f(k_t)$. A similar study was done by Erbs et al. ([29]) developed relationship between diffuse fraction k_d from hourly, daily and monthly-averaged global radiation.

Iqbal ([41]) use two parameters, including clearness index k_t and solar elevation α (shown in Figure 3.6), as predictors in this model to predict hourly diffuse solar radiation from measured global radiation. Skartveit and Olseth ([90]) employed the same two parameters approach in their correlation and then later they further included a new parameter hour-to-hour variability index in their model ([91]). Reindl et al. ([79]) taken two more parameters ambient temperature and relative humidity to the clearness index and solar elevation. The full diffuse fraction correlation reduced the residual error by 14% compares to a clearness only index, 9% compares to clearness and solar altitude indices. The hourly diffuse fraction k_d was not only the function of clearness index k_t. Maxwell ([61])'s quasi-physical model converting hourly global horizontal to direct normal radiation by the exponential model. Perez et al. ([74]) improves Maxwell ([61]) model by introducing the hour-to-hour variability index and use surface temperature and relative humidity in this quasi-physical model. Boland et al. ([10]) take another approach, using apparent solar time as a predictor. A new model was purposed by Ridley et al. ([80]) based on logistic function. This model is developed with a new statistical approach by Bayesian inference Lauret et al. ([50]). This model is named as BRL-model (Boland-Ridley-Lauret-Model) with clearness index k_t, apparent solar time (AST), solar elevation α, daily clearness index K_t and persistence index. These works have established the relationship between solar geometry and the total solar radiation on the panel.

As it is shown in Figure 2.3, there are two missing links in the current researcher. The influence of global motion on the resource and the local motion on total solar radiation is unclear. The global motion needs to be integrated into the solar radiation model that difference in a solar resource is missing in the model. Solar geometry model also has to include the local motion when estimating the total solar radiation on the panel.

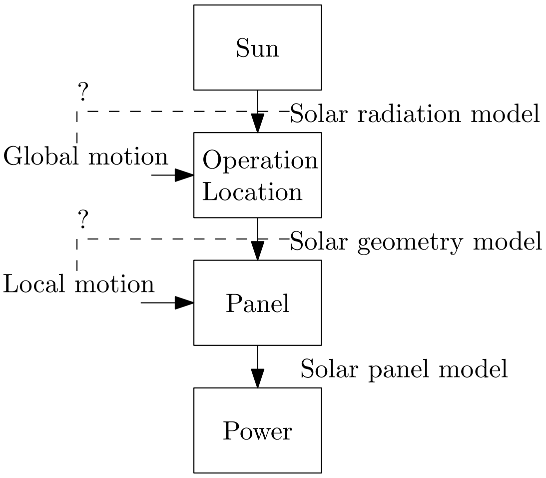

FIGURE 2.3: Research gap in solar power model

2.1.2 Wind power system

Wind power is another source of renewable energy commonly used by the REHS. Previous research on the wind power model have been focused on the wind power generation potential assessment (e.g [3, 78, 82]), wind power harvester design and control (e.g [64, 92, 14, 83, 68, 1]), and wind resource forecasting (e.g [87, 6, 69, 103]). Most of these studies were carried out for stationary applications.

Similar to the solar energy harvesting potential, the wind power resource is also highly variable globally (shown in Figure 2.4). The annual averaged wind speed distribution shows the energy harvesting potential.

For long-distance travel, the global wind energy distribution would have an impact on the power generation. However, most related research in this area only estimates the wind power generation for stationary applications. Archer and Jacobson ([3]) evaluated the global wind power generation potential from surface station measurements. The global power generation potential is calculated

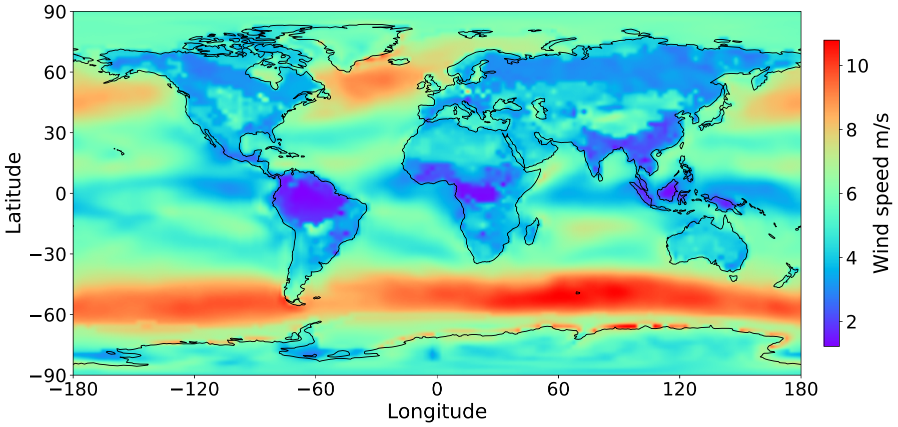

FIGURE 2.4: Global annual averaged wind speed (data source SSE)

from a number of ground measurements. Wind turbine model used in this evaluation is the stationary model. Lu et al. ([56]) derived the global wind-generated electricity potential through meteorological assimilation data. Stationary wind turbine model was used with those data. Zheng and Pan ([112]) assessed the global wind energy resource on the ocean. The global ocean wind energy generation potential is analysed by a stationary wind turbine model.

In those literature, the wind power generation model is often modelled as a piecewise function Equation 2.8.

$$P(u) = \begin{cases} 0 & u \leq v_{\text{cut-in}} \\ \frac{1}{2}\rho C_p(\lambda) A u^3 & v_{\text{cut-in}} \leq u \leq v_{\text{rated}} \\ \frac{1}{2}\rho C_p(\lambda) A v_{\text{rated}}^3 & v_{\text{rated}} \leq u \leq v_{\text{cut-off}} \\ 0 & u > v_{\text{cut-off}} \end{cases} \tag{2.8}$$

where u is wind speed, $v_{\text{cut-in}}$ is cut-in wind speed, v_{rated} is rated wind speed, and $v_{\text{cut-off}}$ is cut-off wind speed. C_p is power coefficient (where typical values can be found in Figure 2.5) that depends on the shape of wind turbine and tip speed ratio λ.

This stationary model reflected the operation characteristic of a stationary wind turbine. When the wind speed is lower than the cut-in speed, there isn't enough momentum from the wind to overcome the inertia of the rotor to produce any electricity. As the wind speed goes higher, the power generation from wind turbine follows the cubic rule. When the turbine operates at wind speed higher than rated speed, the power generation is limited to the rated level with active control. If the wind speed exceeds the cut-off speed, the wind turbine will stop to prevent itself from over speeding.

For a stationary turbine, there is no local motion that the base would move, so the wind speed u is the same as the true wind speed. However, the wind power generation on a moving system, in the case when wind speed experienced by the turbine is different from true wind speed, is still unclear.

More pieces of literature can be found on the application of wind energy on moving systems. Those studies evaluated the benefit of using wind energy for several moving systems.

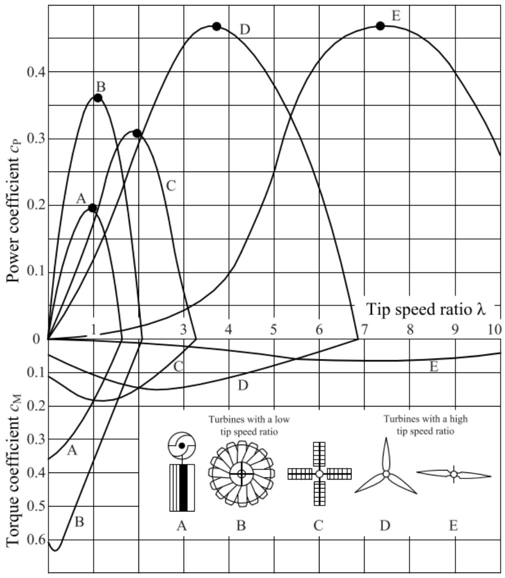

FIGURE 2.5: Power coefficient of different types of turbine [98]

Chen et al. ([23]) developed a small (30 cm rotor diameter) horizontal-axis wind turbine for an automobile. In this paper, the author claimed that the moving automobile is suitable for the turbine installation for two reasons. Firstly, the wind on a moving vehicle has a higher speed and more stable than natural wind. Secondly, the turbine can avoid or minimise the additional aerodynamic drag when installing at a proper location. However, the author hasn't provided any detail on how to reduce drag while generating power. Furthermore, how much power would be lost due to the aerodynamic drag of the wind turbine is not considered by the authors.

Traut et al. ([97]) studied the direct use of wind energy in the form of kinetic energy capture. It compares the potential energy saving from a kite and a Flettner rotor. Traut et al. considered the additional drag of the wind turbine. The net power saves also discount the additional drag that depends on the wind velocity. The paper concludes that power saving depends on the course of the ship and true wind velocity. For the moving wind power system model, if a similar approach

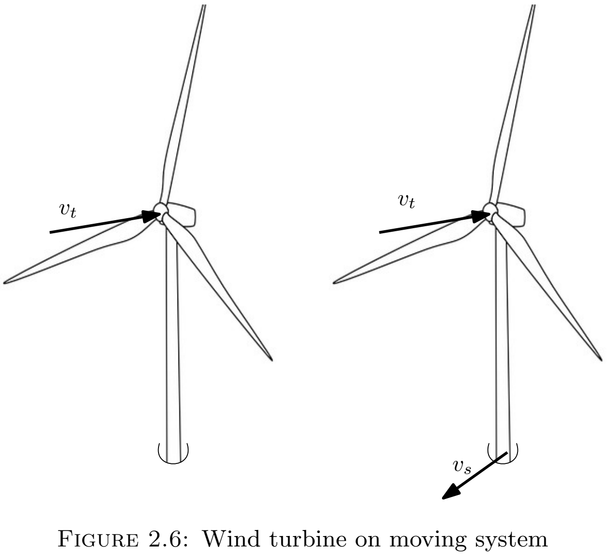

FIGURE 2.6: Wind turbine on moving system

is taken, the power generation would also depend on the course of the robot and the true wind velocity.

Viola et al. ([99]) also studied the potential of using wind energy to reduce the emission of merchant ships. In this study, wind energy is directly harvested as the kinetic energy to propel the vehicle. The saving on the propulsion depending on the wind direction as well.

Due to the lack of moving wind turbine model, this research will investigate the wind power generation under both local and global motion. This will help us to estimate the power generation when the robot is moving.

2.1.3 Battery model

The battery system is the energy storage device in the REHS. It stores excessive energy if the generated power is unused. When there is a power generation shortage, the battery can discharge to make up the difference. As one of the key components in REHS, the battery help mitigate the variability and intermittency of renewable energy resources. The battery's normal operation is important to the reliability of the power system.

In most REHS literature, the battery system is modelled as a non-ideal energy storage model with charge and discharge efficiency. The energy remains in the battery is indicated by the state of charge (SOC). SOC of the battery can not fall under a certain level to prevent the battery from over discharging. The minimal level of energy has to remain in the battery is called the depth of discharge (DOD).

During the long period of travel, the battery may be subject to the different working condition compared to stationary application. The vibration and stress impact due to local motion has been studied and tested in various literatures. The lithium-ion battery vibration test Brand et al. ([16]) shows there is no failure in all tested cases. Durability test conducted by Hooper et al. ([38]) shows there is no statistically significant electro-mechanical degradation when subject to 10 years of representative vibration. From that research, the impact of local motion considered to be minimal that which be neglected in the battery model.

Temperature difference due to long-distance travel may also have an impact on battery performance. Gao et al. ([31]) analyse the temperature effect on the lithium-ion battery by the simulation model. The comparison between datasheet values shows a significant drop in battery voltage at the extremely cold environment (-10 to -20 $^{\circ}C$ which is considered as below averaged operating temperature for the robot). The temperature effect can be modelled as charge and discharge inefficiency at a low temperature similar to Bhuiyan and Ali Asgar ([9]).

Another factor to consider is the battery capacity will degrade over time. Erdinc et al. ([30]) reported how the charge cycles would affect the battery capacity. It has been showed that the lithium-ion battery capacity has a 5% reduce after 100 charges and 18 % lost after 600 charges. The battery model needs to correct the capacity for the operation depending on the charge cycles. Research on high current discharge of the lithium-ion battery [101] shows the voltage drops much quciker than the lower current. In order to the maintian the best performance of the battery, the discharge rate of battery also have to be carefully consider to extend the life.

Global and local motion only had an indirect impact on the battery. The battery system would operate in a similar manner on renewable robots according to the above findings.

2.1.4 Demand load

The demand load is the total electrical power consumption required by the mobile robot. The REHS provide power supply to support the operation of the robot. To design a REHS an understanding of the demand load is required.

In mobile robot power system design (e.g in [105, 60]), the demand load is modelled as propulsion and hotel load. The propulsion load is the total energy consumption used to drive the robot. Hotel load is the demand on all peripheral systems such as navigation system, communication system and sensory payloads. This classification is proposed for finite energy sources powered robots, such as battery, fuel or biomass.

Most of the papers on stationary REHS uses a fixed representative load profile as load demand in the model. In Borowy and Salameh's work([12]), they design an REHS using a typical house energy consumption load profile. Yang et al. ([109]) design a hybrid power system for telecommunication relay station with constant demand load. Koutroulis et al. ([48]) propose a design strategy of a stand-alone REHS to a residential household. In their model, the load demand was derived from daily power consumption. The shortcoming of using daily load profile in a moving system is the demand load of the renewable robot is not only temporal but spatial dependent. According to the classification of the propulsion and demand load, all power consumed is hotel load.

Demand load of small stationary REHS systems such as wireless sensor network are often modelled as variable power consumption. This is due to the power generation on these devices are limited by space. To cope with the intermittent power generation, the demand load has to dynamically adjusted according to energy availability. Kansal et al. ([44]) modelled the demand load as a controllable power consumption managed by the REHS. Torah et al. ([96]) self-powered autonomous wireless sensor node also models the demand load as a controllable variable. Park et al. ([73]) uses the REHS in structural health monitoring sensor networks. Power consumption of a wireless sensor network is modelled as a dynamic demand load.

Renewable robot's demand load is similar but different from stationary applications. It has a size constraint similar to the small stationary application while the power system has to provide a minimal level of supply for the safe operation. Renewable robots have a power supply reliability requirement as well as limited by the space on board.

To date, there is demand load model include both variable and constant components. However, a demand load model with a continous changing operation location is not avaliable. Such a demand load model would be useful to guarantee a minimal level of power supply and to adjust the power supply according to the energy availability.

2.2 REHS capacity planning

There are multiple objectives when designing REHS for renewable robots. Optimisation based design methods are often used to find the best trade-off in between those objectives and help to plan the capacity of the REHS. Two most common objectives are optimised in the design stage. The reliability of the power system and the economic performance of the REHS. Reliability of the power system is often indexed as the ratio of time that demand load is not supplied by the power generation. Economic performance can be the device cost or averaged cost of the energy.

There are many optimisation based design methods in the literature that been used to plan the capacity of the REHS. Borowy and Salameh ([12]) design an REHS with hybrid wind and solar sources for house electricity supply. An optimisation method is used to find the most cost-effective configuration with a constraint on reliability. The reliability was measured by lost power supply probability (LPSP), the fraction of time that the power system failed to supply sufficient power to the demand load. The optimisation algorithm is an iterative search method. The optimal capacity by incrementally searching on the battery and the numbers of photovoltaic (PV) modules. Koutroulis et al. ([48]) plan the capacity of wind and solar hybrid renewable energy system. The design has multiple objectives to achieve at the same time. The total capital cost and maintenance cost are both optimised. A heuristic search algorithm called a genetic algorithm (GA) was used in the optimisation process. Yang et al. ([109]) optimise an REHS for telecommunication system using a similar model. The design goal is to minimise the levelised cost of energy with a constraint on LPSP. An iterative search method was used to find the best configuration for the REHS. They further developed their model in [110] and use GA to optimise both levelised energy cost and lost power supply probability. Belfkira et al. ([8]) design the stand-alone hybrid renewable energy system for rural energy supply. They use a global search optimisation algorithm called DIRECT to find the configuration with minimal energy cost. This method is a heuristic search based on REHS reliability and cost. Wang et al. ([102]) present their work on the community based smart grid with a design goal to minimise the use of grid power and energy cost. They modelled the grid and solve the design problem by a mixed-integer linear programming method. Singh and Fernandez ([88]) use another heuristic search algorithm to optimally plan the capacity of the REHS. The optimisation algorithm Cuckoo Search mimics breeding behaviour. The design objectives are reliability, total system cost and energy cost.

TABLE 2.5: Overview on REHS capacity planning literatures

	Application	Constraint	Objective(s)	Optimisation algorithm
[12]	house electricity	LPSP	minimise device cost	incremental search
[37]	not specified	LPSP	-	neural network
[48]	commercial use	LPSP	minimise device capital and maintenance cost	GA
[109]	telecommunication	LPSP	minimise energy cost	iterative search
[110]	telecommunication	LPSP	minimise energy cost replacement cost maintenance cost	GA
[8]	not specified	LPSP	minimise energy cost	heuristic search
[102]	smart grid	LPSP power ramping	minimise energy cost	linear programming (LP)
[88]	rural area	LPSP	minimise device cost and energy cost	cuckoo search

Table 2.5 summarised research in the application, design constraint, design objective and optimisation algorithm.

In those discussions, the REHS were all designed for stationary applications. Design objectives are different from application to application. A common goal to optimise is the device capital cost of REHS. Averaged energy cost is also a typical objective in those applications.

Design objectives in stationary REHS are similar but different from mobile robots'. Most stationary REHS capacity planning optimises the system configuration for a minimised cost of energy. The goal is to design the REHS for the lowest levelised energy cost under reliability constraint. While the goal of having REHS on the mobile robot is not only energy itself but also to use the energy to support reliable long-term operation.

It is not uncommon to have both size and reliability constraint for REHS with conventional power supply backup. However, when both size and reliability are both included as optimisation constraints, the REHS may fail to meet some of the requirement. If the REHS capacity designed by the optimisation algorithm failed to meet the reliability requirement. The renewable robot will lose power supply since there are no conventional power sources to access during the operation. If the design failed to meet the size constraint, the REHS won't able to be installed on the renewable robot.

The REHS capacity has to be planned under both size constraint and reliability requirements. A further review on optimisations algorithm will show how to deal with those requirements.

2.2.1 Optimisation algorithms

The REHS capacity planning often involved with the optimisation on several conflicting objectives. This section will review optimisation algorithms on various applications. The optimisation algorithms in REHS capacity planning have been listed in Table 2.6. The design constraint, number of objectives, type of optimisation and related applications have been listed in the table.

Table 2.6: Review on the optimisation algorithms in capacity planning

	Constraint	Objectives	Optimisation type	Applications
Classical methods				
Linear Programming	✓	single	local	[76]
Non-linear Programming	✓	single	local	[111, 4]
Heuristic methods				
Genetic Algorithm	✓	multiple	global	[48, 110]
Particle Swarm Optimisation	✓	multiple	global	[104, 85, 47]
Simulated Annealing	✓	multiple	global	[28, 45]
Harmony Search	✓	multiple	global	[5, 22, 32]
Other methods				
Neural Network	×	single	-	[37]
Iterative Search	✓	single	local	[12, 109]

Linear programming (LP) form the optimisation problem as a set of linear equality constraints (shown in Equation 2.9). The goal of the optimisation is to maximise (or minimise) the cost of the system. Cost of the REHS is modelled as a linear function to the design variables.

$$\begin{aligned} \max \quad & c^T x \\ s.t \quad & Ax \leq b \\ & x \geq 0 \end{aligned} \tag{2.9}$$

where x is design variables, c is cost vector and A is constraint matrix. LP optimisation is commonly solved by simplex and interior-point methods. Privitera et al. ([76]) consider REHS capacity planning in building applications as an LP optimisation problem. LP can design the configuration with a minimised capital cost. However, no reliability constraint has been included in the study. This is partly because the reliability of the REHS is usually not a linear function to the capacity of RHES. In Yang et al.'s study [110] on multi-objective REHS design confirm the reliability constraint LPSP is non-linear in regards to REHS design variables. LP optimisation algorithms cannot handle the reliability constraint under the linear model assumption.

Non-linear programming (NLP) solve this problem by extending the constraint from linear to non-linear equations. The general form of an NLP optimisation problem is shown in Equation 2.10.

$$\begin{aligned} \min \quad & f(x) \\ s.t \quad & g(x) \leq 0 \\ & h(x) = 0 \end{aligned} \tag{2.10}$$

where x is design variable, f is a non-linear cost (also called fitness) on the design, g and h are inequality and equality non-linear constraints. The goal of NLP optimisation is the same as LP – minimise (or maximise) the fitness of the REHS design. El-Zeftawy et al. ([111]) and Ashok ([4]) did similar work in using NLP to optimise the REHS capacity. They defined the cost of energy as the objective and LPSP as the constraint. The REHS capacity is optimised to minimise the energy cost under reliability constraint. The optimal solution from NLP optimisation is chosen as the REHS capacity. NLP and LP are local optimisation algorithm. Optimisation result depends on the initial condition and may not be the global optimum if there is a local minimum (or maximum). Both LP and NLP are single objective optimisation algorithms. If there are more than one goals, multiple optimisation objectives have to be weighed and mixed as a single objective.

Another way to solve this problem is to use a multiple objectives optimisation algorithm. The multi-objective optimisation (MOO) problem involves multiple goals and the general form is shown in Equation 2.11.

$$\begin{aligned} \min \quad & [f_1(x), f_2(x), \cdots, f_n(x)] \\ s.t \quad & x \in X \end{aligned} \tag{2.11}$$

Genetic Algorithm (GA) is one of the most commonly used multiple objectives optimisation algorithms. This algorithm can natively handle the many design objectives at the same time. GA algorithm imitates the biological natural selection process. Each REHS is a candidate solution in the optimisation problem. A population of candidates represent the possible REHS solution. During each generation, a portion of candidates will be selected to breed a new generation based on their fitness. A new generation is produced after genetic crossover and mutation. As the population will keep evolving, the remained candidates are the best among all objectives. Those candidates formed the Pareto front – best objective against another objective.

Compared to single objective NLP optimisation, the MOO problem minimise several objectives at the same time. For the REHS optimisation, it means the optimisation algorithms can natively handle multiple objectives in the capacity planning e.g. minimise the cost of energy and minimise the maintenance cost at the same time.

Koutroulis et al. ([48]) and Yang et al. ([110]) plan the REHS capacity with GA optimisation. There are multiple objectives in their REHS capacity planning: the maintenance cost, the cost of energy and minimise the capital cost of devices. The GA method helped to find the best configuration among these objectives. Similar work have also been presented by Wang and Singh ([104]), Sharafi and ELMekkawy ([85]) and Khare et al. ([47]).

The relationship between each objective was also acquired from the Pareto front. These optimal configurations x are shown as black box in Figure 2.7. The outcome of GA is not a specific REHS configuration x but configurations that best on both objectives.

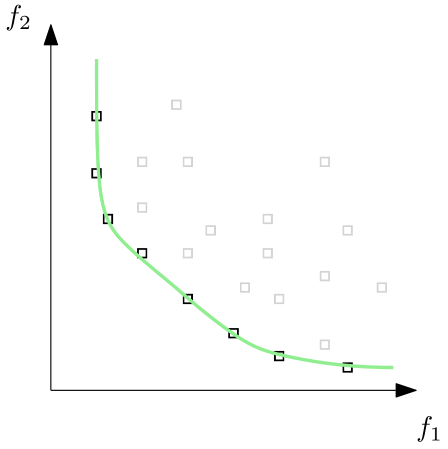

FIGURE 2.7: Pareto Front of multiple objectives optimisation

Similar heuristic-based algorithms such as Particle Swarm Optimisation (PSO), Simulated Annealing (SA) and Harmony Search (HS) are also found. Those algorithms are natively designed for the single objectives of optimisation problems. However, through the mixture of multiple objectives, those algorithms are able to solve the MOO problem in the following way:

$$\begin{aligned} \min \quad & f(x) = w_1 f_1(x) + w_2 f_2(x) + \cdots w_n f_n(x) \\ s.t \quad & g(x) \leq 0 \\ & h(x) = 0 \end{aligned} \tag{2.12}$$

where $w_1, w_2, \cdots, w_n$ are the weights on each objectives.

The result of this optimisation method is the optimal REHS configuration of x. Compared to Evolution Algorithms that natively handle multiple objectives at the same time, those algorithms present a single REHS configuration.

For the REHS capacity planning, both classes of optimisation algorithms are useful for the design. The Pareto front on multiple objectives is important to understand the relationship between each design goals. Pareto front based optimisation methods can be first used to explore the design space. If there are REHS configurations that meet the reliability and economic performance requirements, the mixed objectives optimisation method can then be employed to find the best among them.

2.2.2 Model data

The REHS capacity planning is formed as multiple objectives optimisation problem. To solve the multiple objectives optimisation problems, the reliability and economic performance of the REHS has to be simulated using representative data. Data on the power generation, demand load and economic factor have to be collected for the power system simulation.

On the power generation side, both solar and wind power generation requires data for the simulation. The simulation-based REHS capacity planning has commonly been found in the literature on the stationary REHS design. Simulation of the power system usually requires hourly data on the solar radiation, wind speed and temperature.

A global solar radiation database released by the World Radiation Monitoring Center [71] Baseline Surface Radiation Network (BSRN) is often used as the data source of global solar radiation. This network consists of 76 stations around the world that report the solar radiation on various parameters. Research on the REHS capacity collects the data from the nearest weather station to simulate the solar power generation. If there is no observation close to the design location, synthetic generated solar radiation data is also found in simulation. Graham and Hollands ([34]) developed a method to generate synthetic hourly solar radiation data globally.

In order to estimate the power generation of the panel, the solar radiation component is required on a specific time at a given location s. Measurement-based method and model-based method are two common ways to estimate solar radiation components. Measurement-based method use land [34] or satellite [27] radiation observation to quantify the total solar radiation. Model-based method regards the solar radiation as the Auto Regressive Moving Averaged (ARMA) process or Markov Chain Model (MCM), estimate solar radiation using a stochastic model. Land-based observation on solar radiation using a pyranometer sensor, it usually located at sites across the field. It provides global horizontal radiation with high precision (less than 2% uncertainty in hourly average, less than 1% uncertainty in daily average measurement) but also limited by its geospatial coverage across the world, especially over the oceans. Satellite-based observation has much greater spatial coverage over the land-based observation. Satellite estimates based on a physical model to derive downward solar irradiance at the surface of the Earth. Satellite computes the downward solar irradiance at the top of the atmosphere and subtracts the reflected energy measured by the satellite.

On the demand load side, the power system simulation also needs data support. For example, the power consumption of the renewable robot will depend on the change of wind direction and speed. Most studies in the field of renewable energy have only focused on the data collection on a single operation location. Data collection for the demand load simulation has to be solved for the REHS modelling and optimisation.

The challenge of power system simulation on the renewable robot is its spatial-temporal nature. To simulate the power generation and demand load, the renewable energy resources data has to cover a large area at sufficient resolution.

Data-driven simulation method could solve this problem by retrieving and processing renewable energy resources data in the simulation. Satellite-based observation at high spatial coverage is used in data-driven method to correct the weather model-based numerical simulation, giving a higher data resolution. The effect of cloud coverage, time, latitude are included in the solar radiation data. This dataset is often available for earth science purpose most notable is released by NASA Global Modeling and Assimilation Office – Modern-Era Retrospective analysis for Research and Application, Version 2 (MERRA-2) and European Centre for Medium-Range Weather Forecast (ECMWF) – Copernicus Atmosphere Monitoring Service (CAMS).

Compared to a measurement-based method and the model-based method, the data-driven approach has higher spatial resolution and better temporal coverage. More importantly, it also provides us with information on the temperature which is important to model the efficiency of the solar panel model.

2.3 REHS power management

During the operation of the REHS, the power generation from renewable energy resources may vary from the design scenario. The role of the power management system is to dynamically adjust the demand load according to the energy availability. The power management system decides the best use the energy after it been harvested. An overly aggressive power management strategy may increase the short-term performance of the power system but damage the long-term power supply stability. At the same time, a too conservative power management strategy may result in a waste of energy. The power management system has to achieve the balance between the performance and robustness during the operation.

Research on the REHS power management has been mostly restricted to stationary applications. Although extensive research has been carried out for stationary applications, no single study exists on the long-term performance for renewable robots.

2.3.1 Reactive method

Reactive power management strategies are the simplest way to plan energy usage. The power management system reacts to the change in the power generation and/or the demand load. Reactive power management strategies do only plan the power usage depends on observations of current states. No prediction method is used when scheduling the power usage. States of the power system may include one or more of the followings:

- Power generation
- Demand load
- Energy in the battery

Generation absolute follow (GAF) strategy reacts to the power generation only and it will consume all the energy it generated by following the power generation. It is a naive power management strategy that does not need any management over the excessive energy.

Glykas et al. ([33]) presents a cost-benefit analysis on solar power installation on merchant marine vessels. In this study, GAF was used in the model, the power generated from the solar resource is assumed to be supplied to the marine vessel directly. The power generated by the solar panels on the marine vessel is much less than the total power consumption. The goal of the renewable energy power system installation is to try to mitigate the greenhouse gas emission for the vehicle. For this application, the GAF strategy simply follows the power generation. The advantage is that without the storage the loss on the charge and discharge would be minimal. This improves the energy conversion efficiency between the power generation and actual supply.

Hagerman ([36]) designed a wave recharging station for an autonomous underwater vehicle. In order to maximize energy harvesting, the power generation from wave energy was stored in the battery. The power management strategy for the recharging station is GAF between wave energy and the battery.

The downside of the GAF strategy is renewable resource variance affects the stability of the power supply. GAF strategy will pass on variance on renewable energy from the resource side to the demand load. This will introduce the problem for renewable energy such as the loss of power supply. For the renewable robot, the GAF strategy would not be the ideal candidate due to the reliability issue. The GAF strategy is more suitable for systems with conventional power supply as a backup.

Demand load follow (DLF) strategy plan the power usage according to the demand load. The native DLF strategy always plans power usage as demand load requested. In Borowy and Salameh ([11])'s REHS design, the power management system follows the native DLF strategy. The load of the REHS is hourly household electricity demand. REHS configuration is designed to supply electricity for the typical load condition. Native DLF is computationally inexpensive that is suitable for the simulation-based optimisation. The drawback of native DLF is the strategy does not include the energy buffer while planning the power usage. A better power management shall able to adjust the power supply depends on the energy left in the battery.

A strategy extends the native DLF strategy to include the battery and power generation for the planning. The extended DLF strategy found in [100]'s work on the wind, PV and fuel cell stand alone system. The battery model is integrated as part of the model to plan the power usage under SOC constraint. The extended DLF strategy compares the power generation and the demand load. When the power generation is higher than the demand load and the battery is not fully charged, power will be supplied to the REHS and excessive power would be used to charge the battery. When the power generation is lower than the demand load and the battery SOC does not fall under the DOD, power will be supplied to the REHS by discharging from the battery.

The drawback of reactive power management strategies is that they make no attempt to dynamically adjust the demand load. The main weakness of the GAF strategy is that future reliability is not provided. DLF strategy on the other hand reserve energy for future use but do not adjust demand load.

Extended DLF strategy shares the simplicity with the native DLF strategy but includes more information. The battery energy level and the power generation are considered while planning the power usage. Reactive power management strategies are found common in off-grid applications that demand load is not adjustable. For example, the off-grid power supply to 4G mobile station requires the system online at 24/7. Also due to its simplicity, the extended DLF strategy is often used as a baseline algorithm in the optimisation and management.

2.3.2 Prediction based method

Prediction based power management strategies plan the power usage and adjust the demand load accordingly. These strategies do not only plan but also change the demand load based on energy availability.

Kansal et al. ([44]) argue that the worst-case design scenario, developing REHS with minimum energy output at any time is greater than the maximum demand load, is high cost and may not be feasible for space constraint applications. This argument also holds for the renewable robot with limited space. Kansal et al. proposed a dynamic prediction based power management strategy for the sensor networks. This strategy uses a prediction model based on an exponentially weighted moving average (EWMA) filter. The power management system dynamically adjusts the demand load depends on current and future energy availability.

The sensor network adjusts power consumption by turning on and off regularly. The total fraction of time the system turned on is the duty cycle of the power system. Although this prediction based method achieved a higher energy conversion efficiency and higher online time compared to DLF strategy in this study, the minimal power supply is zero in between each cycle. For a renewable robot, a zero watt power supply will result in a totally lost control.

Piorno et al. ([75]) employed a similar prediction and management scheme to plan the demand load. The prediction model used in this strategy is the weather conditioned moving average (WCMA). This model takes both current and past days weather condition and reduces the prediction error on solar energy. Moser et al. ([67]) use linear programming technique with predicted power generation for short term power management. However, the same problem is that the minimum power supply is zero if the management strategy is used.

Prediction based power management strategies are limited to sensor network applications where the reduction of the demand load have no detrimental influence on the sensor. In order to minimise the risk of completely lost control on the demand load, a minimal level of the power supply is required. Prediction based power management strategies have seen great success in a wireless sensor network. The completely lost on the power supply cast doubt in using prediction-based method for renewable robots.

2.3.3 Learning based strategy

Learning-based power management strategies take a different approach to plan the demand load. The strategy learns to plan power usage from previous experience.

Tan et al. ([93]) present the adaptive power management using reinforcement learning strategy. This is an online learning algorithm that learns the optimal decision from history and improves itself against changes in the environment. The power system was modelled as a black box environment with states that can be observed by the power management system. The power management system makes a decision on power usage based on those observations. For each decision the power management strategy made, the environment gives feedback. Positive feedback, which usually called reward, encourage the action on the system. On the contrary, negative feedback will penalise a bad decision made by the power management strategy. The power system learns to maximise the total reward and improve the power management quality in terms of robustness and performance. Result of [93] shows that the learning-based power management system achieved a 24 % reduction in the power consumption compared to conventional strategy.

Lin et al. ([53]) propose a model-free learning-based power management strategy for an electrical vehicle. The optimal power management policy is derived from the action and the received reward. Actions with higher reward will be chosen more frequently while those result in a penalty will be avoided. The reward of each action depends on the quality of the control decisions. In this work, the goal is to maximise the battery efficiency of the electric vehicle. For each action, the less fuel it consumes, the higher the reward will be given. Since the power management reinforces the possibility of taking actions to maximise the reward, the strategy is called the reinforcement learning-based power management method.

Wu et al. ([107]) take a similar approach to plan power usage through learning. A machine learning approach, deep Q learning, is adopted for the energy management system. The deep Q learning is a learning-by-doing online power management strategy based on the power system model. This strategy achieved a better fuel economy under unknown demand load conditions.

Learning-based power management is attractive to the renewable robot that needs to minimise the risk of the lost power supply under a hard size constraint. Compare to reactive and predictive power management strategies, it is possible to customise the goal of power management for a minimal level power supply for the robot. The power supply to the safety-critical load is important to the reliable operation of the vehicle.

However, there is currently no literature on the long-term performance on the learning-based power system management strategy. The long-term uncertainty and variance of the renewable energy resource have to be included while developing the power management strategy for the renewable robot. Meanwhile, the ability to learn and adapt to the change in the power generation and demand load is critical to the safety and performance of the renewable robot.

2.4 Summary

In this section, the research related to the REHS for renewable robots have been reviewed. It has been found that current research on REHS is limited to stationary applications and REHS application on mobile robot is still domain-specific. As has been reviewed in this chapter, there is no general method or technique available to REHS on mobile robots. For the purpose of a reliable power supply for the robot's fully autonomous operation, the literature review has identified the key research gaps in the model, design and management of REHS.

The following research questions are raised from the study:

- The lack of fundamental understanding on how the mobile robot's motion would influence the power system on both demand load and power generation.
- The scarcity in the design methodology for an reliable and cost-effective REHS configuration under the size constraint.
- The need of power management strategy for long-term reliability performance.

A fundamental understanding of the motion's impact on the moving REHS would contribute to the model of the power system. Based on the power system model, the REHS configuration design method is helpful to study the relationship between the design objectives and constraints. Furthermore, the design methodology is also a tool to size the REHS for reliable and cost-effective performance. Power management is required to plan the power usage during the operation. The above research gaps in different areas but all contribute to the reliable REHS. Method and technique to address these research gaps will be presented from the next chapter.

Chapter 3

Moving REHS model

This chapter presents the moving REHS model for the mobile robot. The model includes the power generation, demand load and energy storage models. As a moving REHS, the model include the global and local motion of the robot. Power generation models of the most common availability renewable energy resources – solar and wind – are first introduced. A generic energy storage model is presented after the demand load model. An assessment will be given to show how global and local motions would impact the power system.

As it has been mentioned in the research objective, the moving REHS model is the foundation of the system. The analytical moving REHS model itself would also have to provide an insight on the performance of power system. Later in this chapter, the data-driven simulation approach is also demonstrated to show how to assess numerically the performance of REHS when it subject to both global and local motion.

3.1 Solar power system model

The local motion of the renewable robot is the locomotion in its reference coordinate system. When the renewable robot experiences a local motion, the solar panel will move along with the robot. The solar angle between the panel and the sun changes when there is a local motion. Total solar radiation received is determined by the solar resource as well as the solar angle. The local motion has an impact on the solar angle hence influence the total power generation.

Global motion of the renewable robot is due to long-distance travel. This would influence the power generation from the resource side. Global solar radiation is unevenly distributed that long-distance travel will have an impact on the resource.

The moving REHS model has to include both local and global motions in solar power generation. In this section, how these two factors influence the solar power generation will be explored.

3.1.1 Local motion on the solar panel

As it has reviewed in Section 2.1, the total radiation on a stationary solar panel consists of beam (direct) radiation, diffused radiation and reflected radiation.

$$\begin{aligned} G_g &= G_b + G_d + G_r \\ &= I_b \cos(\theta_s) + I_d \frac{1+\cos(\beta_s)}{2} + I_b \rho \cdot \frac{1-\cos(\beta_s)}{2} \end{aligned} \tag{3.1}$$

where θ_s is the solar angle, β_s is the surface tilt on the solar panel.

Figure 3.1 shows related solar geometry of a solar panel on a renewable robot. Solar angle θ_s is the angle between the direction of the sun and the normal of the solar panel. Surface tilt β_s is the angle between the panel and the horizontal surface of the earth. When the renewable robot undergoes a local motion, it will influence both on solar angle and surface tilt angle. Because the total radiation on the solar panel is determined by both solar angle and the surface tilt angle, the local motion changes to the total solar radiation.

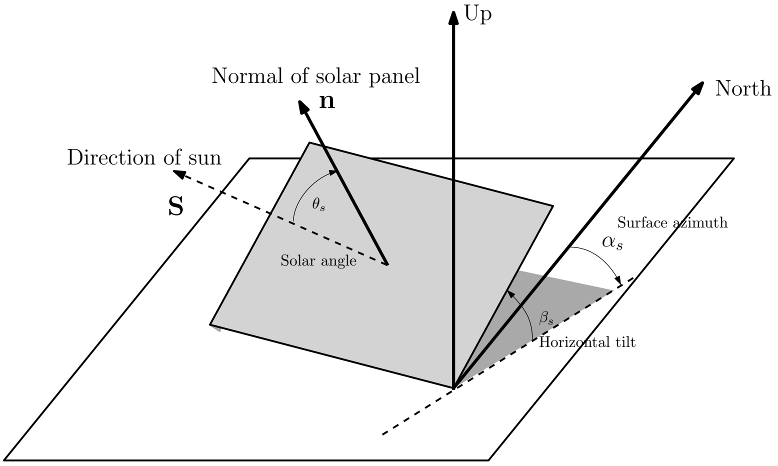

Figure 3.1: Direct radiation of solar panel

The vectorial representation on the normal of solar panel and direction of the sun is used. **S** is solar vector defined as a vector point from the robot on the earth to the sun, and **n** panel vector is defined as the normal of the solar panel. Solar angle θ_s by vector notation in this case is:

$$\cos(\theta_s) = \frac{\mathbf{S} \cdot \mathbf{n}}{\|\mathbf{S}\| \times \|\mathbf{n}\|} \tag{3.2}$$

The base of those vectors is indicated by its underscore. For example, $\mathbf{S}_{\text{earth}}$ means solar vector in earth coordinate.

To include the local motion of the renewable robot in the power generation model, both vectors have to be found in the local reference coordinate. The first step is to find the solar vector in orbit reference system. In this system, the Earth orbits about the Sun in an almost circular trajectory at a period of one year (shown in Figure 3.2). The Earth also rotates about itself with rotation axis by a fixed angle of 23.45° to the normal of the orbit plane.

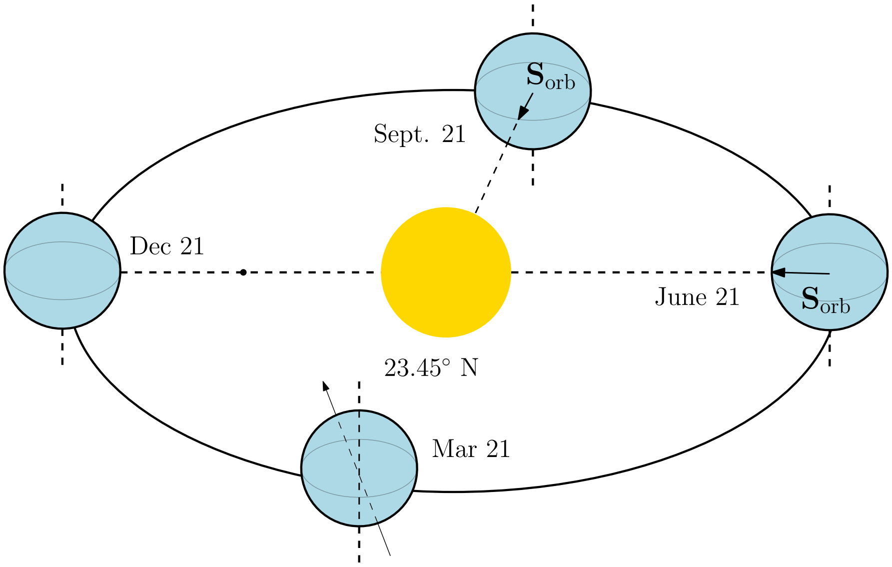

FIGURE 3.2: Orbit of the Earth around the sun

The solar vector in orbit reference system ($\mathbf{S}_{\text{orb}}$) is a vector point from the centre of the Earth to the Sun. When the Earth orbits around the Sun, the apparent path of the Sun's motion on the celestial sphere as seen from Earth is called the ecliptic plane. This plane is circumvented by a grey line shown in Figure 3.2 which is called the ecliptic. Ecliptic is tilted at an angle of $\epsilon \approx 23.45°$ to the celestial equator plane shown as light blue region in Figure 3.3.

In Figure 3.3, ϵ is Earth tilt angle, λ_e is ecliptic longitude. During the year, the ecliptic longitude varies from 0 to 2π, at $\lambda_e = 0$ the Sun is straight over Equator (Spring Equinox), when $\lambda_e = \pi/2$ the Sun reach 23.45° north at Summer Solstice, and at $\lambda_e = \pi$ it is Autumnal equinox the Sun point directly over the Equator and finally when $\lambda_e = 3\pi/2$ the sun will be directly overhead at latitude of 23.45° south (Winter Solstice). By the definition, the solar vector in orbit reference system (orb) is:

$$\mathbf{S}_{\text{orb}} = \begin{bmatrix} \cos\lambda_e & \sin\lambda_e & 0 \end{bmatrix}^T \tag{3.3}$$

The solar vector is now in the orbit reference system. In this reference system, the Earth itself is regarded as a point mass which makes it difficult to include the motion of the robot in the model. Solar vector has to be converted into an earth fixed coordinate system for modelling the local motion.

The earth centred earth fixed (ECEF) coordinate system has an origin centred at the earth. In the ECEF system, xOy forms a plane that passes the equator of the earth. Meanwhile, the sun will always orbit on the ecliptic regardless of the change in the coordinate reference system.

The geometry relationship between the orbit reference system and ECEF coordinate system is by rotating clockwise at an angle of ϵ about x_{orb}. Such a transformation can be represented as a matrix multiplication:

$$\mathbf{S}_{\text{ecef}} = \mathbf{R}_{\text{orb}}^{\text{ecef}} \mathbf{S}_{\text{orb}} \tag{3.4}$$

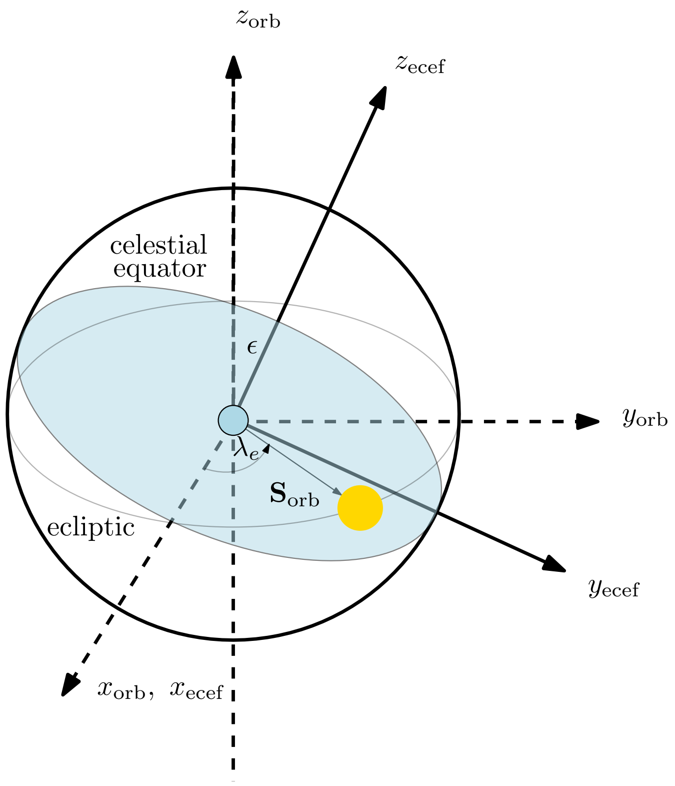

Figure 3.3: Geometry relationship between orbit to earth centred earth fixed coordinate

The rotation matrix $\mathbf{R}_{\mathrm{orb}}^{\mathrm{ecef}}$ transform the solar vector in orbit (orb) reference system to (ecef) in Euclidean space. In a simple 2D scenario shown in Figure 3.4, a vector (x, y) is in both xOy and $x'Oy'$ reference system. The only difference of two reference system is the new $x'Oy'$ is rotated counter-clockwise by an angle of θ. In the new reference system the coordinate of the vector can be found using trigonometry $(x\cos\theta - y\sin\theta, x\sin\theta + y\cos\theta)$.

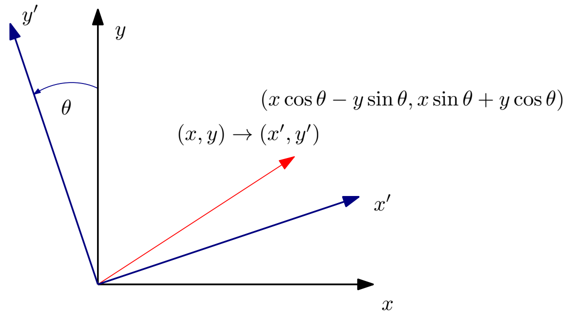

Figure 3.4: Rotation matrix in 2D Euclidean space

If use (x', y') to represent the new coordinate, such operation can be written in matrix form as:

$$\begin{bmatrix} x' \\ y' \end{bmatrix} = \begin{bmatrix} \cos\theta & -\sin\theta \\ \sin\theta & \cos\theta \end{bmatrix} \begin{bmatrix} x \\ y \end{bmatrix} \tag{3.5}$$

The first part of the formula is the rotation matrix, it transforms the base of the vector between two reference systems.

$$\mathbf{R}(\theta) = \begin{bmatrix} \cos\theta & -\sin\theta \\ \sin\theta & \cos\theta \end{bmatrix} \tag{3.6}$$

The rotation matrix $\mathbf{R}_{\text{old}}^{\text{new}}$ is from *old* frame xOy to *new* frame $x'Oy'$. The direction of rotation follows the right-hand rule. In this case, the rotation is positive when a vector turns counter-clockwise. For a negative rotation angle, the rotation matrix is:

$$\mathbf{R}(-\theta) = \begin{bmatrix} \cos\theta & \sin\theta \\ -\sin\theta & \cos\theta \end{bmatrix} \tag{3.7}$$

The extension from 2D to 3D is straightforward, a rotation of a vector (x, y) by an angle of θ about z axis will only change coordinate in $x - y$. The rotation matrix will keep all z dimensions the same as the vector turn around z axis and the multiplication matrix is:

$$\mathbf{R}_z(\theta) = \begin{bmatrix} \cos(\theta) & -\sin(\theta) & 0 \\ \sin(\theta) & \cos(\theta) & 0 \\ 0 & 0 & 1 \end{bmatrix} \tag{3.8}$$

For three axes in a 3D Cartesian coordinate system, $R_x(\theta), R_y(\theta)$ and $R_z(\theta)$ represent the counter-clockwise rotation about each axis at angle θ. Equation 3.8, 3.9, and 3.10 are three main basic rotation matrices that will be most frequently used.

$$\mathbf{R}_y(\theta) = \begin{bmatrix} \cos(\theta) & 0 & \sin(\theta) \\ 0 & 1 & 0 \\ -\sin(\theta) & 0 & \cos(\theta) \end{bmatrix} \tag{3.9}$$

$$\mathbf{R}_x(\theta) = \begin{bmatrix} 1 & 0 & 0 \\ 0 & \cos(\theta) & -\sin(\theta) \\ 0 & \sin(\theta) & \cos(\theta) \end{bmatrix} \tag{3.10}$$

The rotation matrix $\mathbf{R}_{\text{orb}}^{\text{ecef}}$ from orbit reference system to the ECEF system could be found using the rotation matrix. The transformation is a counter-clockwise rotation about x axis by ecliptic angle of ϵ.

$$\mathbf{R}_{\text{orb}}^{\text{ecef}}(\epsilon) = \mathbf{R}_x(\epsilon) \tag{3.11}$$

The solar vector in earth centre earth fixed system can be found by matrix multiplication:

$$\begin{aligned} \mathbf{S}_{\text{ecef}} &= \mathbf{R}_{\text{orb}}^{\text{ecef}} \mathbf{S}_{\text{orb}} \\ &= \begin{bmatrix} 1 & 0 & 0 \\ 0 & \cos\epsilon & -\sin\epsilon \\ 0 & \sin\epsilon & \cos\epsilon \end{bmatrix} \begin{bmatrix} \cos\lambda_e & \sin\lambda_e & 0 \end{bmatrix}^T \\ &= \begin{bmatrix} \cos(\lambda_e) & \sin(\lambda_e)\cos(\epsilon) & \sin(\lambda_e)\sin(\epsilon) \end{bmatrix}^T \end{aligned} \tag{3.12}$$

As is have been mentioned, the solar vector $\mathbf{S}_{\text{orb}}$ in orbit is defined by ecliptic longitude λ_e. Ecliptic longitude as it shown in Figure 3.3 is the angle between x_{orb} and direction of sun. This can be regarded as an unit vector on x_{orb} axis was rotated about z_{orb} by λ_e and the result

$$\begin{aligned} \mathbf{S}_{\text{orb}} &= \mathbf{R}_z(\lambda_e)\begin{bmatrix}1 & 0 & 0\end{bmatrix}^T \\ &= \begin{bmatrix}\cos(\lambda_e) & -\sin(\lambda_e) & 0 \\ \sin(\lambda_e) & \cos(\lambda_e) & 0 \\ 0 & 0 & 1\end{bmatrix}\begin{bmatrix}1\\0\\0\end{bmatrix} \\ &= \begin{bmatrix}\cos\lambda_e & \sin\lambda_e & 0\end{bmatrix}^T \end{aligned} \tag{3.13}$$

matches the definition given before.

The solar vector in the ECEF system is one step closer to the moving solar panel.

$$\mathbf{S}_{\text{ecef}} = \begin{bmatrix}\cos(\lambda_e) & \sin(\lambda_e)\cos(\epsilon) & \sin(\lambda_e)\sin(\epsilon)\end{bmatrix}^T \tag{3.14}$$

The ECEF can then be transformed into a NEU frame such that the global position can be expressed using latitude and longitude. The coordinate is fixed at a single point on the earth with reference in the east, north and up direction.

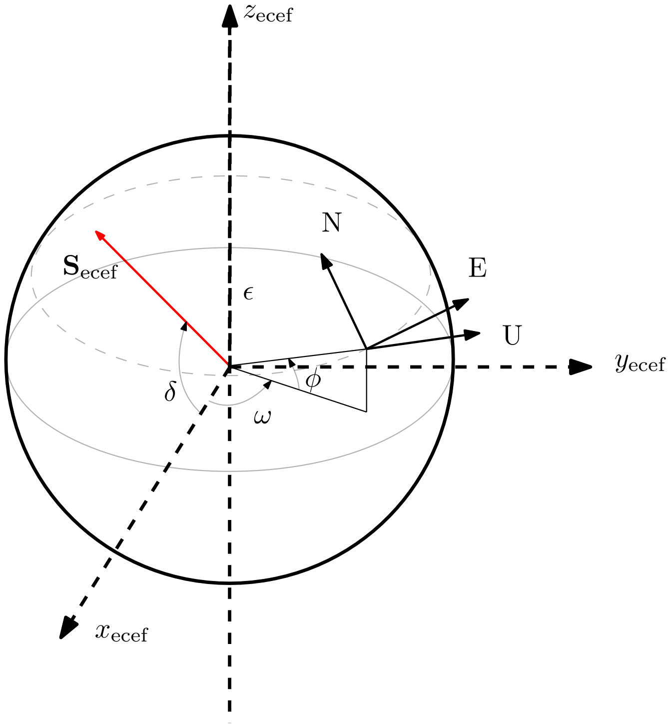

FIGURE 3.5: Rotation matrix from earth centred to east-north-up

For an arbitrary point on the earth, the location can be determined by the latitude ϕ and the hour angle ω in the ECEF global coordinate system. As the ENU revolves with the self-rotation of the earth (shown Figure 3.5) the hour angle ω is

$$\omega = (\text{hour} - 12)\cdot \pi/6 \tag{3.15}$$

where hour is apparent solar time (AST) at that location.

Relationship between the ECEF system and ENU system have shown in Figure 3.5. There are two steps in the transformation from ECEF to ENU. First, a clockwise rotation over east-axis by an angle $\pi/2-\phi$ to align the up-axis with the x-axis. This transformation using matrix notation is $\mathbf{R}_x[-(\pi/2-\phi)]$. Then a clockwise rotation over the z-axis by and angle $\pi/2+\omega$ to align the east-axis with the x-axis. This transform matrix is $\mathbf{R}_z[-(\pi/2+\omega)]$. The transformation matrix is a combination of them.

$$\begin{aligned}\mathbf{R}_{\text{ecef}}^{\text{enu}} &= \mathbf{R}_x[-(\pi/2-\phi)]\mathbf{R}_z[-(\pi/2+\omega)] \\ &= \begin{bmatrix} 1 & 0 & 0 \\ 0 & \sin(\phi) & \cos(\phi) \\ 0 & -\cos(\phi) & \sin(\phi) \end{bmatrix} \begin{bmatrix} -\sin(\omega) & \cos(\omega) & 0 \\ -\cos(\omega) & -\sin(\omega) & 0 \\ 0 & 0 & 1 \end{bmatrix} \\ &= \begin{bmatrix} -\sin(\omega) & \cos(\omega) & 0 \\ -\cos(\omega)\sin(\phi) & -\sin(\phi)\sin(\omega) & \cos(\phi) \\ \cos(\phi)\cos(\omega) & \cos(\phi)\sin(\omega) & \sin(\phi) \end{bmatrix}\end{aligned} \tag{3.16}$$

Solar vector in ENU reference $\mathbf{S}_{\text{enu}}$ system can be found by repeatedly apply the transformation from $\mathbf{S}_{\text{orb}}$:

$$\begin{aligned}\mathbf{S}_{\text{enu}} &= \mathbf{R}_{\text{ecef}}^{\text{enu}}\mathbf{R}_{\text{orb}}^{\text{ecef}}\mathbf{S}_{\text{orb}} \\ &= \begin{bmatrix} \sin(\lambda_e)\cos(\omega)\cos(\epsilon) - \cos(\lambda_e)\sin(\omega) \\ \sin(\lambda_e)[\sin(\epsilon)\cos(\phi) - \sin(\omega)\cos(\epsilon)\sin(\phi)] - \cos(\lambda_e)\cos(\omega)\sin(\phi) \\ \cos(\lambda_e)\cos(\omega)\cos(\phi) + \sin(\lambda_e)[\sin(\omega)\cos(\epsilon)\cos(\phi) + \sin(\epsilon)\sin(\phi)] \end{bmatrix}\end{aligned} \tag{3.17}$$

Notice that Earth rotation tilt angle ϵ is a constant value at 23.45°. It is possible to introduce an intermediate variable δ to simplify solar vector in ENU coordinate system.

$$\sin\delta = \sin\lambda_e \sin\epsilon \tag{3.18}$$

The solar vector in the ENU coordinate system can be rewritten as:

$$\mathbf{S}_{\text{enu}} = \begin{bmatrix} -\cos(\delta)\sin(\omega) \\ \sin(\delta)\cos(\phi) - \cos(\delta)\cos(\omega)\sin(\phi) \\ \cos(\delta)\cos(\omega)\cos(\phi) + \sin(\delta)\sin(\phi) \end{bmatrix} \tag{3.19}$$

It is possible to further simplify the solar using more intermediate variables. The solar vector in ENU reference system can be further simplified using a pair of variables α elevation angle and azimuth angle A.

Azimuth angle A is defined as the clockwise angle between the north and the projection line of the sun, elevation angle α is the angle between the sun and the ground. According to the

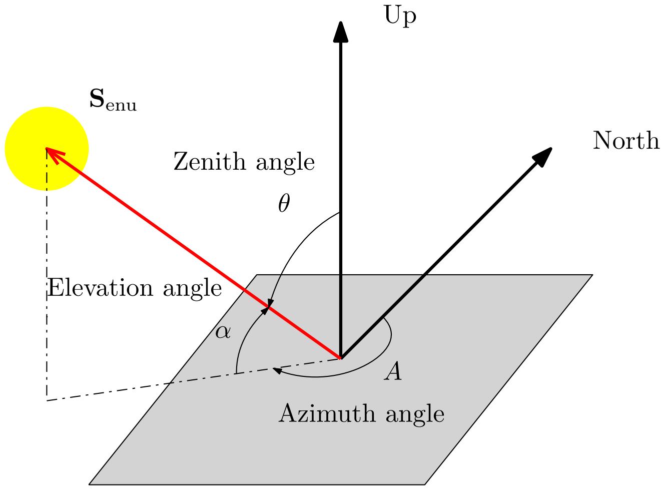

FIGURE 3.6: Azimuth angle and elevation angle defined in ENU

definition of azimuth angle and elevation angle, the solar vector in ENU is:

$$\begin{aligned}\mathbf{S}_{\text{enu}} &= \mathbf{R}_z(-A)\mathbf{R}_x(\alpha)\begin{bmatrix}0 & 1 & 0\end{bmatrix}^T \\ &= \begin{bmatrix}\cos(A) & \sin(A) & 0\\ -\sin(A) & \cos(A) & 0\\ 0 & 0 & 1\end{bmatrix}\begin{bmatrix}1 & 0 & 0\\ 0 & \cos(\alpha) & -\sin(\alpha)\\ 0 & \sin(\alpha) & \cos(\alpha)\end{bmatrix}\begin{bmatrix}0\\1\\0\end{bmatrix} \\ &= \begin{bmatrix}\cos(\alpha)\sin(A) & \cos(\alpha)\cos(A) & \sin(\alpha)\end{bmatrix}^T\end{aligned} \tag{3.20}$$

The solar vector has been derived using rotation matrix multiplication in the ENU frame. With a different number of intermediate variables, the solar vector can be expressed in the following equivalent ways.

$$\begin{aligned}\mathbf{S}_{\text{enu}} &= \begin{bmatrix}\cos(\alpha)\sin(A)\\ \cos(\alpha)\cos(A)\\ \sin(\alpha)\end{bmatrix} \\ &= \begin{bmatrix}-\cos(\delta)\sin(\omega)\\ \sin(\delta)\cos(\phi)-\cos(\delta)\cos(\omega)\sin(\phi)\\ \cos(\delta)\cos(\omega)\cos(\phi)+\sin(\delta)\sin(\phi)\end{bmatrix} \\ &= \begin{bmatrix}\sin(\lambda_e)\cos(\omega)\cos(\epsilon)-\cos(\lambda_e)\sin(\omega)\\ \sin(\lambda_e)[\sin(\epsilon)\cos(\phi)-\sin(\omega)\cos(\epsilon)\sin(\phi)]-\cos(\lambda_e)\cos(\omega)\sin(\phi)\\ \cos(\lambda_e)\cos(\omega)\cos(\phi)+\sin(\lambda_e)[\sin(\omega)\cos(\epsilon)\cos(\phi)+\sin(\epsilon)\sin(\phi)]\end{bmatrix}\end{aligned} \tag{3.21}$$

Next step is to find the direction of solar panel on renewable robots in ENU system. For a stationary flat panel on the even surface, the normal vector of solar panel in the ENU coordinate system is an upward unit vector:

$$\mathbf{n}_{\text{enu}}\begin{bmatrix}0 & 0 & 1\end{bmatrix}^T \tag{3.22}$$

If the solar panel has a surface tilt, the direction of the solar vector would change accordingly. The surface rotates around up axis is surface azimuth, it is defined as the clockwise angle between north as α_s. Horizontal tilt β_s is the clockwise angle between north-east plane.

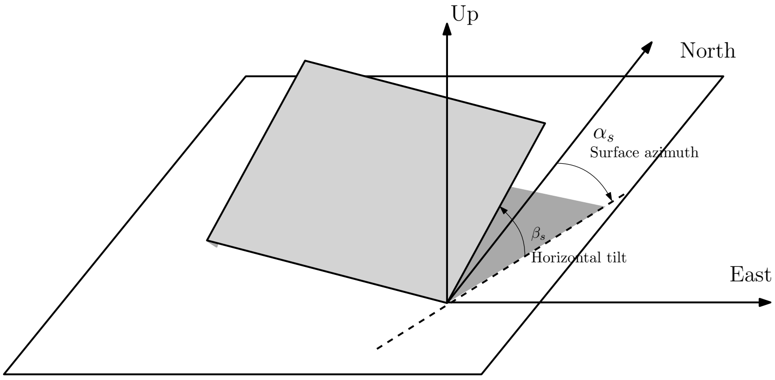

FIGURE 3.7: Rotation of solar panel norm vector

Using matrix notation, such rotation can be represented as two transformations. First, the solar vector is rotating counter-clockwise about the east axis (equivalent to x-axis) by an angle of β_s. Then a clockwise rotation about up axis (equivalent to z-axis) by an angle of α_s.

$$\mathbf{R}_x(\beta_s)\mathbf{R}_z(-\alpha_s) \tag{3.23}$$

The pre-tilted panel vector on stationary robots is then,

$$\begin{aligned}\mathbf{n}_{\text{enu}} &= \mathbf{R}_x(\beta_s)\mathbf{R}_y(-\alpha_s)\begin{bmatrix}0 & 0 & 1\end{bmatrix}^T \\ &= \begin{bmatrix}\sin(\alpha_s)\sin(\beta_s) \\ \cos(\alpha_s)\sin\beta_s) \\ \cos(\beta_s)\end{bmatrix}\end{aligned} \tag{3.24}$$

Solar angle according to Equation 3.2 in ENU system is,

$$\cos(\theta_s) = \frac{\mathbf{S}_{\text{enu}} \cdot \mathbf{n}_{\text{enu}}}{\|\mathbf{S}_{\text{enu}}\| \times \|\mathbf{n}_{\text{enu}}\|} \tag{3.25}$$

notice that $\mathbf{S}_{\text{enu}}$ and $\mathbf{n}_{\text{enu}}$ are all unit vectors, Equation 3.25 is equivalent to:

$$\cos(\theta_s) = \mathbf{S}_{\text{enu}} \cdot \mathbf{n}_{\text{enu}} \tag{3.26}$$

With intermediate variable defined in ENU system, the inner product of solar vector and panel vector give the solar angle on a pre-tilted panel on stationary robots:

$$\begin{aligned}\cos(\theta_s) &= \mathbf{S}_{\text{enu}} \cdot \mathbf{n}_{\text{enu}} \\ &= \begin{bmatrix}\cos(\alpha)\sin(A)\\ \cos(\alpha)\cos(A)\\ \sin(\alpha)\end{bmatrix} \cdot \begin{bmatrix}\sin(\alpha_s)\sin(\beta_s)\\ \cos(\alpha_s)\sin\beta_s)\\ \cos(\beta_s)\end{bmatrix} \\ &= \cos(\alpha)\cos(A)\cos(\alpha_s)\sin(\beta_s) + \cos(\alpha)\sin(A)\sin(\alpha_s)\sin(\beta_s) \\ &\quad + \sin(\alpha)\cos(\beta_s) \\ &= \cos(\alpha)\sin(\beta_s)\cos(A-\alpha_s) + \sin(\alpha)\cos(\beta_s)\end{aligned} \tag{3.27}$$

For the moving robot undergoes a roll-pitch-yaw motion, the panel on the robot will experience the same motion. The local motion can be also be represented as several rotations transform. The effect of the motion of the robot in the ENU coordinate system on the normal of the solar panel is:

$$\mathbf{n}'_{\text{enu}} = \mathbf{R}_x(p)\mathbf{R}_y(q)\mathbf{R}_z(r)\mathbf{n}_{\text{enu}} \tag{3.28}$$

where p is roll angle, q is pitch angle, r is yaw angle.

The solar angle on tilt moving surface of the solar panel is:

$$\begin{aligned}\cos(\theta_s) &= \mathbf{S}_{\text{enu}} \cdot \mathbf{n}'_{\text{enu}} \\ &= \mathbf{S}_{\text{enu}} \cdot \mathbf{R}_x(p)\mathbf{R}_y(q)\mathbf{R}_z(r)\mathbf{n}_{\text{enu}} \\ &= \begin{bmatrix}\cos(\alpha)\sin(A)\\ \cos(\alpha)\cos(A)\\ \sin(\alpha)\end{bmatrix} \cdot \begin{bmatrix}1 & 0 & 0\\ 0 & \cos(p) & -\sin(p)\\ 0 & \sin(p) & \cos(p)\end{bmatrix} \begin{bmatrix}\cos(q) & 0 & \sin(q)\\ 0 & 1 & 0\\ -\sin(q) & 0 & \cos(q)\end{bmatrix} \begin{bmatrix}\cos(r) & -\sin(r) & 0\\ \sin(r) & \cos(r) & 0\\ 0 & 0 & 1\end{bmatrix} \begin{bmatrix}\sin(\alpha_s)\sin(\beta_s)\\ \cos(\alpha_s)\sin\beta_s)\\ \cos(\beta_s)\end{bmatrix} \\ &= a\cos(\alpha)\sin(A) + b\cos(\alpha)\cos(A) + c\sin(\alpha)\end{aligned} \tag{3.29}$$

where a, b, c are:

$$\begin{aligned}a &= -\cos(q)\sin(r)\cos(\alpha_s)\sin(\beta_s) + \cos(q)\cos(r)\sin(\alpha_s)\sin(\beta_s) + \sin(q)\cos(\beta_s) \\ b &= \cos(\alpha_s)\sin(\beta_s)(\cos(p)\cos(r) - \sin(p)\sin(q)\sin(r)) + \sin(\alpha_s)\sin(\beta_s)(\sin(p)\sin(q)\cos(r) \\ &\quad + \cos(p)\sin(r)) + \sin(p)(-\cos(q))\cos(\beta_s) \\ c &= \cos(\alpha_s)\sin(\beta_s)(\cos(p)\sin(q)\sin(r) + \sin(p)\cos(r)) + \sin(\alpha_s)\sin(\beta_s)(\sin(p)\sin(r) \\ &\quad - \cos(p)\sin(q)\cos(r)) + \cos(p)\cos(q)\cos(\beta_s)\end{aligned}$$

In Equation 3.29, it can be found that solar angle depends on two factors: solar geometry and panel geometry. Solar geometry is influenced by the solar position which is determined by the location and the time of the robot. Panel geometry is a combination of solar panel pre-tilt and local motion of the robots.

The same treatment can be applied to a surface tilt angle to study the influence of the local motion to the diffused and reflected radiation on the panel. The surface tilt angle using vectorial representation is the angle between the norm of the panel and the up direction of the earth plane

$[0, 0, 1]^T$. Another symbol B_s is employed here to differentiate surface tilt to the pre-tilt β_s of a stationary panel. Therefore, the surface tilt angle is:

$$\begin{aligned}\cos(B_s) &= \begin{bmatrix}0 & 0 & 1\end{bmatrix}^T \cdot \mathbf{n}_{\text{enu}}^{'} \\ &= \sin\left(\beta_s\right)\left(\cos(p)\sin(q)\sin\left(r-\alpha_s\right)+\sin(p)\cos\left(r-\alpha_s\right)\right)+\cos(p)\cos(q)\cos\left(\beta_s\right)\end{aligned} \tag{3.30}$$

In Equation 3.30, it can be found that both solar panel pre-tilt (α_s, β_s) and local motion have an influence on the surface tilt angle.

In summary, the total solar radiation on the pre-tilt moving panel on the renewable robot is:

$$\begin{aligned}G_g &= G_b + G_d + G_r \\ &= I_b\cos(\theta_s) + I_d\frac{1+\cos(B_s)}{2} + I_b\rho\cdot\frac{1-\cos(B_s)}{2}\end{aligned} \tag{3.31}$$

where θ_s is the solar angle, B_s is the moving surface tilt of the solar panel,

$$\cos(\theta_s) = a\cos(\alpha)\sin(A) + b\cos(\alpha)\cos(A) + c\sin(\alpha) \tag{3.32}$$

and

$$\cos(B_s) = \sin\left(\beta_s\right)\left(\cos(p)\sin(q)\sin\left(r-\alpha_s\right)+\sin(p)\cos\left(r-\alpha_s\right)\right)+\cos(p)\cos(q)\cos\left(\beta_s\right). \tag{3.33}$$

Equation 3.31 presents the total solar radiation on a pre-tilted moving panel at any moment with a given rotation angle. Renewable robots often experience a periodic local pitch, roll or yaw motion. It is useful to find the averaged solar radiation instead of the instantaneous one. The averaged solar angle is defined as:

$$\cos(\bar{\theta}_s) = \frac{1}{V}\iiint_V \cos(\theta_s)dp\,dq\,dr \tag{3.34}$$

The integral part of the averaged solar angle has a closed-form.

$$\begin{aligned}\iiint_V \cos(\theta_s)dp\,dq\,dr = {} & p\cos(\alpha)\sin(A)\sin(q)\cos(r)\cos\left(\alpha_s\right)\sin\left(\beta_s\right) \\ & + p\cos(\alpha)\sin(A)\sin(q)\sin(r)\sin\left(\alpha_s\right)\sin\left(\beta_s\right) \\ & + \cos(\alpha)\cos(A)\left(q\sin(p)\sin\left(\beta_s\right)\sin\left(r-\alpha_s\right)+r\cos(p)\sin(q)\cos\left(\beta_s\right)\right) \\ & + \cos(q)\left(\cos(\alpha)\left(\cos(A)\cos(p)\sin\left(\beta_s\right)\cos\left(r-\alpha_s\right)-pr\sin(A)\cos\left(\beta_s\right)\right)\right. \\ & \qquad \left.+\sin(\alpha)\sin(p)\sin\left(\beta_s\right)\cos\left(r-\alpha_s\right)\right) \\ & + r\sin(\alpha)\sin(p)\sin(q)\cos\left(\beta_s\right) - q\sin(\alpha)\cos(p)\sin(r)\cos\left(\alpha_s\right)\sin\left(\beta_s\right) \\ & + q\sin(\alpha)\cos(p)\cos(r)\sin\left(\alpha_s\right)\sin\left(\beta_s\right)\end{aligned} \tag{3.35}$$

For a flat panel on renewable robot($\alpha_s = \beta_s = 0$), the integral part can be further simplified into:

$$\begin{aligned}
&\iiint \cos(\theta_s) dp\, dq\, dr \\
&= -pr\cos(\alpha)\sin(A)\cos(q) + r\cos(\alpha)\cos(A)\cos(p)\sin(q) + r\sin(\alpha)\sin(p)\sin(q)
\end{aligned} \tag{3.36}$$

If the robot experience a linear periodical motion with amplitude p_0 in pitch, q_0 in roll and r_0 in yaw the averaged solar angle is

$$\begin{aligned}
\cos(\bar{\theta}_s) &= \frac{1}{2p_0 \cdot 2q_0 \cdot 2r_0} \int_{-r_0}^{r_0} \int_{-q_0}^{q_0} \int_{-p_0}^{p_0} \cos(\theta_s) dp\, dq\, dr \\
&= \frac{8 \cdot r_0 \cdot \sin(\alpha)\sin(p_0)\sin(q_0)}{2p_0 \cdot 2q_0 \cdot 2r_0} \\
&= \frac{\sin(\alpha)\sin(p_0)\sin(q_0)}{p_0 \cdot q_0}
\end{aligned} \tag{3.37}$$

Equation 3.37 can be rearranged into

$$\cos(\bar{\theta}_s) = \underbrace{\frac{\sin(p_0)\sin(q_0)}{p_0 \cdot q_0}}_{\text{local motion}} \cdot \underbrace{\sin(\alpha)}_{\text{solar geometry}} \tag{3.38}$$

where the first part accounts for the local motion and the second part depends on the solar geometry.

This section has present the total solar radiation on a pre-tilted moving panel as well as the averaged solar angle of a non-tilted moving panel under periodical motion. The influence of global motion in the solar radiation will be discussed in the next section.

3.1.2 Global motion on the solar panel

As the renewable robot undergoes a global motion, its location also changes. For every location s on the earth surface, the total solar radiation consists of the beam and diffused components.

$$I_g(s) = I_b(s) + I_d(s)\cos[\theta_z(s)] \tag{3.39}$$

where $I_b(s)$ is beam radiation (DHI) at location s and $I_d(s)$ is diffused radiation (DNI) at location s.

The total solar radiation on the panel when global motion is included

$$G_g(s) = I_b(s)\cos(\theta_s) + I_d(s)\frac{1+\cos(B_s)}{2} + I_b(s)\rho \cdot \frac{1-\cos(B_s)}{2}. \tag{3.40}$$

Global motion of the renewable robot influence the total solar radiation on the panel. During long-distance travel, the geographical distribution of the solar energy resource also needs to be considered in the power generation model. In practice, surface solar radiation is commonly presented by global horizontal irradiance (GHI). The beam and diffused components are decomposed from the GHI using the diffused fraction.

$$I_d(s) = I_g(s) \cdot k_d(s) \tag{3.41}$$

where $k_d(s)$ is diffused fraction of the global solar radiation.

BRL solar radiation model correlates the diffused fraction to multiple parameters including, the clearness index k_t (hourly) and K_t (daily), apparent solar time and

$$k_d(s) = \frac{1}{1 + \exp(\alpha_0 + \alpha_1 k_t + \beta_1 AST + \beta_2 \alpha + \beta_3 K_T + \beta_4 \psi)} \tag{3.42}$$

where $k_t(s) = I_g(s)/1367$ is clearness index, AST is apparent solar time, α is the solar angle, K_T is daily clearness index, ψ is the lag factor that

$$\psi = \begin{cases} \dfrac{k_{t-1} + k_{t+1}}{2} & sunrise < t < sunset \\ k_{t+1} & t = sunrise \\ k_{t-1} & t = sunset \end{cases} \tag{3.43}$$

Parameters of α_0 to β_4 are taken from [50], where $\alpha_0 = -5.32$, $\alpha_1 = 7.28$, $\beta_1 = -0.03$, $\beta_2 = -0.0047$, $\beta_3 = 1.72$, $\beta_4 = 1.08$.

The global motion of the renewable robot can then be integrated into the solar power generation model at given location s. Solar power generation on the panel is

$$P[G_g(s), T(s)] = P_{\mathrm{STC}} \cdot \frac{G_g(s)}{G_{\mathrm{STC}}} \cdot \eta_s(G', T') A_s \tag{3.44}$$

where G' and T' are normalized solar radiation and temperature $G' = G_g/G_{\mathrm{STC}}$ and $T' = T_{\mathrm{STC}}$, P_{STC} is unit area rated power at standard test condition (STC) measured under STC solar radiation $G_{\mathrm{STC}} = 1000W/m^2$ and STC temperature $T_{\mathrm{STC}} = 25°C$, A_s is area of solar panel, G_g is global solar radiation on the panel and T is PV module temperature. Solar panel efficiency η_s is dependent on G' and T'

$$\eta_s(G', T') = 1 + k_1 \ln G' + k_2 (\ln G')^2 + T'(k_3 + k_4 \ln G' + k_5 (\ln G')^2) + k_6 T'^2 \tag{3.45}$$

k_1 to k_6 are parameters taken from [39].

Solar power generation under both global and local motion is

$$P[G_g(s), T(s)] = \frac{P_{\mathrm{STC}}}{G_{\mathrm{STC}}} \cdot G_g(s) \cdot \eta_s(G', T') A_s \tag{3.46}$$

where

$$G_g(s) = I_b(s)\cos(\theta_s) + I_d(s)\frac{1+\cos(B_s)}{2} + I_b(s)\rho\cdot\frac{1-\cos(B_s)}{2}. \tag{3.47}$$

3.1.3 Assessment

Equation 3.29 states the instantaneous solar angle for a panel under pitch, roll, and yaw motion (p, q, r correspondingly) is:

$$\cos(\theta_s) = a\cos(\alpha)\sin(A) + b\cos(\alpha)\cos(A) + c\sin(\alpha)$$

where a, b, c are:

$$\begin{aligned}
a &= -\cos(q)\sin(r)\cos(\alpha_s)\sin(\beta_s) + \cos(q)\cos(r)\sin(\alpha_s)\sin(\beta_s) + \sin(q)\cos(\beta_s)\\
b &= \cos(\alpha_s)\sin(\beta_s)(\cos(p)\cos(r) - \sin(p)\sin(q)\sin(r)) + \sin(\alpha_s)\sin(\beta_s)(\sin(p)\sin(q)\cos(r)\\
&\quad + \cos(p)\sin(r)) + \sin(p)(-\cos(q))\cos(\beta_s)\\
c &= \cos(\alpha_s)\sin(\beta_s)(\cos(p)\sin(q)\sin(r) + \sin(p)\cos(r)) + \sin(\alpha_s)\sin(\beta_s)(\sin(p)\sin(r)\\
&\quad - \cos(p)\sin(q)\cos(r)) + \cos(p)\cos(q)\cos(\beta_s)
\end{aligned}$$

For a flat solar panel without pre-tilt, $\alpha_s = \beta_s = 0$ so a, b, c can be simplified into

$$\begin{aligned}
a &= \sin q\\
b &= -\cos q\sin p\\
c &= \cos p\cos q
\end{aligned} \tag{3.48}$$

Solar angle for a flat panel on the renewable robot is then:

$$\cos(\theta_s) = \sin(q)\cos(\alpha)\sin(A) - \cos(q)\sin(p)\cos(\alpha)\cos(A) + \cos(p)\cos(q)\sin(\alpha) \tag{3.49}$$

This equation is a function of solar elevation angle, azimuth angle, pith motion, roll motion but not yaw motion. That is, the yaw motion (about the north axis in the ENU coordinate system) does not influence the solar angle.

This can be confirmed with the numerical simulation at solar elevation angle $\pi/3$ and solar azimuth angle $\pi/3$. The result is shown in Figure 3.8.

The red dot in the figure shows the solar angle without any local motion $p, q, r = 0$. Solar angle response differently on independent local pitch, roll and yaw motions. For pitch motion, there is a 35 % decrease in the direct solar radiation on the solar panel at 0.5 rad. A 40 % decrease on the instantaneous direct radiation on the panel can also be found at -0.5 rad roll angle. The yaw motion, however, does not change the solar angle at all.

Averaged solar angle Equation 3.37 of flat panel under periodic motion states that

$$\cos(\bar{\theta}_s) = \frac{\sin(p_0)\sin(q_0)}{p_0\cdot q_0}\cdot\sin(\alpha) \tag{3.50}$$

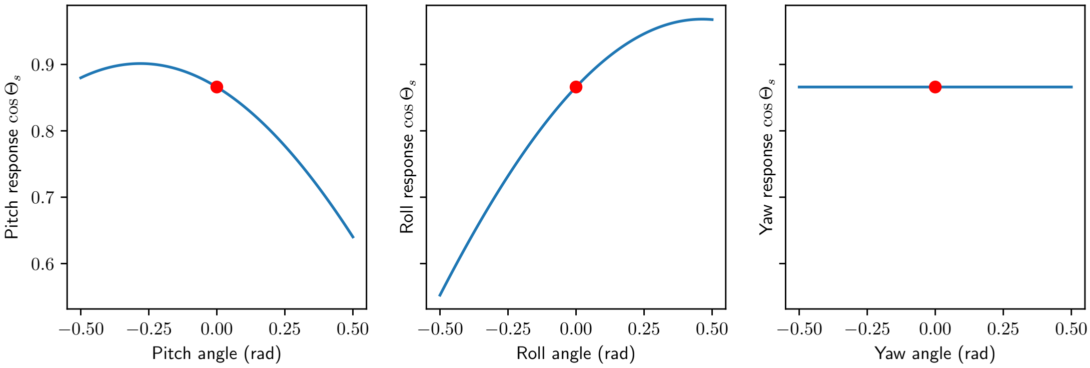

(Red dot shown at bottom left is no motion)

FIGURE 3.8: The influence of local motion on flat solar panel direct radiation

When there is coupling between pitch and roll motion, the averaged solar angle is depending on the amplitude of the motion. Figure 3.9 shows the reduction on the direct solar radiation due to the coupled pitch and roll motion.

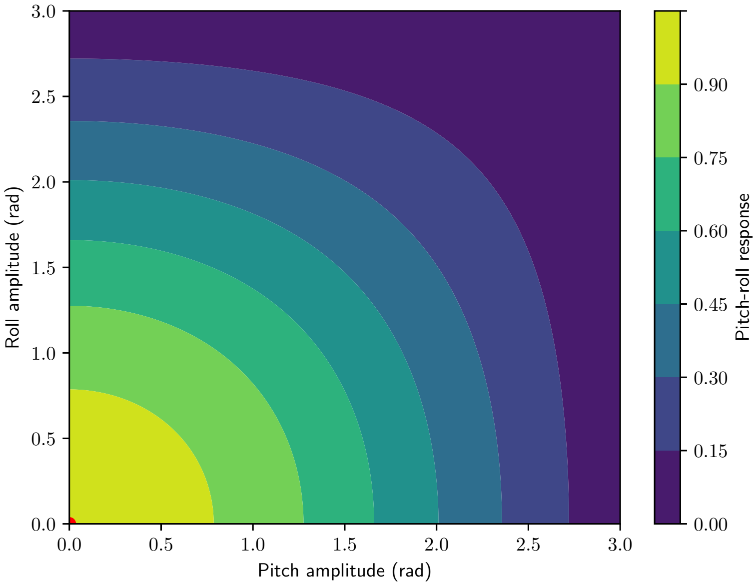

Fraction of the direct solar radiation when subject to the pitch and roll motion (Red dot is no motion)

FIGURE 3.9: The influence of local motion on flat solar panel power radiation

The red dot shown at the bottom left of the figure is the stationary state of the panel without any pitch and roll motions. For a coupled pitch and roll motion at 0.5 rad, there is approximately 10 % reduce on the direct solar radiation on the panel. A larger local motion will introduce a greater reduction on the direct solar radiation on the panel, hence decrease the power generation from direct radiation part.

The total radiation on a flat solar panel under periodical pitch, roll and yaw motions is:

$$\begin{aligned} G_g &= G_b + G_d + G_r \\ &= I_b(s)\cos(\theta_s) + I_d(s)\frac{1+\cos(B_s)}{2} + I_b(s)\rho \cdot \frac{1-\cos(B_s)}{2} \end{aligned} \tag{3.51}$$

The surface tilt of the flat panel would also decrease, resulting in a lower power generation from diffused radiation.

$$\cos(B_s) = \cos(p)\cos(q).$$

Direct and diffused radiations are major components in the total solar radiation on the panel. Even there is an increase in the reflected solar radiation, the total power generation will be lower due to the periodic motion.

Two numerical simulations have been done to study the influence of local motion on solar radiation. The first case is clear sky situation that beam radiation $I_b = 900W/m^2$ and diffuse radiation $I_d = 100W/m^2$. Assuming the same solar elevation with azimuth angle and surface albedo at 0.06, the total radiation in response to an individual motion angles are:

It can be confirmed that the total radiation on the solar panel is influenced by different radiation components. Pitch and roll motions change the total solar radiation on the panel. Yaw motion has no effect on the total solar radiation because both solar angles the surface tilt angle remain the same. Each component of the radiation response to the pitch and roll motion differently. Diffused radiation component is symmetric about the stationary point due to the isotropic sky model assumption. Direct radiation is skewed to one direction because of the solar geometry in this example.

Compare to the stationary case (shown as a red dot), the total radiation is decreased by 18 % at extreme pitch angle at 0.5 rad, decreased by 38 % at extreme roll angle at -0.5 rad. Only 6 % of the variance was found in the diffused radiation component due to local motion. Reflected radiation only accounts for 2 % in total radiation and doesn't have significantly influence the total radiation.

As have been mentioned before, the local motion has an influence on the power generation by the effect the direct radiation on the panel. The cosine of solar angle when it is stationary at an elevation angle $\pi/3$ and azimuth angle $\pi/3$ is 0.87 (shown as a red dot in the figure). If the renewable robot pitch from $-\pi/3$ to $\pi/3$, the direct radiation on the panel would be reduced by 28%. If the renewable robot roll from $\pi/3$ to $-\pi/3$ the direct solar radiation on the panel would be reduced by 39 %.

The second case is cloudy sky with beam radiation $I_b = 100W/m^2$ and diffuse radiation $I_d = 300W/m^2$. The total radiation in response to the individual motion of mobile robots is shown in Figure 3.11.

As for total radiation, in this case, diffused solar radiation is the major component. The variance in the total radiation is less than that in the clear sky case. This is because the diffused component

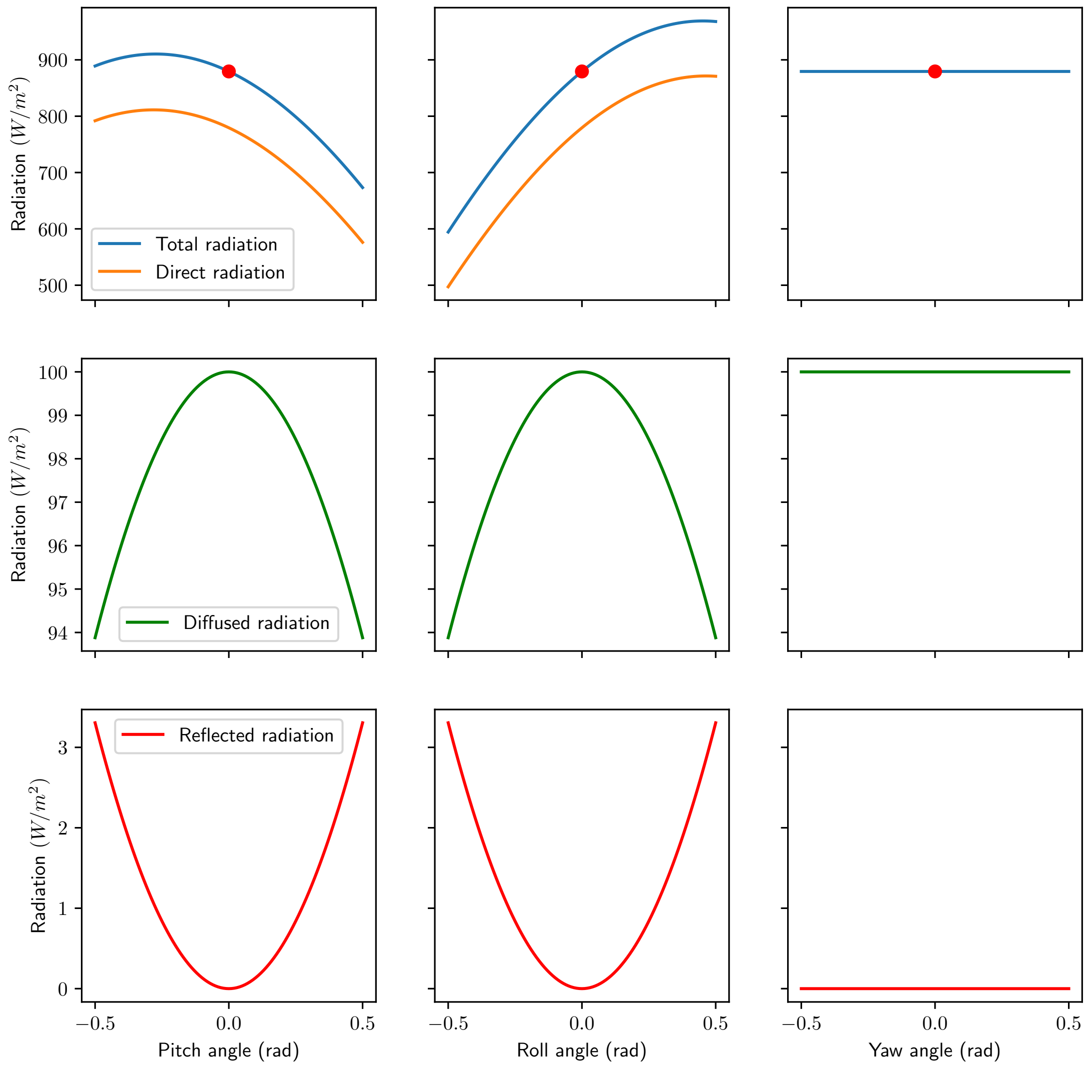

FIGURE 3.10: The influence of local motion radiation parts – clear sky

is not as sensitive to the pitch and roll motion. Periodic pitch and roll motions has less influence on the total solar power generation in the cloudy sky situation.

Global motion of the renewable robot affects the power generation from the resource side. The difference in the global solar radiation distribution is a dominant factor in the change of total solar power generation while the robot undergoes a global motion. Several aspects are known to be associated with solar radiation distribution. The total solar power generation is associated with the route of the renewable robot and the impact of global motion has to be analysed on a case by case basis. The location, time, cloud coverage and terrain have played a vital role in the local solar radiation. Many of the factors are included in the data-driven simulation that the variability of solar radiation distribution is accounted for by actual solar radiation data.

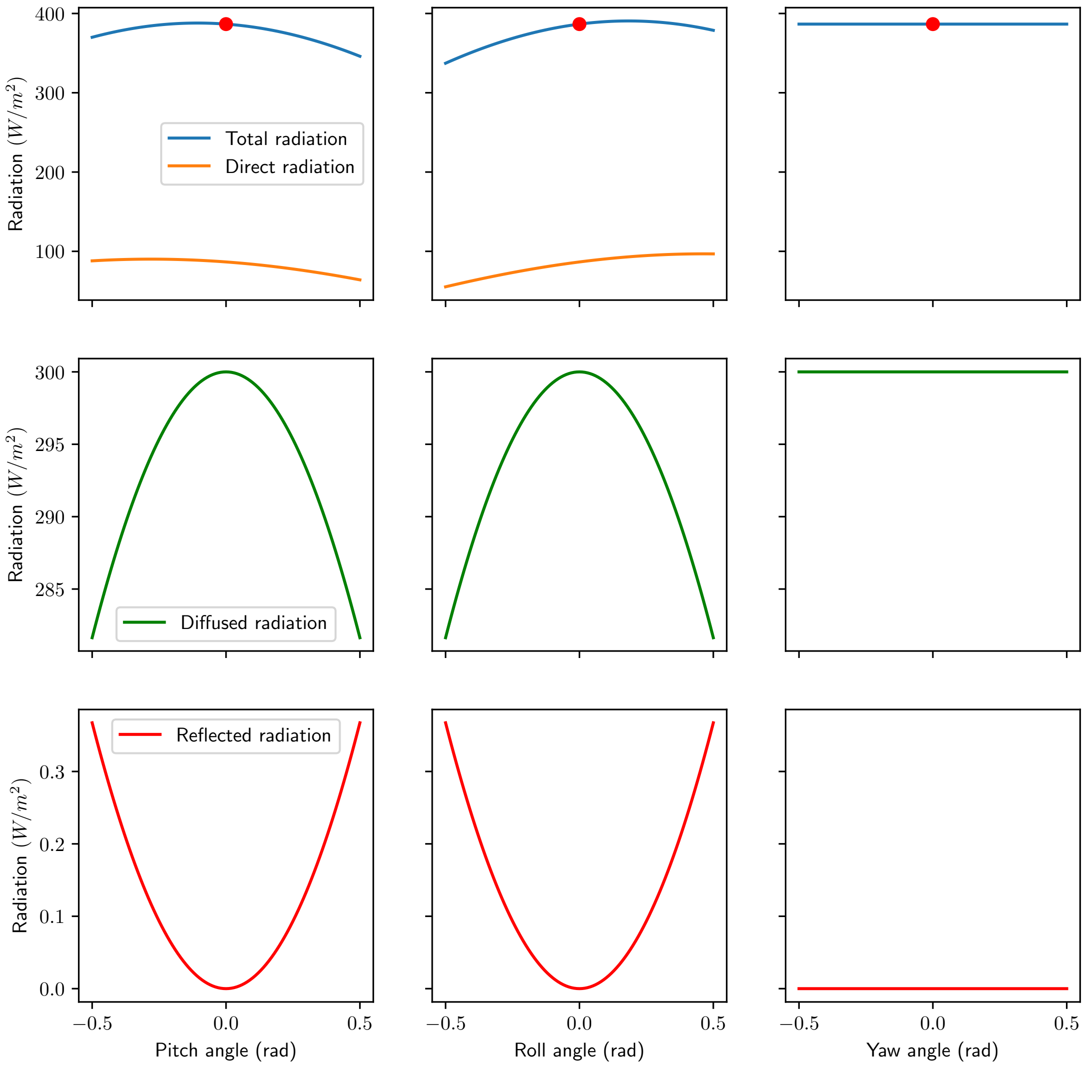

FIGURE 3.11: The influence of local motion radiation parts – cloudy sky

3.2 Wind power system model

The wind turbine is another common renewable energy harvesting device that is also subjects to the local and global motion of the robot. For the wind turbine installed on the robot, the wind power model has to include the motion to estimate the wind power generation. In this section, the influence of both local and global motions will be first presented. The wind power generation model for moving REHS will then be introduced.

3.2.1 Local motion on the wind turbine

The power generation of the wind turbine is determined by the apparent wind velocity on the moving renewable robots. As it is shown in Figure 3.12, apparent wind velocity $\mathbf{v}$ experienced by the wind turbine is:

$$\mathbf{v} = \mathbf{v}_t - \mathbf{v}_s \tag{3.52}$$

where $\mathbf{v}_t$ is true wind velocity when static observed, $\mathbf{v}_s$ is the velocity of the robot.

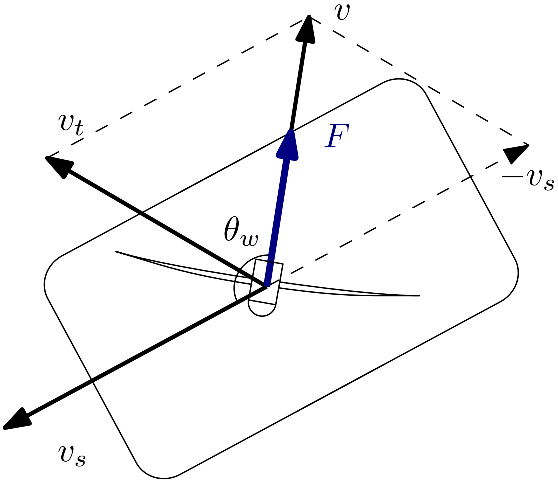

Figure 3.12: Top view of wind turbine on a mobile robot

The motion of the robot creates a virtual wind as if there is a wind blow toward the turbine. The virtual wind $\mathbf{v}_s$ has the same magnitude but the opposite direction. Wind triangle shows that the apparent wind is the true wind velocity plus the virtual wind $-\mathbf{v}_s$.

When the mobile robots experience a local motion, the apparent wind velocity will be influenced as well. Because the translation motion of the mobile robots has been included in $\mathbf{v}_s$, the rotation is the factor that needs to be explored here. Assuming the mobile robots is having pitch, roll and yaw motion about their axis, the rotation transformation matrix is then:

$$\mathbf{R}(p,q,r) = \mathbf{R}_x(p)\mathbf{R}_y(q)\mathbf{R}_z(r) \tag{3.53}$$

The rotation of the platform will transform the robots velocity as:

$$\begin{aligned} \mathbf{v}'_s &= \mathbf{R}_x(p)\mathbf{R}_y(q)\mathbf{R}_z(r)\mathbf{v}_s \\ &= \mathbf{R}(p,q,r)\mathbf{v}_s \end{aligned} \tag{3.54}$$

During a period of time, the wind velocity can be assumed as constant.

$$\mathbf{v}' = \mathbf{v}_t - \mathbf{v}'_s \tag{3.55}$$

The wind resistance on the wind turbine when subject to local rotation is then:

$$\mathbf{F}' = \frac{1}{2}\rho C_T(\lambda) A_w ||\mathbf{v}'||\mathbf{v}' \tag{3.56}$$

It can be seen that the local motion would have influence on the wind resistance. The true wind velocity can be written as $\mathbf{v}_t = [v_{te}, v_{tn}, v_{tu}]$ and the robot velocity can be written as $\mathbf{v}_s = [v_{se}, v_{sn}, v_{su}]$ to quantify the influence of local motion. The robot velocity under local rotation motion is:

$$\begin{aligned}\mathbf{v}'_s &= \mathbf{R}(p,q,r)\mathbf{v}_s \\ &= \begin{bmatrix} v_{se}\cos(q)\cos(r) - v_{sn}\cos(q)\sin(r) + v_{su}\sin(q) \\ v_{se}(\sin(p)\sin(q)\cos(r) + \cos(p)\sin(r)) + v_{sn}(\cos(p)\cos(r) - \sin(p)\sin(q)\sin(r)) - v_{su}\sin(p)\cos(q) \\ v_{se}(\sin(p)\sin(r) - \cos(p)\sin(q)\cos(r)) + v_{sn}(\cos(p)\sin(q)\sin(r) + \sin(p)\cos(r)) + v_{su}\cos(p)\cos(q) \end{bmatrix}^T\end{aligned} \tag{3.57}$$

The new apparent wind velocity when the robot is moving is:

$$\begin{aligned}\mathbf{v}' &= \mathbf{v}_t - \mathbf{R}(p,q,r)\mathbf{v}_s \\ &= \begin{bmatrix} -v_{se}\cos(q)\cos(r) + v_{sn}\cos(q)\sin(r) - v_{su}\sin(q) + v_{te} \\ -v_{se}(\sin(p)\sin(q)\cos(r) + \cos(p)\sin(r)) - v_{sn}(\cos(p)\cos(r) - \sin(p)\sin(q)\sin(r)) + v_{su}\sin(p)\cos(q) + v_{tn} \\ -v_{se}(\sin(p)\sin(r) - \cos(p)\sin(q)\cos(r)) - v_{sn}(\cos(p)\sin(q)\sin(r) + \sin(p)\cos(r)) - v_{su}\cos(p)\cos(q) + v_{tu} \end{bmatrix}^T\end{aligned} \tag{3.58}$$

The local motion of the robot would result in a change of apparent wind velocity: its magnitude is closely related to the power generation from the turbine and the direction will affect the direction of the wind resistance. From power generation point of view, the averaged norm of the wind velocity is useful to estimate the power generation of the wind turbine while it undergoes a local motion.

$$||\bar{\mathbf{v}}'|| = \frac{1}{\text{Volume of V}} \iiint_V ||\mathbf{v}'|| dp\,dq\,dr \tag{3.59}$$

The square of an integral part is

$$\begin{aligned}\iiint_V ||\mathbf{v}||^2 dp\,dq\,dr = {} & [p(qrv_{te} + rv_{su}\cos(q) - \sin(q)(v_{sn}\cos(r) + v_{se}\sin(r)))]^2 \\ & + [-pqrv_{tn} + q\sin(p)(v_{sn}\sin(r) - v_{se}\cos(r)) + \cos(p)(v_{sn}\cos(q)\cos(r) + \\ & \quad rv_{su}\sin(q) + v_{se}\cos(q)\sin(r))]^2 + [pqrv_{tu} + q\cos(p)(v_{sn}\sin(r) - v_{se}\cos(r)) - \\ & \quad \sin(p)(v_{sn}\cos(q)\cos(r) + rv_{su}\sin(q) + v_{se}\cos(q)\sin(r))]^2\end{aligned} \tag{3.60}$$

the average norm of apparent wind velocity is

$$||\bar{\mathbf{v}}'|| = \sqrt{\frac{1}{2p_0 \cdot 2q_0 \cdot 2r_0} \int_{-r_0}^{r_0} \int_{-q_0}^{q_0} \int_{-p_0}^{p_0} ||\mathbf{v}||^2 dp\,dq\,dr} \tag{3.61}$$

Similarly, the averaged wind velocity in the vector can also be found using

$$\bar{\mathbf{v}}' = \frac{1}{\text{Volume of V}} \iiint_V \mathbf{v} dp\,dq\,dr \tag{3.62}$$

for the robot undergoes a periodic linear location motion, the averaged apparent wind

$$\begin{aligned}\bar{\mathbf{v}}' &= \frac{1}{2p_0 \cdot 2q_0 \cdot 2r_0}\int_{-r_0}^{r_0}\int_{-q_0}^{q_0}\int_{-p_0}^{p_0}\mathbf{v}'dp\,dq\,dr \\ &= \begin{bmatrix} \dfrac{q_0 r_0 v_{te} - v_{se}\sin(q_0)\sin(r_0)}{q_0 r_0} \\ \dfrac{p_0 r_0 v_{tn} - v_{sn}\sin(p_0)\sin(r_0)}{p_0 r_0} \\ \dfrac{p_0 q_0 v_{tu} - v_{su}\sin(p_0)\sin(q_0)}{p_0 q_0} \end{bmatrix}^T\end{aligned} \tag{3.63}$$

which can be decomposed into three parts:

$$\begin{aligned}\bar{\mathbf{v}}' &= \frac{1}{2p_0 \cdot 2q_0 \cdot 2r_0}\int_{-r_0}^{r_0}\int_{-q_0}^{q_0}\int_{-p_0}^{p_0}\mathbf{v}'dp\,dq\,dr \\ &= \underbrace{\begin{bmatrix} v_{te} \\ v_{tn} \\ v_{tu}\end{bmatrix}^T}_{\text{Wind resource}} - \underbrace{\begin{bmatrix} \dfrac{\sin(q_0)\sin(r_0)}{q_0 r_0} \\ \dfrac{\sin(p_0)\sin(r_0)}{p_0 r_0} \\ \dfrac{\sin(p_0)\sin(q_0)}{p_0 q_0}\end{bmatrix}^T}_{\text{Local rotation}} \cdot \underbrace{\begin{bmatrix} v_{se} & v_{sn} & v_{su}\end{bmatrix}}_{\text{Global translation}}\end{aligned} \tag{3.64}$$

The first part is due to the difference in wind resource. Wind distribution is globally unevenly distributed, and it will mostly be influenced by global motion.

The second part is associated with the local motion of the robot. A small periodic local rotation at small p_0, q_0, r_0 does not significantly change the apparent wind velocity. The local rotation is negligible at small pitch-roll-yaw amplitude e.g. the term $\sin(q_0)\sin(r_0)/q_0 r_0$ is close to one when both q_0 and r_0 are small.

However, a large local rotation could have a dominant influence on the apparent wind velocity. The wind turbine may not be suitable for those robots with large local rotation. As the net power generation analysis will show the robot move faster than the wind speed does not have any net gain in power generation. Wind turbine can't respond quick enough to align itself to the wind direction to maximise the power generation.

The last part related to the factor of the robot's global speed. Its impact on the power generation will be examined in the next section.

3.2.2 Global motion on the wind turbine

The wind turbine is assumed yaw aligned and the net power generation is modelled as a piecewise function. Net wind power generation from the turbine is

$$P_t(v) = \begin{cases} 0 & v < v_{\text{cut-in}} \\ \frac{1}{2}\rho C_p(\lambda) v^3 A_w & v_{\text{cut-in}} \leq v \leq v_{\text{rated}} \\ \frac{1}{2}\rho C_p(\lambda) v_{\text{rated}}^3 A_w & v_{\text{rated}} \leq v \leq v_{\text{cut-off}} \\ 0 & v > v_{\text{cut-off}} \end{cases} \tag{3.65}$$

where ρ is density of the air, A_w is wind swept area of the turbine, v is wind speed of apparent wind $v = ||\mathbf{v}_{\text{apparent}}||$, $C_p(\lambda)$ is the power coefficient that is function of tip speed ratio $\lambda = \omega R/v$ and ω is the angular velocity of the wind turbine, R is radius of the turbine.

At low wind speed, the wind turbine does not generate any electricity because the moment create by the turbine blade rotation is too low to overcome the inertia and the friction. The minimum wind speed is the cut-in speed of the wind turbine. As the wind speed goes higher, the wind turbine will start to harness electric power from the wind. When the wind speeds further increases, the power generation stays the same the turbine controller will reduce the angular velocity to protect the generator. This is rated speed of wind turbine that limits its maximum power supply. If the wind speed is even higher, the wind turbine will brake to protect the wind turbine elements. This is the maximum wind speed of the wind turbine. In this case, there will be no power generation from the wind turbine.

Equation 3.64 shows that the global motion has contributed to the change in the apparent wind velocity from the resource side. Apparent wind velocity is a confounding factor in the net wind power generation. Robot's motion in the global reference framework also leads to the alternation in the wind power generation. When the wind turbine generating power from its rotation, there is also a wind resistance introduced by the wind.

As Figure 3.12 shows wind resistance is collinear with the direction of the apparent wind. Wind resistance for a stationary turbine is counterbalanced by its base. For renewable robot undergoes a global motion, the resistance has to be balanced by the propulsion system to keep the speed of the robot. The power discount due to wind resistance $\mathbf{F}$ at speed $\mathbf{v}_s$ is

$$\begin{aligned} P_d &= -\mathbf{F} \cdot \mathbf{v}_s / \eta_p \\ &= -\frac{F v_s}{\eta_p} \cos(\theta_w) \end{aligned} \tag{3.66}$$

where θ_s is wind angle as it shown in Figure 3.12, η_p is propulsion efficiency.

Wind resistance on the turbine depends on the turbine characteristic and the apparent wind velocity:

$$\mathbf{F} = \frac{1}{2}\rho C_T(\lambda) A_w ||\mathbf{v}|| v \tag{3.67}$$

where ρ is density of the air, $C_T(\lambda)$ is thrust coefficient, λ is tip speed ratio, A_w is wind turbine swept area, v is apparent wind speed. The direction of axial force is in align with the direction of apparent wind.

It is surprising that the power discount is not always negative that the robot has to consume energy to balance the resistance. At certain wind angle, the power discount can be positive that save the propulsion power for the robot.

For example, if the wind angle is 0 then the apparent wind is collinear with robot velocity. The discount power P_d help to reduce propulsion power consumption. Another example is at a wind angle of π, the apparent wind is the opposite of the mobile velocity. The discount power will increase the propulsion power consumption due to wind resistance.

The total discounted power generation P_w from a wind turbine is

$$P_w = P_t(v) - P_d(\mathbf{v}, \mathbf{v}_s) \tag{3.68}$$

where P_t is net power generation, P_d is power generation discount, v is apparent wind and $\mathbf{v}_s$ is robot velocity.

Power discount due to the global motion of the renewable robot is another factor to consider in the wind power model. The complex interaction between the wind and the robot is simplified as a discounted power model. It is clear that for renewable robot with a much higher global speed than the true wind $v_s >> v_t$, the apparent wind is dominant by the virtual wind generated by its motion. The actual discounted power generation needs to be further studied to understand the net gain of installing a wind turbine on those robots.

When the thrust coefficient and power coefficient of the turbine is not provided by the manufacturer, the momentum theory is used to figure out those coefficients in Equation 3.68.

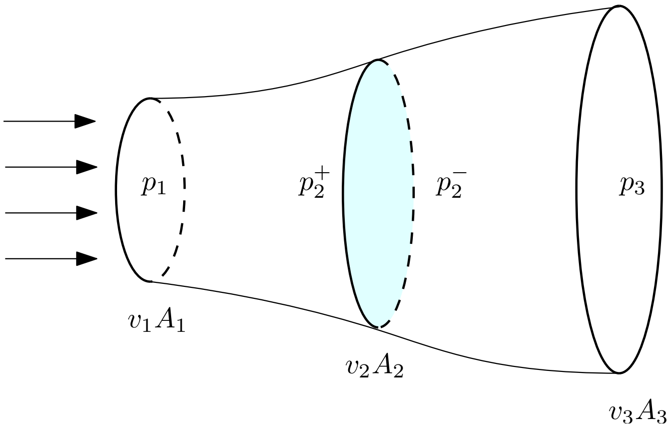

FIGURE 3.13: Idealised wind turbine

The momentum theory abstract the wind turbine as an actuator disc shown as a blue disk in Figure 3.13. The flow is assumed to be incompressible, steady, ideal fluid and the actuator disc extracts energy from the flow. Velocity and pressure at upstream location, near actuator disc and at far end is v_1, p_1, v_2, p_2 and v_3, p_3 correspondingly.

The actuator disc creates a discontinuity before and after the flow, the change of momentum is the source for the power generation. The change of momentum can be found using the pressure drop between pressure before disc p_2^+ and after disc p_2^-. According to Bernoulli's equation, the pressure before and after rotation disc are:

$$p_1 + \frac{1}{2}\rho v_1^2 = p_2^+ + \frac{1}{2}\rho v_2^2 \tag{3.69}$$

$$p_2^- + \frac{1}{2}\rho v_2^2 = p_3 + \frac{1}{2}\rho v_3^2 \tag{3.70}$$

since the upstream location and the far end are distant from the rotation disc, pressure at those two places is the same as the atmosphere pressure $p_1 = p_3$. The pressure drop before and after the disc is then

$$\Delta p = p_2^+ - p_2^- \tag{3.71}$$

Subtract Equation 3.69 and Equation 3.70, the pressure drop is then

$$\Delta p = \frac{1}{2}\rho(v_1^2 - v_3^2) \tag{3.72}$$

Also the conservative of mass tell us

$$\Delta p = \rho v_2(v_1 - v_3) \tag{3.73}$$

from Equation 3.72 and Equation 3.73, the velocity at disc is then

$$v_2 = \frac{v_1 + v_3}{2} \tag{3.74}$$

however, we only know the relationship between v_2 and the average of v_1 and v_3, the axial induction factor a can be defined as

$$a = \frac{v_1 - v}{v_1} \tag{3.75}$$

wind speed at rotation disc is then

$$v_2 = (1 - a)v_1 \tag{3.76}$$

The thrust acting on the disc is

$$T = \Delta p A_2 \tag{3.77}$$

and the power extracted from the wind is

$$\begin{aligned} P &= T v_2 \\ &= \Delta p A_2 v_2 \end{aligned} \tag{3.78}$$

with axial induction factor a the thrust and extracted power is then

$$T = 2\rho A_2 v_1^2 a(1 - a) \tag{3.79}$$

$$P = 2\rho A_2 v_1^3 a(1 - a)^2 \tag{3.80}$$

notice that v_1 is wind speed of upstream and A_2 is swept area of wind turbine. If we let $v = v_2$ and $A_w = A$, the thrust coefficient and power coefficient are

$$C_T = T/\frac{1}{2}\rho A v^2 = 4a(1 - a) \tag{3.81}$$

$$C_P = P/\frac{1}{2}\rho A v^3 = 4a(1 - a)^2 \tag{3.82}$$

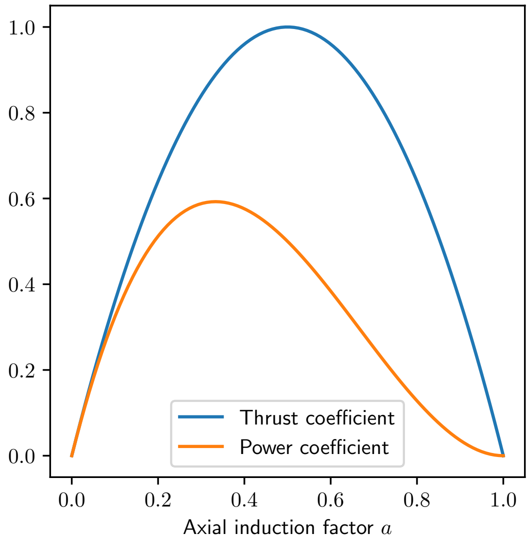

FIGURE 3.14: Power and thrust coefficient of idealised turbine

The thrust coefficient and power extraction coefficient as a function of the axial induction factor is shown in Figure 3.14.

The power coefficient is lower than the thrust coefficient at the same axial induction factor. Maximum power coefficient 16/27 is found at axial induction factor $a = 1/3$. The maximum power coefficient is also known as the Betz limit of the wind turbine. No wind turbine can capture more kinetic energy from the wind higher than this limit. The thrust coefficient of the wind turbine has a maximum when $a = 1/2$.

3.2.3 Assessment

The discounted wind power generation due to local and global motion of the renewable robot is

$$\begin{aligned} P_w &= P_t(\mathbf{v}') + P_d(\mathbf{v}', \mathbf{v}_s) \\ &= \frac{1}{2}\rho C_p A_w ||\mathbf{v}'||^3 + \frac{\mathbf{F}\cdot\mathbf{v}_s}{\eta_p} \\ &= \frac{1}{2}\rho C_p A_w ||\mathbf{v}'||^3 + \frac{1}{2\eta_p}\rho C_t A_w ||\mathbf{v}'||\mathbf{v}' \cdot \mathbf{v}_s \end{aligned} \tag{3.83}$$

where $\mathbf{v}'$ is apparent wind velocity under local motion. The averaged apparent wind under small periodic local rotation amplitude is

$$\begin{aligned} \bar{\mathbf{v}}' &= \frac{1}{2p_0 \cdot 2q_0 \cdot 2r_0} \int_{-r_0}^{r_0} \int_{-q_0}^{q_0} \int_{-p_0}^{p_0} \mathbf{v}' dp\, dq\, dr \\ &\approx \begin{bmatrix} v_{te} & v_{tn} & v_{tu} \end{bmatrix}^T - \mathbf{I} \begin{bmatrix} v_{se} & v_{sn} & v_{su} \end{bmatrix}^T \\ &= \mathbf{v}_t - \mathbf{v}_s \end{aligned} \tag{3.84}$$

Compare the net wind turbine power generation P_t and the wind resistance discount P_d

$$\begin{aligned}\frac{P_t}{P_d} &= \frac{\rho C_p A_w ||\mathbf{v}'||^3}{\rho C_t A_w ||\mathbf{v}'||\mathbf{v}' \cdot \mathbf{v}_s/\eta_p} \\ &= \eta_p \frac{C_p}{C_t} \cdot \frac{||\mathbf{v}^{'}||^2}{\mathbf{v}' \cdot \mathbf{v}_s}\end{aligned} \tag{3.85}$$

for an idealised wind turbine, both power and thrust coefficient can be written as function of axial induction factor a:

$$\begin{aligned}\frac{P_t}{P_d} &= \eta_p \frac{4a(1-a)^2}{4a(1-a)} \cdot \frac{||\mathbf{v}^{'}||^2}{\mathbf{v}' \cdot \mathbf{v}_s} \\ &= \eta_p(1-a)\frac{||\mathbf{v}^{'}||^2}{\mathbf{v}^{'} \cdot \mathbf{v}_s} \\ &= \eta_p(1-a)\frac{||\mathbf{v}_t - \mathbf{v}_s||^2}{(\mathbf{v}_t - \mathbf{v}_s) \cdot \mathbf{v}_s}.\end{aligned} \tag{3.86}$$

Commonly, the propulsion efficiency η_p is smaller than 1 and the ratio between power and thrust coefficient is less than 1 when the turbine is rotating. The relative speed and direction between true wind and robot will determine if there is a net gain to install a wind turbine.

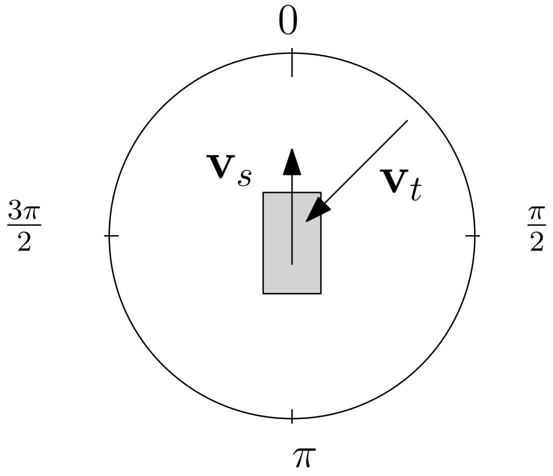

FIGURE 3.15: Relative wind angle on moving robot

Assume the true wind is angled θ from the north, the vector

$$\mathbf{v}_t = \begin{bmatrix} v_w \sin(\theta) & -v_w \cos(\theta) & 0 \end{bmatrix}^T \tag{3.87}$$

represents the true wind v_w.

The net to discount power ratio can be demonstrated in three examples. A renewable robot moving northward at a global speed of 3 m/s. True wind at a lower (1 m/s), the same (3 m/s) and a higher (10 m/s) speed is coming from various angles (shown in Figure 3.15). The swept area of the wind turbine is $1m^2$.

Lower wind speed

For true wind speed of 1 m/s, the cut-in speed of the wind turbine is temporally neglected to study the power generation potential at low wind speed. The discounted power generation on various true wind angle is shown in Figure 3.16.

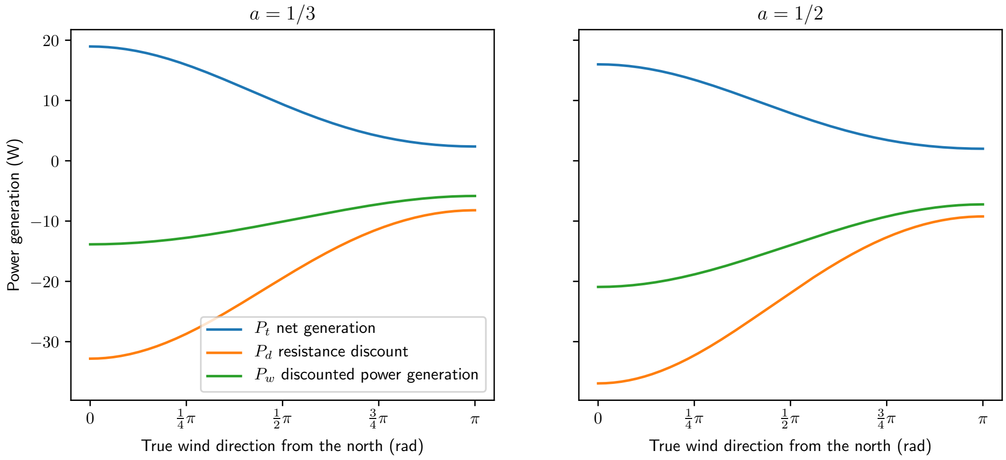

FIGURE 3.16: Discount wind power generation when $v_t < v_s$

The result seems counter intuitive that the discounted power generation is negative. Figure 3.16 shows the net wind power generation and resistance discount at two induction factor $a = 1/3$ and $a = 1/2$. Net wind power generation in both cases is positive on all wind angle. However, the resistance discount is higher than the net wind power generation. When the wind resistance is included, the renewable robot consumes more energy in propulsion than the wind turbine generated. This situation is worst in headwind condition where the wind comes from the north.

Same wind speed

At true wind speed of 3 m/s, the discounted power generation is shown in Figure 3.17.

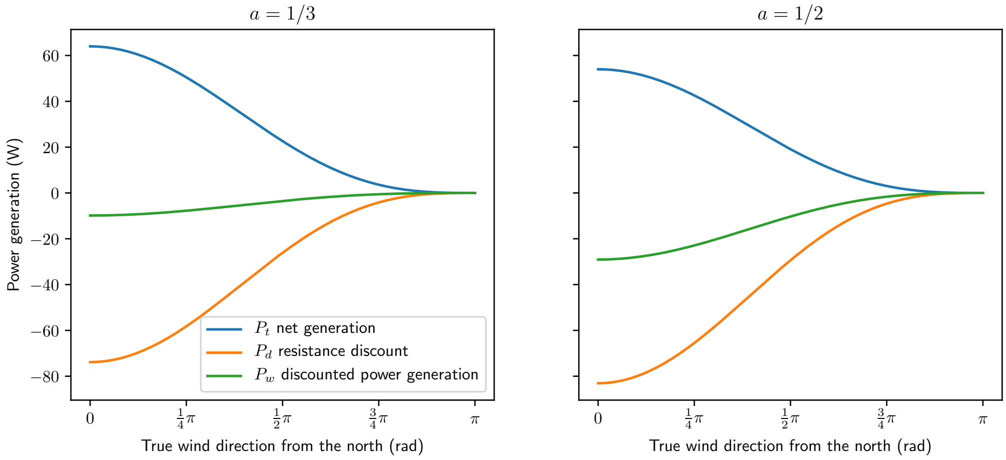

FIGURE 3.17: Discount wind power generation when $v_t = v_s$

A wind turbine generates more power from a higher true wind speed but also suffer from a larger resistance. In the headwind condition, the resistance discount is slightly larger than the net power generation. Discounted power generation in both cases is negative due to the resistance. At wind angle π, the true wind has the same speed and direction as the robot. Apparent is cancelled out and there is no wind power generation and resistance discount.

Higher wind speed

At higher true wind speed of 10 m/s, the discounted power supply at two axial induction factor is shown in Figure 3.18.

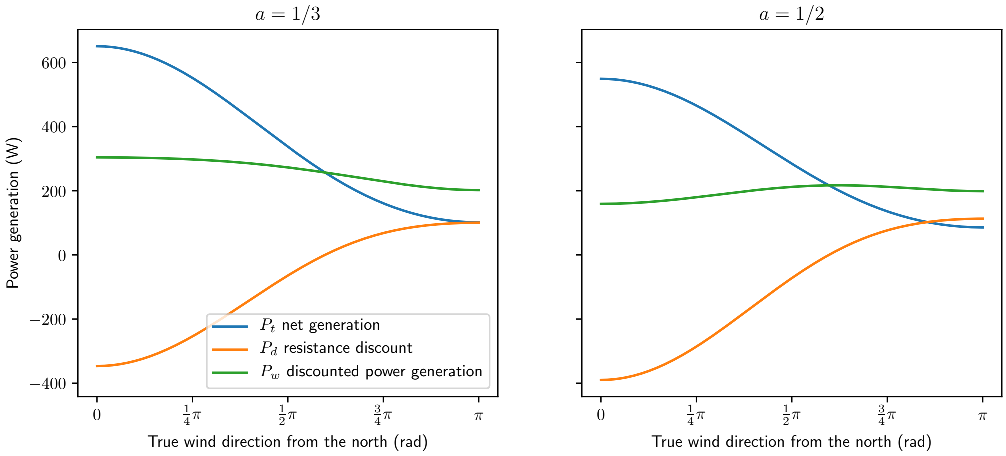

FIGURE 3.18: Discount wind power generation when $v_t > v_s$

Discounted power generation on both axial induction factors is positive. Net power generation can compensate for the wind resistance discounted due to the wind drag. Power generation curve shows the resistance discount is positive between true wind angle $3\pi/4$ to π at $a = 1/3$. The apparent wind is in the range is in the direction of robot forward velocity. Propulsion power is saved as the resistance of the wind could help to drive the robot.

However, this is a virtual power that the resistance contribution to the propulsion only save power but does not generate any actual power. This explains why the wind turbine has a higher discounted power generation when the axial induction factor is maximised for thrust $a = 1/2$ compared to $a = 1/3$ between true wind $3\pi/4$ to π. When resistance discount is larger, the potential power saving to the robot propulsion will be greater as well.

In the power system model, the electrical power generation of the wind turbine would always be the net power generation and the potential energy-saving or additional resistance spending is discounted in the propulsion system. This is not a limitation but rather an advantage of this model. The actual benefit of installing a wind turbine can be evaluated without a propulsion model in great detail.

In summary, the global and local motions all have their influence on the wind power generation. The local motion changes the local wind speed due to its rotation. Such impact is minimal when the amplitude of the local rotation is small. For robots with large local motion, the change rate of the wind speed also depends on the speed of the robot.

Global motion, on the other hand, has an impact on the wind speed from the resource side. Another important factor is the global motion requires the robot to balance the resistance of the wind turbine while keeping the speed and direction of the robot. This will introduce additional resistance spending or potential energy saving based on the direction and relative speed of the wind.

3.3 Demand load model

Demand load is the total energy consumption of the renewable robot. The operation of the robot requires an electrical power supply to the navigation and control, communication, sensor and propulsion systems. In this section, the demand load model of the renewable robot will be introduced.

A novel demand load model will be presented in this section. The conventional propulsion and hotel load based method is a convenient way to estimate the total power consumption based on the role of the robot. A novel critical and performance load based method introduce the concept of safety level in the power consumption model.

3.3.1 Propulsion and hotel load

Propulsion and hotel load classification is the classical power consumption model. The propulsion load is the power consumed to drive the renewable robot. At the speed of v, the propulsion load of the robot is:

$$P_{prop} = R_T \cdot v_s / \eta_p \tag{3.88}$$

where R_T is the propulsion resistance of the robot and η_p is electric propulsion efficiency. The model of propulsion resistance is domain-specific to each type of robots that depends on the propulsion mechanism, actuator characteristic and electric driving system.

If the wind turbine is used, the propulsion power discount would also need to be included. Additional resistance that balanced by the propulsion system is

$$P_d = \frac{1}{2\eta_p} \rho C_t A_w ||\mathbf{v}|| \mathbf{v} \cdot \mathbf{v}_s \tag{3.89}$$

where ρ is density of the air, C_t is thrust coefficient, A_w is wind turbine swept area, and v is apparent wind.

The wind power discount would spend or save energy for the propulsion system depending on the relative speed and direction of the wind. However, the minimal propulsion power after discount shouldn't smaller than zero if there are no regenerative devices in the system. The total discounted propulsion power consumption if the wind turbine is installed is:

$$\max\{R_T \cdot v_s / \eta_p - P_d, 0\} \tag{3.90}$$

The hotel load is the total power consumption of all other systems than the propulsion system. These systems support the navigation, control and sensory functionality of the renewable robot. and operate on their own duty cycle.

$$p_i = p_{i,\min} + (p_{i,\text{norm}} - p_{i,\min}) d_i \tag{3.91}$$

where $p_{i,\mathrm{min}}$ is stand-by power consumption at idle state, $p_{i,\mathrm{norm}}$ is power consumption at norm operating state, $d_i \in [0, 1]$ is duty cycle.

Hotel load of all sub-systems is:

$$\begin{aligned} P_{hotel} &= \sum_{i=0}^{j} p_i \\ &= p_{1,\mathrm{min}} + (p_{1,\mathrm{norm}} - p_{1,\mathrm{min}})d_1 + \cdots + p_{j,\mathrm{min}} + (p_{j,\mathrm{norm}} - p_{j,\mathrm{min}})d_j \\ &= \mathbf{p}_{\mathrm{min}} + (\mathbf{p}_{\mathrm{norm}} - \mathbf{p}_{\mathrm{min}})\mathbf{d} \end{aligned} \tag{3.92}$$

where $\mathbf{p}_{\mathrm{min}} = [p_{1,\mathrm{min}}, p_{2,\mathrm{min}}, \cdots, p_{j,\mathrm{min}}]$ is the minimal power consumption of each subsystem, $\mathbf{p}_{\mathrm{norm}} = [p_{1,\mathrm{norm}}, p_{2,\mathrm{norm}}, \cdot, p_{j,\mathrm{norm}}]$ and $\mathbf{d} = [d_1, d_2, \cdots, d_j]$ are normal power consumption and duty cycle of each sub-system.

Let

$$\mathbf{P} = \begin{bmatrix} \mathbf{p}_{\mathrm{min}} \\ \mathbf{p}_{\mathrm{norm}} \end{bmatrix} \tag{3.93}$$

and

$$\mathbf{D} = \begin{bmatrix} \mathbf{I} - \mathbf{d} & \mathbf{d} \end{bmatrix} \tag{3.94}$$

the hotel load of renewable robot is

$$P_{hotel} = \mathbf{P} \cdot \mathbf{D}. \tag{3.95}$$

Demand load of a renewable robot consists of both propulsion and hotel load.

$$\begin{aligned} P_l &= P_{prop} + P_{hotel} \\ &= \max\{R_T \cdot v_s/\eta_p - P_d, 0\} + \mathbf{P} \cdot \mathbf{D} \end{aligned} \tag{3.96}$$

3.3.2 Critical and performance-related load

Critical and performance load method model the power consumption as critical and performance-related parts:

$$P_l = P_c + P_p \tag{3.97}$$

where P_c is critical load and P_p is performance-related load.

The critical load is the minimal level of power supply for the safe operation of the renewable robot. Depending on the type of robot, this may include the safe-critical electronic devices and the propulsion power to manoeuvre the robot.

The critical load consists of safe-critical electronic devices that are always on. These devices are on the full duty cycle

$$\begin{aligned} P_{hotel,c} &= \mathbf{P}_{c,hotel}\mathbf{D}_{c,hotel} \\ &= P_c \begin{bmatrix} \mathbf{I}-\mathbf{d} & \mathbf{d} \end{bmatrix} \\ &= \begin{bmatrix} \mathbf{p}_{\min,c} \\ \mathbf{p}_{\mathrm{norm},c} \end{bmatrix} \begin{bmatrix} \mathbf{0} & \mathbf{I} \end{bmatrix} \\ &= \mathbf{p}_{\mathrm{norm},c} \end{aligned} \tag{3.98}$$

Critical load for safe manoeuvre requires a minimum speed of v_c,

$$P_{prop,c} = R_T \cdot v_c/\eta_p \tag{3.99}$$

where η is the propulsion efficiency.

The performance-related load

$$P_{hotel,p} = \mathbf{P}_p\mathbf{D}_p \tag{3.100}$$

where $\mathbf{D}_p$ is adjustable performance related load duty cycle.

Performance-related load also include the increase in the speed of the robot.

$$P_{prop,p} = R_T \cdot v_s/\eta_p \tag{3.101}$$

where v_s is the speed of robot.

Total demand load of a renewable robot consists of critical load and performance-related load:

$$\begin{aligned} P_l &= P_c + P_p \\ &= [R_T \cdot v_c + \mathbf{p}_{\mathrm{norm},c}] + [R_T \cdot v_s + \mathbf{P}_p\mathbf{D}_p] \end{aligned} \tag{3.102}$$

If the wind turbine is installed, the discounted total demand load is

$$\begin{aligned} P_l &= P_c + P_p \\ &= \max\{R_T \cdot v_c + R_T \cdot v_s - P_d, 0\} + \mathbf{p}_{\mathrm{norm},c} + \mathbf{P}_p\mathbf{D}_p \end{aligned} \tag{3.103}$$

An relationship between two models can be found in Figure 3.19.

Conventional hotel and propulsion load model is a deterministic model that can be quickly estimated. This model is widely used for the initial design of the REHS as it is computationally inexpensive to optimise the configuration. Critical load model is a dynamic model that the selection of the duty cycle and robot speed depends on the power generation that is highly variable in nature. The critical load model is powerful to design a safe management strategy after an REHS configuration is found. The critical load is the minimal level of power supply to guarantee for the robot. While the performance-related is adjustable according to energy availability.

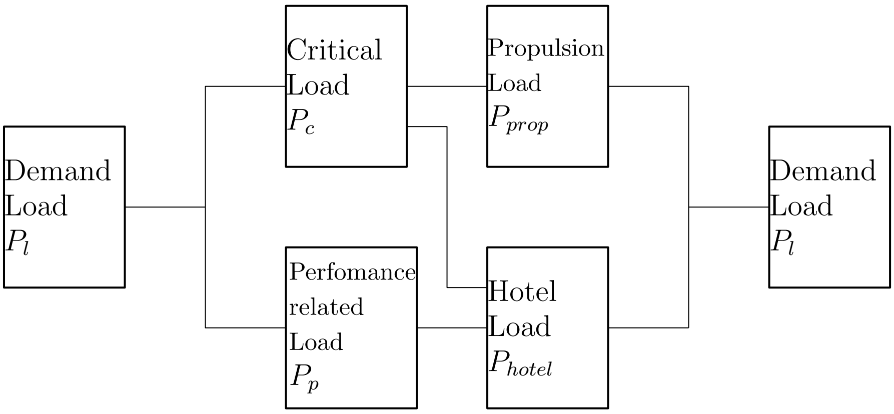

FIGURE 3.19: The relationship between demand load components

3.4 Battery and control model

Battery and control module is at the centre of the REHS connecting the power generation and demand load. As it is shown in Figure 3.20, the battery and control model integrates a finite state machine based battery energy model and a power management unit.

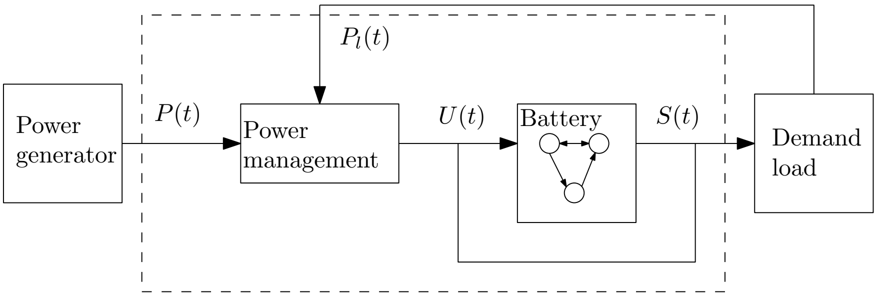

FIGURE 3.20: The power flow in battery model (dashed part as model)

The power generated from renewable energy harvesting devices $P(t)$ is the input and actual supplied power $S(t)$ is the output of the system. When generated power is received by the battery system, the power management system decides on the planned power usage $U(t)$ based on the power generation, the demand load requirement $P_l(t)$ and optionally the state of the battery. The battery energy model then calculates the power supply depending on the energy availability and planned energy usage.

The battery energy model is a finite state machine with three states: charge, discharge and floating. The state is determined by the relationship between power generation $P(t)$ and planned power usage $U(t)$. The state transfer is shown in Figure 3.21.

When the power generation is greater than the planned power usage, if the battery isn't full the excessive power will be stored in the battery, otherwise, it will enter floating model that excessive energy will be wasted. When the power generation is less than the planned power usage, if the battery has energy storage higher than the depth of discharge, the battery will discharge to meet the difference between the user demand and the power generation. The battery will not discharge if the battery after discharge will be lower than the depth of discharge. This is to protect the

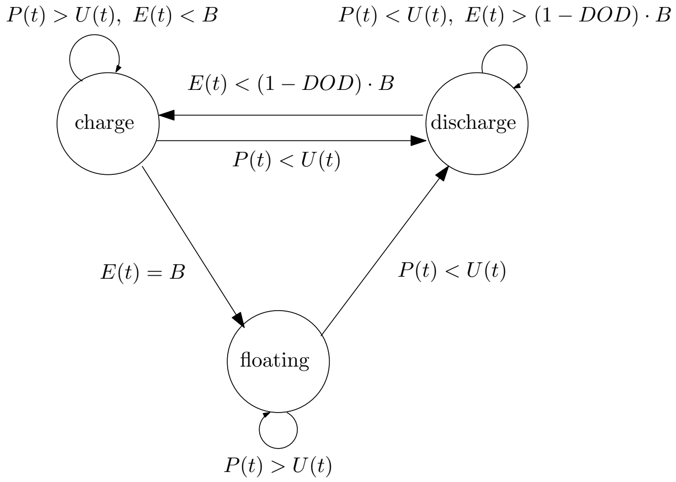

Figure 3.21: Finite state battery model

battery from being over-discharged. In each state, the remaining energy in the battery can be calculated from the power generation, planned power usage and the battery self-discharge rate.

$$E(t+\Delta T) = \begin{cases} E(t)(1-\sigma) + \eta_{in}[P(t) - U(t)] \cdot \Delta T & \text{charge} \\ E(t)(1-\sigma) + \frac{[U(t)-P(t)]}{\eta_{out}} \cdot \Delta T & \text{discharge} \\ E(t)(1-\sigma) & \text{floating} \end{cases} \tag{3.104}$$

where $E(t)$ is energy remains in the battery, $P(t)$ is renewable power generation, $U(t)$ is load demand, σ is self-discharge rate of batteries, ΔT is time step in the simulation. η_{in} is battery charging efficiency, η_{out} is battery discharge efficiency. The state of charge SOC for a battery at capacity B is often used to indicate the level of charge of the battery. $SOC(t) = E(t)/B$

Using the concept of actual power supply $S(t)$,

$$S(t) = \begin{cases} U(t) & P(t) \geq U(t) \\ U(t) & P(t) < U(t) \text{ and } E(t) \geq (1-DOD)\cdot B \\ 0 & P(t) < U(t) \text{ and } E(t) < (1-DOD)\cdot B \end{cases} \tag{3.105}$$

where DOD is depth of discharge. A naive power management strategy can simply plan the power usage as the demand load requirement $U(t) = P_l(t)$. At the time when the power generation is greater than the planned power usage, the power requirement can be then met by the system. In the case when power generation is less than the demand load requirement and the energy in the battery is higher than the lowest capacity defined by the depth of discharge, the planned power usage can still be satisfied through battery discharge. The lost power supply will happen if the power generation is less than the planned power usage and the battery could not make up the difference. Such an event will cause an operational problem for the mobile robot e.g, performance degradation, service discontinuity and even the loss of autonomy.

The power supply $S(t)$ could bypass the battery storage and directly reach the demand load. It is also reasonable to discharge the battery to supply power while the generation is in a shortage. However, in the case when the battery is undercharged, the battery system would not be able to supply any power to the system. This is a lost power supply event and the total fraction of time that power supply is lost is defined as lost power supply probability (LPSP).

$$
\begin{aligned}
LPSP &= \mathbb{P}[S(t) < P_l(t)] \\
&= \frac{1}{T_t}\sum_{t=0}^{T_t}[S(t) < P_l(t)]
\end{aligned}
\tag{3.106}
$$

In the system capacity planning of REHS, one of the objectives is to design a system at lower lost power supply probability. This is often involved with the selection of appropriate renewable energy generator and the capacity of the battery. A battery with small capacity couldn't store enough energy that can be used in the future. The battery that is too big will increase the cost and the size of the renewable energy system which is not ideal for a mobile robot with limited space. How to find a good trade-off between LPSP, size, and cost of the battery system is the topic that will be discussed in the next chapter.

3.5 Moving REHS simulation

The reliability and economy performance of the power system can be simulated by the moving REHS model. In the previous section, the impact of global and local motions of renewable robot has been analysed. The moving REHS simulation needs to consider both factors for the optimisation process.

During the renewable robots' long-term operation, it will travel a long-distance to finish its duty. The locations that the robot have to visit can be defined as the route.

$$
\mathcal{R} := [s_1, s_2, \cdots, s_n] \tag{3.107}
$$

where s_1 to s_n are way points.

Knowing only the route is not enough to simulate moving REHS because both location and the time matters to REHS operation. For example, the solar power generation $P_s = P_s(s, t, A_s)$ does not only depending on the area of solar panel A_s, but also influenced both by s, which is the location of the renewable robot, and t that is the time at that location.

It is not uncommon to find the typical working scenario that renewable robots have to reach each waypoint timely. In the design stage, the route can be planned as a mission that includes the arrival time of each waypoint. The concept called the mission of the renewable robot:

$$
\mathcal{M} := [(s_1, t_1), (s_2, t_2), \cdots, (s_n, t_n)] \tag{3.108}
$$

where t_1 to t_n are the planned arrival time for each corresponding way points.

3.5.1 Power generation simulation

During the mission, for the configuration with solar panel area A_s and wind turbine size A_w, the total power generation from both sources is:

$$P = P_s(s, t, A_s) + P_w(s, t, A_w) \tag{3.109}$$

where P_s is solar power generation and P_w is wind power generation.

For the solar panel at the area of A_s, the power generation is:

$$\begin{aligned} P_s &= P_s[G(s,t), T(s,t), A_s] \\ &= P_{\mathrm{STC}} \cdot \frac{G_g(s,t)}{G_{\mathrm{STC}}} \cdot \eta_s(G, T) A_s \end{aligned} \tag{3.110}$$

where G is global horizontal irradiance (GHI), G_g is the total solar radiation incident on the panel and T is ambient temperature, P_{STC} and G_{STC} are rated power and solar radiation at standard test condition (STC) correspondingly.

Total solar radiation incident on the panel is G_g calculated by

$$G_g(s,t) = I_b(s,t)\cos(\bar{\Theta}_s) + I_d(s,t)\frac{1+\cos(\bar{B}_s)}{2} + I_b(s,t)\rho \cdot \frac{1-\cos(\bar{B}_s)}{2} \tag{3.111}$$

where $\bar{B}_s$ is averaged solar angle considering the local motion of the renewable robot, I_b is beam radiation, I_d is diffused radiation, ρ is surface albedo.

Beam and diffused solar radiation are decomposed from the GHI. First the clearness index k_t is calculated as:

$$k_t(s,t) = \frac{I_g(s,t)}{TOA(s,t)\cos[\theta_z(s,t)]} \tag{3.112}$$

where I_g is GHI, TOA is the extraterrestrial global irradiance, $\theta_z(s,t)$ is zenith angle of the solar panel.

Diffused fraction $k_d = I_d(s,t)/I_g(s,t)$ then can be estimated from the clearness index k_t. The beam and direct radiation on the moving solar panel is then:

$$I_b(s,t) = I_g(s,t) \cdot k_d \tag{3.113}$$

and

$$I_d(s,t) = I_g(s,t) \cdot (1 - k_d). \tag{3.114}$$

For wind turbines at a size of A_w, the power generations are:

$$P_t(v) = \frac{1}{2}\rho_w C_p(\lambda) v^3(s,t) \tag{3.115}$$

where ρ_w is the density of the air, C_p is wind turbine coefficient, v is apparent wind speed.

Wind turbine resistance has to be account as propulsion load.

$$P_d(\mathbf{v}, \mathbf{v}_s) = \frac{1}{2\eta_p} \rho_w C_t(\lambda) A_w \mathbf{v}^2(s,t) \mathbf{v}_s(s,t) \tag{3.116}$$

where C_t the thrust coefficient of the wind turbine, η_p is electrical to propulsion efficiency, and $\mathbf{v}_s$ is the velocity of renewable robot.

The velocity of the renewable robot can be inferred from the mission $\mathcal{M}$, the renewable robot velocity between i-th leg of the waypoint is:

$$\mathbf{v}_i = \frac{s_{i+1} - s_i}{t_{i+1} - t_i}, \quad \forall (s_i, t_i) \in \mathcal{M} \tag{3.117}$$

The apparent wind velocity could be calculated from robot velocity and true wind velocity:

$$\mathbf{v} = \mathbf{v}_t - \mathbf{v}_s \tag{3.118}$$

In this simulation, the spatial-temporal data on wind and solar energy resources are required. For the solar power generation simulation, the temperature $T(s,t)$, GHI $I_g(s,t)$ and $TOA(s,t)$ are needed. The influence of local motion is included in the averaged solar angle on the moving panel. True wind velocity data $\mathbf{v}_t$ is necessary to simulate the wind power generation. Local motion effect in wind power generation is considered as a power generation discount. Those spatial-temporal wind and solar resources data also take the global motion into account.

3.5.2 Demand load simulation

Demand load is modelled by the propulsion and hotel classification at the design stage.

$$P_l = P_{prop}(s,t) + P_{hotel}(\mathbf{D}) \tag{3.119}$$

where v is the speed of the renewable robot and $\mathbf{D}$ is the design duty cycle.

For a renewable robot, the propulsion power can be estimated from the resistance and the speed of the robot v inferred from the mission $\mathcal{M}$.

$$\mathbf{v}_i = \frac{s_{i+1} - s_i}{t_{i+1} - t_i}, \quad \forall (s_i, t_i) \in \mathcal{M} \tag{3.120}$$

Spatial-temporal demand load of the renewable robot is

$$\begin{aligned} P_l &= P_{prop}(s,t) + P_{hotel}(\mathbf{D}) \\ &= R_T(s,t) \cdot v_i / \eta_p + \mathbf{P}D(s,t) \end{aligned} \tag{3.121}$$

where $\mathbf{P}$ is minimal and normal power consumption of the hotel load devices, $D(s,t)$ is an realisation of the duty cycle

$$D(s,t) \sim \mathcal{N}(\mu, \mathbf{\Sigma}) \tag{3.122}$$

where $\mu = \mathbf{D}^T$ and $\mathbf{\Sigma}$ is covariance matrix of hotel load.

The demand load could also be modelled as critical and performance-related parts

$$\begin{aligned} P_l &= P_c + P_p \\ &= [R_T \cdot v_c + \mathbf{p}_{\text{norm},c}] + [R_T \cdot v_s + \mathbf{P}_p \mathbf{D}_p] \end{aligned} \tag{3.123}$$

Compare to the critical and performance load model, the duty cycle of the performance-related load has to be dynamically determined by the energy availability. It is more computationally inexpensive to simulate the demand load with a semi-deterministic demand load model. Due to this reason, in the design stage, the demand load is modelled after propulsion and hotel loads. The critical and performance load model is used in the power management system where the renewable robot plan power usage.

3.5.3 Battery and control simulation

For the mission, $\mathcal{M}$, both power generation and demand load could be estimated on a given configuration A_s and A_w. The battery energy simulation is now at the centre of the REHS. On one hand, it receives the power generated from renewable energy sources. On the other hand, the battery system plans the use of energy and dispatch it to the demand load. Many important design objectives can be quantitatively assessed by simulating the battery system e.g. the power supply reliability and the capital cost of the renewable energy devices.

The power generation $P(s,t)$ and demand load profile $P_l(s,t)$ will increase monotonically on time t. This allows the simulation on the battery system on every time steps.

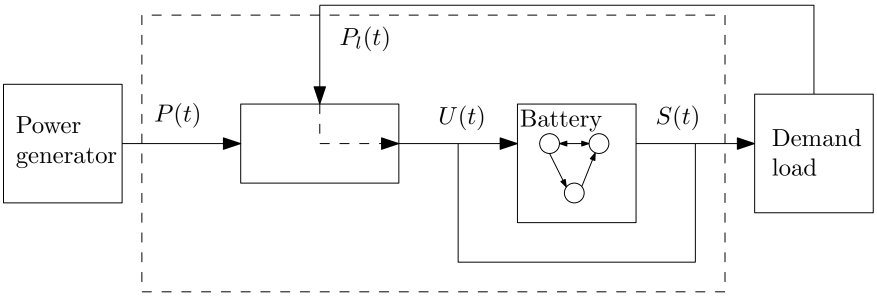

FIGURE 3.22: REHS battery energy simulation

The battery system is shown as dashed area in Figure 3.22. The power generated from renewable sources received by the battery system and it plans the power usage $U(t)$ internally. In the design of REHS, a simple demand load follow (DLF) power strategy was applied. This strategy simply plans the power usage $U(t)$ the same as demand load $P_l(t)$.

The actual power supply $S(t)$ depends on the energy left in the battery and the power generation at that time. The rule to determine the power supply $S(t)$ was modelled as a finite state machine in section 3.4. For a given capacity of the battery B, both energy in the battery $E(t)$ and the actual power supply $S(t)$ could be simulated. Battery and control simulation is shown in algorithm 1.

```
foreach $t$ in $T_t$ do
    if $U(t) \leq P(t)$ ;
    then
        $S(t) = U(t)$;
        Battery charge $P(t) - U(t)$;
    else
        if $E(t) \geq (1 - SOC) \cdot B$ then
            Battery discharge $U(t) - P(t)$;
            $S(t) = U(t)$
        else
            $S(t) = 0$ ;
            Battery charge $P(t)$;
        end
    end
end
```

Algorithm 1: Battery finite state machine

Power supply reliability

As a result of the simulation, the fraction of time that demand load is not supplied can be measured.

$$\begin{aligned} LPSP &= \mathbb{P}[S(t) < P_l(t)] \\ &= \frac{1}{T_t} \sum_{t=0}^{T_t} [S(t) - P_l(t) < 0] \end{aligned}$$

This index is called lost power supply probability (LPSP) and often used to represent the reliability of the power supply. In the REHS design, one of the goals is to minimise the LPSP.

REHS capital cost

Another goal in the REHS design is to find an economic configuration. The capital cost of REHS can be modelled as:

$$C = c_w \cdot A_w + c_s \cdot A_s + c_b \cdot B \tag{3.124}$$

where c_w is unit price cost of wind turbine, c_s is unit price cost of solar panel and c_b is unit price cost of battery.

3.6 Summary

In this chapter, the REHS model for mobile robots have been introduced. This novel moving REHS model is developed to include the motion of the robot in the power system. The motion of the robot is decomposed into global and local components. Each component has shown an influence on both power generation and demand load in the power system. An assessment on the solar and wind power generation shows some quite surprising result.

First of all, the global motion of the robot is found to influence the power generation from the resources side. As the renewable energy resource is unevenly distributed both temporally and spatially, the power generation from wind and solar resources changes as the robot moves. Since the time and location of robot both determine the power generation, the power system have to include the global motion in the model.

Secondly, the local motion impact the solar and wind power generation differently. Solar power generation is subject to the change in the solar angle between the panel and the sun. The solar angle would change as the orientation of the panel move. As a result, the total solar radiation on the panel as the irradiance components change with the solar angle. For a solar panel with a flat initial installation orientation, the yaw motion of the robot has no influence on its power generation. However, the pitch and roll motion of the robot would increase or decrease the power generation depending on the solar position and the amplitude of the motion. Further assessment on the solar power generation under the local motion shows how periodical pitch and roll motion would impact the power generation. When the solar panel is subject to an periodic pitch and roll motion around 23 degrees, there will 10 percent loss in the solar power generation on average. A larger motion amplitude would result a higher loss in solar power generation. Instantaneous power generation may reduce by 39 % on a clear day and 13 % on a cloudy day.

The local motion on the wind power generation study yields a more surprising result. Depending on the wind direction, the net wind power generation may be negative due to the wind turbine resistance. The wind resistance of the turbine has to be counterbalanced to keep the location and the speed of the robot. This would require the propulsion system to fight against the wind resistance. If the direction of wind is the opposite to the velocity of the robot, additional power is consumed in propulsion system. However, wind in the same direction to the robot's velocity could also save some propulsion power to increase the net power generation. The assessment shows that due to the local motion of the robot, the wind power generation is subject to both wind and robot velocity. For robot's applications with a speed much higher than the wind speed, there is no benefit in using wind turbine at all. To take the most advantages of the wind power, the speed and the direction of robot are important.

Demand load model, on the other hand, is also found influenced by the robot's global and local motions. Comparing to the propulsion load, the hotel load of the mobile robot is less sensitive to the motion of the robot. This is due to the hotel load of the robot are mostly electronic devices for the control, communication and sensory systems. Power consumption of these systems are largely determined by the duty cycle.

There are many factors that influence the propulsion load of the mobile robot e.g. type of robot, propulsion mechanism and efficiency. Moving REHS model includes a generic propulsion load in the power system. While the propulsion power is subject to the change in environment, the motion of the robot also would impact the propulsion load. However, because the propulsion system is specific to the robot, the motion influence has to be accounted on an application basis.

In general, the moving REHS model includes the motion of the robot in the power system. This model itself provides an insight on the moving REHS. A data-driven simulation approach is also developed for a numerical study on the power system. Data-driven approach using the historical meteorological data to simulate the performance of the REHS. This is a foundation to the model and the design of REHS in next chapter.

Chapter 4

REHS configuration design

In this chapter, the REHS configuration design methods are presented. The first method is the design feasibility exploration that investigates the best possible reliability and economic performance of the REHS under the size constraint. As a design exploration method, it also shows the relationship between the design objectives and the constraint. From the information given by the design feasibility exploration, it can be decided whether it is possible to design the REHS for a required performance level.

The second method is the optimal REHS configuration optimisation that recommend a design with the best compromise between the cost and reliability of the system. Together with the design exploration, the REHS configuration design method will allow the power system design for a size constraint moving system.

In the REHS configuration design, the objective of the cost is to reduce the device capital. A more cost-effective REHS configuration improve the economic performance of the renewable robot. Two methods that will presented in this chapter are complimentary to each other. The feasibility, optimality and the long term performance of the design optimisation method will also be studied in several design cases.

4.1 REHS configuration design problem formulation

4.1.1 Design objectives and constraints

In the REHS configuration design, the most important factors to consider are the cost and the reliability of the system. For a given mission, those two design objectives are determined by the REHS configuration. An REHS configuration consists of the area of solar panel A_s, swept area of wind turbine A_w and capacity of the battery B.

Reliability of the REHS has to be simulated from a given mission. For a mission, $\mathcal{M}$, the power generation and the demand load can be estimated using the moving REHS model and data-driven simulation approach. By comparing the power generation and demand load, the reliability index LPSP is available to the optimisation.

$$\begin{aligned} LPSP &= \mathbb{P}[S(t) < P_l(t)] \\ &= \frac{1}{T_t}\sum_{t=0}^{T_t}[S(t) - P_l(t) < 0] \end{aligned} \tag{4.1}$$

In the REHS configuration, the design objective on the reliability is to optimise the LPSP to an expected level. For example, fully autonomous operation of the renewable robot requires the power system to support the demand load during the whole mission. The reliability requirement, in this case, is a zero LPSP for the mission.

Cost of the REHS C is a function of the size of solar panel, wind turbine and capacity of the battery. The capital cost of renewable energy devices instead of maintenance cost is selected because the renewable robot is supposed to operate fully autonomous during the mission. The capital cost of the REHS is

$$C = c_w \cdot A_w + c_s \cdot A_s + c_b \cdot B \tag{4.2}$$

where c_w is unit cost of wind turbine, c_s is unit price cost of solar panel and c_b is unit price cost of battery.

Constraints on the REHS configuration are the size limits of each renewable energy harvesting devices (include energy storage devices). The size constraint on those devices is due to the limited space on the renewable robot.

$$\begin{aligned} &0 \leq A_w \leq \bar{A}_w \\ &0 \leq A_s \leq \bar{A}_s \\ &0 \leq B \leq \bar{B} \end{aligned} \tag{4.3}$$

where $\bar{A}_w$ is the maximum swept area of the wind turbine, $\bar{A}_s$ is maximum size of solar panel, and $\bar{B}$ is the maximum capacity of the battery.

The size limits are hard constraints that violating REHS configurations can not physically installed on the robot. Given the size constraint, there are two classes of the optimisation problem to be solved to find a suitable REHS configuration.

The problem is the feasibility problem that searches the design space to find whether it reaches the design goal under the size constraint. On top of that, the second class of the problem is an optimisation problem in selecting the best configuration among a set of configurations satisfied the design goal. Two classes of optimisation problem will be introduced in the next section.

4.1.2 Design feasibility problem

In the REHS configuration design, the power system is expected to reach a certain level of reliability and cost performance. However, the capital cost of the REHS (C) and the LPSP are competing objectives in the REHS configuration design. An increase in reliability performance will also increase the device cost. REHS configuration has to compromise between the cost and the reliability to reach design objectives. Furthermore, hard constraints on the size of RHES is a crucial limiting factor to a feasible REHS configuration design.

In order to find the feasible reliability and cost performance that is achievable under the size constraint, a constraint multiple objectives optimisation methods are employed. Both reliability and cost of the REHS configuration are optimised against each other.

$$\begin{aligned} \underset{A_w, A_s, B}{\text{minimize}} \quad & f_1 = C(A_w, A_s, B) \\ & f_2 = LPSP(A_w, A_s, B) \\ \text{subject to} \quad & 0 \leq A_w \leq \bar{A}_w \\ & 0 \leq A_s \leq \bar{A}_s \\ & 0 \leq B \leq \bar{B} \end{aligned} \tag{4.4}$$

where C is device cost function, $LPSP$ is lost power supply probability.

Result of the multiple objectives optimisations is REHS configuration Pareto front solutions that no objective could be further improved without sacrificing another objective. One extreme case is the most cost-effective REHS configuration at the minimal f_1. This solution will suggest a zero cost REHS configuration by not using any REHS devices at all. Due to the design trade-off between cost and reliability, the reliability index is also expected to be high for this configuration.

Compare to the most-effective configuration, the design feasibility problem more interested in finding a more reliable REHS configuration. The most reliable REHS configuration has a minimal f_2 in Pareto front solutions.

$$LPSP_{\text{min}} = \min f_2 \tag{4.5}$$

The feasibility problem address the fundamental REHS configuration planning challenge that whether is possible to design a system to reach the reliability goal.

$$\min f_2 = LPSP_{\text{min}} \leq LPSP_{\text{goal}} \tag{4.6}$$

Among a set of REHS configurations, REHS configurations with a $LPSP_{\text{min}} = 0$ are particularly attractive to the renewable robot. At zero LPSP, the REHS configuration can fully support the renewable robot's autonomous operation.

If the lowest LPSP is higher than zero, $LPSP_{\text{min}} > 0$ there is a risk that the renewable robot may lose power supply during the mission. It has to rely on a backup energy source at the time when it lost the power supply.

As a multiple objectives design optimisation problem, the design feasibility problem also presents the relationship between the cost and the reliability. An example is shown in Figure 4.1.

In this example, the minimal LPSP of the REHS configuration under the size constraint is pointed by the red arrow. The lowest LPSP suggests the most reliable REHS configuration in

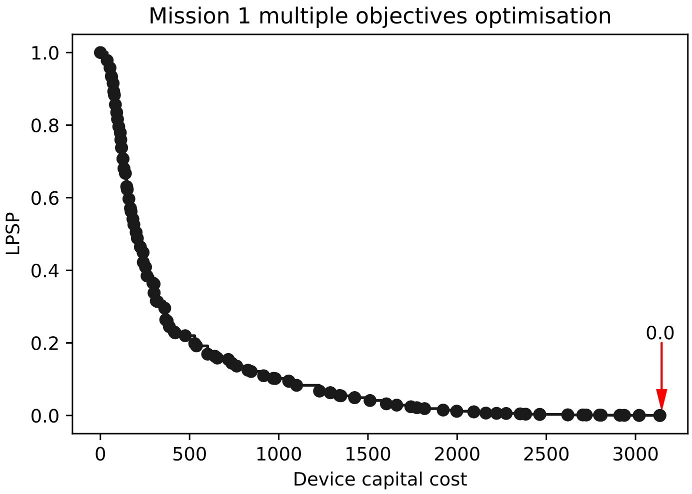

FIGURE 4.1: Example on design feasibility problem

the design space. Relationship between the LPSP and the device capital cost is outlined by the Pareto front configurations. An optimisation algorithm for the multiple objectives optimisation will be introduced in section 4.2.

4.1.3 Optimal configuration design

The result of design feasibility problem is a set of REHS configurations under the size constraint. The renewable robot cannot use all of them as the REHS configuration design for the power system. However, the renewable robot has select one design from all feasible solutions as the REHS configuration.

Design feasibility exploration does not suggest a single REHS configuration because both objectives are equally important according to the multiple objectives of optimisation principles.

Selecting one configuration is a compromise between the cost and reliability of the power system. The goal of the optimal configuration design is to pick a configuration with the best compromise in those two objectives. Since the objective is to balance the cost and reliability factor, the fitness function could be written as:

$$C(A_w, A_s, B) + \lambda \cdot LPSP(A_w, A_s, B) \tag{4.7}$$

where C is device capital cost of the RHES and $LPSP$ is the lost power supply problem. λ is a positive lagrangian multiplier of the LPSP that weight the importance of reliability performance.

In this fitness function, there are multiple objectives to be minimised. Compared to the multiple objectives optimisation, these objectives are mixed as a single objective to find the optimal configuration. Similar to design feasibility exploration, the optimal configuration design problem also has to limit the size of REHS devices. The design problem when formed as the optimisation problem is shown in Equation 4.8.

$$\begin{aligned}
\underset{A_w, A_s, B}{\text{minimize}} \quad & C(A_w, A_s, B) + \lambda \cdot LPSP(A_w, A_s, B) \\
\text{subject to} \quad & 0 \le A_w \le \bar{A}_w \\
& 0 \le A_s \le \bar{A}_s \\
& 0 \le B \le \bar{B}
\end{aligned} \tag{4.8}$$

where $\bar{A}_w, \bar{A}_s,$ and $\bar{B}$ are limits on the size of wind turbine, area of solar panel and capacity of battery.

The result of the optimisation is the best REHS configuration with a balanced cost and reliability. It suggests a single REHS configuration under the hard size constraint. REHS configuration with balanced performance has the lowest fitness $C + \lambda \cdot LPSP$ in the design space. In the optimal configuration design, the importance of economic and reliability performance is based on the Lagrangian multiplier λ. A smaller λ weights the cost more in the objective function. On the other hand, a larger λ increases the reliability factor in the design objective. Consequently, the economic and reliability performance of the optimal REHS configuration is depending on the weight of λ.

For a reliable fully autonomous operation of the renewable robot, the REHS configuration with a zero LPSP is necessary. However, whether it is possible to achieve such power supply reliability performance is also determined by the size limits on the RHES devices. A larger weight on the LPSP itself does not always guarantee a reliable REHS configuration at zero LPSP. This is due to the size limits, the maximum power generation and storage are restricted by the energy generator and capacity of the battery.

Luckily, if the result from the design feasibility exploration shows there is a configuration achieved a zero LPSP, the optimal configuration design approach should able to guarantee the reliability performance with a significantly large lagrangian multiplier. This is because the optimal algorithm has to minimise the total fitness and a large part of it is reliability. For this reason, to find the REHS configuration with minimal fitness, a more expensive but reliable design will have a lower objective compared to a cheaper but less reliable design. Albeit the Lagrangian multiplier λ is large, whenever the design feasibility exploration suggests there is a configuration has a zero LPSP, the minimal value of the $\lambda \cdot LPSP$ is also zero. In other words, the optimal design is the compromise of cost to the power supply reliability.

4.2 Optimisation algorithms

4.2.1 Design feasibility problem

Design feasibility problem has to optimise multiple objectives at the same time. Multiple objectives optimisation method is mainly solved by heuristic approaches. Unlike the gradient based optimisation methods, the meta heuristic algorithms are able to optimise the problem without begin trapped in local optima. Common meta heuristic algorithms including simulated annealing, genetic algorithms, differential evolution, ant conlony optimisation, bee algorithms, harymony search, cuckoo search etc.

Those algorithms are insipred by many different natural processes such as the cuckoo search minimic the breed strategy of the bird. A well-known heuristic-based multiple objectives optimisation algorithm NSGA-II is adapted to solve this design problem. There are high quality implementation with parallel optimisation support thanks to the popularity. In this work, the NSGA-II is selected as the optimisation algorithm to solve the multiple objectives optimisation problem.

$$\begin{aligned} \underset{A_w, A_s, B}{\text{minimize}} \quad & f_1 = C(A_w, A_s, B) \\ & f_2 = LPSP(A_w, A_s, B) \\ \text{subject to} \quad & 0 \leq A_w \leq \bar{A}_w \\ & 0 \leq A_s \leq \bar{A}_s \\ & 0 \leq B \leq \bar{B} \end{aligned} \tag{4.9}$$

A shortcoming of NSGA-II is the algorithm cannot handle the optimisation constraint natively. Two common ways to include the size constraint of REHS on renewable robots are adding a penalty in the objective function or using a modified Pareto-dominance approach to incorporate constraint violations. The first method is employed in the design feasibility exploration. In the optimisation process, the reliability objective is 1 if any REHS device exceeds the hard size constraint.

The size constraint on the RHES devices turn the multiple objective optimisation problem Equation 4.9 into Equation 4.10. Hard constraint on the size is included as a penalty if any of the REHS devices violates the size limit. As a penalty, the LPSP of any RHES configuration that violates the size constraint will be set as 1.

$$\begin{aligned} \underset{A_w, A_s, B}{\text{minimize}} \quad & f_1 = C(A_w, A_s, B) \\ & f_2 = \begin{cases} LPSP(A_w, A_s, B) & \begin{array}{l} A_w \leqslant \bar{A}_w \quad \text{and} \\ A_s \leqslant \bar{A}_s \quad \text{and} \\ B \leqslant \bar{B} \end{array} \\ 1 & \begin{array}{l} A_w > \bar{A}_w \quad \text{or} \\ A_s > \bar{A}_s \quad \text{or} \\ B > \bar{B} \end{array} \end{cases} \end{aligned} \tag{4.10}$$

Figure 4.2 shows the optimisation process flow diagram. The optimisation process consists of an optimisation loop and a simulation loop. On the left-hand side, the simulation loop is represented by the grey shaded blocks. These blocks are part of the data-driven simulation loop that estimates the economic and reliability performance of every REHS configurations. Outside the simulation loop, the optimisation loop is in charge of searching feasible REHS configurations through the NSGA-II algorithm.

The optimization process is based on the data-driven simulation-based approach to estimate a given REHS configuration's cost and LPSP. At the same time, each REHS configuration's output dictates how to select the next generation. Constrained multiple objectives optimisation process is summarised as follows:

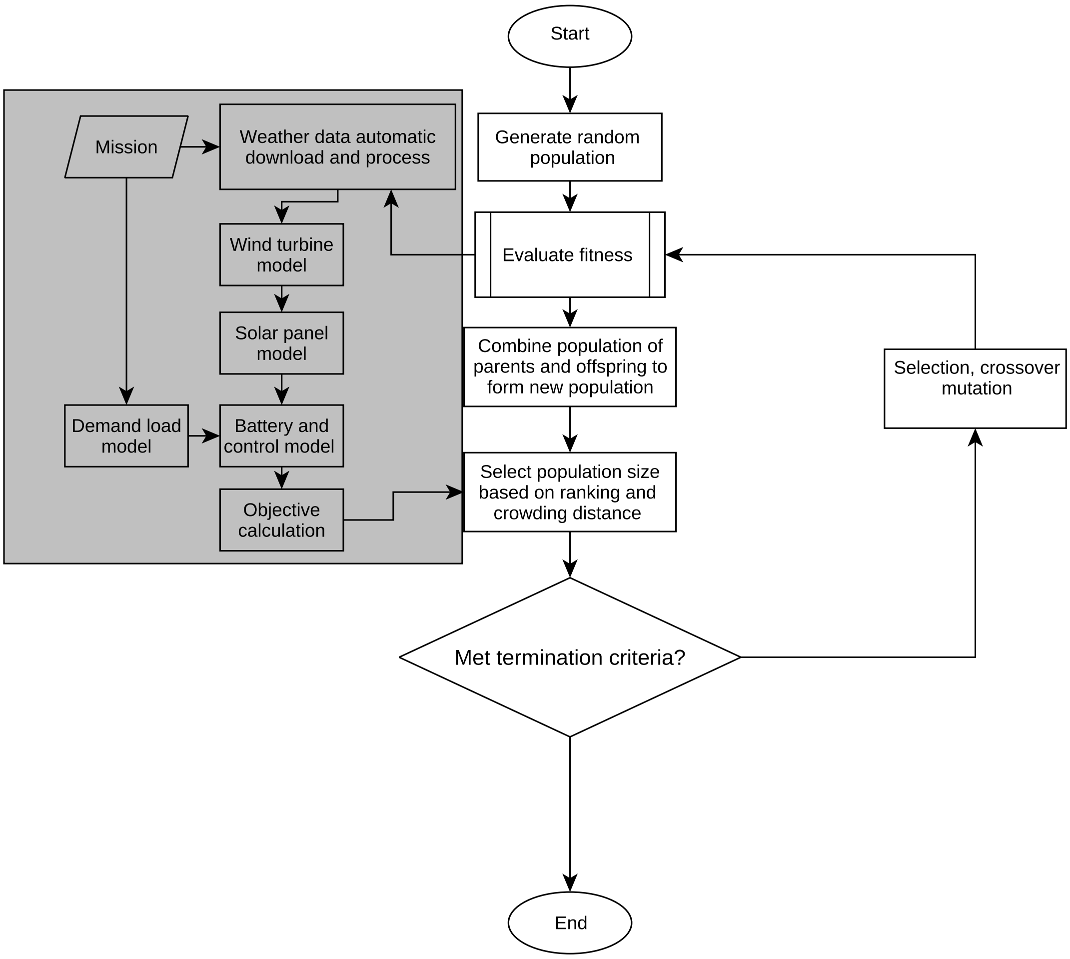

FIGURE 4.2: Constrained multiple objectives optimisation algorithm flow chart

1. Generate random population within the size constraint, a population is group of solutions consists of REHS configuration A_w, A_s, B.

2. Evaluate the fitness f_1 and f_2 of all populations. This is done through the following steps:

   (a) Download and process meteorological data on solar radiation, wind velocity and temperature.

   (b) Calculate power generation from the wind turbine on configuration A_w using moving REHS model.

   (c) Calculate power generation from a solar panel on configuration A_s using moving REHS model.

   (d) Estimate demand load on the mission.

   (e) Discount the wind resistance from the propulsion demand load.

   (f) Simulate the power system with battery and control model on configuration B.

3. Combine population of parents and offspring to form a new population.

4. Select population size based on ranking and crowding distance.

5. Check if the termination condition is reached? (Maximum number of iteration reached or converged to accuracy). Go to step 7. If not continue to step 6.
6. Select the best individuals, crossover and mutation. Continue to step 2.
7. Save the population and output the configuration

Optimisation loop 2-6 continues to search the REHS configurations in the design space. Two objectives f_1 and f_2 are found using a data-driven simulation method on moving REHS model. A more detailed description of the power system simulation for the renewable robot is described in section 3.5.

The selection of the individuals is based on the non-dominated raking and crowding distance of the population. Non-dominant raking sorts the REHS configuration in two objectives by decreasingly rank the population on one of the objectives. The maxima of the sorted configuration against another objective are the non-dominated front of the problem. Crowding distance estimates the density of the solutions, defined as the average distance between two neighbouring solutions. This selection mechanism maintains the diversity of the non-dominated front of the population.

Mutation and crossover mimic the nature breed process. A crossover is a genetic operator to combine an individual from parental (previous generation) population. There is also a chance for the individual to mutate before they added to the population. While keeping the elite individual in the populations, the crossover and mutation offer a chance to explore new individuals that is potentially better than its ancestors.

The result of the optimisation is the Pareto front REHS configurations under the size constraints. These solutions represent the best achievable reliability against the best REHS capital cost. As the solutions violate the size constraint have removed from the Pareto front, the optimisation outcome also shows the best reliability performance under the size constraint.

Pseudocode of the constraint multiple objectives optimisation algorithms is shown in Algorithm 2. The input of the algorithm includes the mission of the robot, designed duty cycle and motion estimation. The optimisation also requires the size limits on the wind turbine, solar panel and the battery. Optimisation parameters are the unit size cost of renewable energy devices.

```
Input: Mission $\mathcal{M}$, Duty cycle $\mathbf{D}$, motion estimation
Limits: Size limits $\bar{A}_w, \bar{A}_s, \bar{B}$
Parameters: Unit cost of the REHS devices $c_w, c_s, c_b$
Output: Pareto front solutions of $A_w, A_s, B$
foreach $(s, t)$ in $\mathcal{M}$ do
    $v \leftarrow \mathcal{M}(s, t)$;
    Calculate $P_{prop}$ and $P_{hotel}$;
    $P_l(s, t) = P_{prop}(s, t, v) + P_{hotel}(\mathbf{D})$
end
Initialise a group of population;
while $N <$ max generations do
    foreach $(s, t)$ in $\mathcal{M}$ do
        Simulate $P_s$ and $P_w$ on $A_s, A_w$;
        $P(s, t) = P_s + P_w$;
        Simulate $S(t)$ from $P(s, t)$, $P_l(s, t)$ and $B$;
        Combine population of parents and offspring to form new population;
        Select population size based on ranking and crowding distance;
    end
    $LPSP = \mathbb{P}(S(t) < P_l(t))$, estimate cost $C$;
    if $g$ convergence within $\epsilon$ then
        Found Pareto front, save the population $A_s$, $A_w$, $B$;
        break;
    end
end
Output saved population as Pareto front;
```

Algorithm 2: Multiple objectives REHS optimisation algorithm

Due to the size constraint on the REHS devices, the Pareto front solutions may not be able to fully support the demand load. The minimal LPSP achieved by all possible configuration is greater than zero in this case. This suggests the change of mission and/or decrease the demand load of the renewable robot.

Constraint multiple objectives optimisation suggests a set of REHS configurations that have the best economic and reliability performance. The outcome of constraint multiple objectives optimisation does not only reveal the relationship between those two objectives but also indicate the best possible reliability performance. When the minimal LPSP is zero, it suggests there is at least one configuration met the demand load requirement. That is, the robot could be purely powered by renewable energy on this mission.

Multiple RHES configurations suggested by the optimisation outcome is valuable to the designer. In practice, we often need a single REHS configuration to deploy renewable energy devices on the renewable robot. In order to find the optimal REHS configuration for the mission, the constraint mixed objectives optimisation method will be presented.

4.2.2 Optimal configuration design

The optimal configuration design problem is to find one REHS configuration with the best compromise between the cost and reliability performance. A flow chart in Figure 4.3 shows the optimisation algorithm. Data-driven simulation-based moving REHS model in the left-hand blocks evaluate the reliability and cost performance of each configuration. The main optimisation starts from the particle swarm optimisation parameter initialisation and population generation.

Each particle in the swarm is a possible REHS configuration. The configuration $[A_w, A_s, B]$ determines its position p in the design space. For each particle, the initial position $p(0) = [A_w, A_s, B]$ is randomly generated within the size limits.

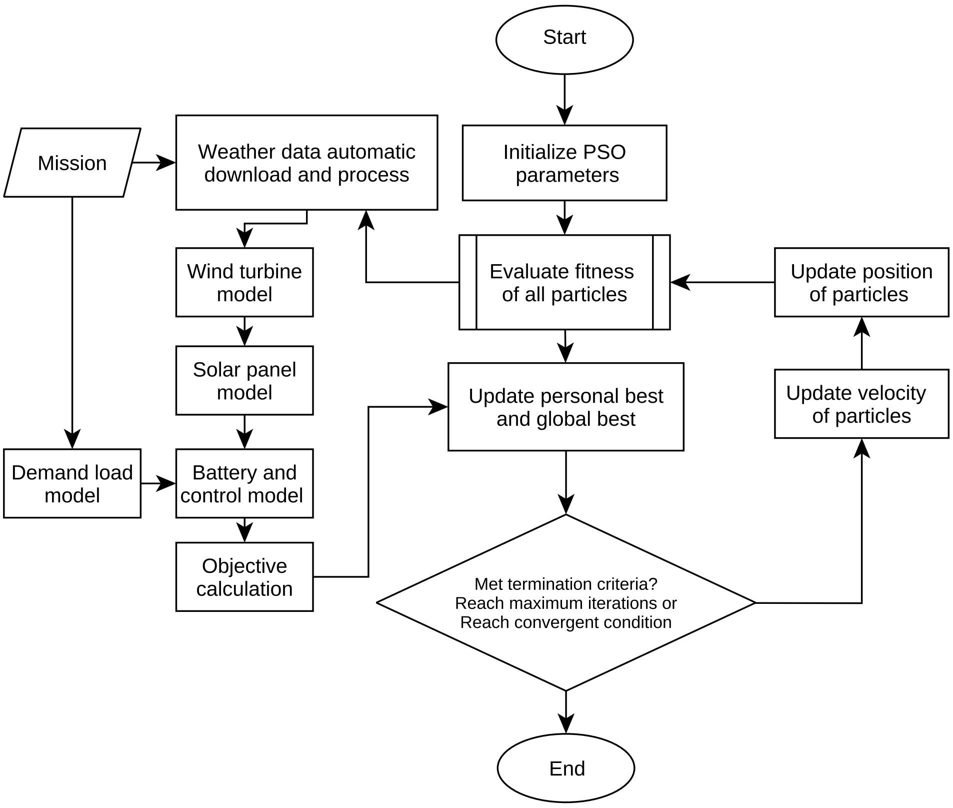

FIGURE 4.3: Optimisation algorithm flow chart

When a group of particles are ready for the optimisation, the iteration could start by evaluating the fitness of the particle. The REHS configuration will keep updating until it reaches the termination criteria.

1. Evaluate the fitness $f = C + \lambda \cdot LPSP$ of all particles on their own configuration A_w, A_s, B. This is done through the following sub-steps:
   (a) Download and process meteorological data on solar radiation, wind velocity and temperature.
   (b) Calculate power generation from the wind turbine on configuration A_w
   (c) Calculate power generation from a solar panel on configuration A_s

   (d) Estimate demand load on the mission
   (e) Discount the wind energy on the propulsion power
   (f) Simulate the power system with battery and control model on configuration B
   (g) Find the objective function from the simulation

2. Update the history of each particle and the global best-performed particle.
3. Check if the termination condition is reached?(Maximum number of iteration reached or converged to accuracy) Save the global best performed when the termination critical is met. If not continue to next step.
4. Update the particle's position and velocity and go to step 1.

This optimisation algorithm takes advantage of swarm intelligence to find the globally optimal configuration if there is a sufficient number of iterations. On every generation, the best-performed particle's position is updated as the global best location $p_{g,best}$. The particle will move around to search the design space to find this location according to its own best historical location $p_{p,best}$ and the global best location $p_{g,best}$. From generation k to next-generation $k+1$, the velocity can be updated based on the position of these particles.

$$v(k) = v(k-1) + c_1 \cdot r_1[p_{g,best} - p(k-1)] + c_2 \cdot r_2[p_{p,best} - p(k-1)] \tag{4.11}$$

where c_1 and c_2 are global and local update rate and r_1 and r_2 are two random numbers to allow a random walk. Next location of the particle is:

$$p(k+1) = p(k) + v(k). \tag{4.12}$$

Figure 4.4 illustrated the position update process of a swarm of particles in the design space.

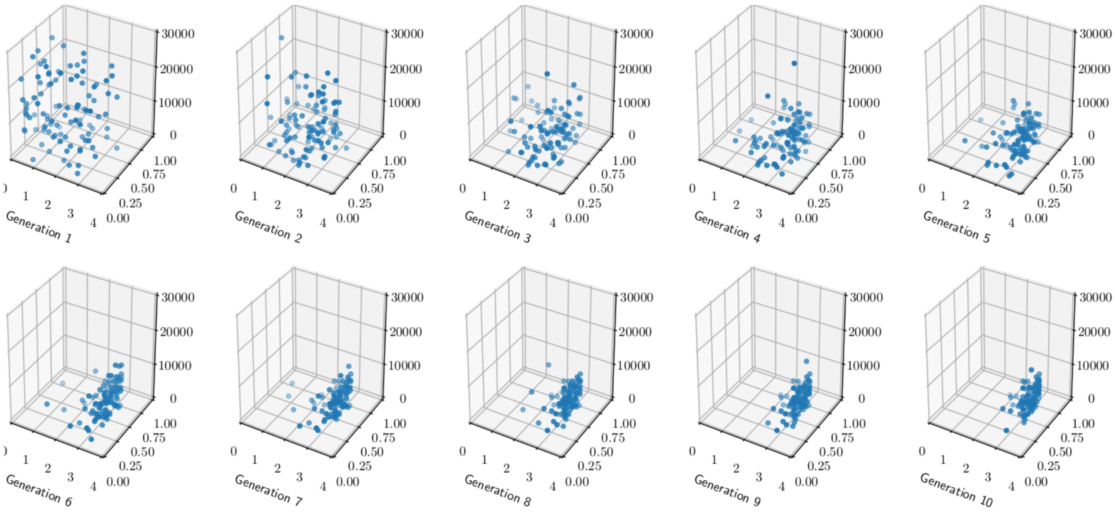

FIGURE 4.4: Example on the move of particles: the x, y, z axes represents the size of solar panel, wind turbine and battery capacity respectively

The position update also takes the size constraint into account. A minmax function is applied to guaranteed the position of the particle is always within the design space e.g. for $p(k) = [A_w(k), A_s(k), B(k)]$

$$\begin{aligned} p(k+1) &= [A_w(k+1), A_s(k+1), B(k+1)] \\ &= \begin{bmatrix} \min[\bar{A}_w, \max(0, A_w(k) + v_1(k))] \\ \min[\bar{A}_s, \max(0, A_s(k) + v_2(k))] \\ \min[\bar{B}, \max(0, B(k) + v_3(k))] \end{bmatrix}^T \end{aligned} \tag{4.13}$$

where $v_i(k)$ is the component of the velocity.

Pseudocode of the optimisation algorithm is listed in Algorithm 3. Inputs for the optimisation algorithm are the mission of the robot, designed duty cycle and the motion estimation of the robot. The optimisation also requires the information of the size limits on the REHS devices. Parameters including unit size cost of the wind turbine, solar panel and battery are necessary for the capital cost estimation. Lagrangian λ is also needed to weight the importance of reliability. The output of the optimisation is the best REHS configuration combining the cost and reliability factors.

```
Input: Mission $\mathcal{M}$, Duty cycle $\mathbf{D}$, motion estimation
Limits: Size limits $\bar{A}_w, \bar{A}_s, \bar{B}$
Parameters: Unit cost of the REHS devices $c_w, c_s, c_b$, $\lambda$
Output: Best REHS configuration $A_w, A_s, B$
foreach $(s,t)$ in $\mathcal{M}$ do
    $v \leftarrow \mathcal{M}(s,t)$;
    Calculate $P_{prop}$ and $P_{hotel}$;
    $P_l(s,t) = P_{prop}(s,t,v) + P_{hotel}(\mathbf{D})$
end
Initialise $p(0) = [A_s, A_w, B]$ under constraint;
while $N <$ max generations do
    foreach $(s,t)$ in $\mathcal{M}$ do
        Simulate $P_s$ and $P_w$ on $A_s, A_w$;
        $P(s,t) = P_s + P_w$;
        Simulate $S(t)$ from $P(s,t)$, $P_l(s,t)$ and $B$;
    end
    $LPSP = \mathbb{P}(S(t) < P_l(t))$, estimate cost $C$;
    $g = C + \lambda \cdot LPSP$;
    if $g$ convergence within $\epsilon$ then
        Found best configuration, save $A_s$, $A_w$, $B$;
    else
        Update the velocity of the particle $v(k)$;
        Update the position of the particle $p(k+1)$ under constraints;
    end
end
```

Algorithm 3: Optimal REHS configuration design algorithm

4.3 Results

4.3.1 Test case

A renewable robot power system design case will test the performance of the proposed REHS design methods. The robot is a maritime renewable robot planning for a long-term oceanographic survey mission. The design goal of the REHS is to fully power the robot from renewable energy resources for fully autonomous operation at the sea. In the case test, the design method has to figure out whether it is possible to fully power the robot with renewable energy or not. Furthermore, if the REHS can fully support the robot, the optimal REHS configuration has to be given by the optimisation algorithm under the size constraint.

The maritime robot is an autonomous surface vehicle (ASV) that equipped with an autopilot system, sensor payload and electrical propulsion system. This robot has both hotel and propulsion that has to be supplied by the REHS. Basic dimensions of the robot is listed in Table 4.1.

Table 4.1: Basic dimension

Dimensions	Symbol	Value
Length	L	5.72
Draught	T	0.25
Beam	B	0.76
Slenderness coefficient	C_{sl}	6.99
Prismatic coefficient	C_P	0.613

To estimate the propulsion power of the vehicle, a ship resistance program was used. This program estimates the ship resistance from the dimension of the vehicle. Propulsion load of the vehicle is estimated by the ship resistance program. The detail on those parameters is available in section A.3. The total electrical power consumption on propulsion depends on the speed of the robot as well as the resistance.

$$\begin{aligned} P_{prop} &= R_T \cdot V/\eta_p \\ &= \frac{1}{2\eta_p}[(1+c_w)(C_F+C_R)+C_A]\rho_w S V^3 \end{aligned} \tag{4.14}$$

where V is the water speed of the vehicle, water speed is the relative speed to the water including the ocean current, η_p is electrical to mechanical power transmission efficiency, C_F is frictional resistance coefficient, C_R is residual resistance coefficient, C_A is added resistance coefficient and S is surface area of the robot. Note the water speed V is relative to the moving water to account for the ocean current influence on the resistance.

Hotel load of the ASV is listed in Table 4.2. The navigation computer and necessary sensors are critical hotel load that has to be always turned on. Payload sensors and the data transmission system are operating in their duty cycle.

Wind and solar hybrid renewable energy resources are available on the ocean surface. A wind generator and a solar panel are used to harvest energy from those resources. However, due to the size limitation on the ASV, the maximum area of each energy harvesting device is restricted. The largest area of solar panel, wind turbine and the battery capacity are listed in Table 4.3.

TABLE 4.2: Hotel load on the renewable robot

Components	Power usage	Critical load	Duty cycle
Navigation computer	5 W	Yes	1
Camera	650 mW	Yes	1
Global Positioning System (GPS)	50 to 800 mW	Yes	1
Inertial Measurement Unit (IMU)	40 to 700 mW	Yes	1
Integrated radio transmitter	0.5 to 20 W	No	0.2
Temperature sensor	40 to 50 mW	No	0.9
Wind sensor	0.4 to 1.2 W	No	0.5
Salinity sensor	40 to 100 mW	No	0.9

TABLE 4.3: Size constraint on the REHS device

Constraints	Value	Unit
Solar panel area	3.36	m^2
Wind turbine area	0.65	m^2
Battery capacity	27398	Wh

The mission of the robot is scientific data collection in the ocean. Power supply from renewable energy resource is heavily depending on the mission. Part of the demand load is also influenced by the mission due to the ocean current is varied from place to place. A fundamental challenge for the design algorithm is to determine if it is feasible to design an REHS for the robot's autonomous operation. Eight different missions are included as test cases, the route and start-end points are shown in the following figures.

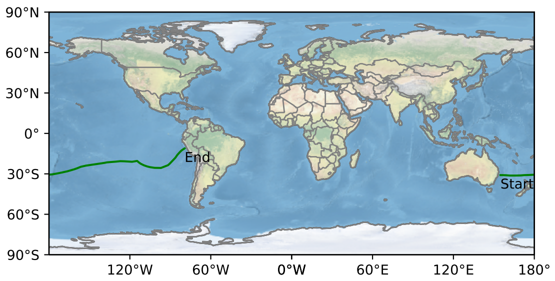

FIGURE 4.5: Mission 1
Australia - Chile

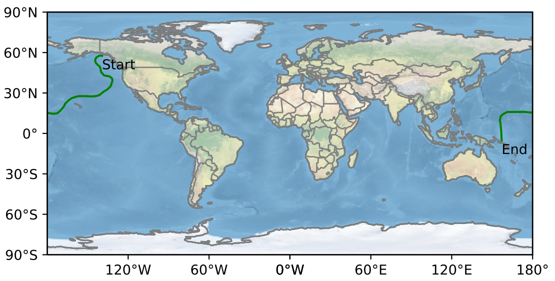

FIGURE 4.6: Mission 2
Solomon Islands - Canada

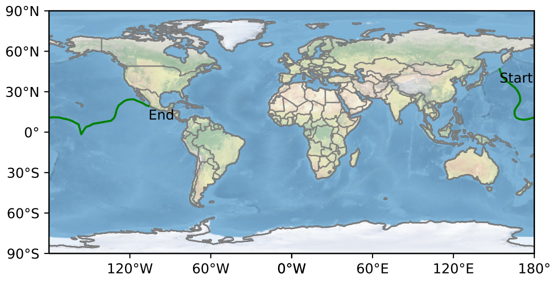

FIGURE 4.7: Mission 3
Kuril Islands - Mexico

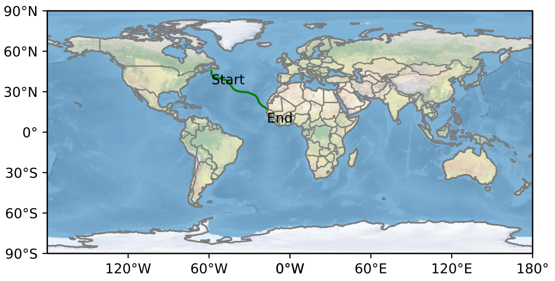

FIGURE 4.8: Mission 4
Newfoundland - Mauritania

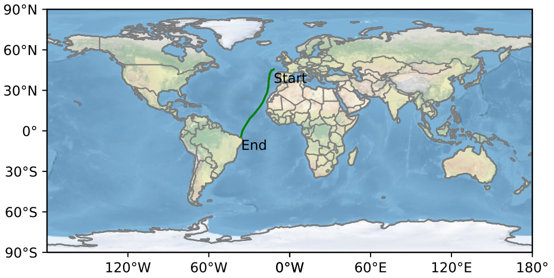

Figure 4.9: Mission 5
West France - Brazil

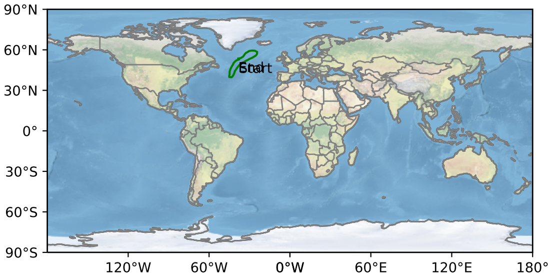

Figure 4.10: Mission 6
Loop in North Atlantic Ocean

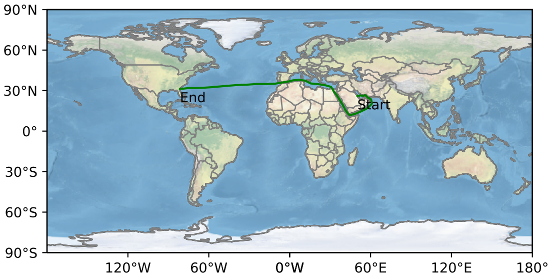

Figure 4.11: Mission 7
Middle East - US

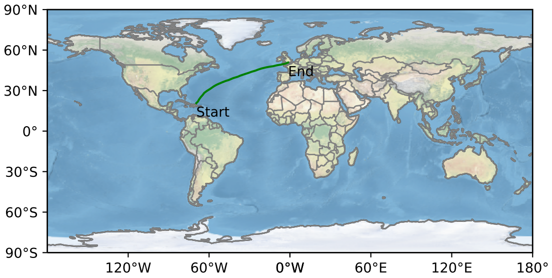

Figure 4.12: Mission 8
UK - Dominican Republic

Economic and local motion parameters of the robot are listed in the Table 4.4. The unit cost of renewable energy generators and energy storage device are economic parameters. The local motion of the robot is estimated by the pitch and roll motion amplitude.

Table 4.4: Economic parameters and local motion in the optimisation

Parameter	Meaning	Value	Unit
c_w	Wind turbine unit cost	3000	$£/m^2$
c_s	Solar panel unit cost	210	$£/m^2$
c_b	Battery	1	$£/Wh$
p_0	Amplitude of pitch motion	0.1	rad
q_0	Amplitude of roll motion	0.1	rad

Parameters on the renewable energy generator including the efficiency of wind and solar energy harvesting devices, battery charge and discharge efficiency, propulsion system efficiency are listed in section A.4. For each mission, the start time and the averaged global speed are the same. Mission can start from any time on the ocean. However, due to the data availability and the start date was set to 1st of January 2014 for the best simulation data coverage. Also the speed of the vehicle has to below the average wind speed for the wind turbine to generate energy. For this purpose, the average voyage speed was set to 2 km/h to compare the design result on various missions. All missions are starting at 1st of January 2014 and the averaged global speed of the robot is 2 km/h.

4.3.2 Design feasibility result

As the first step in the REHS configuration, the design feasibility result presents the best possible economic and reliability performance on a given mission. In the design feasibility exploration, the REHS design problem is formulated as a multiple objectives optimisation problems that device capital cost and LPSP are minimised at the same time.

$$
\begin{aligned}
&\underset{A_w, A_s, B}{\text{minimize}} \quad f_1 = C(A_w, A_s, B) \\
&f_2 = \begin{cases} LPSP(A_w, A_s, B) & \begin{array}{l} A_w \leqslant \bar{A}_w \quad \text{and} \\ A_s \leqslant \bar{A}_s \quad \text{and} \\ B \leqslant \bar{B} \end{array} \\ 1 & \begin{array}{l} A_w > \bar{A}_w \quad \text{or} \\ A_s > \bar{A}_s \quad \text{or} \\ B > \bar{B} \end{array} \end{cases}
\end{aligned}
\tag{4.15}
$$

Result of the design feasibility exploration is the Pareto front solutions to the optimisation problem shown above. As the size constraint is included in the reliability objective as a penalty to any violations, the smallest LPSP in the non-dominant solutions is also the best possible LPSP of the mission.

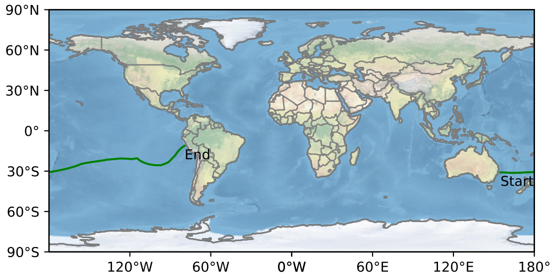

FIGURE 4.13: Mission 1 Australia - Chile

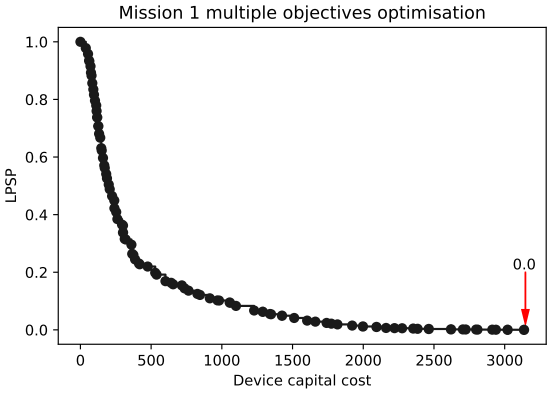

FIGURE 4.14: Mission 1 design exploration

Mission 1 started from the east coast of Australia and ended up at the west coast of Chile. Design exploration shows there is at least one configuration achieved a zero LPSP during the mission.

Results of other mission are listed in the following figures.

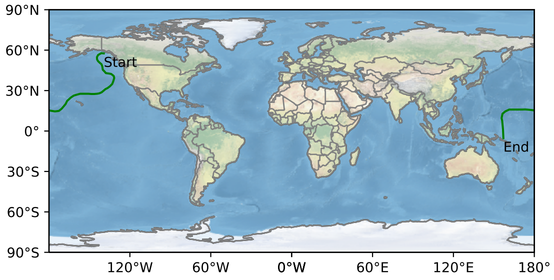

FIGURE 4.15: Mission 2 Solomon Islands - Canada

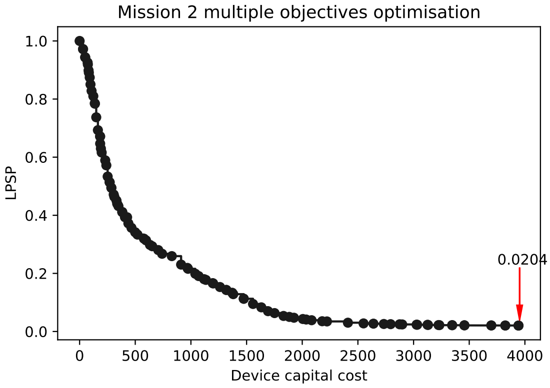

FIGURE 4.16: Mission 2 design exploration

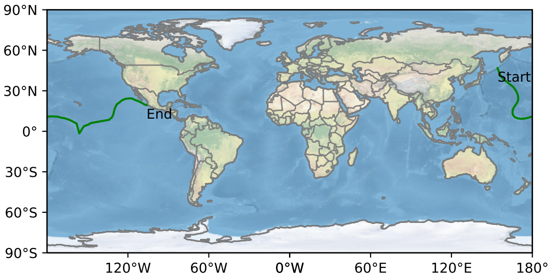

FIGURE 4.17: Mission 3
Kuril Islands - Mexico

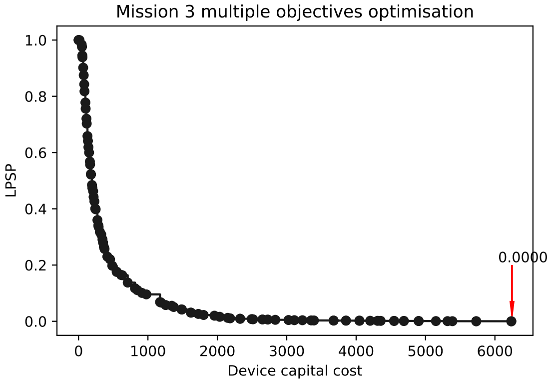

FIGURE 4.18: Mission 3 design exploration

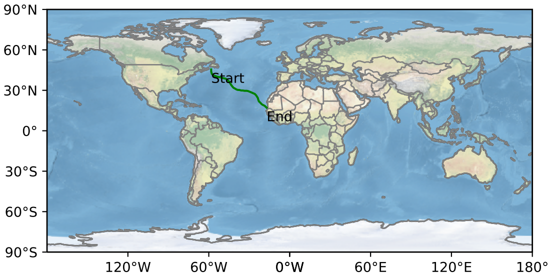

FIGURE 4.19: Mission 4
Newfoundland - Mauritania

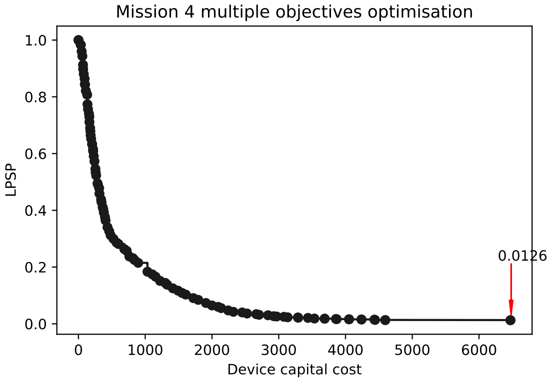

FIGURE 4.20: Mission 4 design exploration

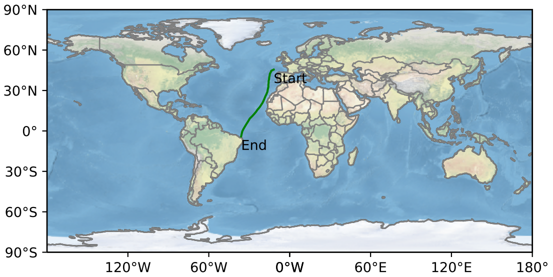

FIGURE 4.21: Mission 5
West France - Brazil

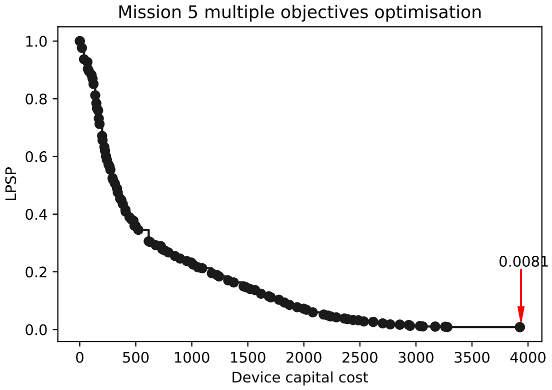

FIGURE 4.22: Mission 5 design exploration

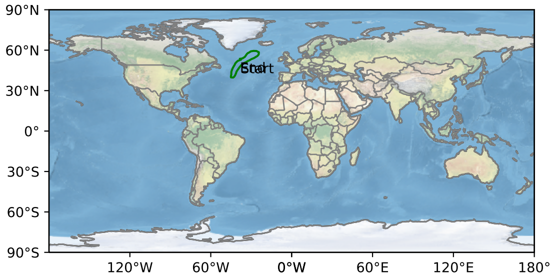

FIGURE 4.23: Mission 6
Loop in North Atlantic Ocean

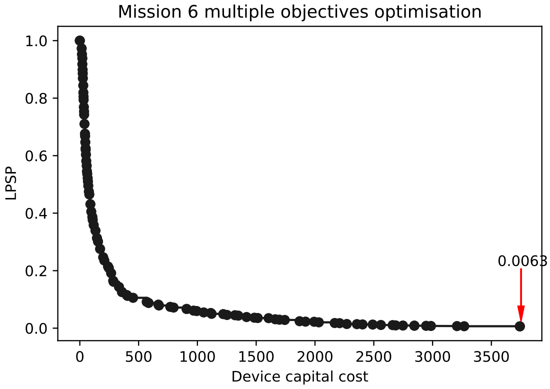

FIGURE 4.24: Mission 6 design exploration

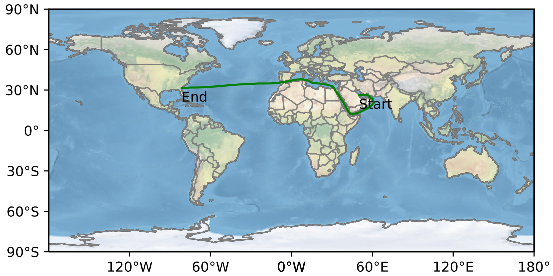

FIGURE 4.25: Mission 7
Middle East - US

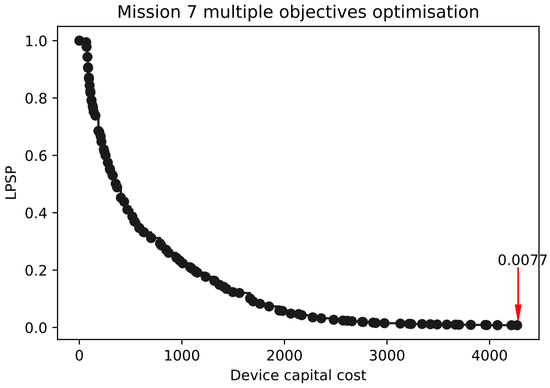

FIGURE 4.26: Mission 7 design exploration

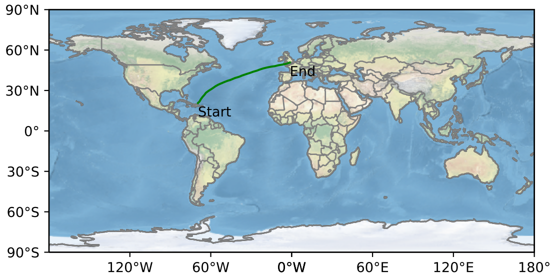

FIGURE 4.27: Mission 8
UK - Dominican Republic

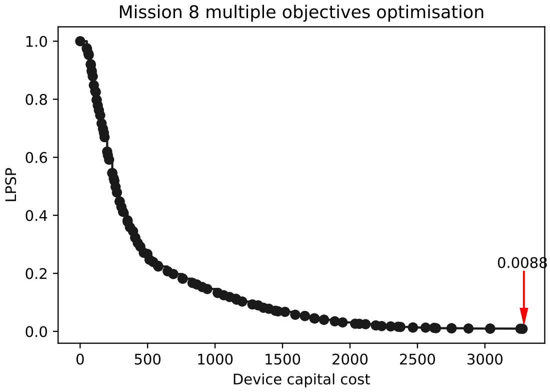

FIGURE 4.28: Mission 8 design exploration

The best possible LPSP of each mission are varied depends on the route. Mission 1 and 3 have a zero LPSP according to the design feasibility exploration result. It is possible to fully power the robot from solar and wind renewable energy resources on these missions. However for other missions, the design exploration suggests a non-zero LPSP there will be a chance that power supply might be lost during the operation. There are multiple reasons for the loss of power supply for that mission.

First of all, renewable energy resources have a limited energy density per unit area. Mean unit area power generation from wind and solar energy devices are listed in Table 4.5.

Table 4.5: Averaged energy density on missions

	Mission 1	Mission 2	Mission 3	Mission 4
Solar power W/m^2	22.4	21.7	24.1	17.1
Wind power W/m^2	42.8	27.4	36.4	37.9
	Mission 5	Mission 6	Mission 7	Mission 8
Solar power W/m^2	21.3	5.9	29.8	16.6
Wind power W/m^2	33.7	92.3	7.9	36.3

Averaged solar power generation range from 5.4 W/m^2 to 29.8 W/m^2. Compared to the solar panel's rated power density (section A.4) at 140 W/m^2, the capacity factor is between 3 % to 21 %. Low energy density poses a challenge to generate enough electricity for a renewable robot.

Secondly, the size limitation on the REHS devices further restricted the maximum power generation and the capacity of the energy storage device. At a low energy density, the robot requires larger energy harvesting devices for sufficient power supply. However, the maximum size of the energy harvesting device is limited due to space restriction. Under the size constriant shown in Table 4.3, the maximum power generation from each resources is listed in Table 4.6.

Table 4.6: Averaged maximum power generation

	Mission 1	Mission 2	Mission 3	Mission 4
Solar power (W)	72.26	72.91	80.97	57.45
Wind power (W)	27.82	17.81	23.66	24.63
Total power (W)	100.08	90.72	104 .63	82.09
	Mission 5	Mission 6	Mission 7	Mission 8
Solar power (W)	71.57	19.82	100.12	55.77
Wind power (W)	21.90	59.99	5.13	23.60
Total power (W)	93.47	79.81	105.26	79.37

Total averaged maximum power generation under the size limit is from 79.37 W to 105.26 W. Low energy density and the size restriction limit the total power generation from solar and wind resources. Mission 8 has the highest LPSP due to its lowest total averaged maximum power generation.

Lastly, the distribution of renewable energy resources is uneven both temporally and spatially. Solar energy, for example, has no power generation during the night. The solar resource is also more abundant in lower latitude regions near the equator. As the robot travel across the ocean, the power generation is intermittent because of the spatial-temporal variance and uncertainty. At the time when the energy storage cannot compensate for the power supply intermittency, there will be a power supply lost.

4.3.3 Optimal configuration result

Result of design feasibility exploration shown that there are two missions have a zero LPSP. It is possible to power the renewable robot for fully autonomous operation on those missions.

However, the design feasibility result does not suggest a specific REHS configuration for the renewable robot. The optimal REHS configuration algorithm can find a design for the best compromise between the cost and reliability. Besides, if the REHS design exploration shows there is configuration achieved no power supply lost, the optimal REHS design could guarantee the reliability performance and the economic performance at the same time.

$$\begin{aligned} \underset{A_w, A_s, B}{\text{minimize}} \quad & f = C(A_w, A_s, B) + \lambda \cdot LPSP(A_w, A_s, B) \\ \text{subject to} \quad & 0 \leq A_w \leq \bar{A}_w \\ & 0 \leq A_s \leq \bar{A}_s \\ & 0 \leq B \leq \bar{B} \end{aligned} \tag{4.16}$$

The lagrangian λ selected in the optimisation is listed in section A.4. A relatively large lagrangian 1×10^6 prioritise the reliability over the cost performance. Optimisation result is shown in Table 4.7.

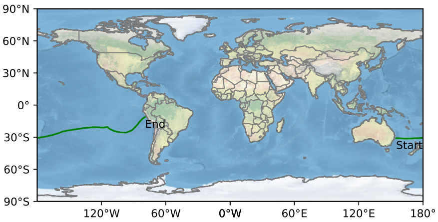

FIGURE 4.29: Mission 1

	Result	Limit
Solar panel size	3.26 m^2	3.36 m^2
Wind turbine size	0.58 m^2	0.65 m^2
Battery capacity	2723 Wh	27398 Wh

TABLE 4.7: Mission 1 optimal configuration

The performance of the REHS configuration can be verified by simulating the power system. Power generation, supply and battery SOC on this mission is shown in Figure 4.30.

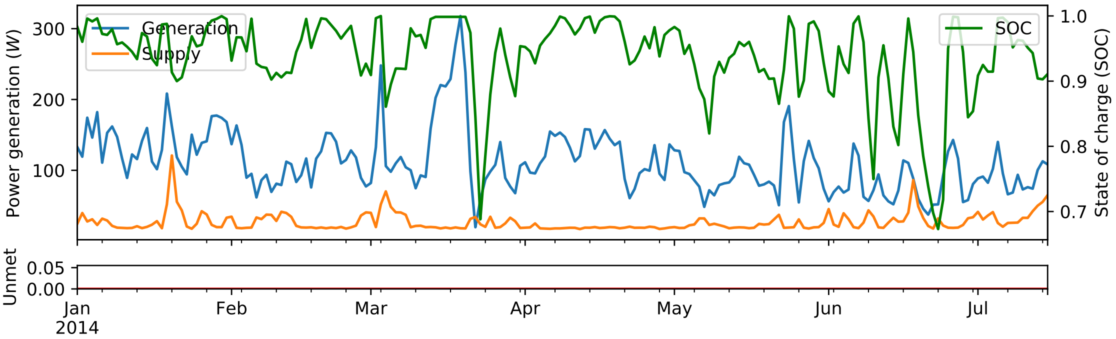

FIGURE 4.30: Power generation, supply and battery SOC on Mission 1

Power generation is the total power generation from renewable resources. The power management plans the power supply based on the demand load and the battery remaining energy. In Figure 4.30, the unmet power is the difference between the power supply and the demand load. Unmet power occurs when the demand load is not fulfilled by the power supply. As it can be shown in the figure, there is no unmet power event for the suggested REHS configuration.

Mission 3 also has a zero LPSP according to the design exploration. This result guarantees the REHS optimal design can find a configuration to achieve a full power supply to the robot. The optimisation result of the REHS optimal configuration design is listed in Table 4.8.

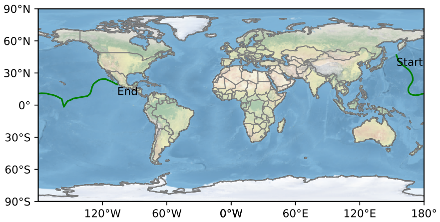

FIGURE 4.31: Mission 3

	Result	Limit
Solar panel size	3.19 m^2	3.36 m^2
Wind turbine size	0.65 m^2	0.65 m^2
Battery capacity	1140 Wh	27398 Wh

TABLE 4.8: Mission 3 optimal configuration

Power generation, supply, battery SOC and unmet power are shown in Figure 4.32. The configuration suggested by the optimal REHS configuration design algorithm also shows that there is no unmet power supply during the mission.

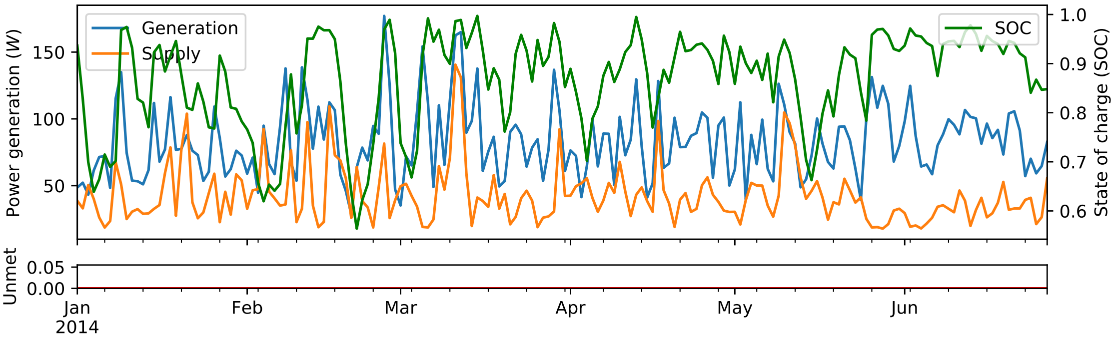

FIGURE 4.32: Power generation, supply and battery SOC on Mission 1

Those two results show that the proposed optimal REHS configuration design algorithm is able to find a reliable design for the robot. Furthermore, those designs are also the most economic configuration that achieved zero LPSP.

As it is shown in Figure 4.33 and Figure 4.34, mixed objective decreases as the optimisation loop iterates. The objective function $C + \lambda \cdot LPSP$ is converged after 10000 number of iterations on both missions.

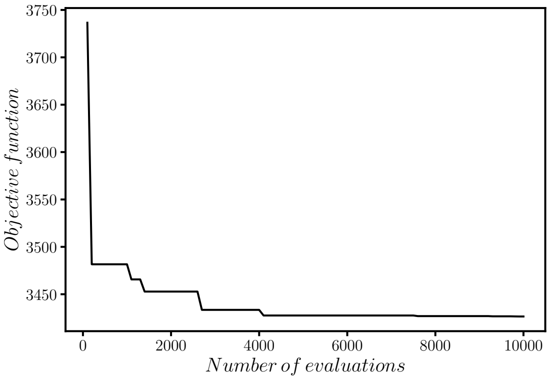

FIGURE 4.33: Fitness Convergence on Mission 1

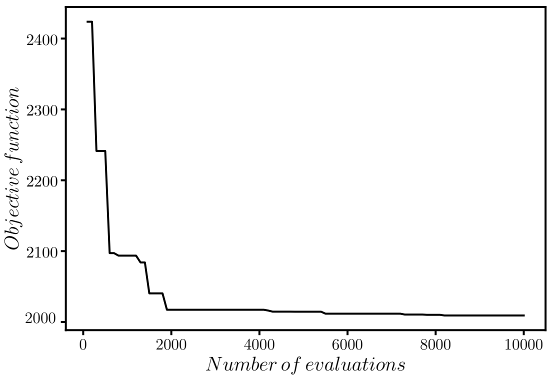

FIGURE 4.34: Fitness Convergence on Mission 3

The initial fitness of randomly selected configurations is high because of a relatively large λ overweight the capital cost even at a small LPSP. As the optimisation goes on, the particles are moving towards the position with a lower LPSP to minimise the objective function. After several iterations, the optimisation algorithm found a REHS configuration that achieves a zero

LPSP. Objective function from that point on has no contribution from the LPSP. In order to further decrease fitness, the optimisation algorithm chooses a more economic configuration that has a zero LPSP. After a number of iterations, the objective function converged as the cost of the REHS configuration is minimised.

Design exploration also suggested there is no feasible REHS configuration under the size constraint for other missions to achieve a zero LPSP. Optimal REHS configuration algorithm could not design the power system for a guaranteed power supply reliability for those missions. However, the algorithm is still able to find the best trade-off between the cost and reliability under the hard size constraint. Design result is shown in Table 4.9. The REHS configuration has a solar panel at its maximum possible size.

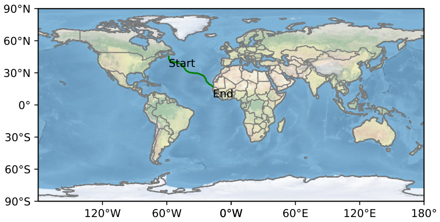

FIGURE 4.35: Mission 4

	Result	Limit
Solar panel size	3.36 m^2	3.36 m^2
Wind turbine size	0.59 m^2	0.65 m^2
Battery capacity	13123 Wh	27398 Wh

TABLE 4.9: Mission 4 optimal configuration

Power system history shown in Figure 4.36 has unmet power supply. When the battery is about to drop below its DOD, the robot lost power supply due to the shortage in power generation.

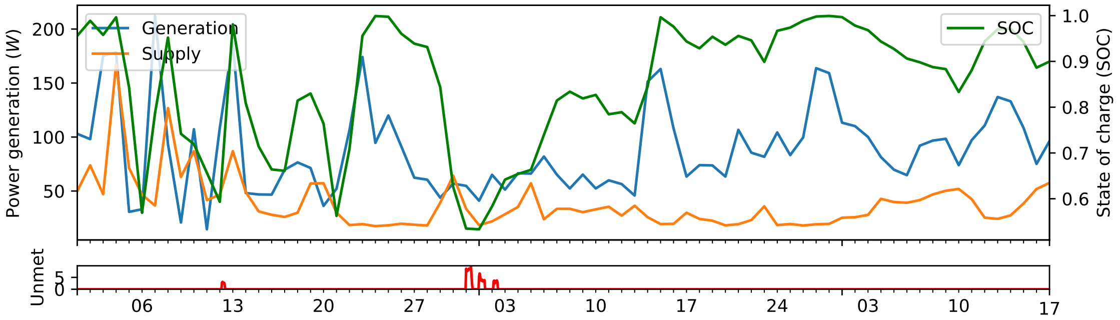

FIGURE 4.36: Power generation, supply and battery SOC on Mission 4

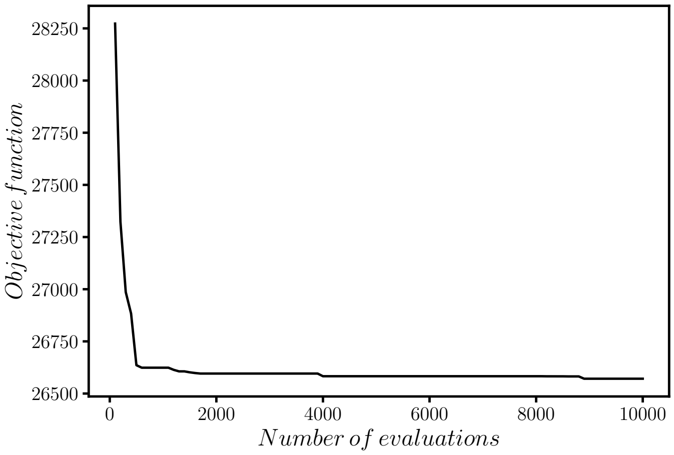

FIGURE 4.37: Fitness Convergence on Mission 4

Fitness convergence plot Figure 4.37 shows the optimisation process for non-zero LPSP mission. Due to the limitation on the size constraint, renewable energy density and the variance in the power generation, there is no configuration that can guarantee a zero LPSP. The REHS optimal configuration design algorithm, in this case, degrading into an algorithm compromising between cost and reliability.

4.3.4 Long-term performance result

The design feasibility exploration and the optimal configuration method can design an REHS with guaranteed cost and reliable performance for a mission. However, the actual mission of the robot cannot be fully known before the deployment. In the design stage, the REHS configuration is designed against the estimation of the mission. The most common approach is to use historical data to represent a future operation scenario. Therefore, the performance of the robot relies on how the historical data matches the actual operation scenario. How the REHS configuration would perform in the future, especially in a longer-term is important to robot's safe operation. However, future operation data such as solar radiation, temperature, and wind speed is not known. Since there is no data available on the future, the long-term performance study is done by the historical simulation. The REHS configuration in this work use historical data for the simulation to evaluate the long term performance . The renewable robot with the same REHS configuration is going to run on the same route and speed. To evaluate how year to year variance in the power generation and demand load might impact the reliability of the robot, the robot's journey is starting on the same day in the year. For example, the REHS configuration on mission 1 was started at January 1^{st} 2014, the historical simulation in 2013 should begin with January 1^{st} 2013.

Among eight missions, the optimal design algorithm suggests that there are two mission have an REHS configuration achieved a zero LPSP. For these configurations, if the mission started not from that specific year, the performance may differ from the design scenario. The data-driven simulation will run on the same configuration with the actual meteorological data on historical years.

Table 4.10: Performance of the optimal configuration in Misison 1

	1995	1996	1997	1998	1999	2000	2001	2002	2003	2004
LPSP	0.000	0.000	0.000	0.000	0.000	0.000	0.000	**0.003**	0.000	0.000
Solar W	74.68	81.52	77.72	81.76	80.15	79.83	79.74	79.57	80.11	77.79
Wind W	27.71	26.39	27.64	39.54	32.99	27.77	28.19	34.28	28.83	26.63
Load W	24.05	22.85	21.68	23.70	22.55	22.33	24.20	24.96	22.51	22.94

	2005	2006	2007	2008	2009	2010	2011	2012	2013	2014
LPSP	0.000	0.000	0.000	0.000	0.000	0.000	0.000	0.000	0.000	0.000
Solar W	79.38	77.98	79.40	79.45	78.47	82.15	80.22	79.11	78.16	73.81
Wind W	27.11	26.18	27.52	31.22	25.60	31.06	31.68	30.14	31.40	26.74
Load W	23.40	22.12	24.14	23.59	22.18	22.79	22.56	22.63	23.67	22.76

Historical performance of the REHS configuration suggested by the optimisation algorithm on mission is listed in Table 4.10. The LPSP, averaged solar power generation, wind power generation and demand load are listed.

It is expected that the LPSP of mission 1 in the long term performance at 2014 is zero. On the other years, the power generation and demand load are on average with that in 2014. In the last 20 years, the LPSP stay as low as zero except the year of 2002.

Power generation and unmet power supply at the design year 2014 is shown in Figure 4.38.

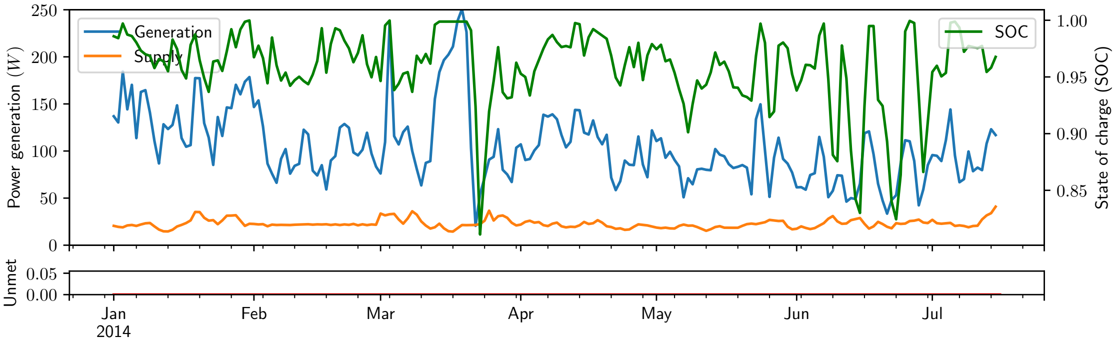

FIGURE 4.38: Mission 1 SOC and solar/wind power generation at 2014 (24 hours averaged)

For the same configuration operating in 2002, the power generation and unmet supply are shown in Figure 4.39. There is unmet power generation in early March 2002 that result in a lost power supply.

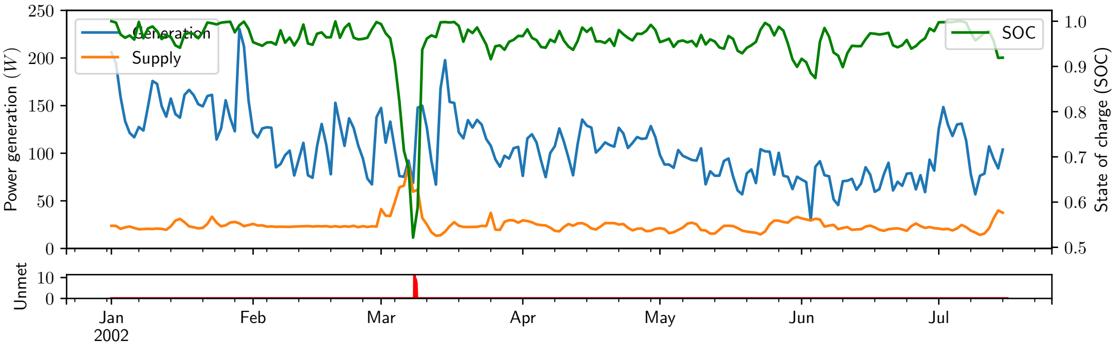

FIGURE 4.39: Mission 1 SOC and solar/wind power generation at 2002 (24 hours averaged)

Compare to the same period in 2014 (Figure 4.40), the power generation in early 2002 is lower in early March. What makes is worse is the demand load in 2002 is also higher than in 2014. As the demand load increases, the REHS discharge the battery to supply the power. However, the battery stops to discharge to prevent the SOC from falling below the DOD.

Demand load in the year 2002 in higher in the early March due to the difference in the propulsion power. Figure 4.41 compares the propulsion load during the same period in the year of 2014 and 2002. The propulsion load in 2002 is higher than that in 2014. In the long term performance study, the averaged speed is the same on different years. To keep the speed of the robot, the REHS has to supply enough power to the propulsion system. Propulsion system needs electrical power to drive the robot under the water and wind resistance. Water resistance including the ocean current account for the propulsion load in relative to the water. Water resistance in 2014 and 2002 are similar. However, the wind direction in 2002 is most opposed to the robot's moving direction in early March.

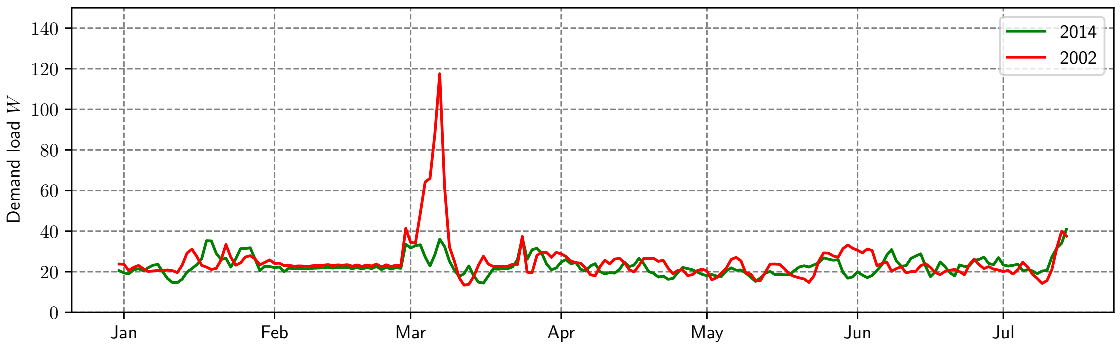

FIGURE 4.40: Mission 1 demand load comparison between 2014 and 2002 (24 hours averaged)

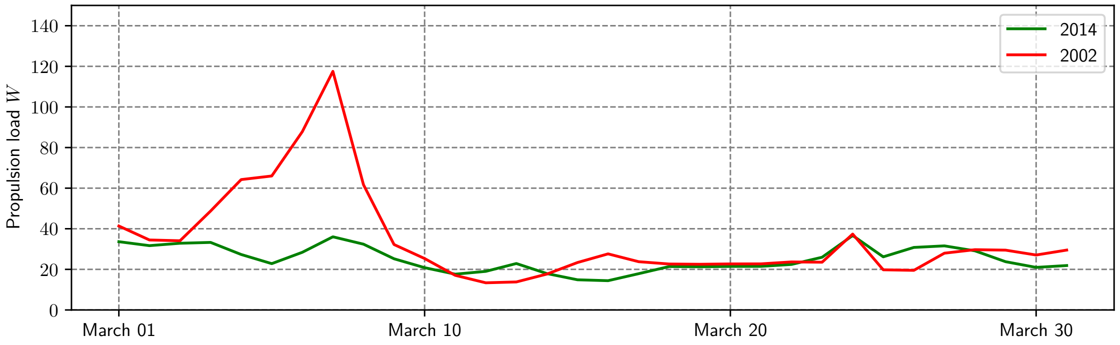

FIGURE 4.41: Mission 1 propulsion load comparison between 2014 and 2002 (24 hours averaged)

The difference in the propulsion load increases the total demand load. Power generation at the same time can not keep up with the demand load. The variance in renewable energy resource and demand load is the main cause of the loss of power supply.

TABLE 4.11: Performance of the optimal configuration in Misison 3

	1995	1996	1997	1998	1999	2000	2001	2002	2003	2004
LPSP	0.000	0.000	0.000	0.000	0.000	0.000	0.000	0.000	**0.008**	0.000
Solar W	84.10	83.43	79.62	84.23	83.71	86.02	85.32	82.42	84.95	81.95
Wind W	31.89	35.08	35.45	37.99	31.08	37.34	34.30	34.72	34.87	42.53
Load W	18.74	18.19	20.91	18.86	18.48	20.38	20.86	23.90	26.30	20.82
	2005	2006	2007	2008	2009	2010	2011	2012	2013	2014
LPSP	0.000	0.000	0.000	0.000	0.000	**0.006**	0.000	0.000	0.000	0.000
Solar W	82.44	84.97	85.50	83.41	82.20	81.90	82.02	85.13	86.22	80.70
Wind W	41.65	38.42	36.65	35.12	33.50	35.82	38.50	35.00	34.65	37.44
Load W	20.24	20.20	21.35	21.52	22.61	24.49	19.99	21.85	22.18	19.20

Mission 3 also shows a zero LPSP in the optimal configuration design. In the long term performance evaluation, the year 2003 and 2010 both have a chance to lost the power supply. Averaged demand load on those years are higher than the design scenario (shown in Table 4.11).

Propulsion load in 2003 and 2010 account for the major difference in the demand load. Albeit the power generation are similar in those years, the demand load variance leads to reliability performance degradation.

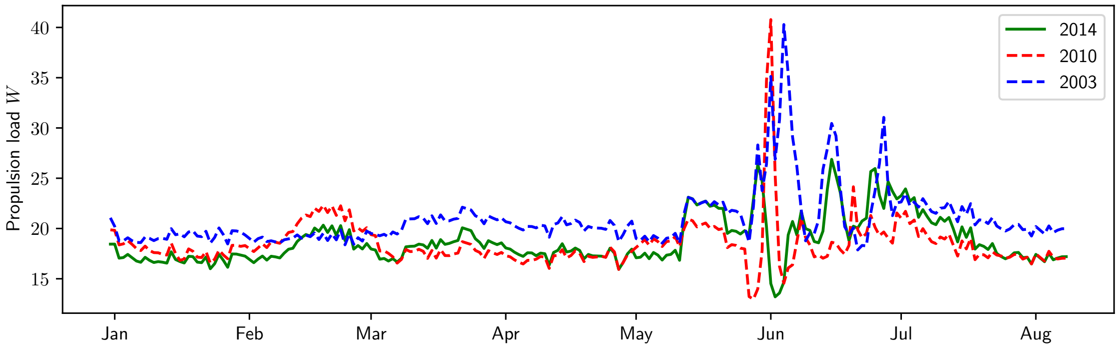

Figure 4.42: Mission 3 multiple years propulsion load comparison

In general, the long term performance result shows the optimal result has an expected reliability performance on the design mission. However, there is no guarantee on the long term because of the variance and uncertainty in both demand load and power generation. One way to improve the reliability performance of the REHS for the future is to use the exact demand load and power generation for the mission. In reality, it is hard to acquire exact information in the future. Another way to improve reliability performance is to adjust the demand load according to the power generation. The loss of power supply happens when the power generation or the demand load deviate too much from the design scenario. Such improvement requires a dynamic power management strategy to plan power usage during the operation.

4.4 Summary

In this chapter, the REHS configuration to explore and optimal design the power system have been proposed. The former problem is solved as multiple objectives optimisation methods and the later one is solved by the constraint mixed objectives optimisation method. The result has shown that both methods helped the design of REHS configuration on a size constraint renewable robot. REHS configuration exploration can determine the best possible reliability and economic performance of the renewable robot under the hard size constraint. If there is a configuration that can achieve a zero LPSP for the mission, the REHS configuration design exploration algorithm could find such design.

Furthermore, the mixed multiple objectives optimisation algorithm will find the optimal REHS configuration in terms of the cost and reliability with the LPSP guarantee by the REHS configuration exploration. For renewable robot limited by the size on the REHS devices, the design exploration could also suggest a minimal LPSP. Even the configuration might achieve a fully autonomous power supply from a renewable resource, the mixed objectives optimisation method would able to find the best combination of cost and reliability.

On the other hand, if there is no configuration can achieve a zero LPSP due to the size constriant. The mixed multiple objectives optimisation would suggest the configuration with a compromise between cost and reliability. The trade-off in the optimal configuration is also available as a Pareto front of the problem.

The long term reliability test was carried out using historical data-driven simulation. Compare the reliability performance in the last 20 years, there are some cases that REHS configuration is not able to achieve a zero LPSP. However, in most cases, the REHS configuration suggested by the mixed objectives optimisation algorithm keeps a reliable performance level with no lost power supply. The variance and uncertainty in both demand load and power generation are problematic to the safe operation of the power system. To mitigate the influence of the variance and uncertainty, the data-driven design could use more accurate estimation on the future mission. Another way to improve reliability performance is to dynamically manage the power usage depends on the power generation and demand load. In particular, adjust the demand load while it deviates from the design scenario to keep a continuous, reliable power supply.

Chapter 5

Learning based power management

This chapter presents the work on the power management strategy for the mobile robot in a long term situation. At the time when the power generation or demand load deviate from the design scenario, the power management system has to dynamically plan the power usage.

A learning-based power management method is proposed in this chapter. The strategy learn to improve the long term power reliability through self-supervision on historical operation data.

A brief introduction to the learning method will be first presented. The learning power management strategy is then followed by its implementation. The performance of the algorithm is compared against the state-of-art strategies later in the chapter.

5.1 Reinforcement learning background

5.1.1 Problem formulation

Reinforcement learning refers to the method that explores and learn the strategy to maximise the objective in a particular situation. Reinforcement learning is a type of unsupervised machine learning algorithm that learns how to behave in the environment by performing actions.

Thanks to the learning capability, the reinforcement learning approach is attractive to the power mangement problem that the optimal control strategy can be generalised from the experience. It is also possible to transfer the experience that learnt from similar environment to a new robot as a initial power management strategy. The main advantage of reinforcement learning based strategy could help the robot learn to manage the power usage without demonstration. Further more, the data-driven simulation and design fit well with the reinforcement learning framework. The robot could learn from history data in the simulated environment and transfer those knowledge into the real hardware.

The general structure of the reinforcement learning problem is shown in Figure 5.5.

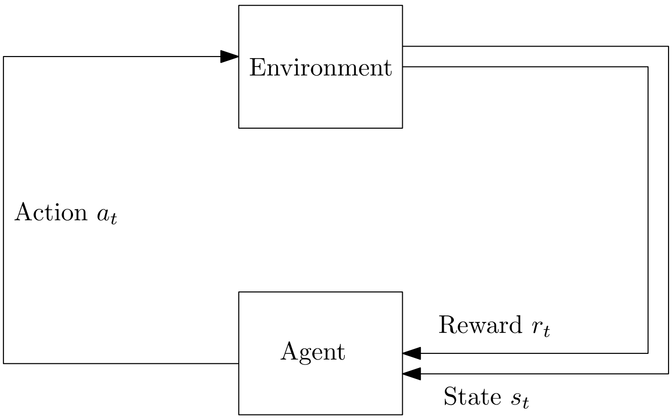

Figure 5.1: Reinforcement learning general structure

The agent is the reinforcement learning algorithm itself and the environment represent the control object. The state s describes current information on the control object and the action a is the steps taken by the agent. An agent can interact with the environment by taking an action based upon the observation on the state. For an agent, it follows its own strategy to interact with the environment. The strategy that maps the state to the action is called policy π:

$$a \sim \pi(\cdot|s) \tag{5.1}$$

The action taken by the agent will change the state of the environment and the environment also react to the action by giving a reward r to the agent. The goal in the reinforcement learning problem is to find the policy that can maximise the total reward.

$$\max R(t) = \sum_{t=0}^{T} r(t) \tag{5.2}$$

The interaction between the agent and the environment is shown in Figure 5.2. From the initial state s_0, the agent takes an action a_0 by follow the policy π. At the next step, the state of environmental changes due to the action. Meanwhile, a reward is given to the agent based on the state of the environment.

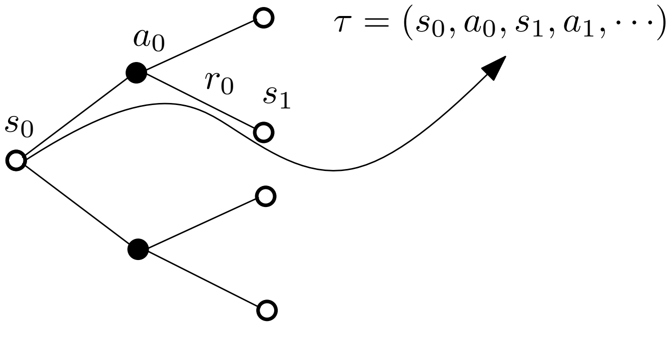

Figure 5.2: State action trajectory

State transition between each action is stochastic, e.g. after the action a_0 has taken, there are two possible outcomes of the same action. The next stage in the trajectory not only depends on the action but also the state transition probability. This helps the reinforcement learning strategy to take into account the uncertainty in the environment.

$$s_{t+1} \sim P(\cdot|s_t, a_t) \tag{5.3}$$

An agent continues to interact with the environment and forms a trajectory that consists of the state, the action and the reward.

$$\tau = (s_0, a_0, r_0, s_1, a_1, r_1 \cdots) \tag{5.4}$$

On this trajectory, the total return is the sum of all reward in history.

$$R(\tau) = \sum_{t=0}^{T} r_t \tag{5.5}$$

Consider the conditional probability for begin on the trajectory τ,

$$P(\tau|\pi) = \sum_{t=0}^{T} P(s_{t+1}|s_t, a_t)\pi(a_t|s_t) \tag{5.6}$$

the averaged expected return on all possible trajectories is

$$J(\pi) = \int_{\tau} P(\tau|\pi)R(\tau) \tag{5.7}$$

The goal in reinforcement learning is to find the policy π to maximise the expected reward of J.

$$\pi^* = \arg\max_{\pi} J(\pi) \tag{5.8}$$

5.1.2 Exploration and exploitation strategy

As a class of unsupervised machine learning method, the reinforcement learning algorithm finds the optimal policy by an exploration and exploitation strategy. The agent explores the environment to gather more information by taking possible actions.

A stochastic policy can choose random actions to explore in the environment.

$$a \sim \pi(\cdot|s) \tag{5.9}$$

Once the agent starts to explore the environment, the information on future expected reward can be collected.

The value function estimates the expected return on the trajectory that starts in state s for always following the policy π.

$$V^{\pi}(s) = \mathbb{E}_{\tau\sim\pi}[R(\tau)|s_t = s] \tag{5.10}$$

The action-value function estimates the expected return on the trajectory that starts in state s, take arbitrary action a and then follow the policy π.

$$Q^{\pi}(s,a) = \mathbb{E}_{\tau\sim\pi}[R(\tau)|s_t = s, a_t = a] \tag{5.11}$$

An advantage function describes how much better (or worse) if a specific action a was taken at state s overtaking action follow π thereafter.

$$A^{\pi}(s,a) = Q^{\pi}(s,a) - V^{\pi}(s) \tag{5.12}$$

When there is enough information gathered from the environment, the best overall decision can be made.

5.1.3 Deep neural network reinforcement learning

The policy is a function which can be approximated by a parametrised neural network

$$a_t \sim \pi_{\theta}(\cdot|s_t) \tag{5.13}$$

A neural network represents by a group of nodes, each node has have one or more input(s) and output(s). Nodes are connected with the others to form a layered network. For each node, the output of one layer is the input for the next layer. The output is determined by the weight and bias in the network. Such operation is shown in Figure 5.3, when there are inputs for the node, it first computes the summed value on the weight and bias. Then an activation function applied to the summed value. The summed value then become the input of the next layer. In the example shown in Figure 5.3, the node a_3 is part of neural network belongs to the second layer. After receives inputs from node a_1 and a_2, with weights x_{13} and x_{23}, bias b_3, the node compute its internal summed value annotated by a dot. The summed value is then applied to the activation function, a class of function add non-linearity to the neural network, to output the final value x_{36} to the node in the next layer. A neural network is parametrised via weights and biases.

The goal of reinforcement learning is to maximise the averaged expected return on all possible trajectory. For a policy parametrised by a neural network, this goal is to find the parameters in the neural network.

$$\theta^{*} = \arg\max_{\theta} J(\pi_{\theta}) \tag{5.14}$$

The averaged expected return for the parametrised policy neural net π_{θ} according to Equation 5.7 is

$$J(\pi_{\theta}) = \int_{\tau\sim\pi_{\theta}} P(\tau|\theta)R(\tau) \tag{5.15}$$

where $P(\tau|\theta)$ is conditional probability for on begin trajectory τ

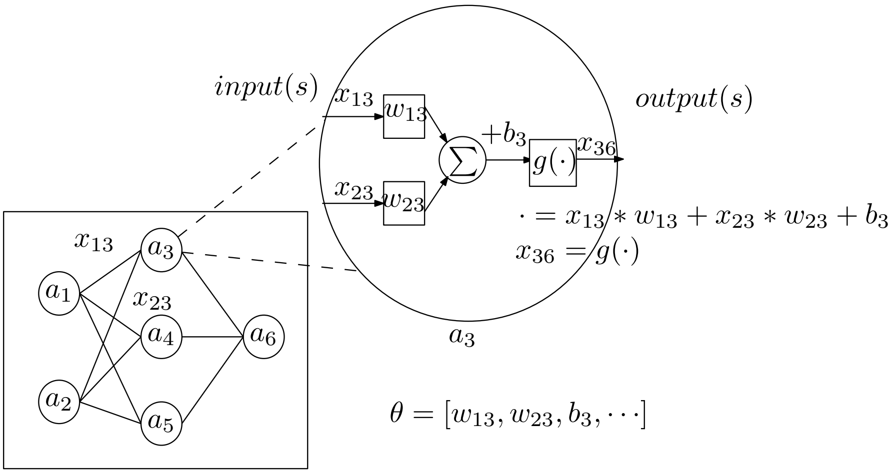

FIGURE 5.3: Concept of a parametrised neural network

$$P(\tau|\theta) = \sum_{t=0} P(s_{t+1}|s_t, a_t)\pi_\theta(a_t|s_t) \tag{5.16}$$

and $R(\tau)$ is the total return. The expectation on the averaged return on parametrised neural network π_θ is

$$J(\pi_\theta) = \mathbb{E}_{\tau\sim\pi_\theta} R(\tau) \tag{5.17}$$

It is possible to increase the expected averaged return by update the parameter using its gradient. The gradient of the expected averaged return with regard to the parameters is:

$$\begin{align}
\nabla_\theta J(\pi_\theta) =& \nabla_\theta \mathbb{E}_{\tau\sim\pi_\theta} R(\tau) \tag{5.18}\\
=& \nabla_\theta \int_\tau P(\tau|\theta)R(\tau) \tag{5.19}\\
=& \int_\tau \nabla_\theta P(\tau|\theta)R(\tau) \tag{5.20}\\
=& \int_\tau P(\tau|\theta\nabla_\theta \log P(\tau|\theta)R(\tau) \tag{5.21}\\
=& \mathbb{E}_{\tau\sim\pi_\theta}[\nabla_\theta \log P(\tau|\theta)R(\tau)] \tag{5.22}
\end{align}$$

Notice the logarithm probability on a trajectory is

$$\log P(\tau|\theta) = \sum_{t=0}^{T} (\log P(s_{t+1|s_t,a_t}) + \log \pi_\theta(a_t|s_t)) \tag{5.23}$$

so the gradient is

$$\nabla_\theta \log P(\tau|\theta) = \sum_{t=0}^{T} (\nabla_\theta \log P(s_{t+1|s_t,a_t}) + \nabla_\theta \log \pi_\theta(a_t|s_t)) \tag{5.24}$$

where the gradient on the logarithm probability on the state transition between current state and next state is independent to the parameters of the policy (the parameter in the agent's policy neural network has no influence on the dynamics of the environment). The first term in a gradient of the logarithm probability of a trajectory is zero

$$\nabla_{\log} P(\tau|\theta) = \sum_{t=0}^{T} \nabla_\theta \log \pi_\theta(a_t|s_t) \tag{5.25}$$

replace that in Equation 5.18, the gradient on the expected averaged return is then

$$\nabla_\theta J(\pi_\theta) = \mathbb{E}_{\tau\sim\pi_\theta}[\sum_{t=0}^{T} \nabla_\theta \log \pi_\theta(a_t|s_t) R(\tau)]. \tag{5.26}$$

When the gradient of the policy parameter on the expected averaged return is known, a neural network can be trained as a policy to maximise the total reward.

In the training process, it is common to estimate the gradient of the policy using the advantage function. Recall advantage function $A^\pi(s_t, a_t) = Q^\pi(s_t, a_t) - V^\pi(s_t)$ describe how better or worse for taking action a_t on state s_t over only simply follow policy π. It can be proven that using the advantage function can reduce the variance without change the expectation.

$$\begin{align}
\nabla_\theta J(\pi_\theta) &= \mathbb{E}_{\tau\sim\pi_\theta}[\sum_{t=0}^{T} \nabla_\theta \log \pi_\theta(a_t|s_t) R(\tau)] \tag{5.27}\\
&= \mathbb{E}_{\tau\sim\pi_\theta}[\sum_{t=0}^{T} \nabla_\theta \log \pi_\theta(a_t|s_t) A^{\pi_\theta}(s, t)] \tag{5.28}
\end{align}$$

As trajectory follows a policy π, at the time t the action-value function on the state s and action a, the expected return is

$$\begin{align}
Q^\pi(s, a) &= \mathbb{E}_{\tau\sim\pi}[R(\tau)|s_t = s, a_t = a] \tag{5.29}\\
&= \mathbb{E}_\pi[G_t|s_t = s, a_t = a] \tag{5.30}
\end{align}$$

5.2 Deep reinforcement learning power management strategy

5.2.1 Power management objectives

Power management system dynamically plans the power usage for the robot. The goal of the management is to provide reliable and efficient power supply to the renewable robot. The reliable power supply requires the power management to always plan and supply power at least for all critical load. When there is sufficient power, power management also needs to effectively plan the usage to improve the performance of the robot.

The REHS configuration design method in the last chapter suggests an optimal size of renewable energy system devices for a given mission. The configuration is found using multiple objectives optimisation methods by matching the demand load and power generation shown in Figure 5.4. In a longer-term, the reliability performance of the optimal REHS configuration may deteriorate due to the uncertainty and variance in both demand load $P_l(t)$ and power generation $P(t)$.

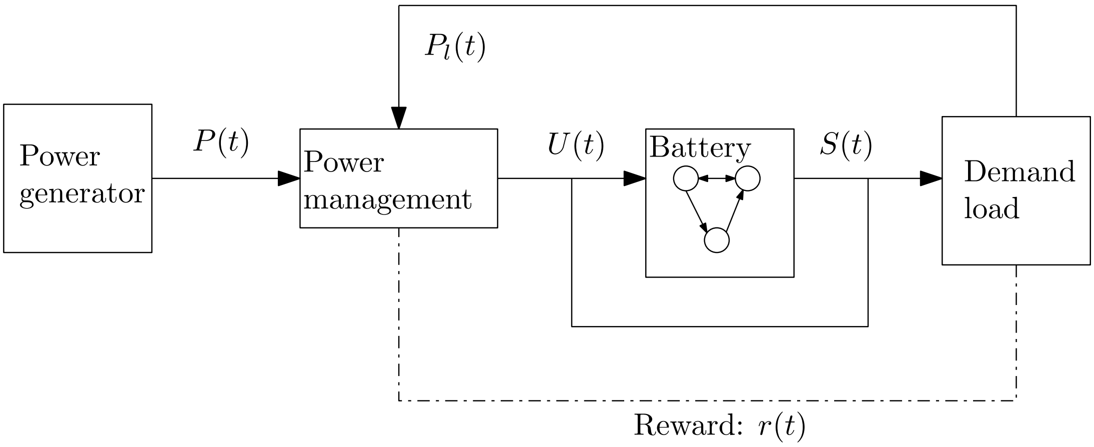

Figure 5.4: Power management in the REHS model

For the renewable robot, power management can reduce the demand load in the event of power generation shortage. However, the reliable operation of the robot needs a minimal level of power supply for the mission-critical systems. The reliability of these robots is no longer the LPSP that indexed as the fraction of time that a specific demand load cannot be met. Instead, the reliability performance of the demand load controllable renewable robot is the fraction of time that the power system failed to supply even critical load. Power management in the REHS has to work together with the power generator(s), the battery and the demand load to ensure the long-term reliability.

At the same time, the efficiency of the power system is also important to the performance of the robot. The power management strategy shouldn't either be too aggressive that scarifies long-term reliability for short-term performance or too conservative that only provide critical load and the overall performance is degraded. An ideal power management system shall plan the power usage between the conservative and aggressive strategy.

Reliability and performance are the two main objectives in the power management system. Reliability is the fraction of time that at least critical load is supplied. Performance is the power conversion efficiency between generation and demand load.

During the operation, the power management system has to plan the power usage $U(t)$ depends on the energy availability in the battery, current power generation and the demand load. Performance of the power management strategy is determined by the actual power supplied to the demand load. For every usage decisions made by the power management system, the demand load also has feedback on the reward for begin able to supply power $S(t)$.

The power management system can be modelled as an agent that interacts with the environment which consists of the power generator(s), battery and the demand load. The agent has to make its own decision on how to plan the power usage and taking that as the action. The action will change the state of the environment. In this problem, the state includes the following observations:

- The total power generation $P(t)$ from renewable resources
- The critical load demand $P_c(t)$ from demand load
- The performance-related load demand $P_p(t)$
- Remaining energy in the battery $E(t)$.

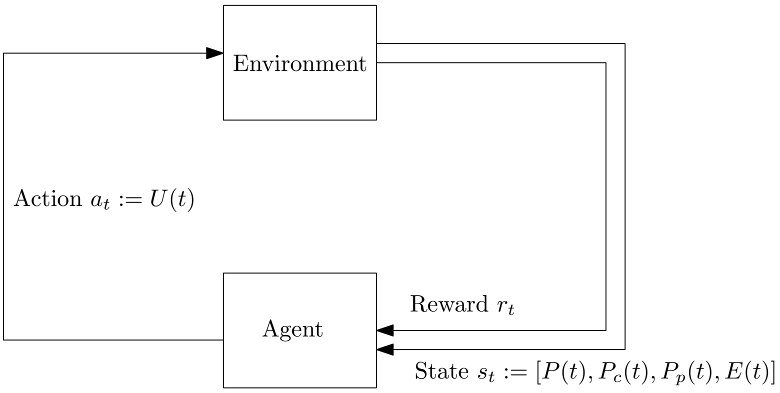

FIGURE 5.5: Reinforcement learning power management

Meanwhile, the environment also gives additional feedback on the action by reward a value r_t depends on the actual power supply $S(t)$. For the supplied power $S(t)$ the reward is

$$r_t = \begin{cases} r_c + \min\left\{\beta[S(t) - P_c(t)], r_a\right\} & S(t) \geq P_c(t) \\ r_p & S(t) < P_c(t) \end{cases} \tag{5.31}$$

where r_c is a reward for supplying critical load. If there is more power supplied to the robot, the additional power could improve the performance of the robot and get an additional reward at the ratio of β. The additional reward is capped at r_a. The reward function penalises the power management system on r_p (as a negative value) for not be able to supply. The goal in the reinforcement learning-based power management strategy is to maximise the total reward.

The action taken by the agent is the planned power usage $U(t)$. To achieve a reliable and efficient power supply, the agent could learn the power generation pattern, adjust the demand load or trade short-term benefit for long-term stability. However, the learning-based method does not directly use any of this strategy to plan the action. Instead, the action shall be learned from the reward and the state from the environment. The reward will encourage the policy to take action that is beneficial to the robot long-term power supply stability. Meanwhile, the learning-based power management system reinforces the strategy to take action for better long-term power supply stability.

5.2.2 Learning algorithm

In the deep reinforcement learning power management problem, the strategy is parametrised as a neural network. The power management system has to learn the strategy from the interaction between the environment. Random weights are first initialised as parameters in the neural networks to form a policy network. This network follows a stochastic policy that acts randomly on the policy π with parameters θ. Reward on the policy can get from the environment as a feedback and more importantly the gradient on how to improve the total expected return on the parameters can also be estimated from those interactions.

The gradient on the parameters in the policy θ has previously derived as:

$$\nabla_\theta J(\pi_\theta) = \mathbb{E}_{\tau\sim\pi_\theta}[\sum_{t=0}^{T} \nabla_\theta \log \pi_\theta(a_t|s_t) A^{\pi_\theta}(s,a)] \tag{5.32}$$

Parameters in the policy network can then be updated to improve the performance in the total expected return. In each iteration, parameters in the policy network updated on learning rate α:

$$\theta_{k+1} = \theta_k + \alpha \nabla_\theta J(\pi_{\theta_k}) \tag{5.33}$$

The policy can learn to improve its own power management strategy through the learning process shown in Figure 5.6. As the policy continues to explore the action and update its own weights, the power management strategy can adapt to the power management problem through iterations of learning.

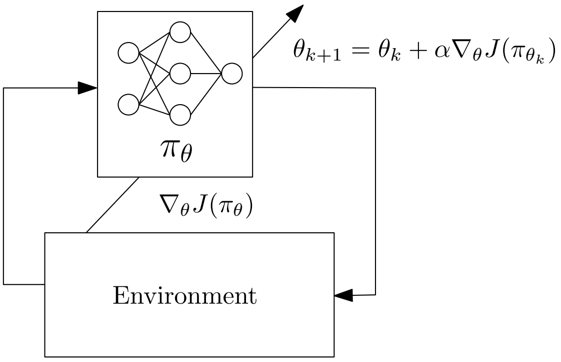

Figure 5.6: Parametrised neural network and training process

The pseudo-code of the learning algorithm is listed in Algorithm 4. This learning algorithm requires data in power generation, demand load and the REHS configuration. The result of the training is the power management policy π that maximise the total expected reward. As the reward encourages the power management strategy to provide reliable power supply for safe operation and to improve the power use efficiency for better service quality, the policy with a higher total expected reward is equivalent to a more reliable and efficient power management strategy.

```
Data: Power generation, demand load and REHS configuration
Result: Power management policy $\pi$
Initialise policy parameters $\theta_0$ and value function parameters $\phi_0$;
Initialise state at start time $t = 0$;
while $k <$ max episodes do
    foreach $t$ in $T$ do
        while $i <$ sample numbers do
            Select action $a$ by run on latest policy $\pi$ on parameter $\theta$;
            Use the selected action to plan the power usage $U(t) = a$ ;
            Receive reward $r_t$ from the REHS simulation ;
            Collect trajectory $\tau_i = (s_0, a_0, r_0, s_1, a_1, r_1, \cdots)$;
            Continute record trajectory until end $t = T$ (when the robot reach the end);
            Reset the time to the strat and save $\tau_i$ to sampled trajectories collection $\mathcal{D}_k$;
        end
        Compute the future expected reward $G_t$;
        Compute advantage function based on value function $A^{\pi_{\theta_k}}$ ;
        Estimate the policy gradient $g_k = \frac{1}{|\mathcal{D}_k|} \sum_{\tau \in \mathcal{D}_k} \sum_{t=0}^{T} \nabla_\theta \log \pi_\theta(a_t|s_t) A^{\pi_\theta}$ ;
        Update policy $\theta_{k+1} = \theta_k + \alpha g_k$;
        Update value function by regression fit
            $\phi_{k+1} = \arg\min_\phi \frac{1}{|\mathcal{D}_k| T} \sum_{\tau \in \mathcal{D}_k} \sum_{t=0}^{T} (V_\phi(s_t) - G_t)^2$
        via gradient descent.
    end
end
```

Algorithm 4: Power management policy training algorithm

Power management learning algorithm is shown in Algorithm 4 started with parameters initialisation on policy and value function. Both policy and value function is approximated as a deep neural network that consists of several layers of nodes.

In the beginning, the stochastic power management policy randomly selects the action based on its own policy. The environment responds to the action on changing the states and also give a reward to the action. As more random actions are taken, the trajectory on the state, action and reward can be collected. A collection of trajectories $\mathcal{D}_k$ could represent the averaged performance of the policy on the stochastic parameters θ.

Once the agent starts to interact with the environment, the actual reward r_t is given for each action. The future expected reward G_t can be computed based on the actual reward. The future expected reward estimates the total reward on state s by follow policy π from time t and onward.

$$G_t = \sum_{t=t}^{T} \gamma r_t \tag{5.34}$$

where $\gamma \in (0, 1]$ is discount factor to weight the future reward. A small discount factor in the policy values a more recent reward.

Similarly, the advantage function $A^{\pi_{\theta_k}}$ can also be computed based on value function and the collection of the trajectories $\mathcal{D}_k$. The gradient on the parameters θ can then be estimated from the advantage function. Parameters in the policy network are updated on the gradient to increase the total expected return.

The last step is to update the value function with the future expected reward G_t as it cannot be explicitly acquired from the environment. In the next time step, the learning process continues with the updated policy.

5.3 Algorithm implementation

The learning algorithm is implemented as an agent in the dynamic power management environment. Dynamic power management has the same structure as the REHS model except the power management strategy is replaced by a neural network-based policy.

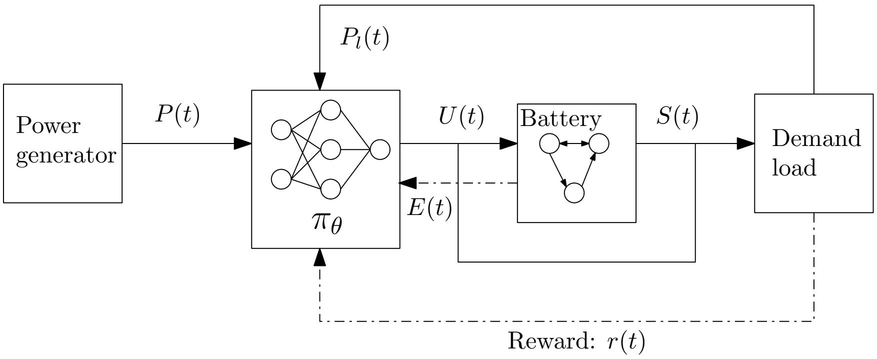

Figure 5.7: Parametrised neural network and learning process

The same power generator, battery and demand load model is used in the dynamic power management environment. Power generation is stimulated by the power generator model that includes both global and local motion of the renewable robot. Battery model with charge and discharge inefficiency takes the self-discharge and DOD into consideration. Demand load are modelled as critical load and performance-related depends on its role in the robot.

A random policy is initialised at the beginning to explore possible actions in the dynamic power management environment. Four states including the power generation, demand load (both critical and performance-related load) and the energy in the battery can be observed by the power management system. Power management system as an agent shall take one action that plans the power usage for the REHS. This action will send as a command to the battery and the actual power supply will depend on the power generation and energy level in the battery. The dynamic power management environment provides an API that compatible with `OpenAI Gym` [17] style. The power management policy can learn to maximise the total expected return through the training algorithm presented in Algorithm 4. After enough information has been collected, the policy would reinforce itself to take more actions that have a higher reward. More detailed implementation and the code can be found in appendix 2.

The algorithm is also implemented for both training and execution mode. In the training mode, the power management system learns to plan power usage in the simulation environment. The outcome of the training is the policy in the power management system. The execution mode follows the policy and plans the power usage for the renewable robot.

5.4 Method evaluation

To evaluate the performance of the learning based power management strategy, an experiment on renewable robot is done. A renewable robot is out for a long-term mission with the route shown below.

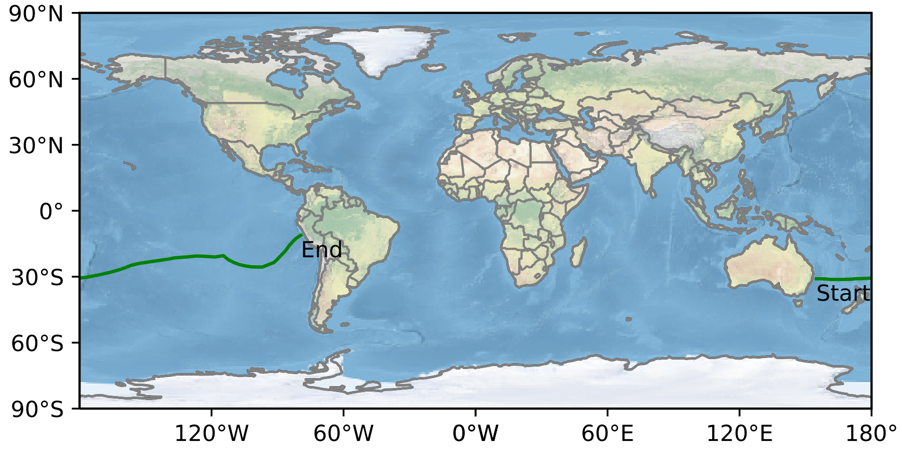

Figure 5.8: Mission in methodology evaluation

The optimal configuration for this route using the meteorological data in 2014 is listed below.

Table 5.1: REHS design result

Constraints	Design	Unit
Solar panel area	3.32	m^2
Wind turbine area	0.63	m^2
Battery capacity	1382	Wh

The learning-based power management system needs to learn how to plan the power usage for long-term reliable and efficient power supply. In order to encourage the power management strategy to continuously provide sufficient power supply to the robot, a constant value 20 is given when the power supplied is higher than or equal to the demand. An additional reward that capped at the same value discourage the short term greedy planning on the power supply. A relatively large penalty 500, 25 times of the fixed reward, is given when the power management system failed to provide the critical demand load.

Value is the reward function used for the training is an example:

$$r_t = \begin{cases} 20 + \min\Big\{0.1[S(t) - P_c(t)], 20\Big\} & S(t) \geq P_c(t) \\ -500 & S(t) < P_c(t) \end{cases} \tag{5.35}$$

In practise, the weights in the rewards have to be tuned for a balance between the performance and robustness. Four baseline algorithms and five performance matrices are included to evaluate the performance of the learning-based power management strategy.

5.4.1 Baseline algorithms and performance matrices

Demand Load Follow (DLF) strategy

DLF is a demand load side power management strategy that plans the power usage exactly as the renewable robot request. This management strategy will try its best to supply the power to the robot based on energy availability.

$$U(t) = P_l(t) \tag{5.36}$$

DLF is a passive strategy does not adjust the planned usage based on energy availability.

Generation Absolute Follow (GAF) strategy

GAF is a resource sidetracking power management strategy that always plans power usage as the same as the power generation. The power management strategy simply consumes all energy when it harvested.

$$U(t) = P(t) \tag{5.37}$$

GAF is also a passive strategy that does not adjust the planned power usage.

Exponential Weighted Moving Averaged (EWMA) strategy

EWMA is a predictive power management strategy that uses historical information to plan the demand load in the future. As a predictive power management method, there are two steps to plan power usage. The exponentially weighted moving average on the power generation is estimated first.

$$\bar{P}(t) = \alpha P(t) + (1 - \alpha)\bar{P}_{t-1} \tag{5.38}$$

where α is weight between 0 and 1, a higher weight would discount older observation quicker. $\bar{P}(t)$ start with $P(0)$ at the very beginning.

The demand load is then planned as the exponentially weighted moving average on the power generation.

$$U(t) = \bar{P}(t) \tag{5.39}$$

Global Finite Horizontal (GFH) strategy

GFH power management strategy plan the power usage with prior global knowledge on the power generation and the battery size. GFH plans power usage to maximise the total power supply without depleting the battery.

$$\begin{aligned} \underset{U(t)}{\text{maximise}} \quad & \sum_{t=1}^{T_t} S(t) \\ \text{subject to} \quad & 0 \leq U(t) \leq P(t) + E(t) \\ & E(t) \geq (1 - DOD) \cdot B \end{aligned} \tag{5.40}$$

Performance matrices

Five performance matrices are selected to compare the performance of the learning-based power management strategy. Performance matrices are:

- $\mathbb{P}_c$: Critical load offline ratio

  The fraction of time that the power supply cannot provide at least a critical load.
- η: Energy conversion efficiency

  The ratio between total supplied power to the total generated power.
- $\min S(t)$: Minimal power supply
- $\bar{S}(t)$: Averaged power supply
- $\sigma[S(t)]$: Standard deviation on power supply

Other performance matrices include the reward for the power supply is also assessed in the study.

- $\bar{r}_t$: Averaged reward
- R: Total return

5.4.2 Training result

Figure 5.9 show the training process when the power management system learns to plan power usage. As shown, the power management system continuously increases its averaged total return during the training process. According to the final reward after 1000 epochs, the total reward is close to 1.2×10^5.

The resulting power management strategy achieved an average reward at around 25. This means the learning-based power management strategy, on an average, not only supplied the critical load but also some performance-related load to the renewable robot. Simulation result from the execution mode confirms the ability of this learning-based power management strategy. In Figure 5.10, the power generation, power supply and battery SOC are shown in the upper part of the figure. Critical load unmet – the difference between the power supply and the critical load – is shown in the lower part of the figure.

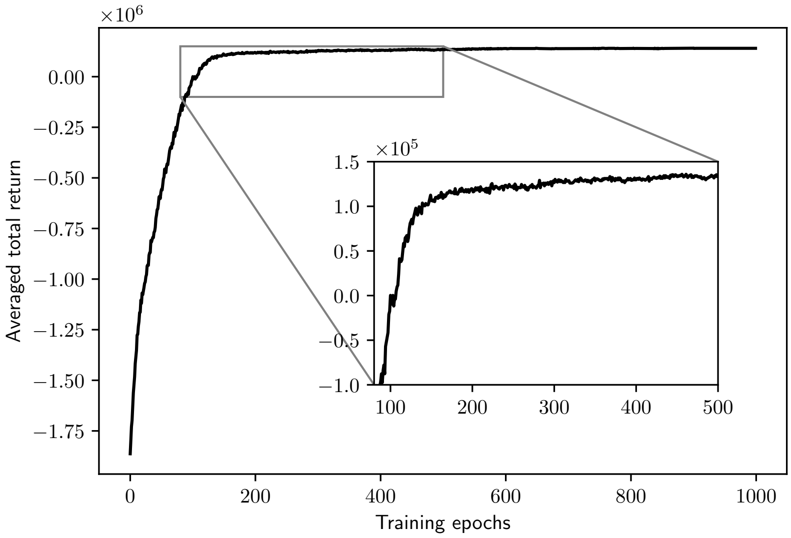

Figure 5.9: Averaged return during the training process

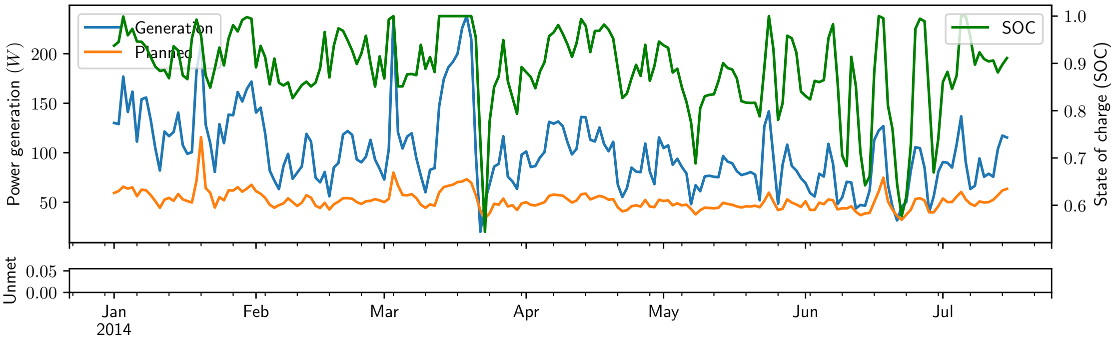

Figure 5.10: RL power management SOC, generation, planned and unmet (24 hours averaged)

What stands out in the unmet part is that there is no loss in power supply to the critical load. RL strategy maintains the reliability to support the critical load during the long-term mission. The SOC of the battery indicates its energy level is always above the DOD in the mission.

The RL strategy also outperforms to the DLF strategy in the actual power supply. Figure 5.11 compares the supplied power to the renewable robot according to each power management strategy. According to the RL power management strategy, the actual power supplied to the renewable has a higher mean value than the DLF strategy.

RL strategy achieved this by learning from the experience in the dynamic power management environment. For the same REHS configuration, the learning-based power management improved the efficiency whilst maintained the reliability in the critical load power supply.

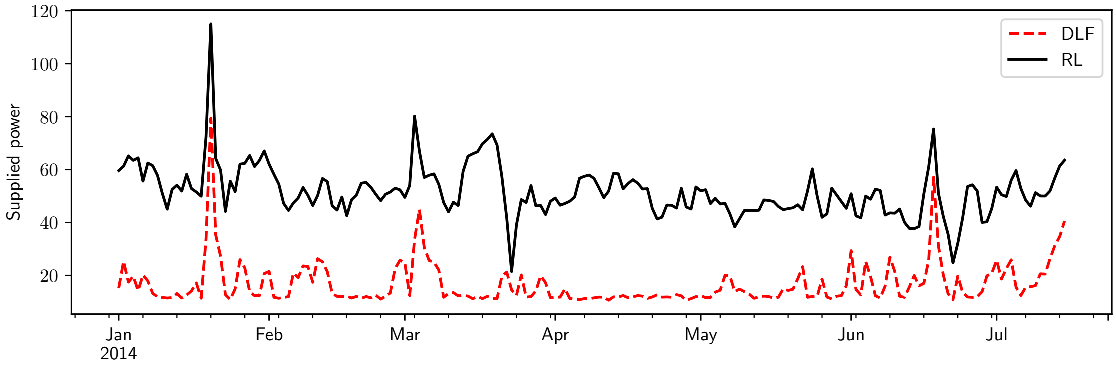

FIGURE 5.11: RL and DLF actual power supply

5.4.3 Benchmark result

Performance of the RL strategy will be further compared against our baseline algorithms in this section. All five power management strategies are simulated in the dynamic power management system using the same RHES configuration. Each power management strategy plans the power usage based on the same power generation and load demand (including critical and performance-related load). Power generation, planned power usage, battery SOC and critical load unmet of other power management strategies are shown from Figure 5.12 to Figure 5.15. The behaviour of each power management strategies as well as its performance will be explained.

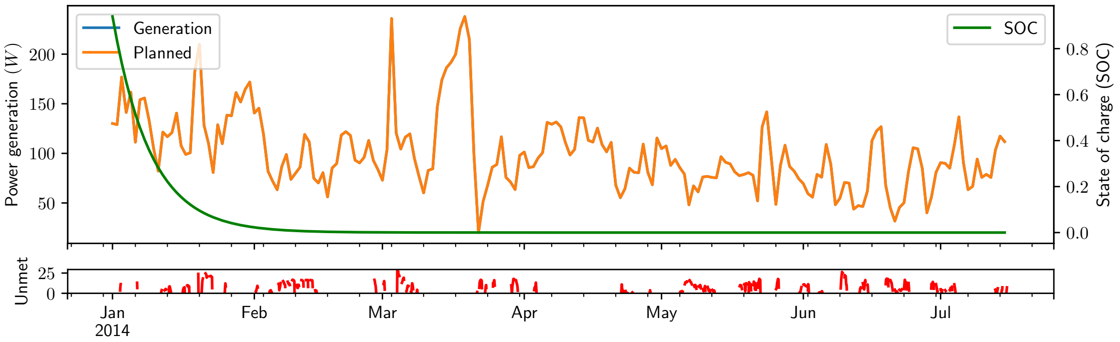

FIGURE 5.12: GAF power management SOC, generation, planned and unmet (24 hours averaged)

The GAF strategy plans power using the same as the power generation. This power management strategy does not take into account other factors such as the demand load or battery energy. The power generated from the renewable resource is consumed immediately so there is no energy saved to the battery.

In Figure 5.12, planned power overlapped with the power generation according to the power management strategy. The SOC dropped to zero after two months due to the battery self-discharge. After the battery is fully depleted, the power system would fail to supply at least a critical load to the renewable robot if there is a shortage in power generation. This will undermine the power supply reliability that the critical load can not be guaranteed. The renewable robot will experience a power loss in safety-related critical load.

However, the GAF strategy has an advantage in power conversion efficiency. As all power is consumed right after its generation, the theoretical power conversion efficiency between generation and supply is 93 per cent (due to DC-DC loss). It is a strength for space-limited renewable energy applications which safety is not influenced by the loss of power supply. For renewable robots, the excessive use of generated power would harm the safety of the robot in the long-term operation.

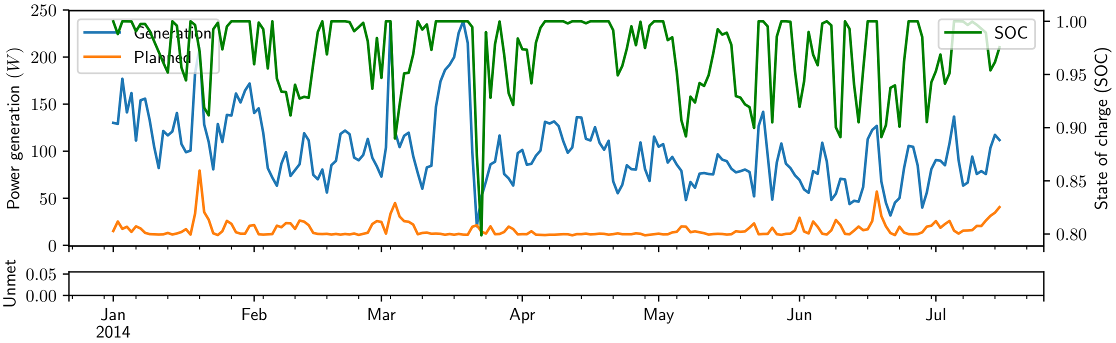

FIGURE 5.13: DLF power management SOC, generation, planned and unmet (24 hours averaged)

The DLF strategy plans the same power usage as the demand load. Demand load of the renewable robot consists of the critical load and performance-related load at the rated duty cycle. In Figure 5.13, the simulation result shows there is no critical load unmet during the operation. The energy level in the battery stays over 80 % on the 24 hours averaged SOC. As the default power management strategy, the DLF does benefit from the REHS configuration that optimised for this specific operating condition. The DLF strategy compromises the power conversion efficiency for the reliability in supplying demand load to the renewable robot. If the renewable robot operates in the same condition as the design scenario, the DLF will able to provide uninterrupted power supply to all demand load. In this case, critical load as a part of demand load shall be supplied by the REHS.

As discussed before, the disadvantage of DLF strategy is the robustness when the operation condition is different from that in the design scenario. This section, however, only discusses the behaviour and performance of each strategy on the design scenario. Multiple year robustness and performance of each management strategy will be discussed in the next section.

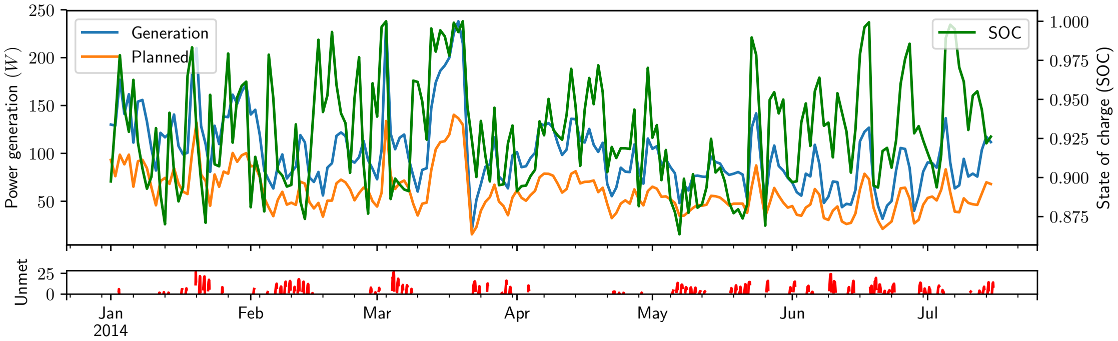

FIGURE 5.14: EWMA power management SOC, generation, planned and unmet (24 hours averaged)

The EWMA strategy plans power usage based on power generation observations. This strategy predicts the future power generation as an exponentially weighted moving average of the past observations and allocates the power usage from the prediction. The power usage will only increase or decrease depending on the expected power generation. Demand load of the renewable robot is not considered when planning the power usage for the future.

Planned power usage, battery SOC and critical load unmet of EWMA strategy can be seen in Figure 5.14. The EWMA strategy predicts the future power generation on a short time horizon and plans the power usage accordingly. This power management strategy was designed to maintain the short-term power supply by adjusting the power usage depending on recent observations. Long-term power supply stability is not guaranteed by the power management strategy because neither demand load nor future variance in power generation is considered.

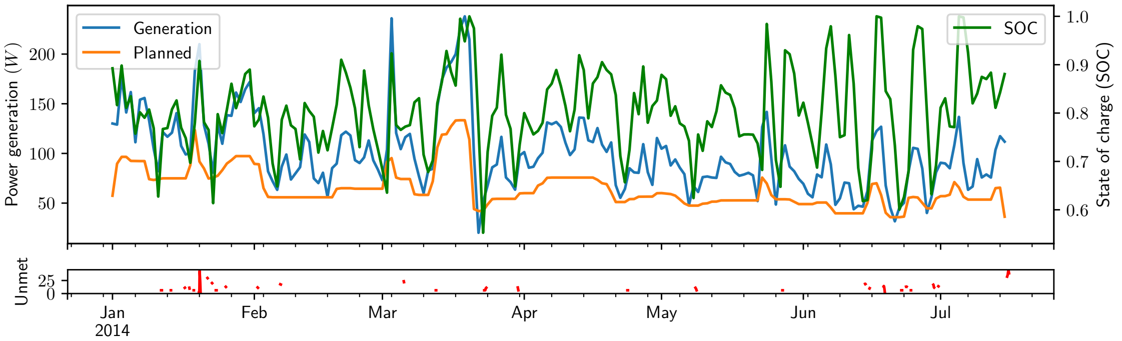

FIGURE 5.15: GFH power management SOC, generation, planned and unmet (24 hours averaged)

The GFH strategy further considers the constraint in the battery while planning the power usage. The power usage is planned to maximise the total power supply without leaving the battery energy level drops below than DOD. This power management strategy is a global optimisation based approach that the future power generation is known while planning the power usage. However, the demand load of the renewable robot is not included when plan power usage.

Result of the GFH strategy is shown in Figure 5.15, the power usage is planned on the finite horizon on future power generation. Compare to EWMA and GAF strategy, GFH has fewer instances in the critical load unmet. This power management strategy also keeps the battery level over the minimum DOD during the operation.

Performance matrices of these power management strategies, including the learning-based, are listed in Table 5.2. The performance of each power management strategy is compared with the reliability and efficiency indexes.

Among five power management strategies, DLF and RL have the best performance in terms of critical load off-line ratio. Both control strategies achieved zero critical load off-line time. GFH strategy has a critical load offline ratio at 0.028. EWMA then followed by the GAF have a critical load offline ratio higher than 10 %. GAF strategy that excessively uses the harvested power has the highest critical load offline ratio.

The GAF strategy has the highest energy conversion ratio at around 93 % that all power collected by the REHS is used by the renewable robot while considering the DC to DC conversion efficiency.

Table 5.2: Performance of learning based power management system on the design mission

	GAF	DLF	EWMA	GFH	RL
$\mathbb{P}_c$	0.178	0.000	0.129	0.028	0.000
$\eta\%$	93	15.46	55.85	58.60	47.93
$\min S(t)$	0.00	7.56	0.58	0.00	6.74
$\bar{S}(t)$	100.56	16.73	60.39	63.46	51.84
$\sigma[S(t)]$	104.39	9.87	49.38	21.92	18.07
$\bar{r}_t$	-64.50	20.55	-42.30	10.45	24.06
R	-303446.2	96679.0	-199008.6	49158.2	113174.0

GFH is second to the GAF in energy conversion ratio as the goal of this strategy is to maximise the total power supply without fully depleting the battery. EWMA is close to the GFH with roughly 60 % of energy conversion ratio. Learning-based strategy RL is in between DLF and DWMA, it has a nearly 50% of energy conversion ratio. DLF is the most conservative power management strategy with the lowest energy conversion ratio.

Table 5.2 also listed the minimal, averaged and the standard deviation on the actual power supply five power management strategies. GAF and GFH have the lowest minimal power supply to the renewable robot. At a time when there is no power generation, the GAF can't supply any power to the renewable robot. Due to this, the minimal power supply is zero. GFH also has a minimal power supply at zero when there is a decrease in the power generation. GFH strategy is aimed to maximise the total power supply to the robot however it doesn't guarantee the minimum level of power supply. EWMA performed slightly better than those two strategies by plan the power usage through the prediction on future power generation. The moving averaged approach to plan the power usage by smoothed out the variance in the power generation. RL and DLF are the top two strategies in the minimal power supply. Since the DLF strategy has a goal to supply-demand load all the time, the minimal power supply of the DLF is the same the minimal demand load.

Compare to RL strategy that guarantees the minimal critical load, the DLF has a higher minimal level of power supply. Mean power supply of these power supply strategies shows a similar trend as the power conversion efficiency. The DLF has the lowest and the GAF has the highest standard deviation in power supply.

This shows a clear trade-off between the reliability and efficiency of those power management strategies. Any power management strategy shall trade part of the efficiency for the reliability during the operation. GAF prioritise the power conversion efficiency over the critical load reliability. This strategy is often used in stationary applications with limited space where efficiency is the key objective. The state of art power management strategies on space limited stationary applications has to focus on the power conversion efficiency to maximise the performance of the system. RL balance the reliability and efficiency to achieve the performance goal on space limited renewable robots.

5.4.4 Multiple years robustness result

The robustness performance of five power management strategies for multiple years are also studied. In this study, the performance of different power strategies is simulated on multiple years with the same REHS configuration. For the same configuration, the power generation and the demand load (including the critical and performance-related) are different from year to year. Each power management strategy shall plan the power usage in the same dynamic simulation environment.

In this simulation, it could still observer the power generation on every time step. The DLF strategy responses to the demand load and it receives that on every time step in the simulation. The EWMA strategy predicts and plans the power usage.

Power generation on each time step is known to the EWMA management strategy. As the GFH strategy requires the prior knowledge of power generation, the global power generation is given this strategy. The RL strategy relies on the policy that is trained by the meteorological data in the design year (2014). Observations on the demand load, power generation and energy in the battery are available to the RL strategy on every time step.

The performance matrices of all five power management strategies are listed in Table A.1. Multiyear critical load reliability performance reflects the robustness of each power management strategy. Reliability performance of five power management strategies ranked similarly to the single year simulation. The GAF strategy has the highest overall critical load unmet ratio over 20 years of simulation. The EWMA strategy has the second-highest overall critical load unmet ratio in the simulation.

Top three power management strategies (RL, DLF, and GFH) are further compared in Figure 5.16. It can be seen that the RL strategy has a zero critical load offline ratio on all studied years.

DLF strategy also managed to stay at zero except in the year 2002. GFH has the highest critical load offline ratio that critical load unmet is close to 0.03 on an average.

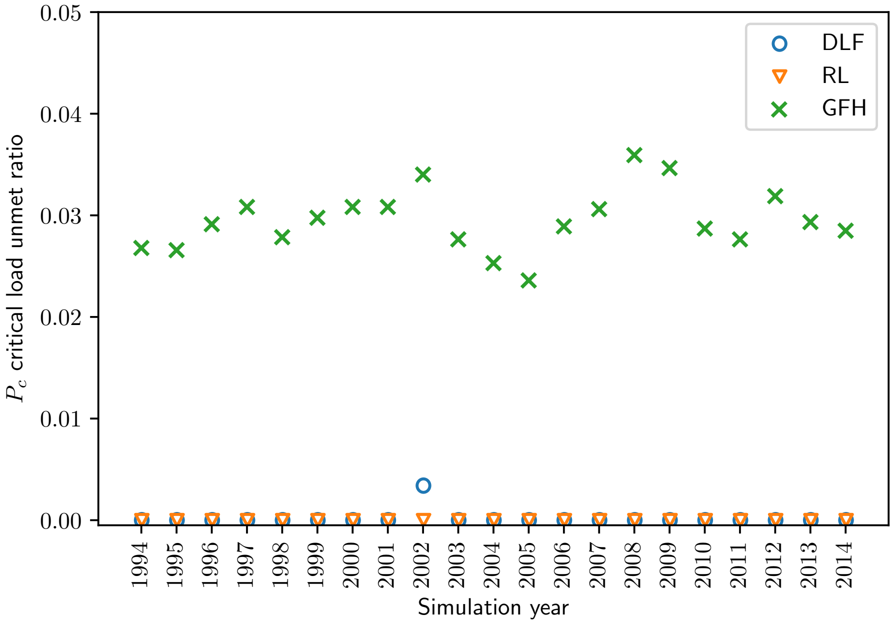

FIGURE 5.16: Multiple years critical load offline ratio

The RL strategy outperforms the DLF strategy in critical load reliability.

Planned power usage of these two strategies in 2002 are compared in Figure 5.17. The renewable robot lost critical power supply in early March of 2002 when using DLF strategy. At the same time, the RL strategy already decreased the power usage and only plan the critical load when there is a shortage of power generation. The battery is fully charged before the increase in critical load. According to RL strategy, all performance-related load has to be turned off to prioritise the power supply to the critical load.

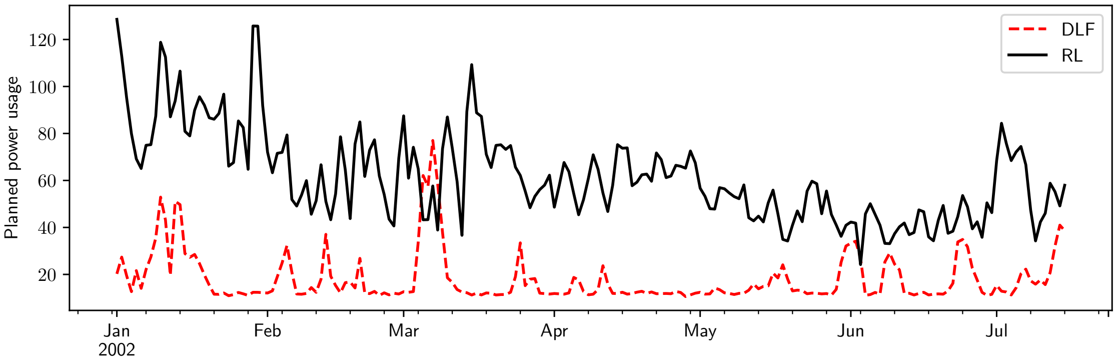

FIGURE 5.17: RL and DLF planned power usage in 2002

The limitation of DLF strategy is it can't adjust the power usage for the robust power supply. Such power management strategy is too conservative when the battery is full and too aggressive when power generation is low. When the battery is full, the extra generated power cannot be consumed by increasing the demand load.

On the contrary, when power generation is low, the DLF strategy cannot adjust the power usage. RL strategy can adapt to the changes in the power generation and compromise short-term performance for long-term power supply stability. The critical load was guaranteed by the RL strategy in the 20 years simulation period.

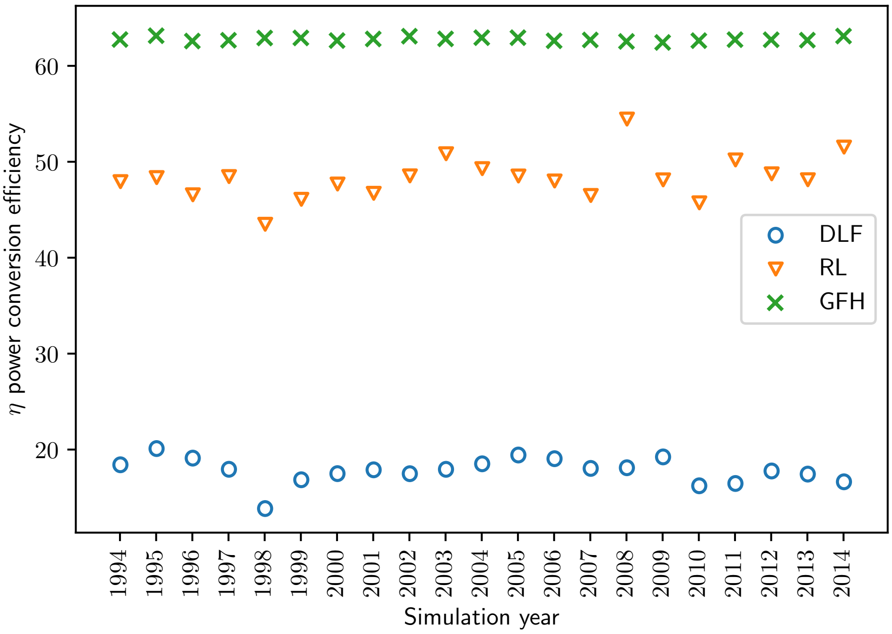

FIGURE 5.18: Multiple years power conversion efficiency

The RL strategy also has a higher power conversion ratio compared to the DLF strategy. The power conversion efficiency of DLF, RL, and GFH strategies are shown in Figure 5.18.

Power usage planned by the GFH strategy yields the highest power conversion ratio among all three strategies. This is because the GFH strategy is designed to maximise the supplied power to the renewable robot. However, the higher power conversion ratio is achieved at the cost of critical load unmet as shown before.

RL strategy performed better than DLF in the power conversion efficiency. The planned power usage in Figure 5.17 shows the difference between these two strategies. When the critical load is met by the generation, the RL strategy could increase the demand load for performance-related load.

This results in a higher energy conversion ratio on the same configuration. A higher energy conversion ratio can improve the performance of the renewable robot.

The study shows the RL strategy could provide a guaranteed power supply to the critical load and improve the performance of renewable robot when it possible. From the experience gained from the training only on the design scenario, the resulting power management strategy excels other state-of-art power management strategies. The efficiency of the power supply is improved without any compromise on the safety of the renewable robot.

5.5 Summary

In this chapter, the background, implementation and result of the learning based power management strategy were presented. The power management strategy is developed for the long term reliability performance of the renewable robot. REHS is subject to the uncertainty and variance in the renewable energy resource, the reliability achieved at the design stage may be guaranteed during the operation.

The situation is common for REHS design that the system has to designed beforehand and the actual operation condition may varies. In order to cope with this challenge, the learning based power management strategy learn the pattern in the power generation and demand load using historical data. It improves the management performance through reinforcement learning that reward the control decision that guarantee a minimal level of power supply and provide more power to performance-related load.

The experiment result shows that the power management strategy could learn to plan the power usage from the power system. Even better, the learned control strategy is applicable to robot's mission in other year. A benchmark result shows that even the energy conversion efficiency is not as high as the best conventional method, the minimal level of power supply is guaranteed in a long term simulation.

Chapter 6

Case study

In this chapter, the case study will demonstrate the feasibility of the theoretical model and method. The model, optimisation and management methods proposed in this thesis will be applied to a single problem to show how our goal to provide reliable, cost-effectively power supply solution to a mobile robot.

6.1 Problem formulation

In this example, the power system design and management of an autonomous surface vehicle (ASV) sailing across the ocean was considered. The route of the vehicle is shown in Figure 6.1. At the averaged cruising speed 3 km/h, the whole journey takes about five months to finish. The year 2014 was used as the typical meteorological year for the design. Started from 1 st of January 2014, the ASV is expected to arrive at its destination on May 2014.

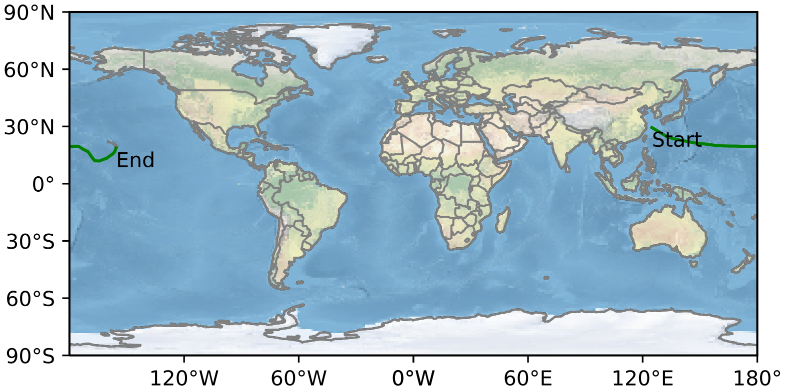

FIGURE 6.1: Route in the case study East China Sea to Hawaii

The ASV is a catamaran design that has two demihulls connected by a beam (as shown in Figure 6.2). Deck area in between two demihulls can be used to install the solar panel and a wind turbine. Battery and control unit is installed inside the hull of the ASV.

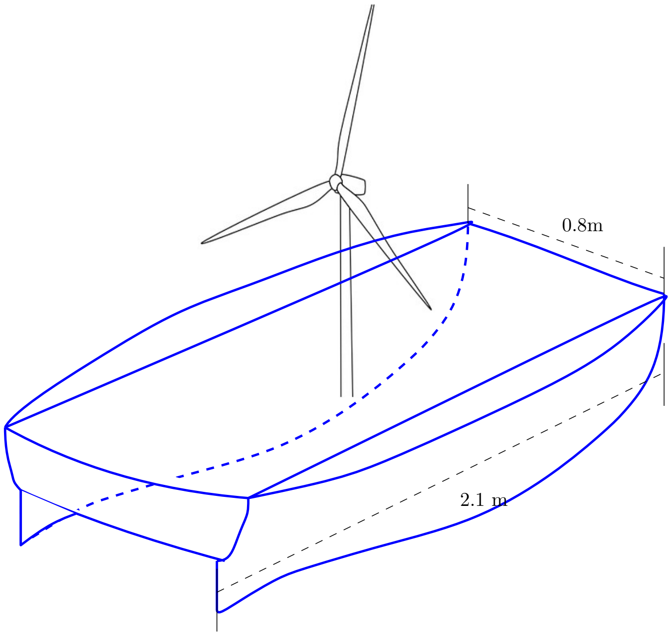

FIGURE 6.2: Catamaran ASV

Table 6.1 listed the basic dimension of this vehicle. This beam of the vehicle is 0.8 metres in total and the beam of each demihull is 0.32 metres.

TABLE 6.1: Basic dimensions

Dimensions	Value	Unit
Length	2.10	metres
Draught	0.16	metres
Beam	0.80 (0.32 demihulls)	metres
Slenderness coefficient	13.1	-
Prismatic coefficient	0.693	-

Limited space on the ASV constraint the maximum size of REHS devices. Table 6.2 listed the constraint on the three main REHS devices.

TABLE 6.2: Limitations on the REHS size

Constraints	Value	Unit
Solar panel area	1.60	m^2
Wind turbine area	0.50	m^2
Battery capacity	4000	Wh

In this journey, the REHS based power system provides electrical supply to both hotel and propulsion load. The core hotel load including navigation and control system, communication system and sensory system. Hotel load of the ASV are listed in Table 6.3. The critical hotel load has to be always powered for the safe operation of the vehicle. At the same time, the REHS power system shall supply sufficient power for the mobile robot's propulsion system. Propulsion load is also a critical load as the delay of arrival would result in a missing observation.

Table 6.3: Propulsion load on the autonomous surface vehicle

Components	Power usage	Critical load	Duty cycle
Navigation computer	5 W	Yes	1
Camera	650 mW	Yes	1
Global Positioning System (GPS)	50 to 800 mW	Yes	1
Inertial Measurement Unit (IMU)	40 to 700 mW	Yes	1
Integrated radio transmitter	0.5 to 20 W	No	0.2
Temperature sensor	40 to 50 mW	No	0.9
Wind sensor	0.4 to 1.2 W	No	0.5
Salinity sensor	40 to 100 mW	No	0.9

Table 6.4 listed the economic and operational parameters of the vehicle. Unit cost of renewable energy devices are collected from market data. The unit price of the wind turbine is 320 per squared metre swept area. The unit cost of the solar panel is 210 per squared metre. The battery has a unit price at 1 per Wh.

The solar panel is installed on the flat surface on the deck so the yaw motion of the ASV does not influence the solar power generation. Pitch and roll motion are assumed as a periodic linear motion at maximum amplitude of 0.1 and 0.2 rads correspondingly.

Table 6.4: Economic and operational parameters

Parameter	Meaning	Value
c_w	Wind turbine unit cost	3000
c_s	Solar panel unit cost	210
c_b	Battery	1
p_0	Amplitude of pitch motion	0.1 rad
q_0	Amplitude of roll motion	0.2 rad

In this case study, both the REHS configuration and the power management strategy has to be designed for the renewable robot's long-term safe operation. The power system configuration first has to be optimised with an objective in providing reliable and cost-effective power supply under the size constraint. Based on the design outcome, a robust power management strategy also need to be designed for multiple year long-term power supply stability.

6.2 Power system simulation

On the averaged cruising speed at 3 km/h, the location and the local time of the ASV is calculated and shown in Table 6.5. This mission is around 9400 km long and it will take 3168 hours for the ASV to reach the destination. In this long-distance voyage, the global motion influence power generation due to variance in renewable resources. The moving REHS model simulates the global motion of renewable robot using a data-driven approach. Following this approach, the power generation is simulated from the nearest hindcast meteorological data to its location.

TABLE 6.5: Voyage information of the vehicle

GMT	Latitude	Longitude	Local time
2014-01-01 00:00:00	29.390872	124.842009	2014-01-01 08:00:00
2014-01-07 06:00:00	27.145370	128.670991	2014-01-07 15:00:00
2014-01-13 12:00:00	24.797757	132.416632	2014-01-13 21:00:00
2014-01-19 18:00:00	23.468335	136.358345	2014-01-20 03:00:00
2014-01-26 00:00:00	22.653696	140.367331	2014-01-26 09:00:00
2014-02-01 06:00:00	21.953204	144.379733	2014-02-01 16:00:00
2014-02-07 12:00:00	21.232669	148.382074	2014-02-07 22:00:00
2014-02-13 18:00:00	20.830241	152.397732	2014-02-14 04:00:00
2014-02-20 00:00:00	20.307651	156.415401	2014-02-20 10:00:00
2014-02-26 06:00:00	19.953760	160.458388	2014-02-26 17:00:00
2014-03-04 12:00:00	19.750092	164.501185	2014-03-04 23:00:00
2014-03-10 18:00:00	19.708186	168.546170	2014-03-11 05:00:00
2014-03-17 00:00:00	19.600020	172.583333	2014-03-17 12:00:00
2014-03-23 06:00:00	19.607256	176.633514	2014-03-23 18:00:00
2014-03-29 12:00:00	19.601453	-179.319578	2014-03-29 00:00:00
2014-04-04 18:00:00	19.595342	-175.279192	2014-04-04 06:00:00
2014-04-11 00:00:00	17.536351	-171.786419	2014-04-10 13:00:00
2014-04-17 06:00:00	14.821195	-168.910037	2014-04-16 19:00:00
2014-04-23 12:00:00	11.969277	-166.234065	2014-04-23 01:00:00
2014-04-29 18:00:00	12.728521	-162.330064	2014-04-29 07:00:00
2014-05-06 00:00:00	14.637577	-158.756459	2014-05-05 13:00:00
2014-05-12 06:00:00	17.678960	-155.979834	2014-05-11 20:00:00

Solar radiation and temperature data are collected for the solar power generation simulation. In this mission, the global direct solar radiation (`SWGDN`) and the global clear sky solar radiation (`SWTDN`) are retrieved from MEERA-2 database. Time indexed solar radiation on this mission is shown in Figure 6.3.

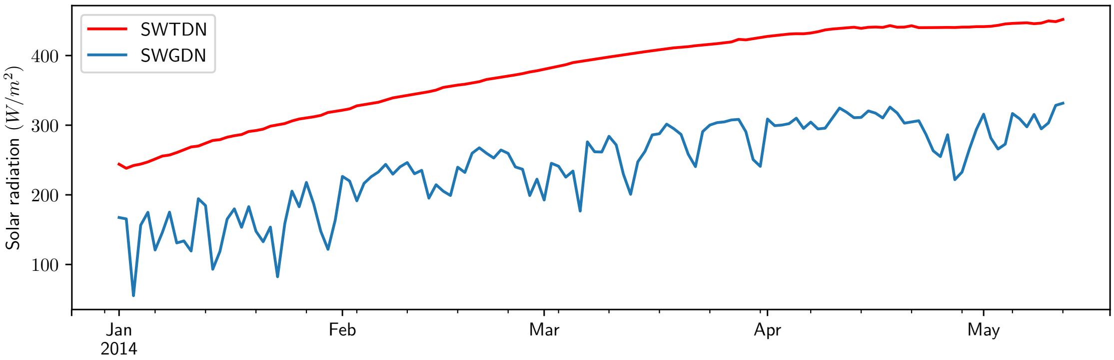

FIGURE 6.3: Solar radiation trend (W/m^2) 24 hours averaged

Global direct solar radiation (`SWGDN`) follows the general trend of global clear sky solar radiation (`SWTDN`) as it is shown in Figure 6.3. But due to the changing weather condition on the sea, the direct solar radiation on each day is varying. A more detailed heatmap in Figure 6.4 shows the distribution of the solar power within the day. In this figure, the horizontal axis represents each day of travel and the vertical axis is the UTC hour on that day. The continued shift in the peak solar radiation time is due to the change of local timezone. The highest solar radiation often found in local noon time while there is no power can be generated during the night.

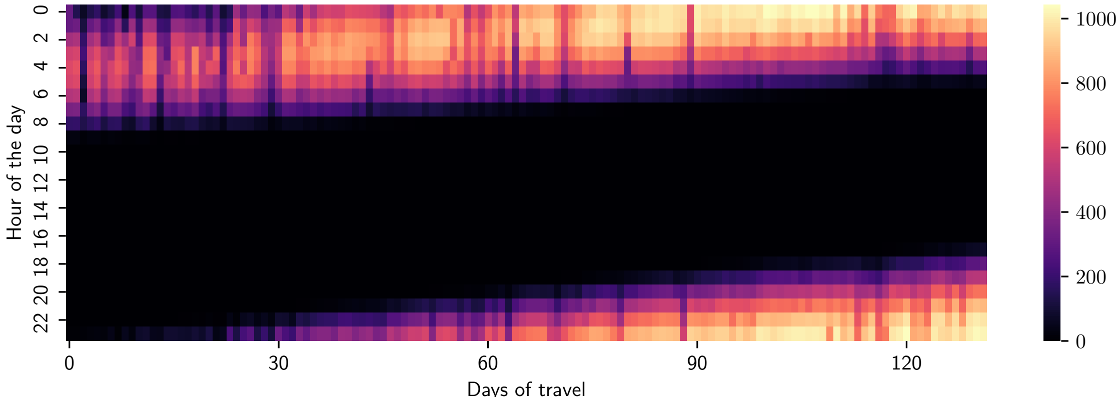

FIGURE 6.4: Global direct solar radiation heatmap (W/m^2)

The ambient temperature of the renewable robot is also collected to take account its influence on the power conversion efficiency. The ambient temperature on this route is shown in Figure 6.5. Since the route started from January from the northern hemisphere, there is an increase in the temperature as the ASV sails into the Pacific ocean.

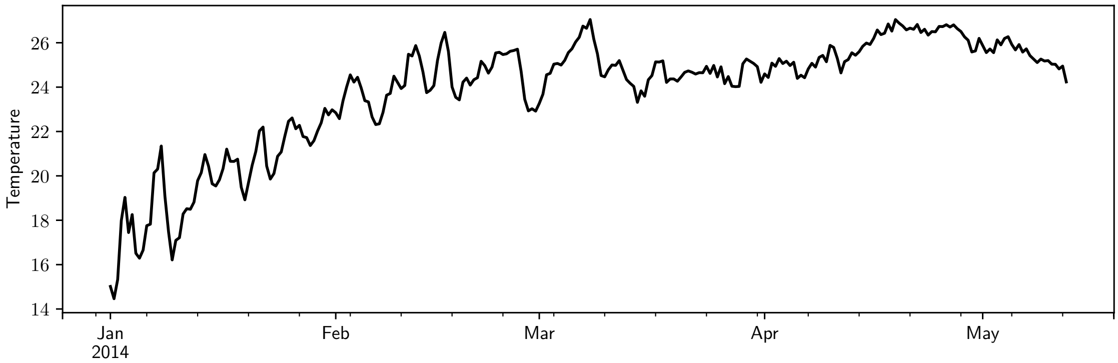

FIGURE 6.5: Ambient temperature on the mission

Solar power generation could be simulated from the solar radiation and the temperature on the mission. The first step in the simulation is to decompose the solar radiation component into direct and diffused irradiance. Figure 6.6 shows the clearness and diffuse index of the solar radiation component.

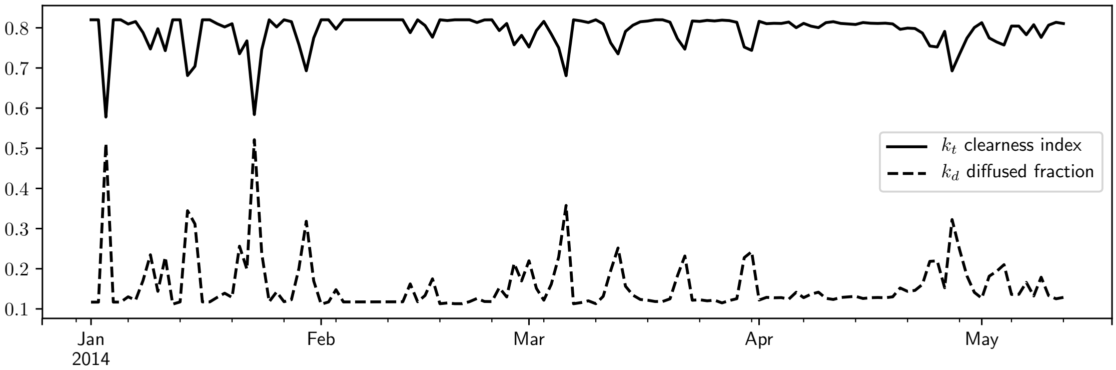

FIGURE 6.6: Clearness and diffuse index in the mission

Local motion including the pitch and roll are integrated into the solar power model when the solar radiation component is decomposed. Using the temperature-dependent power conversion efficiency model Equation 3.44, the per-unit size solar power generation is simulated.

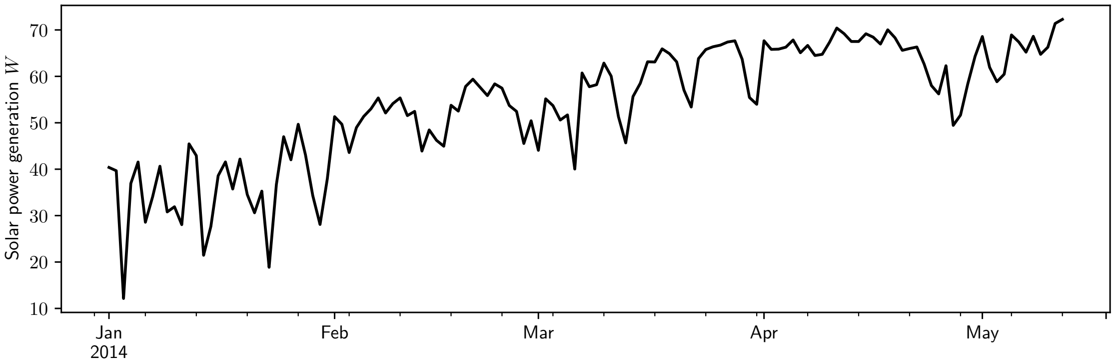

FIGURE 6.7: Solar power generation in mission

Wind power generation is dependent on both wind direction and wind speed. Considering the cruising speed of ASV, the wind observed on the renewable robot is the apparent wind. The speed of the true and apparent wind is shown in Figure 6.8.

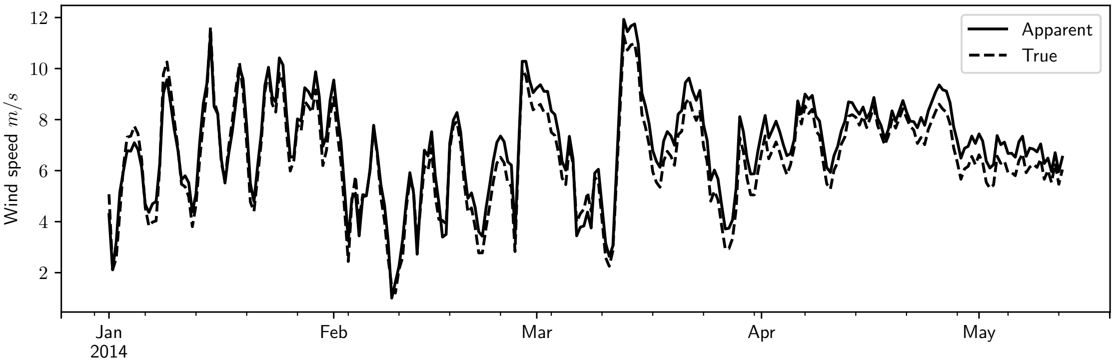

FIGURE 6.8: Wind speed in mission (12 Hours averaged)

The local motion of renewable robot has an impact on the wind power generation in both wind direction and speed. The direction of the true and apparent wind is shown in Figure 6.9.

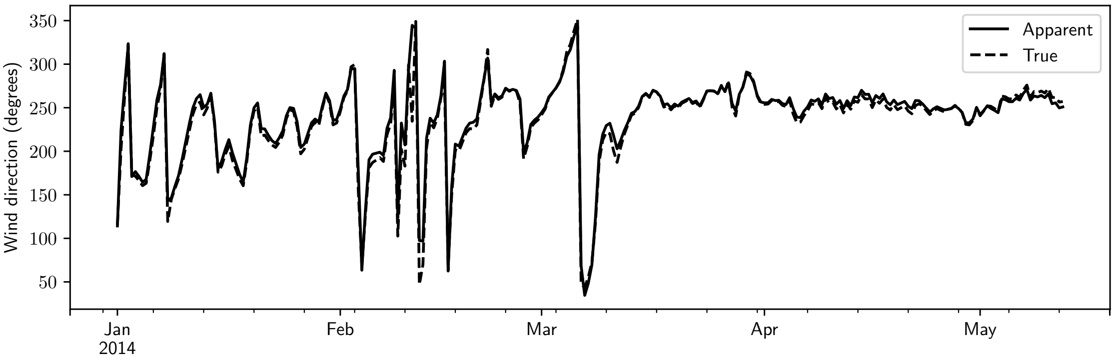

FIGURE 6.9: Wind direction in mission

Compare to the change in the wind speed, there is less change in the apparent wind direction because the true wind speed is higher than the cruising speed most of the time. Raw power generation on the apparent wind and the wind resistance discount are shown in Figure 6.10. The raw power generation is the total electrical power generation from the turbine on cruising speed (GPS speed). Depends on the wind direction, the propulsion system may have to consume electric energy to maintain the speed. Using the moving wind turbine model, the net power generation and the wind resistance discount are shown in Figure 6.10.

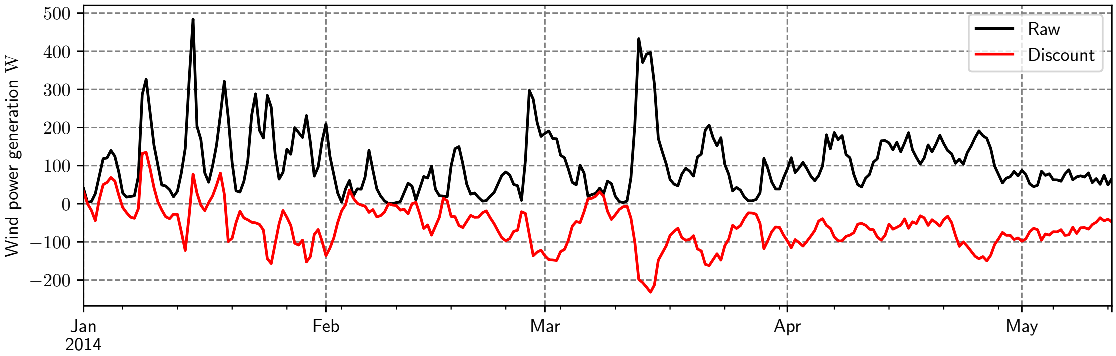

FIGURE 6.10: Wind power generation on the route

A positive wind resistance discount would require the propulsion system to increase the power to counterbalance it. A negative wind resistance discount can potentially save power for the propulsion system. The minimal propulsion power consumption is zero if the vehicle can be driven by the wind completely.

Demand load of the renewable robot includes the hotel and propulsion load. In this case, the ASV also has to arrive each waypoint on time to collect data. The critical load would include part of the hotel load as shown in Table 6.3 and the propulsion load. The performance-related load consists of power consumption of all variable duty cycle components.

Propulsion load of the renewable robot is the total electrical power consumption. The propulsion is estimated by the water speed which is calculated from the vehicle speed and current speed. The water speed of the vehicle when considering the ocean surface current is shown in Figure 6.11.

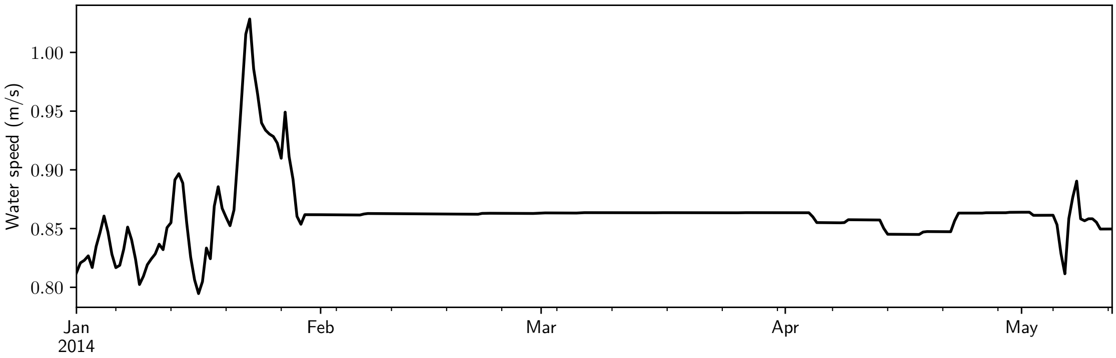

FIGURE 6.11: Water speed of the vehicle (in relative to the moving current)

The propulsion power consumption of the vehicle can be estimated. In this mission, the propulsion power of the robot on the water speed is shown in Figure 6.12.

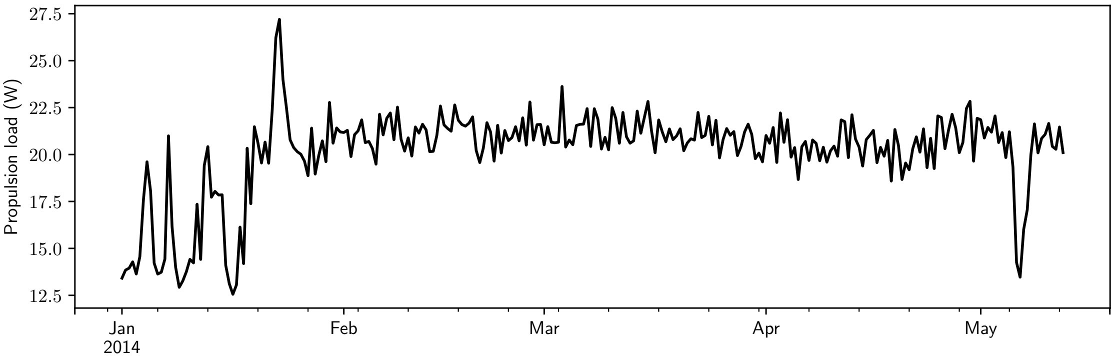

FIGURE 6.12: Propulsion load at water speed

Wind resistance discount also needs to be included in the propulsion load. Figure 6.13 shows the propulsion load when consider the wind resistance discount.

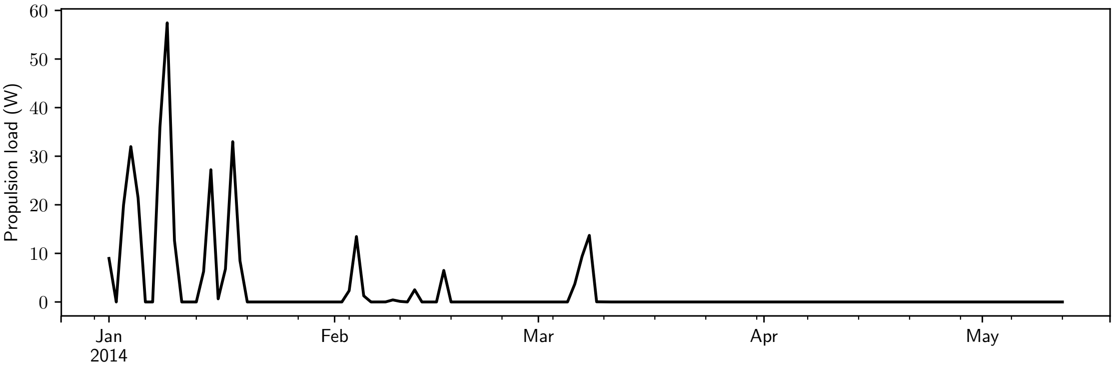

FIGURE 6.13: Propulsion load including resistance discount at water speed

Hotel load is estimated using the model from Equation 3.92 and the result is shown in Figure 6.14.

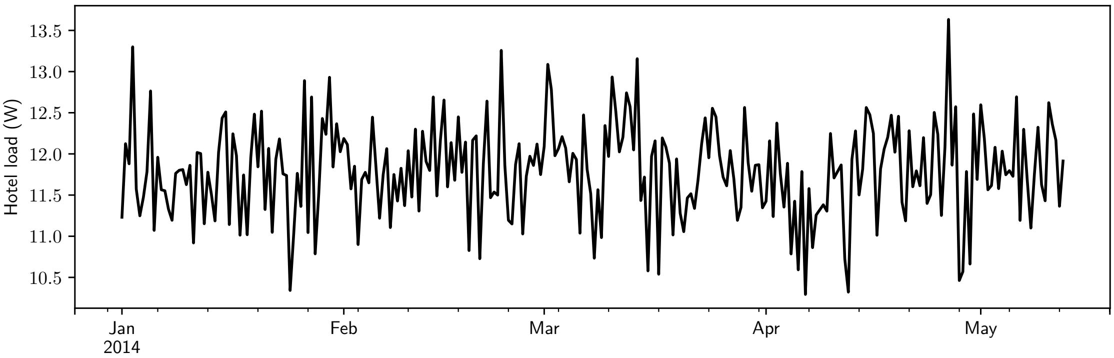

FIGURE 6.14: Hotel load on route

Part of the hotel load is critical to the safe operation of the renewable robot. This part of the hotel load, as well as the propulsion load, are the critical load has to be supplied by the REHS.

Power generation and demand load of the renewable robot now have been estimated in the mission. This simulation considers both global and local motion of the renewable robot during the operation.

6.3 System configuration optimisation

To design the REHS for a reliable and cost-effective power supply to the robot under the size constraints, the REHS configuration has to be optimised for this mission. Design variables including the size of the REHS devices: the size of wind turbine A_w, area of solar panel A_s and capacity of the battery B. Two main objectives in the optimisation are to design the REHS configuration at higher energy supply reliability and lower device capital cost. Energy supply reliability is indexed by the LPSP as the fraction of time that demand load is not supplied.

$$LPSP = \mathbb{P}[S(t) < P_l(t)] \tag{6.1}$$

where $P_l(t)$ is demand load, $S(t)$ is actual power supply.

Device capital C is the total cost of the REHS devices:

$$C = c_w A_w + c_s A_s + c_b B \tag{6.2}$$

where c_w, c_s, c_b are unit price cost of wind, solar and battery system with value specified in Table 6.4.

In the REHS configuration design, the aim is to minimise both LPSP and device capital cost. Multiple objectives optimisation has been done to study the relationship between two objectives without considering the size constraint of REHS devices.

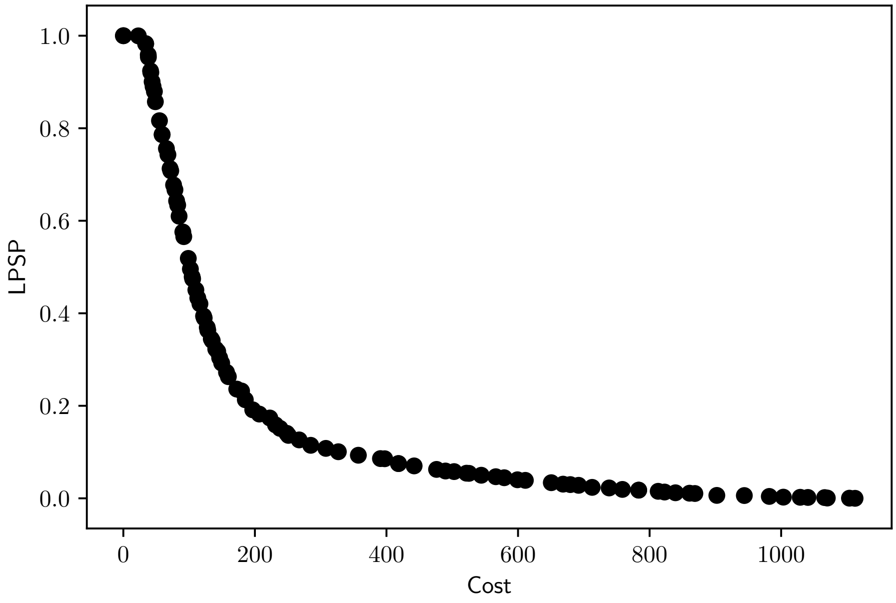

Figure 6.15: Multiple objectives optimisation

Figure 6.15 is the Pareto front of REHS cost compared against LPSP. It can be seen that the cost and reliability are two competing objectives. A more reliable REHS is more expensive in the capital cost. In order to design a reliable, cost-effective REHS under the size constraint, the mixed objectives optimisation method is used. The design method is formed as a constraint optimisation problem shown in Equation 6.3.

$$\begin{aligned} \underset{A_w, A_s, B}{\text{minimize}} \quad & C(A_w, A_s, B) + \lambda \cdot LPSP(A_w, A_s, B) \\ \text{subject to} \quad & 0 \leq A_w \leq \bar{A}_w \\ & 0 \leq A_s \leq \bar{A}_s \\ & 0 \leq B \leq \bar{B} \end{aligned} \tag{6.3}$$

where C is cost of renewable energy devices, $LPSP$ is lost power supply probability, $LPSP$ weight ratio $\lambda = 1 \cdot 10^7$ is picked to minimise the LPSP. A_w, A_s, B are design parameters on the size of wind turbine, area of solar panel, and battery capacity correspondingly, $\bar{A}_w, \bar{A}_s, \bar{B}$ are limits on each REHS devices.

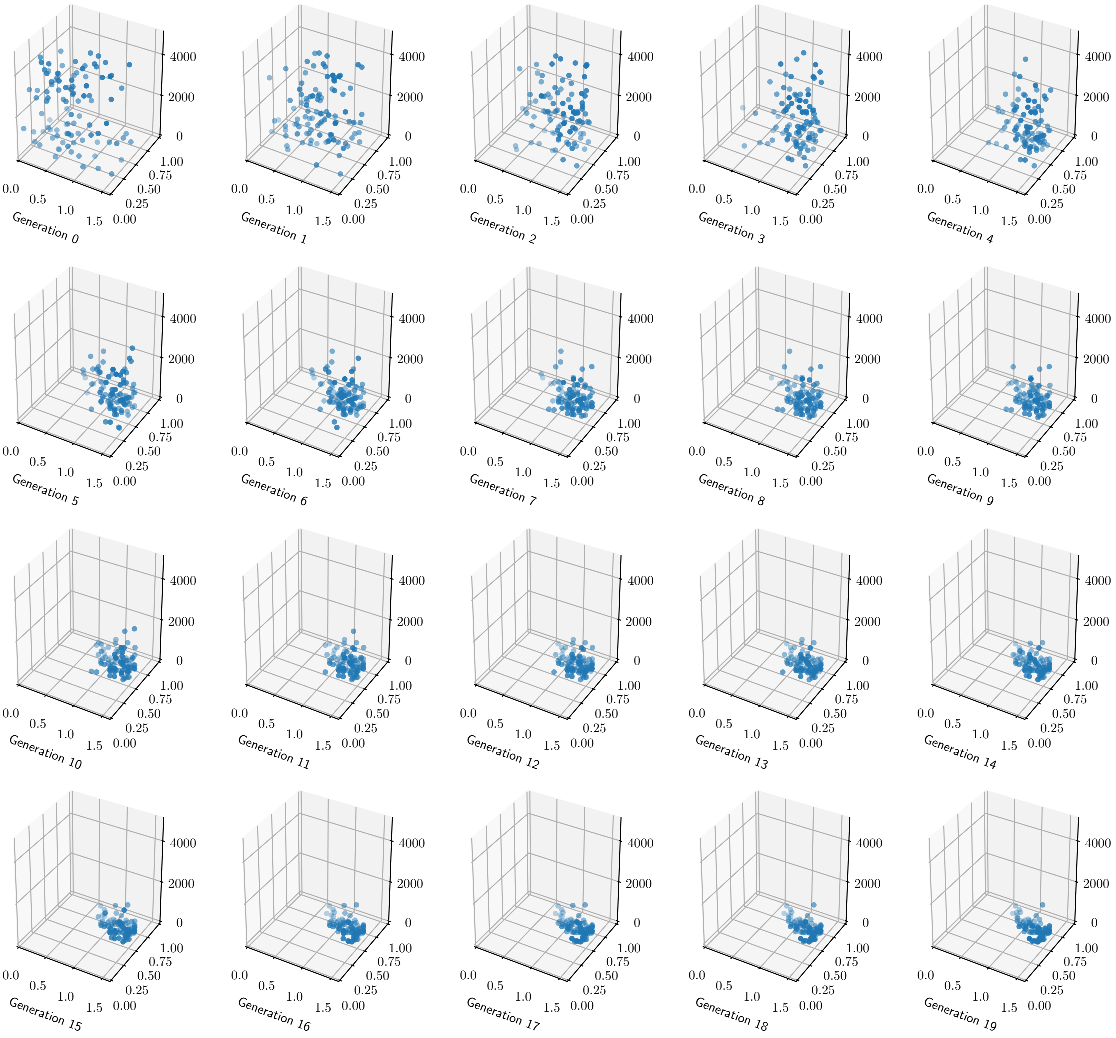

FIGURE 6.16: Population evolution during the optimisation, x, y, z axes are size of solar panel, wind turbine and battery capacity

The optimisation process is illustrated in Figure 6.16. At the beginning of the optimisation, a group of particles will be randomly generated within the constraint of all design parameters.

Each particle is a possible configuration on the size of the wind turbine, solar panel and battery capacity (A_w, A_s, B). Generation 0 in Figure 6.16 shows a population of 100 particles are randomly generated under the constraint.

On every generation, the mixed objective function is evaluated through the data-driven simulation on different REHS configuration. Among all the particles, the configuration with the highest fitness is the global best. For each particle, the best performance it has been achieved is the personal best. Mixed objectives optimisation method (Algorithm 3) update the location and velocity of each particle. Each particle continues to evolve depending on the global best and personal best. When the averaged personal best converge into the global best, the global best configuration is found.

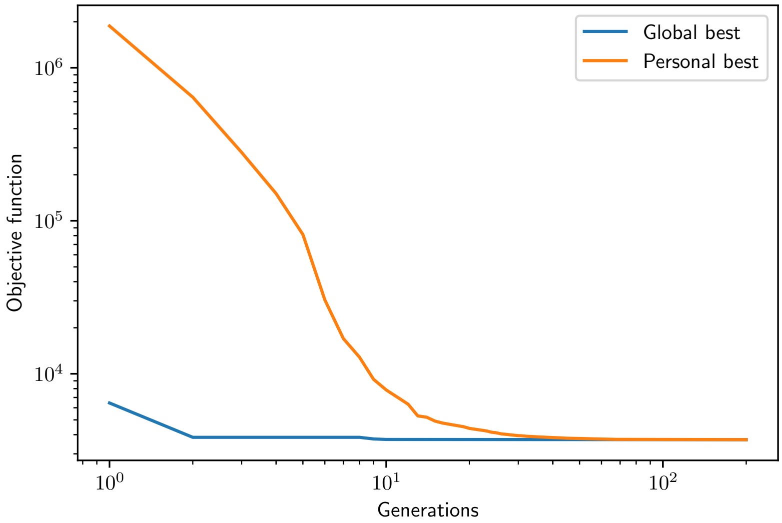

FIGURE 6.17: Convergence on the objective function

Figure 6.17 shows the convergence in the global and personal best after 100 generations. It suggested an REHS configuration with the size of the wind turbine, area of solar panel and capacity of battery listed in Table 6.6. Compare with the limit on the size of REHS devices, the configuration is a feasible design for the surface vehicle.

TABLE 6.6: Optimisation result

Constraints	Result	Unit	Limit
Solar panel area	1.21	m^2	1.60
Wind turbine area	0.45	m^2	0.50
Battery capacity	753	Wh	4000

Power system simulation result on this configuration is shown in Figure 6.18. In this mission, the REHS harvest energy from both wind and solar resources to supply power to the renewable robot. The difference between the demand load and the power supply is unmet power shown below. Unmet power in this mission using the configuration designed by the optimisation method is zero. The optimisation algorithm can effectively find the configuration with higher power supply availability with LPSP at zero.

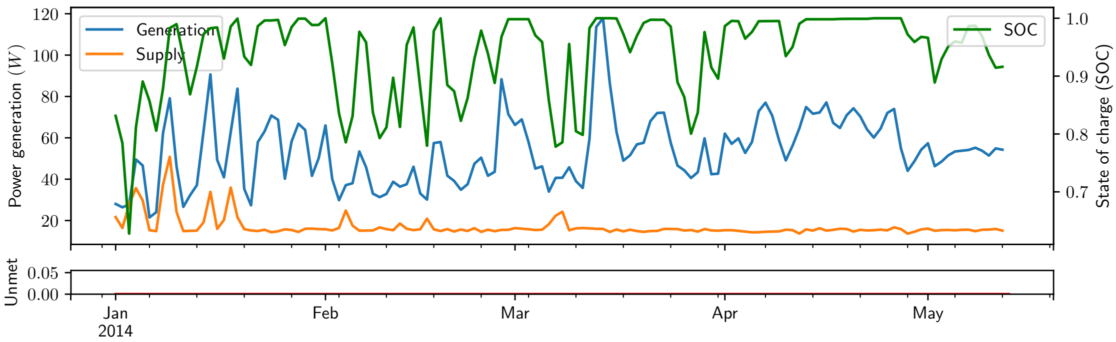

FIGURE 6.18: Power generation and supply to the system

Due to the discounted cost on the LPSP in the mixed objectives fitness function is zero, the resulting REHS is also a cost-effective configuration to achieve long-term power supply reliability. This can be also confirmed by the convergence in the global and personal best during the optimisation.

6.4 Robust management strategy learning

The robustness of the configuration is simulated using the same REHS configuration on different meteorological years. Since the REHS configuration is optimised for the mission started in 2014, the design scenario stays at zero LPSP. The 20 years long power simulation shows such configuration could maintain the zero LPSP in most years. However, in the year of 2003, the REHS configuration failed to supply enough power to the renewable robot on some occasion, resulting in a small LPSP in the last 20 years.

The variance in the power generation and the demand load challenges the long-term power supply robustness. Power generation from wind and solar resource on the same route but a different meteorological year has been shown in Figure 6.19.

When there is a change in the power generation or demand load, the default demand load follow (DLF) strategy can't adjust the power usage for long-term power supply reliability. The lost in the power supply would delay the journey of ASV or even threaten the safe operation of the vehicle. In order to tackle this problem, the learning-based power management strategy is trained for the ASV's long-term operation. This strategy uses the meteorological data and the model of the REHS as an input to train a reinforcement learning agent. The trained agent could learn to plan the power usage based on the observation in power generation, demand load and battery energy level.

In the dynamic power management environment, the power management strategy is trained using Algorithm 4. The reward function on the power supply is Equation 6.4.

$$r(t) = \begin{cases} 20 + \min[0.1[S(t) - P_c(t)], 20] & S(t) \geq P_c(t) \\ -500 & S(t) < P_c(t) \end{cases} \tag{6.4}$$

where $P_c(t)$ is the critical load and $S(t)$ is the REHS power supply.

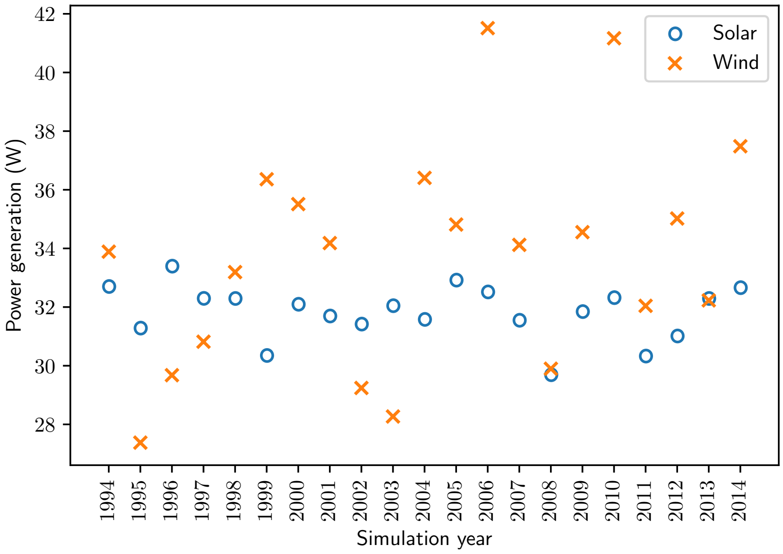

FIGURE 6.19: Multiple year power generation using the designed configuration

The reward function will give a fixed reward to the power management strategy for critical load. If the power management strategy fail to supply power at least for critical load, a negative penalty will be applied. The further reward can be claimed if the extra power is supplied for the performance-related load. However, the maximum extra reward is capped at the same as the critical load to avoid excessive use of energy in purist of extra reward.

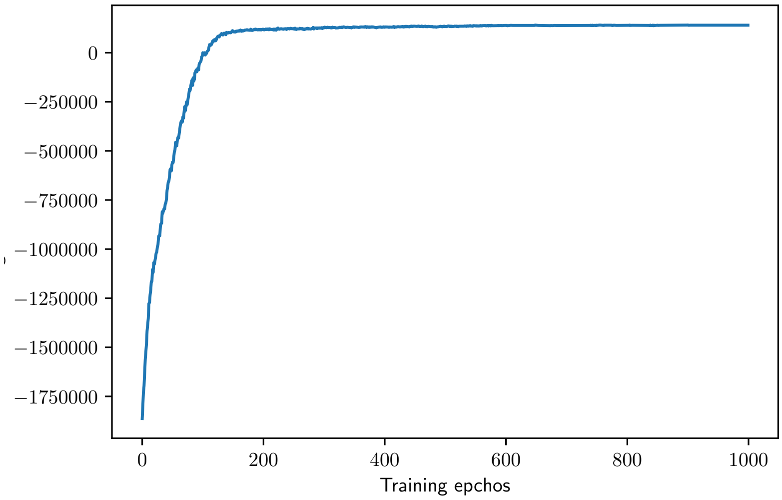

FIGURE 6.20: Averaged total reward during the training

Power management strategy training uses the renewable energy resource data and the system configuration on the year of 2014. The averaged total reward in the learning process has been shown in Figure 6.20. As the agent interacts with the environment, the total reward gradually increased from negative to a positive value and the steady-state is found after 200 training epochs.

The learnt power management strategy at 1000 epochs are used to post simulate the performance on the design scenario. REHS simulation result in using the learning-based power management strategy on the design year 2014 is shown in Figure 6.21.

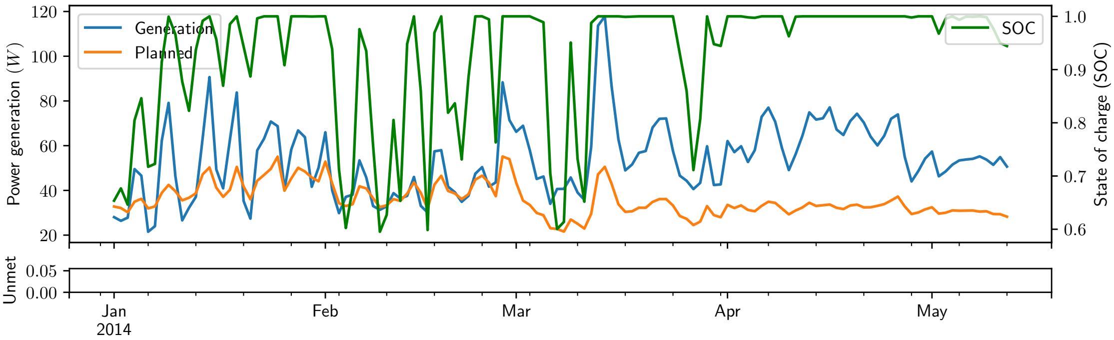

FIGURE 6.21: Power management result on reinforcement learning method

Both strategies managed to plan the power usage for a reliable long-term power supply in the design scenario. Compare to the DLF strategy, the RL strategy is more aggressive when there is abundant power generation. The state of discharge also shows the RL strategy discharge deeper than the DLF for a better power management efficiency.

The learnt power management strategy could not only plan the power usage for the year of 2014 but also improve the power supply quality on the mission on the year of 2003. Power management trained by the meteorological data from the mission 2014 is simulated with the mission started in 2003 using the exact same configuration. Simulation result including the power generation, load demand and the critical load unmet are shown in Figure 6.23.

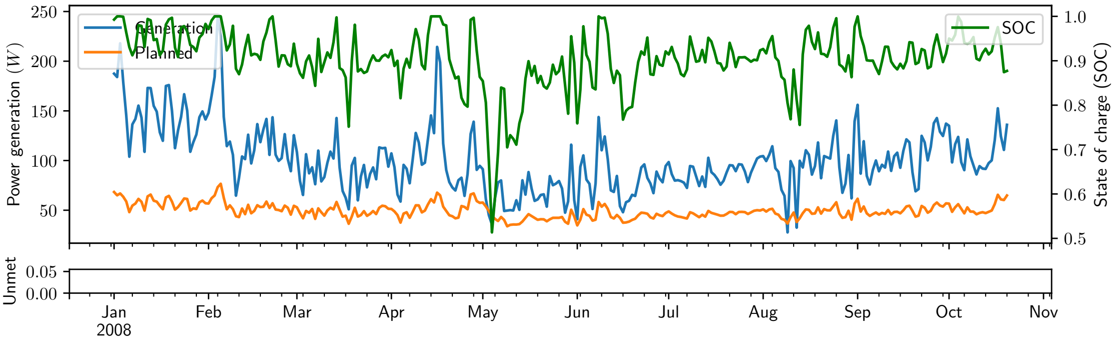

FIGURE 6.22: Power management result on reinforcement learning method

What stands out in is the power management strategy is able to plan the power usage for a reliable power supply despite relying on a highly variable renewable energy resource. The trained power management strategy guaranteed the minimal power supply to the critical load during the mission by reinforcement learning. This power management strategy recognise the type of demand load and prioritise critical load. Critical load unmet ratio shows that the DLF has a chance to lost the critical power supply while RL strategy maintained a zero in the last 20 years.

RL based power management strategy maintains the zero critical loads unmet ratio in the last 20 years. The power usage planed by the DLF and RL are simulated and presented in Figure 6.23 and Figure 6.24.

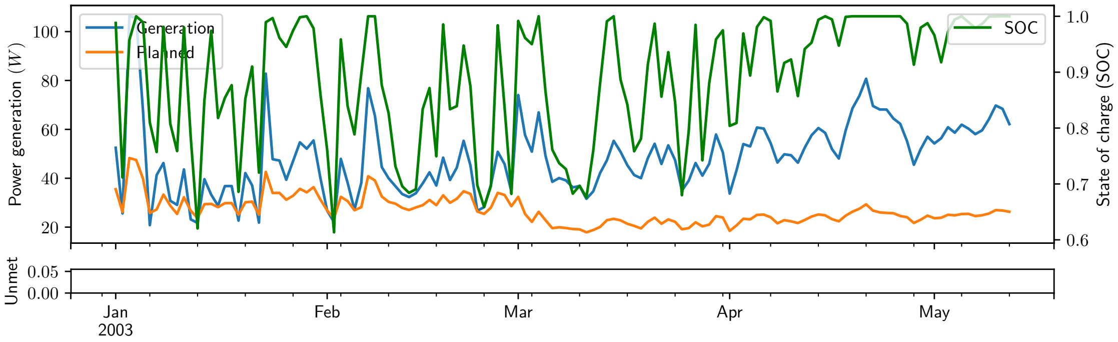

FIGURE 6.23: Power management result on reinforcement learning (RL) method

Figure 6.23 shows the power system simulation result in 2003. While the DLF strategy (shown in Figure 6.24) has a loss in the critical load supply in the year of 2003 if the same configuration is used. This long-term robustness in power management guarantees the safe operation of the renewable robot when the power generation or the demand load deviates from the initial design scenario. Power management learnt to plan the power usage from the training data from the design scenario and adjust the performance-related and critical load for the best compromise between reliability and power conversion efficiency.

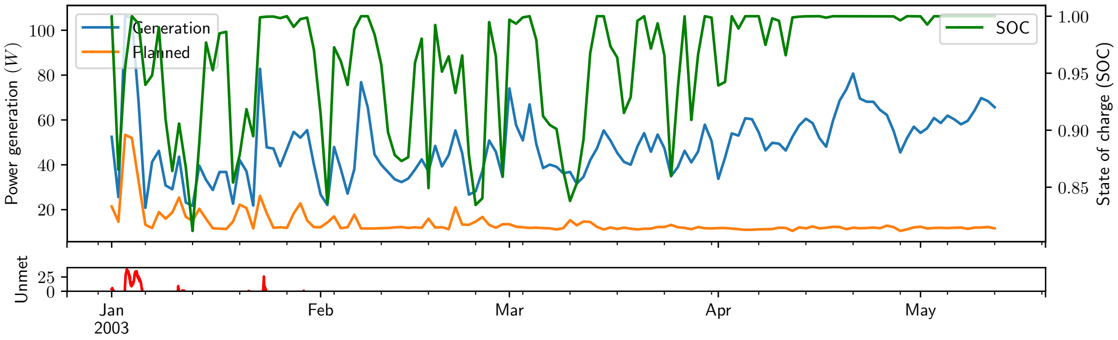

FIGURE 6.24: Power management result on demand load follow (DLF) method

On the other hand, the DLF simply follows the demand load to plan the power usage as the full propulsion load and the hotel load. When there is a shortage in the power generation, the DLF strategy does not change the plan. In early January, the lost power supply happened soon after the demand load increase due to the changing wind direction increases the power generation. RL strategy solves the 10 to 25 watts power supply shortage by reducing the performance-related load beforehand. Such a strategy helped the robot to maintain the power supply on critical load for the safe operation.

GAF aggressively use the power generated in time so the averaged power supply is the highest among all methods. The drawback on this method is that the requirement from the demand load side is neglected so the critical load can't be supplied when the power generation isn't sufficient. As a result, the total reward is worst in all methods.

Exponentially weighted moving averaged (EWMA) method does not perform well on the power management problem compare to the RL method. EWMA is a resource side power management strategy, it plans the usage of the power system with the knowledge on the power generation.

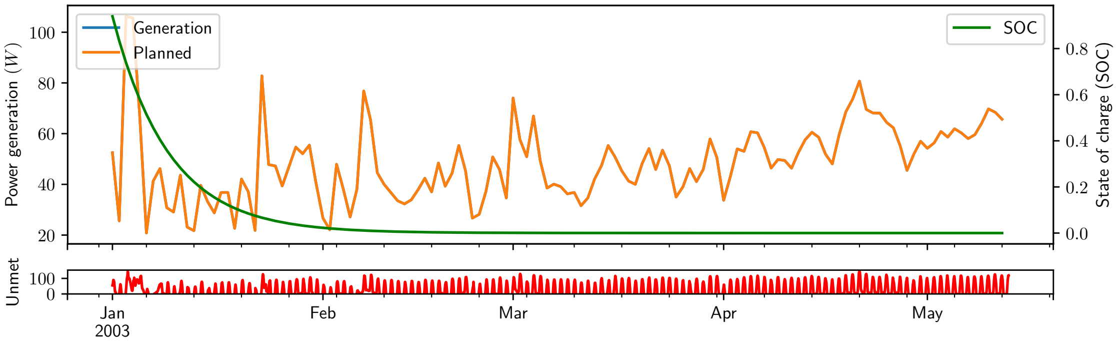

FIGURE 6.25: Power management result on generation absolute follow (GAF) method

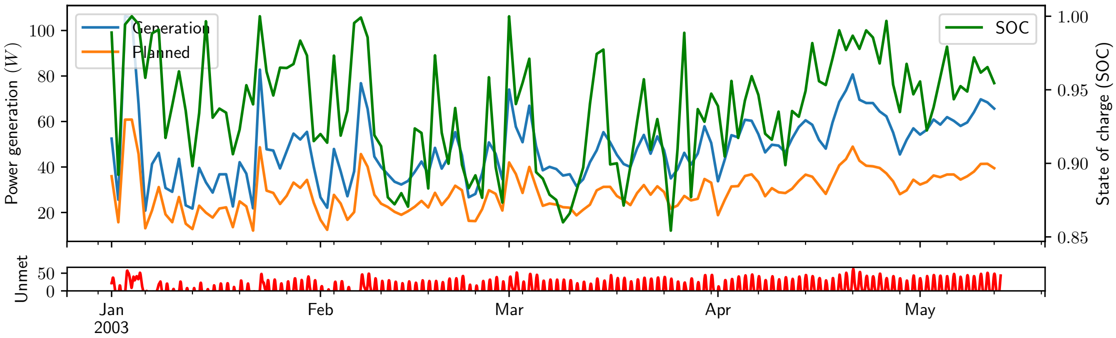

FIGURE 6.26: Power management result on EWMA method

The unmet power supply and SOC illustrated in Figure 6.26 shows the method can't mitigate the fluctuation in power generation and response to the changes in renewable energy resources from year to year.

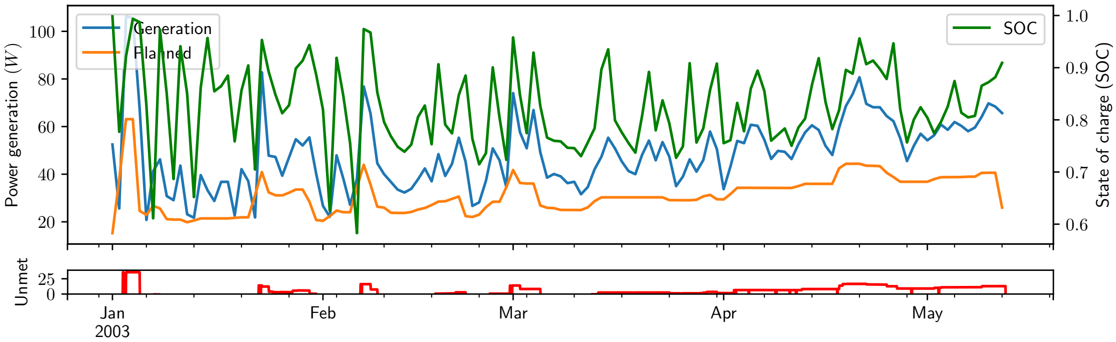

FIGURE 6.27: Power management result on global finite horizon (GFH) method

Global finite horizon (GFH) optimal power management strategy plans the power usage with prior global knowledge on renewable energy resources. The aim of such design is to maximise the total energy usage while maintaining the energy in the battery above minimal level. Similar to EWMA, GFH is also a resource side power management strategy that plans on the power generation based on power generation. What makes it different is this method also work on the battery energy level. One disadvantage of GFH is the idea of maximising the total output during the journey would aggressive plan the power usage for the robot. It achieves a higher averaged power supply level on the cost of failure to supply critical load.

Table 6.7: Power management baseline comparison

	GAF	DLF	EWMA	GFH	RL
Total reward	-139359	58033	10189	12258	84571
Critical load unmet	0.209	0.001	0.145	0.015	0.000
Averaged reward	-81.30	19.81	-50.29	17.37	26.78
Minimum power supply	0.00	0.00	0.43	0.00	22.03
Averaged power supply	51.90	17.40	40.58	42.30	33.45
Std on power supply	109.97	6.34	51.10	18.34	17.71

A summary on the power supply quality is listed in Table 6.7. The total reward, time on the ratio of critical load unmet, averaged reward, minimum power supply, averaged power supply and standard deviation on the power supply of different approaches are presented.

Compared with other baseline power management strategies including DLF, GAF, EWMA and GFH, the RL based power management system achieved the best compromise between the energy conversion efficiency and the long-term power supply reliability. The averaged power supply plan by the power management strategy lower than the other but the critical load can be met.

The resulting power management strategy could be saved as a neural network model for the micro-controller of the renewable robot to plan power usage in the future. Up to this point, a complete design including the REHS configuration and the long-term robust power management strategy have been prepared for the renewable robot's operation. The unified simulation, design and management approach taken in this case study shows the method could help to plan the best capacity of the REHS and maintain the long-term power supply reliability for the robot despite relying on highly variable renewable energy resources.

Chapter 7

Conclusions and recommendations

7.1 Conclusions

The purpose of this study was to develop a methodology to design the renewable energy harvesting system for maritime mobile robots. This dissertation contributes to the area of the energy autonomy for maritime robotics systems. Specifically, it introduces a novel model, design and management methods to the hybrid renewable energy system for self-sustained robots. The primary objective of this dissertation is to develop a general methodology to support the operation of renewable energy powered robots in the whole life cycle. Three parts of work were carried out on the major challenges in using renewable energy system on a moving system:

- Power system simulation with the inclusion of global and local motion of the robot.
- System configuration design optimisation under a size constraint.
- Dynamic power management strategy for a guaranteed critical power supply.

The results of this study indicate that both global and local motion has an impact on the power generation and demand load of renewable robots. Global motion has a significant influence the power generation from the renewable resource side and the demand load on the propulsion load. As the robot travels, the uncertainty and variance in the renewable resources exhibit both temporally and spatially. The local motion of the robot also affects the power generation and demand load. Solar power generation on the robot degraded when there is a large periodic roll and pitch motion. For a small local motion, less than 5% of reduction in solar power generation is found on a flat solar panel. Wind power generation has to include energy consumption that counterbalances the wind turbine added resistance. The wind power generation could be negative if the speed of the robot is much higher than the wind. It is not feasible to install a wind turbine on the robot that cruising speed is higher than the wind speed. The data-driven simulation method takes both global and local motion of the renewable robot into account. Simulation on the power generation, demand load and the battery system is able to suggest the potential reliability and economic performance of the robot at a given mission. The performance of the robot heavily depends on the mission and the configuration of the REHS.

- Global motion influence the power generation from the resource side.
- Global motion also influences the demand load on the propulsion part.
- Solar power generation is sensitive to the local motion.
  - The pitch and roll motion has an impact on the power generation.
  - A larger amplitude of the motion will introduce a greater reduction in solar power generation.
- Wind power generation is sensitive to the wind speed as well as the direction.
  - Wind from the opposite direction of the robot will require additional power to counterbalance the wind resistance.
  - Wind from the same direction of the robot could save propulsion power.
  - Robot with cruising speed higher than the wind speed does not benefit from harvesting wind energy at all as the resistance discount is higher than the harvested power,
- Solar and wind resources have limited energy density compared to conventional stored energy solutions but its advantage in its sustainability.
- Data-driven simulation is able to include all these factors in the power system simulation on a renewable robot.

REHS on the renewable robot has a hard size constraint on the devices. Limited space on the renewable robot is the key challenge to the reliability of the power supply. The hybrid configuration that uses multiple resources at the same time could help to increase total energy density. However, the maximum power generation is limited by the size of the wind turbine and solar panel. Under the size constraint, the multiple objectives optimisation can find the best reliability and economic performance of the REHS for the robot using the data-driven simulation. The REHS design optimisation suggests a configuration with a tradeoff between cost and reliability. If there is a configuration achieved zero lost power during the mission, the mixed objectives optimisation method could further improve the economic performance of the configuration at the given mission. Multiple design cases show that the configuration is optimally designed for both reliability and economic performance under the size constraint.

- Power generation on the REHS is limited by the energy density and the devices size constraint.
- Hybrid system increases the space utility by harvesting multiple resources together.
- Under the size constraint, the multiple objectives optimisation could find the best reliability and economic performance of the REHS on a given mission.
- If the optimisation result suggests there is no configuration achieved a zero LPSP, the multiple objectives optimisation method suggest the configuration with the tradeoff between cost and reliability.

- If the optimisation result suggests there is a configuration achieved a zero LPSP, the mixed objectives optimisation method could further improve the economic performance without scarifying the reliability performance.

Despite the effort in modelling the global and local motion in the power system, the uncertainty in the power generation and demand load still pose a huge challenge to the long term reliability. Long term reliability performance study shows the optimal configuration designed for a specific mission has a risk in the lost power supply for another mission. Conventional power management strategies struggle to adjust the power supply for a guaranteed minimum level of power supply. The learning-based power management strategy solves this challenge by exploiting the historical pattern for the future operation scenario.

- For the renewable robot depends on the function of the demand load. There is a critical load that always to be supplied and performance-related load that improve the service quality if additional power is supplied.
- The power management for the renewable is to minimise the risk of loss of critical load whenever is possible.
- Conventional power management strategies are limited by some of the assumptions on the REHS:
  - The Demand Load Follow (DLF) strategy is ideal for the renewable energy system without size constraint that the power generator can always be designed to match the demand load.
  - The Generation Absolute Follow (GAF) strategy is suitable for the applications with limited power generation and no minimal power supply level requirement.
  - The Exponential Weighted Moving Averaging (EWMA) strategy assumes a repeated temporal pattern in the power generation while the spatial-temporal nature of the renewable robot makes it hard to find such a pattern.
  - The Global Finite Horizon (GFH) optimal strategy assumes a full knowledge into the future which is not usually available for the power management system before the deployment of the robot.
- Learning-based power management could incrementally learn the power generation, demand load and battery energy pattern on a given mission.
- The learnt power management strategy outperform four baseline strategies in terms of the least critical load unmet ratio.

In general, the research shows that renewable energy is capable of supporting the power system of the robot for a fully autonomous operation if there are sufficient renewable resources. Since the power generation is influenced by both global and local motion of the robot, the mission is the key factor to determine whether it is possible to fully supply the power to the robot. On the demand load side, propulsion load is also subject to the spatial-temporal operation condition such as wind, wave and current. The renewable energy power system has to match the demand load and the power generation under the strict size constraint. It is not always possible to design configuration for a reliable power supply. However, if there is a configuration could fully support the robot from renewable resources, the economic performance can also be expected. The renewable robot with a guaranteed reliability and cost performance for a given mission is well sought after among all the feasible designs.

The proposed REHS design method could find such a configuration for the renewable robot. Two steps optimisation firstly search the design space for the best possible reliability performance and then optimise the cost at the same time. Resulting configuration is the best REHS design for a given mission. The challenge is that the mission is spatial-temporal dependent. Reliability performance does not guarantee the future will exhibit the same pattern in power generation and demand load. When any of them is different from the design scenario, the power management strategy shall dynamically plan the power usage according to energy availability. This can be done on the renewable robot because the demand load consist of a critical and performance-related load. In the worst case, the performance-related can be reduced to save energy for the future critical load. Learning-based power management strategy plans the power usage based on the type of demand load using historical data. The power management strategy improves the reliability performance to guarantee a minimal power supply for the critical load.

7.2 Further work suggestions

This work can only be viewed as the beginning of the studies on the REHS for robots. Many new areas and research questions await to be explored, and some points worth to further investigate. Future work along these ideas will deepen the understanding of REHS on the moving system.

In Chapter 3, the moving REHS model addressed the issue of power system simulation under global and local motion. This power generator model was obtained from the two most common renewable energy resources – wind and solar energy. Additional renewable energy resource could be added as the harvesting source for more power generations. Besides, due to the long term historical data on the renewable energy generators, the degradation of those generators is neglected in the model. A future long term experiment on the power generator performance would help the model to better account the change in power conversion efficiency.

Renewable energy system configuration design in Chapter 4 is focused on the power system itself. Hence, the key design variables are the size of renewable energy devices. The mission of the robot plays a significant role in the reliability performance as both power generation and demand load are determined by location and time of the robot. An optimisation on the mission for the robot could improve the performance of the power system through route planning. One possible improvement to use optimisation based method to decide the best start time and cruising speed to minimise the risk of lost power supply. Another direction is to optimise the route to take advantage of environmental factors such as wind and ocean current.

Concerning the power management strategy proposed in Chapter 5, the control algorithm is an inference neural network model that pre-trained from historical data. The strategy was learnt offline due to the limit of power consumption on the embedded system. In the future, such a strategy could be learnt offline first and update in situ. The online learning would allow the power management strategy to adopt the change in power generation and/or demand load autonomously.

The renewable energy system has already been used for many robotics application to partially support the energy demand. With further improvement in the power generators efficiency, mission planning strategy and the online learning power management strategy, the fully autonomous robot is expected to extend its duration and ultimately achieve an unlimited operation in the field.

7.3 Major contribution

Chapter 3 present the moving renewable energy power system model and the data-driven simulation method. As part of the development, the model method laid the foundation in the non-stationary renewable energy system. It is important to acknowledge that much of the motivation for the work is for the robotics applications. However, it is equally important to understand many of the results and methods are not limited to the robots. The first result is surprising: due to the local motion, the wind turbine may consume rather than generate energy for specific wind directions. The local motion would also reduce the power generation on the solar panel if there is a large-amplitude pitch and roll motion. Non-stationary power system simulation includes both factors as none of the existing model considered them.

This foundation is complemented by the REHS configuration design under a size constraint. Chapter 4 contributes to the design optimisation methods for the renewable energy powered robot based on the non-stationary model. While there is a method to deal with the design challenge for stationary application, a concrete design method to explore and optimise the non-stationary application with strict size constraint is still missing. As part of the study, the trade-offs and design considerations are presented. The two steps exploration and optimisation method offers a novel design technique to find a cost-effective and reliable REHS configuration. The proposed design optimisation method is able to the suggest the most economic configuration for a given reliability requirement. Moreover, the optimality, feasibility and long-term robustness were evaluated for the first time using historical data. Both optimality and feasibility have been confirmed in the design case but the 20 years long data-driven simulation is disappointing that the configuration would suffer a reliability issue in a longer-term.

As a response to this issue, Chapter 5 focuses on the power management strategy for the long term power supply reliability. Since the robot has both critical load that always have to be supplied and performance-related load that can be adjusted, the power management strategy could dynamically plan the power usage to avoid a complete loss of power supply. However, conventional power management strategies are unable to prioritise the supply of energy depends on the type of load. Using the learning-based strategy with a reward to encourage a minimal level power supply to the critical load, the proposed power management strategy could improve its performance through unsupervised learning from historical data. The result shows the long-term performance in supplying a minimal level power system can be achieved at a cost of slightly lower power conversion efficiency.

As a final remark, the major contribution of the work is derived from the sustainability in the renewable energy systems. Power supply from a renewable energy system on space limited system subject to global and local motion is the main challenge to its reliability and economic performance. This dissertation provides insight on key aspects of the system model, presents a better understanding of configuration design and introduces a novel management strategy for long term operation. The whole life cycle from the simulation to the design and the operation is enabled by the methods with the supporting open source software implementations.

Appendix A

Additional material

A.1 Solar model derivation and Mathematica notebook

Solar angle using 3 factors solar vectors:

$$\cos(\Theta_s) = \mathbf{S}_{\mathrm{enu}} \cdot \mathbf{n}_{\mathrm{enu}} \tag{A.1}$$

With 3 factors solar vector, solar angle on a tilt surface of solar panel is:

$$\begin{aligned}
\cos(\Theta_s) &= \mathbf{S}_{\mathrm{enu}} \cdot \mathbf{n}_{\mathrm{enu}} \\
&= \begin{bmatrix} -\cos(\delta)\sin(\omega) \\ \sin(\delta)\cos(\phi) - \cos(\delta)\cos(\omega)\sin(\phi) \\ \cos(\delta)\cos(\omega)\cos(\phi) + \sin(\delta)\sin(\phi) \end{bmatrix} \cdot \begin{bmatrix} \sin(\alpha_s)\sin(\beta_s) \\ \cos(\alpha_s)\sin\beta_s) \\ \cos(\beta_s) \end{bmatrix} \\
&= -\cos(\delta)\sin(\omega)\sin(\alpha_s)\sin(\beta_s) - \cos(\delta)\cos(\omega)\sin(\phi)\cos(\alpha_s)\sin(\beta_s) \\
&\quad + \sin(\delta)\cos(\phi)\cos(\alpha_s)\sin(\beta_s) + \cos(\delta)\cos(\omega)\cos(\phi)\cos(\beta_s) \\
&\quad + \sin(\delta)\sin(\phi)\cos(\beta_s)
\end{aligned} \tag{A.2}$$

Norm vector of tilt surface on moving system:

$$\mathbf{n}_{\mathrm{enu}}^{'} = \mathbf{R}_x(p)\mathbf{R}_y(q)\mathbf{R}_z(r)\mathbf{n}_{\mathrm{enu}} \tag{A.3}$$

Full rotation matrix $\mathbf{R}_x(p)\mathbf{R}_y(q)\mathbf{R}_z(r)$ in east-north-up reference system is:

$$\begin{bmatrix} \cos(q)\cos(r) & -\cos(q)\sin(r) & \sin(q) \\ \cos(r)\sin(p)\sin(q)+\cos(p)\sin(r) & \cos(p)\cos(r)-\sin(p)\sin(q)\sin(r) & -\cos(q)\sin(p) \\ \sin(p)\sin(r)-\cos(p)\cos(r)\sin(q) & \cos(r)\sin(p)+\cos(p)\sin(q)\sin(r) & \cos(p)\cos(q) \end{bmatrix} \tag{A.4}$$

$$\begin{aligned}\mathbf{n}^{'}_{\text{enu}} &= \mathbf{R}_x(p)\mathbf{R}_y(q)\mathbf{R}_z(r)\mathbf{n}_{\text{enu}} \\ &= \begin{bmatrix} \cos(q)\cos(r) & -\cos(q)\sin(r) & \sin(q) \\ \cos(r)\sin(p)\sin(q)+\cos(p)\sin(r) & \cos(p)\cos(r)-\sin(p)\sin(q)\sin(r) & -\cos(q)\sin(p) \\ \sin(p)\sin(r)-\cos(p)\cos(r)\sin(q) & \cos(r)\sin(p)+\cos(p)\sin(q)\sin(r) & \cos(p)\cos(q) \end{bmatrix} \\ &\cdot \begin{bmatrix} \sin(\alpha_s)\sin(\beta_s) \\ \cos(\alpha_s)\sin\beta_s) \\ \cos(\beta_s) \end{bmatrix}\end{aligned} \tag{A.5}$$

let

$$\mathbf{n}^{'}_{\text{enu}} = \begin{bmatrix} a & b & c \end{bmatrix}^T \tag{A.6}$$

then

$$\begin{aligned} a &= -\cos(q)\sin(r)\cos(\alpha_s)\sin(\beta_s) + \cos(q)\cos(r)\sin(\alpha_s)\sin(\beta_s) + \sin(q)\cos(\beta_s) \\ b &= \cos(\alpha_s)\sin(\beta_s)(\cos(p)\cos(r) - \sin(p)\sin(q)\sin(r)) + \sin(\alpha_s)\sin(\beta_s)(\sin(p)\sin(q)\cos(r) \\ &\quad + \cos(p)\sin(r)) + \sin(p)(-\cos(q))\cos(\beta_s) \\ c &= \cos(\alpha_s)\sin(\beta_s)(\cos(p)\sin(q)\sin(r) + \sin(p)\cos(r)) + \sin(\alpha_s)\sin(\beta_s)(\sin(p)\sin(r) \\ &\quad - \cos(p)\sin(q)\cos(r)) + \cos(p)\cos(q)\cos(\beta_s) \end{aligned}$$

Solar angle on a moving tilt surface is:

$$\cos(\Theta_s) = \mathbf{S}_{\text{enu}} \cdot \mathbf{n}^{'}_{\text{enu}} \tag{A.7}$$

With 2 factors solar vector, solar angle is:

$$\begin{aligned} \cos(\Theta_s) &= \mathbf{S}_{\text{enu}} \cdot \mathbf{n}^{'}_{\text{enu}} \\ &= \begin{bmatrix} \cos(\alpha)\sin(A) \\ \cos(\alpha)\cos(A) \\ \sin(\alpha) \end{bmatrix} \cdot \begin{bmatrix} a \\ b \\ c \end{bmatrix} \\ &= a\cos(\alpha)\sin(A) + b\cos(\alpha)\cos(A) + c\sin(\alpha) \end{aligned} \tag{A.8}$$

Purpose of this notebook:

Solar geometry is important for the estimation of power production using photovoltaic technology. The derivation of the geometric relationship need to deal with different notation at different reference framework. This is a non-trivial work and the common derivation are prone to sign issue and lead to a wrong result. Also, different literature tends to use different notation system that may not consistent at all. This notebook present a way to deal with this issue by mathematical vector analysis tool and computer science technique in functional programming and symbolic computation.

Solar geometry:
Our planet Earth orbit around the Sun in a slightly elliptical pattern during the year.

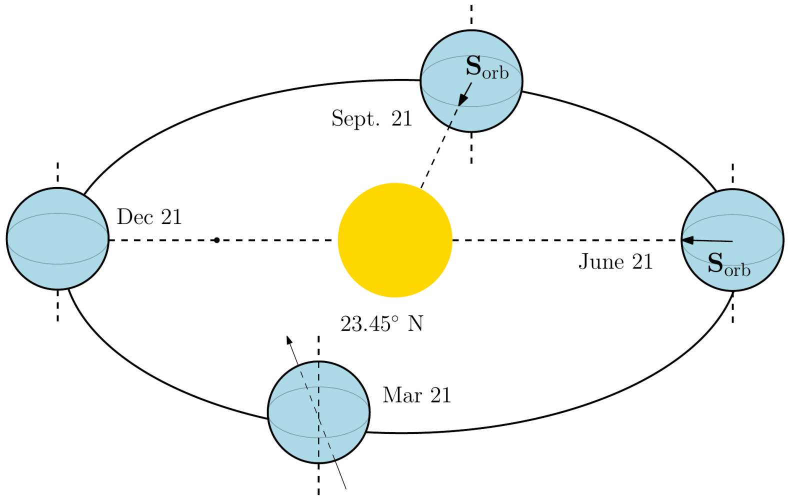

Orbit frame to earth fixed frame

In the solar system, we can regard the elliptical orbit as a circle. At any time in the year, there is always a horizontal plane (the one other than the gray) shown in the figure always facing toward the sun. It is easy to use just a single arrow point from the center of Earth to the Sun at unit length.

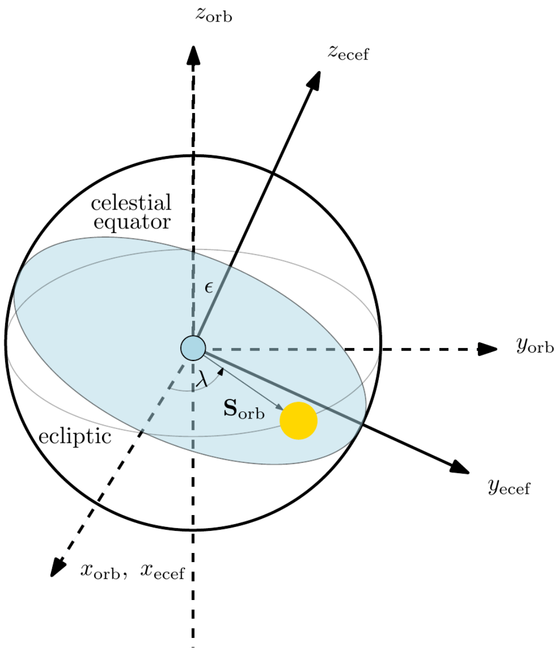

In orbit frame (x’y’z’), the ecliptic longitude λ varies between 0 to 360 degrees.

Ecliptic longitude give us some insight about the solar radiation on the Earth but it is too general to let us know any information about the the exactly position of solar if we stand on the Earth. This is because it is a orbit reference system. To what we usually know on Earth, longitude, latitude, we need to convert those system into our known coordinate system. First step is to convert orbit frame into a earth centered earth fixed system. (ECEF)

The virtual plane that always face to sun is ecliptic, on earth we use celestial equator as the center plane. This could be treat as a virtual rotation between ecliptic plane and celestial plane. The rotation is pretty straightforward, grab the plane rotation along x axis by ϵ and now we are getting more with this summer and winter planet. In this process, the relative direction between Earth and Sun haven’t

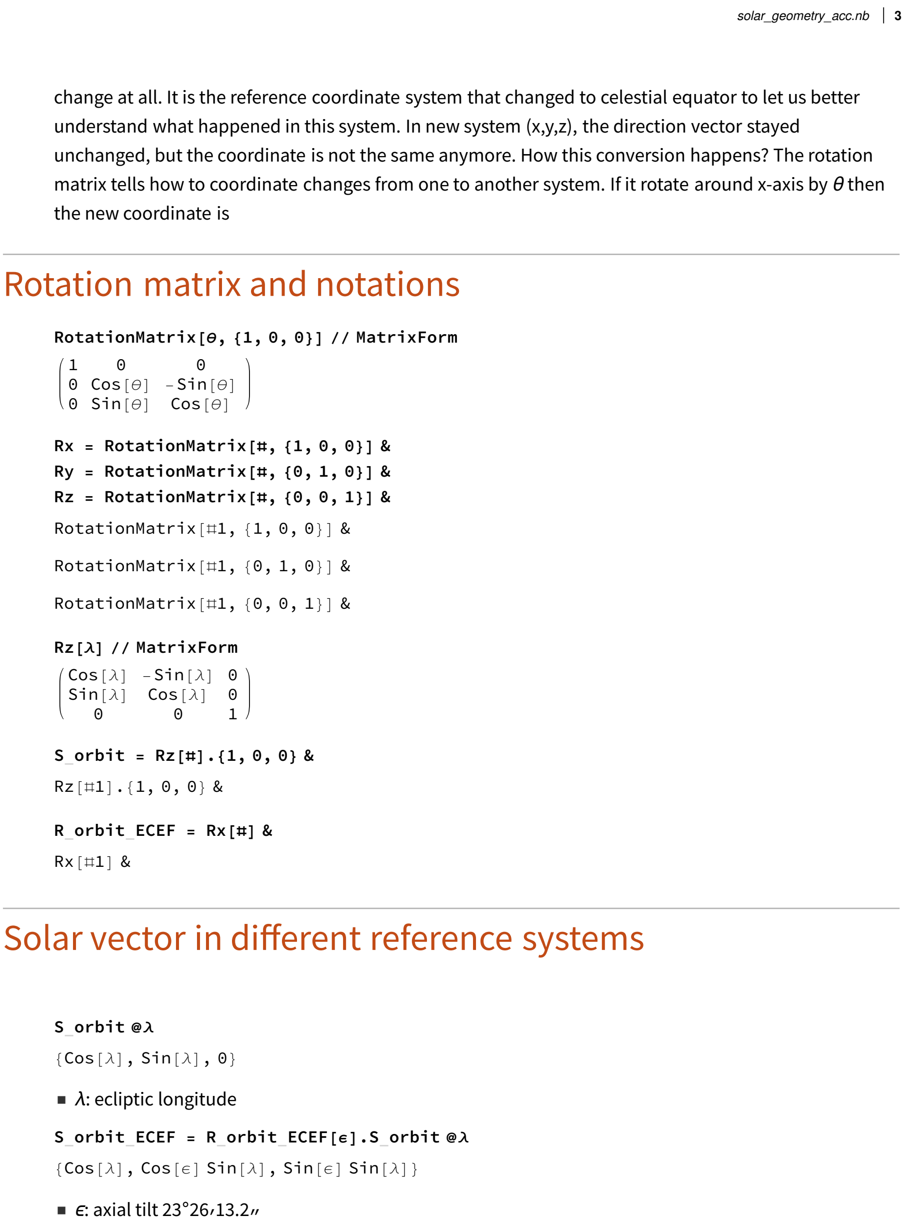

change at all. It is the reference coordinate system that changed to celestial equator to let us better understand what happened in this system. In new system (x,y,z), the direction vector stayed unchanged, but the coordinate is not the same anymore. How this conversion happens? The rotation matrix tells how to coordinate changes from one to another system. If it rotate around x-axis by θ then the new coordinate is

---

Rotation matrix and notations

```
RotationMatrix[θ, {1, 0, 0}] // MatrixForm
```

$$\begin{pmatrix} 1 & 0 & 0 \\ 0 & \mathrm{Cos}[\theta] & -\mathrm{Sin}[\theta] \\ 0 & \mathrm{Sin}[\theta] & \mathrm{Cos}[\theta] \end{pmatrix}$$

```
Rx = RotationMatrix[#, {1, 0, 0}] &
Ry = RotationMatrix[#, {0, 1, 0}] &
Rz = RotationMatrix[#, {0, 0, 1}] &
```

```
RotationMatrix[#1, {1, 0, 0}] &

RotationMatrix[#1, {0, 1, 0}] &

RotationMatrix[#1, {0, 0, 1}] &
```

```
Rz[λ] // MatrixForm
```

$$\begin{pmatrix} \mathrm{Cos}[\lambda] & -\mathrm{Sin}[\lambda] & 0 \\ \mathrm{Sin}[\lambda] & \mathrm{Cos}[\lambda] & 0 \\ 0 & 0 & 1 \end{pmatrix}$$

```
S_orbit = Rz[#].{1, 0, 0} &
Rz[#1].{1, 0, 0} &
```

```
R_orbit_ECEF = Rx[#] &
Rx[#1] &
```

Solar vector in different reference systems

```
S_orbit @λ
{Cos[λ], Sin[λ], 0}
```

- λ: ecliptic longitude

```
S_orbit_ECEF = R_orbit_ECEF[ϵ].S_orbit @λ
{Cos[λ], Cos[ϵ] Sin[λ], Sin[ϵ] Sin[λ]}
```

- ϵ: axial tilt 23°26′13.2″

```
Print[MatrixForm[ R_orbit_ECEF@ ϵ], " x ", S_orbit @λ]
```

```
⎛1    0        0     ⎞
⎜0  Cos[ϵ]  -Sin[ϵ]  ⎟ x {Cos[λ], Sin[λ], 0}
⎝0  Sin[ϵ]   Cos[ϵ]  ⎠
```

```
S_ECEF = Rz[♯1].Ry[-♯2].{1, 0, 0} &
```

```
Rz[♯1].Ry[-♯2].{1, 0, 0} &
```

```
R_ECEF_ENU = (Rx @ - (Pi / 2 - ♯1)).( Rz@- (Pi / 2 + ♯2)) &
```

```
      ⎛π      ⎞         ⎛π      ⎞
Rx[- ⎜─ - ♯1 ⎟].Rz[- ⎜─ + ♯2 ⎟] &
      ⎝2      ⎠         ⎝2      ⎠
```

Ref at http://www.navipedia.net/index.php/Transformations_between_ECEF_and_ENU_coordinates

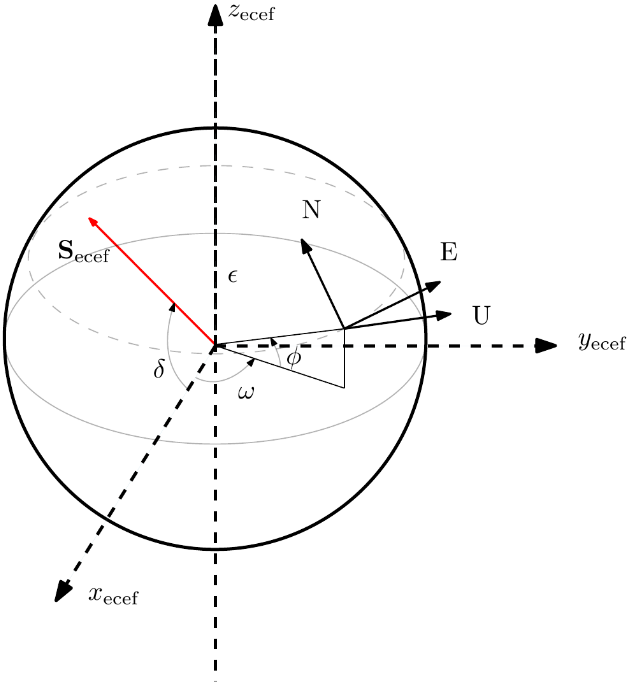

```
(Rz@-(Pi/2+ω)) // MatrixForm
```

```
⎛-Sin[ω]   Cos[ω]   0⎞
⎜-Cos[ω]  -Sin[ω]   0⎟
⎝   0        0      1⎠
```

```
R_ECEF_ENU[ϕ, ω] // MatrixForm
```

```
⎛     -Sin[ω]              Cos[ω]            0    ⎞
⎜-Cos[ω] Sin[ϕ]    -Sin[ϕ] Sin[ω]    Cos[ϕ]⎟
⎝ Cos[ϕ] Cos[ω]     Cos[ϕ] Sin[ω]    Sin[ϕ]⎠
```

- ϕ: longitude
- ω: hour angle

```
S_ECEF_rotate = Ry[-#].{1, 0, 0} &
```

```
Ry[-#1].{1, 0, 0} &
```

```
S_ENU_4 = R_ECEF_ENU[ϕ, ω].R_orbit_ECEF[ϵ].S_orbit@λ
```

```
{Cos[ϵ] Cos[ω] Sin[λ] - Cos[λ] Sin[ω],
 -Cos[λ] Cos[ω] Sin[ϕ] + Sin[λ] (Cos[ϕ] Sin[ϵ] - Cos[ϵ] Sin[ϕ] Sin[ω]),
 Cos[λ] Cos[ϕ] Cos[ω] + Sin[λ] (Sin[ϵ] Sin[ϕ] + Cos[ϵ] Cos[ϕ] Sin[ω])}
```

```
S_ENU_4 // MatrixForm
```

```
⎛                  Cos[ϵ] Cos[ω] Sin[λ] - Cos[λ] Sin[ω]                  ⎞
⎜-Cos[λ] Cos[ω] Sin[ϕ] + Sin[λ] (Cos[ϕ] Sin[ϵ] - Cos[ϵ] Sin[ϕ] Sin[ω])⎟
⎝ Cos[λ] Cos[ϕ] Cos[ω] + Sin[λ] (Sin[ϵ] Sin[ϕ] + Cos[ϵ] Cos[ϕ] Sin[ω])⎠
```

```
S_ENU_3 = R_ECEF_ENU[ϕ, ω].S_ECEF_rotate[δ]
```

```
{-Cos[δ] Sin[ω], Cos[ϕ] Sin[δ] - Cos[δ] Cos[ω] Sin[ϕ],
 Cos[δ] Cos[ϕ] Cos[ω] + Sin[δ] Sin[ϕ]}
```

```
n_NEU = Rz[-#1].Rx[-#2].Ry[#3].{0, 0, 1} &
```

```
Rz[-#1].Rx[-#2].Ry[#3].{0, 0, 1} &
```

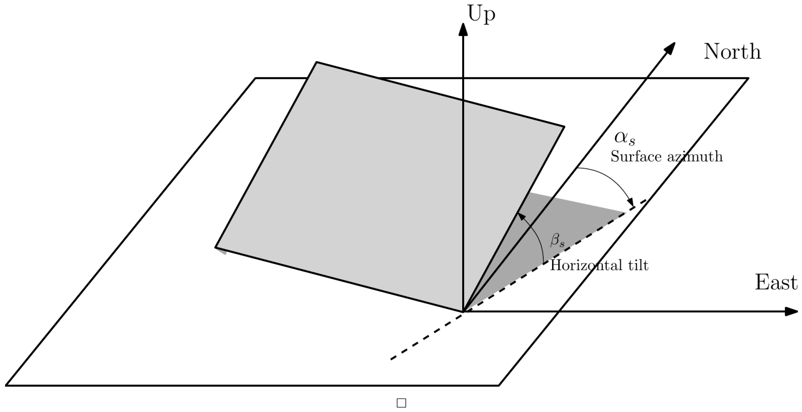

- α_s : surface azimuth
- β_s : horizontal tilt
- γ_s : vertical tilt

```
n_NEU[αs, βs, γs]
```

```
{Cos[γs] Sin[αs] Sin[βs] + Cos[αs] Sin[γs],
 Cos[αs] Cos[γs] Sin[βs] - Sin[αs] Sin[γs], Cos[βs] Cos[γs]}
```

```
n_NEU[αs, βs, 0]
```

```
{Sin[αs] Sin[βs], Cos[αs] Sin[βs], Cos[βs]}
```

```
Rx[α] // MatrixForm
```

$$\begin{pmatrix} 1 & 0 & 0 \\ 0 & \text{Cos}[\alpha] & -\text{Sin}[\alpha] \\ 0 & \text{Sin}[\alpha] & \text{Cos}[\alpha] \end{pmatrix}$$

```
n_NEU[αs, βs, 0].S_ENU_4 // Expand
```

```
Cos[λ] Cos[ϕ] Cos[ω] Cos[βs] + Cos[βs] Sin[ϵ] Sin[λ] Sin[ϕ] +
 Cos[ϵ] Cos[ϕ] Cos[βs] Sin[λ] Sin[ω] + Cos[ϕ] Cos[αs] Sin[ϵ] Sin[λ] Sin[βs] -
 Cos[λ] Cos[ω] Cos[αs] Sin[ϕ] Sin[βs] - Cos[ϵ] Cos[αs] Sin[λ] Sin[ϕ] Sin[ω] Sin[βs] +
 Cos[ϵ] Cos[ω] Sin[λ] Sin[αs] Sin[βs] - Cos[λ] Sin[ω] Sin[αs] Sin[βs]
```

```
n_NEU[αs, βs, 0].S_ENU_4 // FullSimplify
```

```
Cos[βs] (Cos[λ] Cos[ϕ] Cos[ω] + Sin[λ] (Sin[ϵ] Sin[ϕ] + Cos[ϵ] Cos[ϕ] Sin[ω])) +
 Cos[αs] (Cos[ϕ] Sin[ϵ] Sin[λ] - Sin[ϕ] (Cos[λ] Cos[ω] + Cos[ϵ] Sin[λ] Sin[ω])) Sin[βs] +
 (Cos[ϵ] Cos[ω] Sin[λ] - Cos[λ] Sin[ω]) Sin[αs] Sin[βs]
```

```
n_NEU[αs, βs, 0].S_ENU_3 // Expand
```

```
Cos[δ] Cos[ϕ] Cos[ω] Cos[βs] + Cos[βs] Sin[δ] Sin[ϕ] + Cos[ϕ] Cos[αs] Sin[δ] Sin[βs] -
 Cos[δ] Cos[ω] Cos[αs] Sin[ϕ] Sin[βs] - Cos[δ] Sin[ω] Sin[αs] Sin[βs]
```

```
n_NEU[αs, βs, 0].S_ENU_3 // FullSimplify
```

```
Cos[βs] (Cos[δ] Cos[ϕ] Cos[ω] + Sin[δ] Sin[ϕ]) +
 Cos[αs] (Cos[ϕ] Sin[δ] - Cos[δ] Cos[ω] Sin[ϕ]) Sin[βs] - Cos[δ] Sin[ω] Sin[αs] Sin[βs]
```

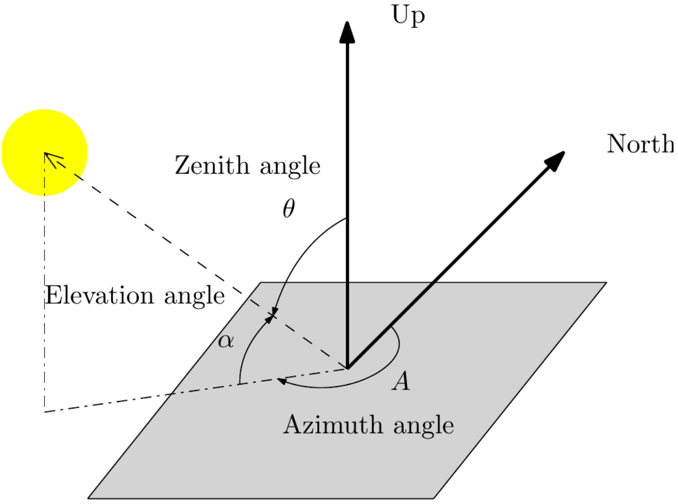

A : Azimuth angle

α : Elevation angle

```
S_ENU_2 = Rz[-A].Rx[α].{0, 1, 0}
```

```
{Cos[α] Sin[A], Cos[A] Cos[α], Sin[α]}
```

```
n_NEU[αs, βs, 0].S_ENU_2 // Expand
```

```
Cos[βs] Sin[α] + Cos[A] Cos[α] Cos[αs] Sin[βs] + Cos[α] Sin[A] Sin[αs] Sin[βs]
```

```
n_NEU[αs, βs, 0].S_ENU_2 // FullSimplify
```

```
Cos[βs] Sin[α] + Cos[α] Cos[A - αs] Sin[βs]
```

```
Rx[p].Ry[q].Rz[r].n_NEU[αs, βs, 0] // MatrixForm
```

```
(                     Cos[βs] Sin[q] - Cos[q] Cos[αs] Sin[r] Sin[βs] + Cos[q] Cos[r] Sin[αs] Sin[βs]                      )
(-Cos[q] Cos[βs] Sin[p] + Cos[αs] (Cos[p] Cos[r] - Sin[p] Sin[q] Sin[r]) Sin[βs] + (Cos[r] Sin[p] Sin[q] + Cos[p] Sin[r]) Sin[αs] Sin[βs] )
(Cos[p] Cos[q] Cos[βs] + Cos[αs] (Cos[r] Sin[p] + Cos[p] Sin[q] Sin[r]) Sin[βs] + (-Cos[p] Cos[r] Sin[q] + Sin[p] Sin[r]) Sin[αs] Sin[βs] )
```

```
(Rx[p].Ry[q].Rz[r].n_NEU[αs, βs, 0] // MatrixForm) /. {αs → 0, βs → 0}
```

```
⎛      Sin[q]     ⎞
⎜ -Cos[q] Sin[p]  ⎟
⎝  Cos[p] Cos[q]  ⎠
```

```
Rx[p].Ry[q].Rz[r].n_NEU[αs, βs, 0] .S_rotate_ENU
```

```
{Cos[βs] Sin[q] - Cos[q] Cos[αs] Sin[r] Sin[βs] + Cos[q] Cos[r] Sin[αs] Sin[βs],
  -Cos[q] Cos[βs] Sin[p] + Cos[αs] (Cos[p] Cos[r] - Sin[p] Sin[q] Sin[r]) Sin[βs] +
   (Cos[r] Sin[p] Sin[q] + Cos[p] Sin[r]) Sin[αs] Sin[βs],
  Cos[p] Cos[q] Cos[βs] + Cos[αs] (Cos[r] Sin[p] + Cos[p] Sin[q] Sin[r]) Sin[βs] +
   (-Cos[p] Cos[r] Sin[q] + Sin[p] Sin[r]) Sin[αs] Sin[βs]}.S_rotate_ENU
```

```
solarangle = Rx[p].Ry[q].Rz[r].n_NEU[αs, βs, 0].S_ENU_2
```

```
Cos[α] Sin[A]
  (Cos[βs] Sin[q] - Cos[q] Cos[αs] Sin[r] Sin[βs] + Cos[q] Cos[r] Sin[αs] Sin[βs]) +
 Cos[A] Cos[α] (-Cos[q] Cos[βs] Sin[p] + Cos[αs] (Cos[p] Cos[r] - Sin[p] Sin[q] Sin[r])
      Sin[βs] + (Cos[r] Sin[p] Sin[q] + Cos[p] Sin[r]) Sin[αs] Sin[βs]) +
 Sin[α] (Cos[p] Cos[q] Cos[βs] + Cos[αs] (Cos[r] Sin[p] + Cos[p] Sin[q] Sin[r]) Sin[βs] +
    (-Cos[p] Cos[r] Sin[q] + Sin[p] Sin[r]) Sin[αs] Sin[βs])
```

```
LaTeXFonts[fsize_: 16] := {LabelStyle → {FontFamily → "CMU Serif", FontSize → fsize}};
```

Yaw response

```
yaw_response = ListLinePlot[
  Table[{r, solarangle /. {A → Pi / 3, α → Pi / 3, p → 0, q → 0, βs → 0, αs → 0}},
   {r, -π / 6, π / 6, 0.01}], Frame → True,
  FrameLabel → {"Yaw angle (rad)", "Solar angle cos(Θs)"}, LaTeXFonts[]]
```

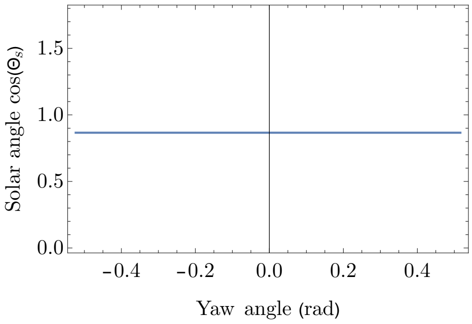

Pitch response

```
pitch_response = ListLinePlot[
  Table[{p, solarangle /. {A → Pi / 3, α → Pi / 3, r → 0, q → 0, βs → 0, αs → 0}},
   {p, -π / 6, π / 6, 0.01}], Frame → True,
  FrameLabel → {"Pitch angle (rad)", "Solar angle cos(Θs)"}, LaTeXFonts[]]
```

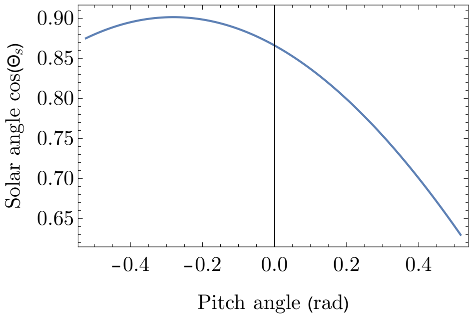

Roll response

```
roll_response = ListLinePlot[
  Table[{q, solarangle /. {A → Pi / 3, α → Pi / 3, p → 0, r → 0, βs → 0, αs → 0}},
   {q, -π / 6, π / 6, 0.01}], Frame → True,
  FrameLabel → {"Roll angle (rad)", "Solar angle cos(Θs)"}, LaTeXFonts[]]
```

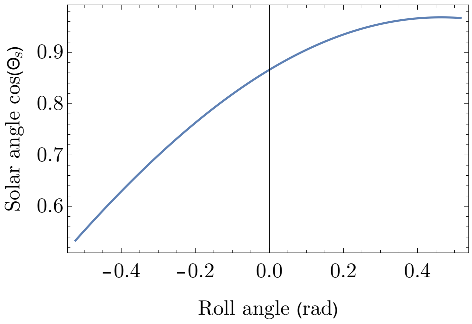

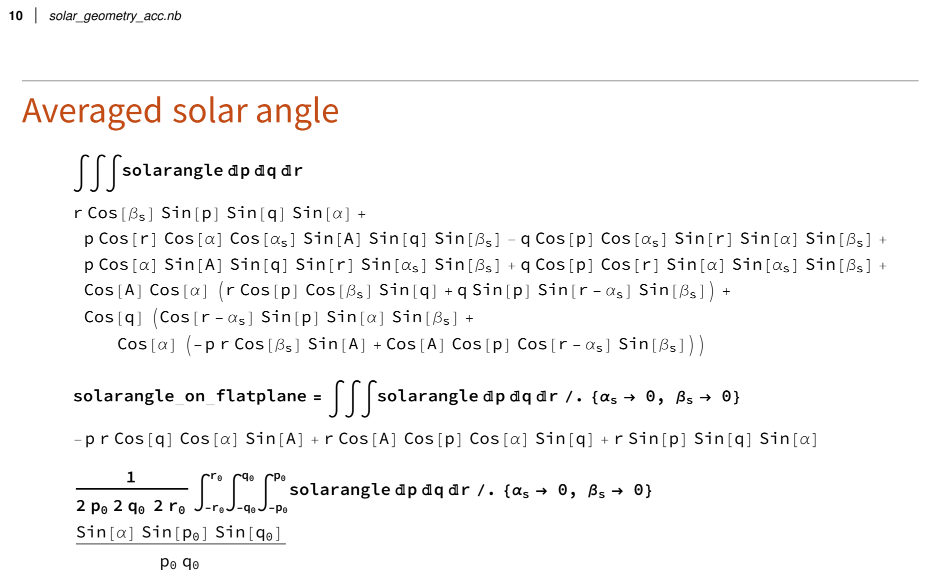

10 | *solar_geometry_acc.nb*

Averaged solar angle

$$\int\int\int \mathbf{solarangle}\, \mathbb{d}p\, \mathbb{d}q\, \mathbb{d}r$$

$$\begin{aligned}
&r\,\mathrm{Cos}[\beta_s]\,\mathrm{Sin}[p]\,\mathrm{Sin}[q]\,\mathrm{Sin}[\alpha] + \\
&\ p\,\mathrm{Cos}[r]\,\mathrm{Cos}[\alpha]\,\mathrm{Cos}[\alpha_s]\,\mathrm{Sin}[A]\,\mathrm{Sin}[q]\,\mathrm{Sin}[\beta_s] - q\,\mathrm{Cos}[p]\,\mathrm{Cos}[\alpha_s]\,\mathrm{Sin}[r]\,\mathrm{Sin}[\alpha]\,\mathrm{Sin}[\beta_s] + \\
&\ p\,\mathrm{Cos}[\alpha]\,\mathrm{Sin}[A]\,\mathrm{Sin}[q]\,\mathrm{Sin}[r]\,\mathrm{Sin}[\alpha_s]\,\mathrm{Sin}[\beta_s] + q\,\mathrm{Cos}[p]\,\mathrm{Cos}[r]\,\mathrm{Sin}[\alpha]\,\mathrm{Sin}[\alpha_s]\,\mathrm{Sin}[\beta_s] + \\
&\ \mathrm{Cos}[A]\,\mathrm{Cos}[\alpha]\,\left(r\,\mathrm{Cos}[p]\,\mathrm{Cos}[\beta_s]\,\mathrm{Sin}[q] + q\,\mathrm{Sin}[p]\,\mathrm{Sin}[r-\alpha_s]\,\mathrm{Sin}[\beta_s]\right) + \\
&\ \mathrm{Cos}[q]\,\left(\mathrm{Cos}[r-\alpha_s]\,\mathrm{Sin}[p]\,\mathrm{Sin}[\alpha]\,\mathrm{Sin}[\beta_s] + \right. \\
&\qquad \left.\mathrm{Cos}[\alpha]\,\left(-p\,r\,\mathrm{Cos}[\beta_s]\,\mathrm{Sin}[A] + \mathrm{Cos}[A]\,\mathrm{Cos}[p]\,\mathrm{Cos}[r-\alpha_s]\,\mathrm{Sin}[\beta_s]\right)\right)
\end{aligned}$$

$$\mathbf{solarangle\_on\_flatplane} = \int\int\int \mathbf{solarangle}\, \mathbb{d}p\, \mathbb{d}q\, \mathbb{d}r \ /.\ \{\alpha_s \to 0,\ \beta_s \to 0\}$$

$$-p\,r\,\mathrm{Cos}[q]\,\mathrm{Cos}[\alpha]\,\mathrm{Sin}[A] + r\,\mathrm{Cos}[A]\,\mathrm{Cos}[p]\,\mathrm{Cos}[\alpha]\,\mathrm{Sin}[q] + r\,\mathrm{Sin}[p]\,\mathrm{Sin}[q]\,\mathrm{Sin}[\alpha]$$

$$\frac{1}{2\,p_0\,2\,q_0\,\,2\,r_0}\int_{-r_0}^{r_0}\int_{-q_0}^{q_0}\int_{-p_0}^{p_0} \mathbf{solarangle}\, \mathbb{d}p\, \mathbb{d}q\, \mathbb{d}r \ /.\ \{\alpha_s \to 0,\ \beta_s \to 0\}$$

$$\frac{\mathrm{Sin}[\alpha]\,\mathrm{Sin}[p_0]\,\mathrm{Sin}[q_0]}{p_0\,q_0}$$

A.2 Solar power generation model validation with UK rooftop database

In order to validate the spatial-temporal solar panel model with real solar power system. The solar power model is used to estimate the power generation of rooftop panels across the UK. Solar power generation data is collected from Sheffield microgen user contributed solar power generation data. Location of each solar panel sites are shown in Figure A.1.

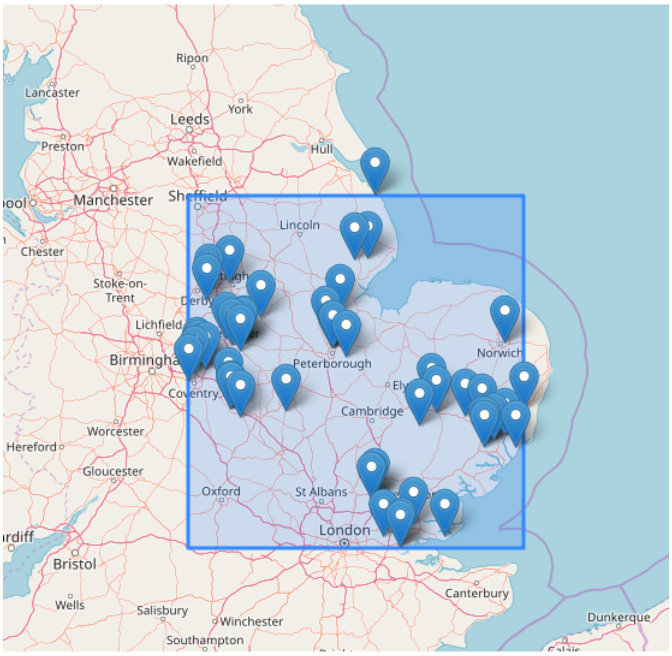

Figure A.1: Location of rooftop solar panels in the dataset

There are 49 microgen user contributions provided in the dataset at the year of 2014. Regional weather data is downloaded first from MERRA-2 database as in Example 3.4. In the dataset, solar panel azimuth, elevation, capacity and the panel technology could be found. The solar power generation data is recorded as aggregated power generation in watts at half hour interval. Since the MERRA-2 dataset only provides on hour resolution at best, we compare hourly correlation on the power generation between the dataset values and model estimated values.

After the regional solar radiation data and temperature data are retrieved from the MERRA-2 database, the same power generation estimation program is then running on each location without the non-stationary modeling option turns on. The outcome, solar power generation on titled solar panel, is compared with the database data. Pearson's r correlation test was then done between those two power generation data.

Among all site, there are 35 sites show a correlation coefficient larger than 0.85 that indicate a good agreement between our model and the dataset. Those sites are shown as green icon on the map. Nine sites have correlation coefficient between 0.8 and 0.85 that are shown as yellow icon on the map. Six sites with correlation coefficient less than 0.8 are shown on the map as red icon.

The source of error and uncertainty may come from the different sources.

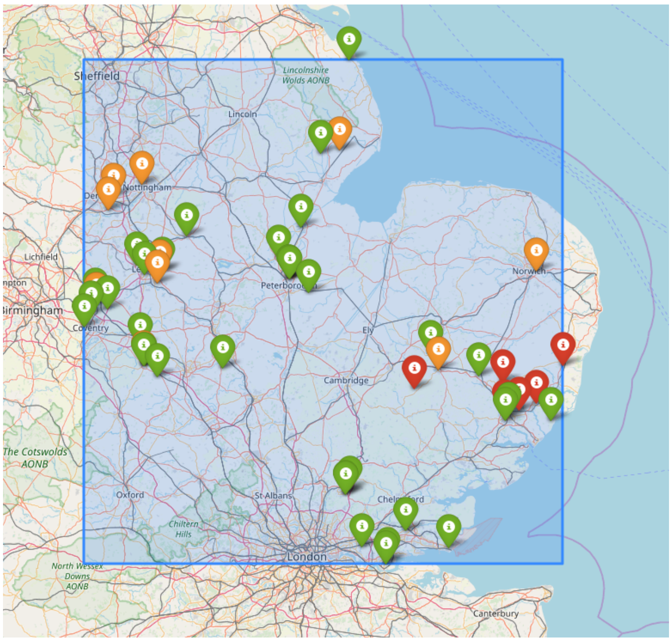

FIGURE A.2: Result of the validation

A.3 Autonomous surface vehicle propulsion power estimation validation

For surface vehicle, the power is mainly consumed to overcome the resistance in the ocean. The total resistance R_T of a ship is:

$$R_T = \frac{1}{2} C_T \rho S V^2 \tag{A.9}$$

where C_T total resistance coefficient, S is wet surface area of the vehicle, V is the speed of the vehicle. The surface area of the vehicle can be estimate from

$$S = 1.025(1.7 \cdot L_{\text{pp}} \cdot T + \frac{\Delta}{T}) \tag{A.10}$$

The total resistance coefficient C_t consists by three components

$$C_t = C_F + C_R + C_A \tag{A.11}$$

including frictional resistance C_F, residual resistance C_R, air resistance C_A. Among all resistance components, frictional and residual resistance are due to water resistance and air added resistance is due to aerodynamic drag.

- Frictional resistance C_F coefficient according to ITTC formula is:

  $$C_F = \frac{0.075}{(\log(R_n) - 2)^2} \tag{A.12}$$

  where R_n is Reynolds number

  $$R_n = V \cdot \frac{L}{\nu} \tag{A.13}$$

here ν is kinematic viscosity of water.

- Residual resistance C_R can be found using Harvald method.

$$C_R = C_R(C_{sl}, C_p, Fr) \tag{A.14}$$

where Froude number $Fr = \frac{V}{\sqrt{gL}}$, slenderness coefficient $C_{sl} = \frac{L}{\Delta^{1/3}}$, prismatic coefficient $C_p = \frac{\Delta}{L \cdot A_m}$. The lookup table can be found in Appendix 1.

- Air resistance C_A can be assume to be fixed at value of 0.001 to account additional resistance due to wind.
- In practise, the influence of the wave is often model as an additional resistance on water resistance as $(1 + c_w)(C_F + C_R)$, where c_w is wave added resistance ratio that depends on the sea state.

The Harvald regression method is used to estimate the residual resistance of ocean going vehicle.

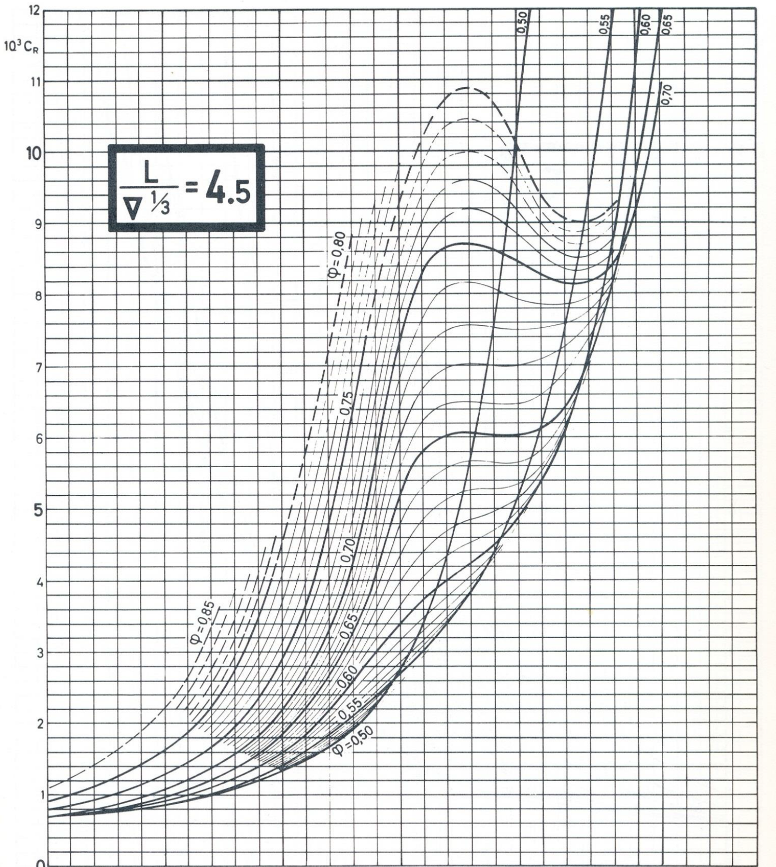

FIGURE A.3: Harvald C_R diagram at 4.5 slenderness

```
------------------------------
C_sl     C_p      Fr       C_R
------------------------------
4.50000 0.50000 0.27912 1.92515
4.50000 0.55000 0.34661 4.97065
4.50000 0.60000 0.33538 4.40411
4.50000 0.65000 0.29721 4.98323
```

```
4.50000 0.70000 0.28664 5.22884
4.50000 0.75000 0.27594 5.81920
4.50000 0.80000 0.26326 6.31877
4.50000 0.50000 0.28600 2.14415
4.50000 0.55000 0.35149 5.36743
4.50000 0.60000 0.34774 4.80721
4.50000 0.65000 0.30270 5.47029
4.50000 0.70000 0.28981 5.72569
4.50000 0.75000 0.27883 6.28109
4.50000 0.80000 0.26658 6.80620
4.50000 0.50000 0.29114 2.35961
                  .....continue
-------------------------------
```

Propulsion power can then be estimated from all resistance components:

$$\begin{aligned} P_{prop} &= R_T \cdot V/\eta_p \\ &= \frac{1}{2\eta_p}[(1+c_w)(C_F+C_R)+C_A]\rho_w S V^3 \end{aligned} \tag{A.15}$$

where η_p is electrical to mechanical power transmission efficiency. The vehicle speed V is relative to the water.

Validation data was taken from towing tank experiment `https://www.iihr.uiowa.edu/wp-content/uploads/2013/06/TR421.pdf`.

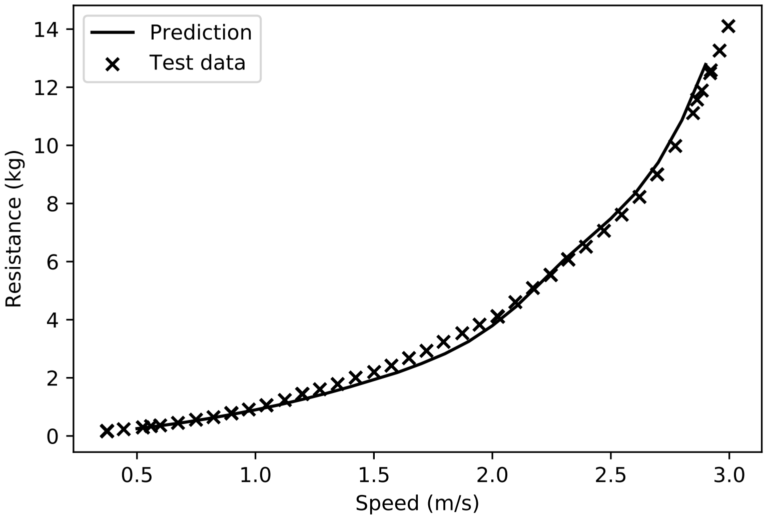

Figure A.4: Resistance estimation method validation

A.4 Full list of parameters and hyper-parameters

```
    source:
    solar:
      brl_parameters:
        a0: -5.32
        a1: 7.28
        b1: -0.03
```

```
      b2: -0.0047
      b3: 1.72
      b4: 1.08

load:
  prop_load:
    sea_margin: 0.2
    prop_eff: 0.7
    temperature: 25

transducer:
  solar:
    tilt: 0
    azim: 0
    tacking: 0
    loss: 0.1
    sationary: False
    pitch: 0.1
    roll: 0.2
    stationary: False
    tech: 'csi'           # Crystalline Silicon
    power_density: 140    # From data mining
    eff:
      k_1 : -0.017162
      k_2 : -0.040289
      k_3 : -0.004681
      k_4 : 0.000148
      k_5 : 0.000169
      k_6 : 0.000005

  wind:
    power_coef: 0.3
    v_in: 2
    v_rate: 15
    v_off: 45
    thrust_coef: 0.6

simulation:
  battery:
    eta_in: 0.9
    eta_out: 0.8
    DOD: 0.5
    sigma: 0.005
    B0: 1
    SED: 500
  coupling: 0.05

optimization:
  cost:
    solar: 210
    wind: 320
    battery: 1
    lpsp: 1000000
  constraints:
    water_plane_coff: 0.88
    volume_factor: 0.1
    turbine_diameter_ratio: 1.2
    solar_area: 1.60
    wind_area: 0.502
    battery_capacity: 5000
  safe_factor: 0.6
  method:
    pso:
      population: 100
      generation: 200
      omega: 0.7298
      eta1: 2.05   #
      eta2: 2.05
```

```
    max_vel: 0.5
    variant: 5
    neighb_type: 2
    neighb_param: 4
  nsga:
    cr: 0.95      # crossover probability
    eta_c: 10     # Distribution index for crossover
    m: 0.01       # Mutation probability
    eta_m: 50     # Distribution index for Mutation
```

Table A.1: Multiple year robustness study

		$\mathbb{P}$	η	$\min S(t)$	$\bar{S}(t)$	$\sigma[S(t)]$	$\bar{r}_t$	R
1994	GAF	0.216	100.000	0.000	97.360	105.204	-85.100	-400311.874
	DLF	0.000	18.413	7.568	17.927	8.556	20.553	96679.024
	EWMA	0.167	60.058	0.508	58.473	49.697	-61.934	-291336.575
	GFH	0.027	62.746	0.000	61.090	22.570	10.980	51647.691
	RL	0.000	47.930	17.357	46.674	18.540	23.427	110178.935
1995	GAF	0.243	100.000	0.000	92.881	101.599	-99.258	-466911.505
	DLF	0.000	20.102	7.628	18.671	9.673	20.553	96679.024
	EWMA	0.194	60.062	0.414	55.786	47.573	-76.257	-358711.985
	GFH	0.027	63.141	0.000	58.646	18.602	10.769	50656.190
	RL	0.000	48.352	22.432	44.919	18.062	23.177	109003.496
1996	GAF	0.218	100.000	0.000	98.610	107.442	-86.021	-404644.579
	DLF	0.000	19.107	7.628	18.841	10.598	20.553	96679.024
	EWMA	0.171	60.069	0.706	59.234	49.964	-64.223	-302105.577
	GFH	0.029	62.584	0.000	61.715	19.004	9.737	45802.372
	RL	0.000	46.558	22.733	45.921	20.038	23.261	109394.229
1997	GAF	0.262	100.000	0.000	96.594	105.729	-108.989	-512683.935
	DLF	0.000	17.942	7.568	17.331	6.853	20.553	96679.024
	EWMA	0.185	60.081	0.567	58.034	49.911	-71.409	-335909.932
	GFH	0.031	62.667	0.000	60.533	22.940	8.883	41787.698
	RL	0.000	48.457	13.328	46.817	17.537	23.501	110525.805
1998	GAF	0.128	100.000	0.000	106.709	108.269	-38.330	-180304.129
	DLF	0.000	13.848	7.628	14.778	6.553	20.553	96679.024
	EWMA	0.095	60.051	0.851	64.081	50.653	-23.955	-112683.234
	GFH	0.028	62.904	0.000	67.125	21.611	11.332	53306.415
	RL	0.000	43.484	22.532	46.412	18.915	23.716	111536.718
1999	GAF	0.212	100.000	0.000	101.602	107.392	-82.476	-387965.258
	DLF	0.000	16.851	7.669	17.121	8.033	20.553	96679.024
	EWMA	0.159	60.015	0.235	60.976	50.535	-57.508	-270519.022
	GFH	0.030	62.913	0.000	63.920	23.449	9.798	46088.158
	RL	0.000	46.087	11.671	46.835	18.714	23.524	110633.483
2000	GAF	0.212	100.000	0.000	97.420	106.179	-82.517	-388158.614
	DLF	0.000	17.491	7.568	17.040	8.529	20.553	96679.024
	EWMA	0.149	60.069	0.626	58.519	49.588	-52.874	-248720.208
	GFH	0.031	62.636	0.000	61.020	19.659	8.961	42150.678
	RL	0.000	47.680	14.657	46.460	18.272	23.495	110496.709
2001	GAF	0.178	100.000	0.000	95.743	104.638	-65.308	-307206.659
	DLF	0.000	17.888	7.568	17.126	9.568	20.553	96679.024
	EWMA	0.133	60.055	1.155	57.498	48.320	-44.471	-209191.202
	GFH	0.031	62.803	0.000	60.130	16.435	8.867	41710.550
	RL	0.000	46.712	23.059	44.733	18.706	23.314	109643.959
2002	GAF	0.158	100.000	0.000	102.935	106.865	-54.095	-254464.768
	DLF	0.003	17.483	0.000	17.997	12.095	18.782	88350.482
	EWMA	0.123	60.063	0.881	61.826	49.922	-38.928	-183116.364
	GFH	0.034	63.090	0.000	64.942	19.177	7.587	35688.297
	RL	0.000	48.530	25.787	49.965	19.159	23.720	111552.876
2003	GAF	0.215	100.000	0.000	98.961	107.833	-84.429	-397156.322
	DLF	0.000	17.939	7.568	17.753	9.763	20.553	96679.024
	EWMA	0.156	60.028	0.965	59.404	50.547	-56.507	-265809.041
	GFH	0.028	62.812	0.000	62.159	22.654	10.662	50156.282
	RL	0.000	50.838	26.812	50.320	17.418	23.810	111977.828
2004	GAF	0.212	100.000	0.000	96.111	103.753	-82.638	-388728.613
	DLF	0.000	18.514	7.568	17.794	8.601	20.553	96679.024
	EWMA	0.152	60.064	1.221	57.728	48.048	-54.366	-255737.394
	GFH	0.025	62.938	0.000	60.490	16.721	11.707	55070.018
	RL	0.000	49.285	23.233	47.379	17.447	23.511	110574.400
2005	GAF	0.239	100.000	0.000	98.506	106.295	-96.755	-455133.526
	DLF	0.000	19.431	7.568	19.141	9.338	20.553	96679.024
	EWMA	0.183	60.055	0.687	59.157	49.792	-70.327	-330818.834
	GFH	0.024	62.936	0.000	61.996	21.181	12.603	59286.099

Appendix B

Code and other contributions

Many software packages have been developed and used during the research. The author values reproducible open research in spirit of open source software. All software packages are freely avaliable via `GitHub`. Software version, at the time when thesis complied, is also specified in the following list.

- `D3HRE` at version `43417b5`, Dynamic Data Driven Hybrid Renewable Energy design framework, is developed by the author and open-sourced under GPL license. `github.com/tsaoyu/D3HRE/`
- `PyResis` at version `c53f835`, Python Ship Resistance and Propulsion estimation package is developed by the author and open-sourced under MIT license. `github.com/MaritimeRenewable/PyResis/`
- `RLenergy` at version `b4a087d`, Reinforcement Learning power management simulation environment is developed by the author and open-sourced under MIT license. `github.com/tsaoyu/RLenergy/`
- `PyVisilibity` at version `88fa4d1`, general purpose visibility computation software package, has major contribution from the author and open-sourced by its contributor under LGPL license. `github.com/tsaoyu/PyVisiLibity/`

Small contributions have been made to improve the simulation, optimisation and management of renewable energy systems.

- `GSEE` at version `088fe12`, Global Solar Energy Estimator, has contribution from the author and open-sourced by its contributor under BSD license. `github.com/MaritimeRenewable/gsee`
- `Synthetic solar` at version `942aa63`, Synthetic solar radiation sequences generator, has contribution from the author and open-sourced by its contributor under GPL license. `github.com/MaritimeRenewable/synthetic_solar`
- `pvlib` developed at Sandia National Laboratories

Bibliography

[1] Ezzeldin S Abdin and Wilson Xu. “Control design and dynamic performance analysis of a wind turbine-induction generator unit”. In: *IEEE Transactions on energy conversion* 15.1 (2000), pp. 91–96.

[2] R J Aguiar et al. “Simple procedure for generating sequences of daily radiation values using a library of Markov transition matrices”. In: *Solar Energy* 40.3 (Jan. 1988), pp. 269–279.

[3] Cristina L Archer and Mark Z Jacobson. “Evaluation of global wind power”. In: *Journal of Geophysical Research: Atmospheres* 110.D12 (2005).

[4] S Ashok. “Optimised model for community-based hybrid energy system”. In: *Renewable Energy* 32.7 (June 2007), pp. 1155–1164.

[5] Alireza Askarzadeh. “Developing a discrete harmony search algorithm for size optimization of wind–photovoltaic hybrid energy system”. In: *Solar Energy* 98.PC (Dec. 2013), pp. 190–195.

[6] T G Barbounis et al. “Long-Term Wind Speed and Power Forecasting Using Local Recurrent Neural Network Models”. In: *IEEE Transactions on Energy Conversion* 21.1 (Mar. 2006), pp. 273–284.

[7] S P Beeby et al. “Energy harvesting vibration sources for microsystems applications”. In: *Measurement science and technology* 17.12 (2006), R175.

[8] Rachid Belfkira et al. “Modeling and optimal sizing of hybrid renewable energy system”. In: *2008 13th International Power Electronics and Motion Control Conference, EPE-PEMC 2008.* Universite du Havre, Le Havre, France. IEEE, Nov. 2008, pp. 1834–1839.

[9] M M H Bhuiyan and M Ali Asgar. “Sizing of a stand-alone photovoltaic power system at Dhaka”. In: *Renewable Energy* 28.6 (May 2003), pp. 929–938.

[10] John Boland et al. “Modelling the diffuse fraction of global solar radiation on a horizontal surface”. In: *Environmetrics* 12.2 (Apr. 2001), pp. 103–116.

[11] B S Borowy and Z M Salameh. “Methodology for optimally sizing the combination of a battery bank and PV array in a wind/PV hybrid system”. In: *IEEE Transactions on Energy Conversion* 11.2 (June 1996), pp. 367–375.

[12] Bogdan S Borowy and Ziyad M Salameh. “Methodology for optimally sizing the combination of a battery bank and PV array in a wind/PV hybrid system”. In: *IEEE Transactions on energy conversion* 11.2 (1996), pp. 367–375. DOI: `10.1109/60.507648`.

[13] Robert J Boucher. “Sunrise, the world’s first solar-powered airplane”. In: *Journal of Aircraft* 22.10 (Jan. 1985), pp. 840–846.

[14] B Boukhezzar et al. “Multivariable control strategy for variable speed, variable pitch wind turbines”. In: *Renewable Energy* 32.8 (July 2007), pp. 1273–1287.

[15] JA Bowker et al. “Experimental study of a wave energy scavenging system onboard autonomous surface vessels (ASVs)”. In: *OCEANS 2015-Genova*. IEEE. 2015, pp. 1–9.

[16] Martin J Brand et al. “Effects of vibrations and shocks on lithium-ion cells”. In: *Journal of Power Sources* 288.C (Aug. 2015), pp. 62–69.

[17] Greg Brockman et al. “OpenAI Gym”. In: *ArXiv* abs/1606.01540 (2016).

[18] Edward M Carapezza and Trent M Molter. “Renewable energy for sustainable ocean sensors and platforms”. In: *Optics/Photonics in Security and Defence*. Ed. by Edward M Carapezza. SPIE, Oct. 2007, 67360H–67360H–12.

[19] Yi Chao. “Autonomous underwater vehicles and sensors powered by ocean thermal energy”. In: *OCEANS 2016 - Shanghai*. IEEE, 2016, pp. 1–4.

[20] J P Charles et al. “A practical method of analysis of the current-voltage characteristics of solar cells”. In: *Solar Cells* 4.2 (Sept. 1981), pp. 169–178.

[21] Anurag Chauhan and R P Saini. “A review on Integrated Renewable Energy System based power generation for stand-alone applications: Configurations, storage options, sizing methodologies and control”. In: *Renewable and Sustainable Energy Reviews* 38 (Oct. 2014), pp. 99–120.

[22] Anurag Chauhan and R P Saini. “Discrete harmony search based size optimization of Integrated Renewable Energy System for remote rural areas of Uttarakhand state in India”. In: *Renewable Energy* 94.C (Aug. 2016), pp. 587–604.

[23] T Y Chen et al. “Development of small wind turbines for moving vehicles: Effects of flanged diffusers on rotor performance”. In: *Experimental Thermal and Fluid Science* 42.C (Oct. 2012), pp. 136–142.

[24] Dorian F Colas et al. “Hale multidisciplinary design optimization part I: Solar-powered single and multiple-boom aircraft”. In: *2018 Aviation Technology, Integration, and Operations Conference*. Facebook, Inc., Menlo Park, United States. Reston, Virginia: American Institute of Aeronautics and Astronautics, Jan. 2018.

[25] Denise Crimmins et al. “Use of a long endurance solar powered autonomous underwater vehicle (SAUV II) to measure dissolved oxygen concentrations in Greenwich Bay, Rhode Island, USA”. In: *Europe Oceans 2005*. Vol. 2. IEEE. 2005, pp. 896–901.

[26] Waltenegus Dargie. “Dynamic Power Management in Wireless Sensor Networks: State-of-the-Art”. In: *IEEE Sensors Journal* 12.5 (May 2012), pp. 1518–1528.

[27] G Dedieu et al. “Satellite estimation of solar irradiance at the surface of the earth and of surface albedo using a physical model applied to Meteosat data.” In: *Journal of Climate & Applied Meteorology* 26.1 (Dec. 1987), pp. 79–87.

[28] Orhan Ekren and Banu Y Ekren. “Size optimization of a PV/wind hybrid energy conversion system with battery storage using simulated annealing”. In: *Applied Energy* 87.2 (Feb. 2010), pp. 592–598.

[29] D G Erbs et al. “Estimation of the diffuse radiation fraction for hourly, daily and monthly-average global radiation”. In: *Solar Energy* 28.4 (Jan. 1982), pp. 293–302.

[30] O Erdinc et al. “A dynamic lithium-ion battery model considering the effects of temperature and capacity fading”. In: *2009 International Conference on Clean Electrical Power* (June 2009), pp. 383–386.

[31] Lijun Gao et al. “Dynamic lithium-ion battery model for system simulation”. In: *IEEE Transactions on Components and Packaging Technologies* 25.3 (Sept. 2002), pp. 495–505.

[32] Zong Woo Geem and Yourim Yoon. “Harmony search optimization of renewable energy charging with energy storage system”. In: *International Journal of Electrical Power & Energy Systems* 86.C (Mar. 2017), pp. 120–126.

[33] Alexandros Glykas et al. “Application and cost-benefit analysis of solar hybrid power installation on merchant marine vessels”. In: *Ocean Engineering* 37.7 (May 2010), pp. 592–602.

[34] V A Graham and K. G.T Hollands. “A method to generate synthetic hourly solar radiation globally”. In: *Solar Energy* 44.6 (Jan. 1990), p. 333.

[35] Martin A Green et al. “Solar cell efficiency tables (Version 55)”. In: *Progress in Photovoltaics: Research and Applications* 23.1 (Dec. 2019), pp. 1–9.

[36] G Hagerman. “Wave energy systems for recharging AUV energy supplies”. In: *Proceedings of the Workshop on Autonomous Underwater Vehicles,* 2002.

[37] L Hontoria et al. “A new approach for sizing stand alone photovoltaic systems based in neural networks”. In: *Solar Energy* 78.2 (Feb. 2005), pp. 313–319.

[38] James Michael Hooper et al. “Multi-axis vibration durability testing of lithium ion 18650 NCA cylindrical cells”. In: *Journal of Energy Storage* 15 (Feb. 2018), pp. 103–123.

[39] Thomas Huld et al. “Mapping the performance of PV modules, effects of module type and data averaging”. In: *Solar Energy* 84.2 (Feb. 2010), pp. 324–338.

[40] Jamshed Iqbal and Zeashan Hameed Khan. “The potential role of renewable energy sources in robot’s power system: A case study of Pakistan”. In: *Renewable and Sustainable Energy Reviews* 75 (Aug. 2017), pp. 106–122.

[41] M Iqbal. “Prediction of hourly diffuse solar radiation from measured hourly global radiation on a horizontal surface”. In: *Solar Energy* 24.5 (Jan. 1980), pp. 491–503.

[42] E P James et al. “An investigation of self-powered systems for condition monitoring applications”. In: *Sensors and Actuators A: Physical* 110.1-3 (Feb. 2004), pp. 171–176.

[43] Keyur B Joshi et al. “Estimation of solar energy harvested for autonomous Jellyfish vehicles (AJVs)”. In: *IEEE Journal of Oceanic Engineering* 36.4 (Oct. 2011), pp. 539–551.

[44] Aman Kansal et al. “Power management in energy harvesting sensor networks”. In: *ACM Transactions on Embedded Computing Systems (TECS)* 6.4 (Sept. 2007), 32–es.

[45] Yiannis A Katsigiannis et al. “Hybrid Simulated Annealing-Tabu Search Method for Optimal Sizing of Autonomous Power Systems With Renewables”. In: *IEEE Transactions on Sustainable Energy* 3.3 (July 2012), pp. 330–338.

[46] Neeta Khare and Pritpal Singh. “Modeling and optimization of a hybrid power system for an unmanned surface vehicle”. In: *Journal of Power Sources* 198 (2012), pp. 368–377.

[47] Vikas Khare et al. "Optimisation of the hybrid renewable energy system by HOMER, PSO and CPSO for the study area". In: *International Journal of Sustainable Energy* 36.4 (Apr. 2015), pp. 326–343.

[48] Eftichios Koutroulis et al. "Methodology for optimal sizing of stand-alone photovoltaic/wind-generator systems using genetic algorithms". In: *Solar energy* 80.9 (2006), pp. 1072–1088. DOI: `10.1016/j.solener.2005.11.002`.

[49] Anthony Lamarca et al. "Making sensor networks practical with robots". In: *Lecture Notes in Computer Science (including subseries Lecture Notes in Artificial Intelligence and Lecture Notes in Bioinformatics)*. Intel Research Laboratories, Santa Clara, United States. Berlin, Heidelberg: Springer Berlin Heidelberg, Jan. 2002, pp. 152–166.

[50] Philippe Lauret et al. "Bayesian statistical analysis applied to solar radiation modelling". In: *Renewable Energy* 49 (Jan. 2013), pp. 124–127.

[51] Sébastien Lemaire et al. "Adaptive Probabilistic Tack Manoeuvre Decision for Sailing Vessels". In: *Robotic Sailing 2018. Proceedings of the 11th International Robotic Sailing Conference.* (Aug. 31–Sept. 1, 2018). Ed. by Sophia M. Schillai and Nicholas Townsend. Southampton, UK, 2018, pp. 95–103. URL: `http://ceur-ws.org/Vol-2331/#paper10`.

[52] J H Lever et al. "Mobility and Power Budget for a Solar-Powered Polar Rover". In: *ISTV 2006.* 2006, pp. 12–18.

[53] Xue Lin et al. "Reinforcement learning based power management for hybrid electric vehicles". In: *Proceedings of the 2014 IEEE/ACM International Conference on Computer-Aided Design.* IEEE Press. 2014, pp. 32–38.

[54] Benjamin Y H Liu and Richard C Jordan. "The interrelationship and characteristic distribution of direct, diffuse and total solar radiation". In: *Solar Energy* 4.3 (July 1960), pp. 1–19.

[55] Joseph J Loferski. "Theoretical Considerations Governing the Choice of the Optimum Semiconductor for Photovoltaic Solar Energy Conversion". In: *Journal of Applied Physics* 27.7 (July 1956), pp. 777–784.

[56] Xi Lu et al. "Global Potential for Wind-Generated Electricity". In: *PNAS* 106.27 (Apr. 2009), pp. 10933–10938.

[57] Emilio Mamarelis et al. "Design of a Sliding-Mode-Controlled SEPIC for PV MPPT Applications". In: *IEEE Transactions on Industrial Electronics* 61.7 (July 2014), pp. 3387–3398.

[58] Patrizio Manganiello et al. "Optimization of Perturbative PV MPPT Methods Through Online System Identification". In: *IEEE Transactions on Industrial Electronics* 61.12 (May 2015), pp. 6812–6821.

[59] Justin Manley and Scott Willcox. *The Wave Glider: A persistent platform for ocean science.* Liquid Robotics, Inc., Sunnyvale, United States: IEEE, 2010.

[60] S Martin and P Corke. "Long term optimisation of a mobile robot with proprioceptive perception". In: *Australasian Conference on Robotics and Automation.* 2015.

[61] Eugene L Maxwell. *A Quasi-physical Model for Converting Hourly Global Horizontal to Direct Normal Insolation.* 1987.

[62] Qiang Mei et al. “A Novel Improved Variable Step-Size Incremental-Resistance MPPT Method for PV Systems”. In: *IEEE Transactions on Industrial Electronics* 58.6 (Apr. 2011), pp. 2427–2434.

[63] Christian Meinig et al. “The use of Saildrones to examine spring conditions in the Bering Sea: Vehicle specification and mission performance”. In: *OCEANS 2015 - MTS/IEEE Washington.* NOAA Pacific Marine Environmental Laboratory, Seattle, United States. Feb. 2016.

[64] Andrew Miller. “A Variable Speed Wind Turbine Power Control”. In: *IEEE Transactions on Energy Conversion* 12 (June 1997), pp. 181–186.

[65] P D Mitcheson et al. “Energy Harvesting From Human and Machine Motion for Wireless Electronic Devices”. In: *Proceedings of the IEEE.* Aug. 2008, pp. 1457–1486.

[66] Scott Morton and Nikolaos Papanikolopoulos. “Two meter solar UAV: Design approach and performance prediction for autonomous sensing applications”. In: *IEEE International Conference on Intelligent Robots and Systems.* University of Minnesota System, United States. IEEE, Nov. 2016, pp. 1695–1701.

[67] Clemens Moser et al. “Adaptive power management in energy harvesting systems”. In: *Proceedings -Design, Automation and Test in Europe, DATE.* Alma Mater Studiorum Università di Bologna, Bologna, Italy. IEEE, Sept. 2007, pp. 773–778.

[68] S M Muyeen et al. “A Variable Speed Wind Turbine Control Strategy to Meet Wind Farm Grid Code Requirements”. In: *IEEE Transactions on Power Systems* 25.1 (Jan. 2010), pp. 331–340.

[69] Henrik Aalborg Nielsen et al. “Using quantile regression to extend an existing wind power forecasting system with probabilistic forecasts”. In: *Wind Energy* 9.1-2 (2006), pp. 95–108.

[70] A J Nozik et al. “Semiconductor Quantum Dots and Quantum Dot Arrays and Applications of Multiple Exciton Generation to Third-Generation Photovoltaic Solar Cells”. In: *Chemical Reviews* 110.11 (Nov. 2010), pp. 6873–6890.

[71] Atsumu Ohmura et al. “Baseline Surface Radiation Network (BSRN/WCRP): New Precision Radiometry for Climate Research”. In: *Bulletin of the American Meteorological Society* 79.10 (Jan. 1998), pp. 2115–2136.

[72] J A Paradiso and T Starner. “Energy Scavenging for Mobile and Wireless Electronics”. In: *IEEE Pervasive Computing* 4.1 (Feb. 2005), pp. 1–10.

[73] G Park et al. “Energy harvesting for structural health monitoring sensor networks”. In: *Journal of Infrastruct System* (2008), pp. 64–79.

[74] R R Perez et al. “Dynamic global-to-direct irradiance conversion models”. In: *ASHRAE Transactions.* University at Albany State University of New York, Albany, United States. Dec. 1992, pp. 354–369.

[75] Joaquin Recas Piorno et al. “Prediction and management in energy harvested wireless sensor nodes”. In: *2009 1st International Conference on Wireless Communication, Vehicular Technology, Information Theory and Aerospace & Electronic Systems Technology* (May 2009), pp. 6–10.

[76] Giovanni Privitera et al. “Optimising the installation costs of renewable energy technologies in buildings: A Linear Programming approach”. In: *Energy & Buildings* 43.4 (Apr. 2011), pp. 838–843.

[77] Peter Pudney and Phil Howlett. “Critical Speed Control of a Solar Car”. In: *Optimization and Engineering* 3.2 (2002), pp. 97–107.

[78] Nishatabbas Rehmatulla et al. “Wind technologies: Opportunities and barriers to a low carbon shipping industry”. In: *Marine Policy* 75 (Oct. 2015), pp. 217–226.

[79] D T Reindl et al. “Diffuse fraction correlations”. In: *Solar Energy* 45.1 (Jan. 1990), pp. 1–7.

[80] Barbara Ridley et al. “Modelling of diffuse solar fraction with multiple predictors”. In: *Renewable Energy* 35.2 (Feb. 2010), pp. 478–483.

[81] Yann Riffonneau et al. “Optimal Power Flow Management for Grid Connected PV Systems With Batteries”. In: *IEEE Transactions on Sustainable Energy* 2.3 (July 2011), pp. 309–320.

[82] I Rojon. “Blowin’ in the wind? Drivers and barriers for the uptake of wind propulsion in international shipping”. In: *Energy Policy* 67 (Apr. 2014), pp. 394–402.

[83] U K Saha et al. “Optimum design configuration of Savonius rotor through wind tunnel experiments”. In: *Journal of Wind Engineering and Industrial Aerodynamics* 96.8-9 (Aug. 2008), pp. 1359–1375.

[84] Dezso Sera et al. “PV panel model based on datasheet values”. In: *2007 IEEE International Symposium on Industrial Electronics*. IEEE, 2007, pp. 2392–2396.

[85] Masoud Sharafi and Tarek Y ELMekkawy. “Multi-objective optimal design of hybrid renewable energy systems using PSO-simulation based approach”. In: *Renewable Energy* 68 (Aug. 2014), pp. 67–79.

[86] Rajanna Siddaiah and R P Saini. “A review on planning, configurations, modeling and optimization techniques of hybrid renewable energy systems for off grid applications”. In: *Renewable and Sustainable Energy Reviews* 58.C (May 2016), pp. 376–396.

[87] G Sideratos and N D Hatziargyriou. “An Advanced Statistical Method for Wind Power Forecasting”. In: *IEEE Transactions on Power Systems* 22.1 (Jan. 2007), pp. 258–265.

[88] Sarangthem Sanajaoba Singh and Eugene Fernandez. “Modeling, size optimization and sensitivity analysis of a remote hybrid renewable energy system”. In: *Energy* 143 (Jan. 2018), pp. 719–731.

[89] R A Sinton. “A quasi-steady-state open-circuit voltage method for solar cell characterization”. In: *16th European Photovoltaic Solar Energy Conference*. May 2000.

[90] Arvid Skartveit and Jan Asle Olseth. “A model for the diffuse fraction of hourly global radiation”. In: *Solar Energy* 38.4 (Jan. 1987), pp. 271–274.

[91] Arvid Skartveit et al. “An hourly diffuse fraction model with correction for variability and surface albedo”. In: *Solar Energy* 63.3 (Sept. 1998), pp. 173–183.

[92] K Tan and S Islam. “Optimum Control Strategies in Energy Conversion of PMSG Wind Turbine System Without Mechanical Sensors”. In: *IEEE Transactions on Energy Conversion* 19.2 (June 2004), pp. 392–399.

[93] Ying Tan et al. “Adaptive power management using reinforcement learning”. In: *2009 IEEE/ACM International Conference on Computer-Aided Design - Digest of Technical Papers* (Dec. 2009), pp. 461–467.

[94] Henerica Tazvinga et al. “Optimal power flow management for distributed energy resources with batteries”. In: *Energy Conversion and Management* 102.C (Sept. 2015), pp. 104–110.

[95] James P Thomas et al. “Energy scavenging for small-scale unmanned systems”. In: *Journal of Power Sources* 159.2 (Sept. 2006), pp. 1494–1509.

[96] R Torah et al. “Self-powered autonomous wireless sensor node using vibration energy harvesting”. In: *Measurement Science and Technology* 19.12 (Oct. 2008), pp. 125202–9.

[97] Michael Traut et al. “Propulsive power contribution of a kite and a Flettner rotor on selected shipping routes”. In: *Applied Energy* 113 (Jan. 2014), pp. 362–372.

[98] John Twidell and Tony Weir. *Renewable Energy Resources.* Routledge, ISBN13: 9780199261789, Jan. 2015.

[99] Ignazio Maria Viola et al. “A numerical method for the design of ships with wind-assisted propulsion”. In: *Ocean Engineering* 105 (Sept. 2015), pp. 33–42.

[100] Caisheng Wang and M H Nehrir. “Power Management of a Stand-Alone Wind/Photovoltaic/Fuel Cell Energy System”. In: *IEEE Transactions on Energy Conversion* 23.3 (Oct. 2008), pp. 957–967.

[101] CH Wang et al. “Temperature response of a high power lithium-ion battery subjected to high current discharge”. In: *Materials Research Innovations* 19.sup2 (2015), S2–156.

[102] Haichao Wang et al. “Modelling and optimization of the smart hybrid renewable energy for communities (SHREC)”. In: *Renewable Energy* 84 (Mar. 2015), pp. 114–123.

[103] J Wang et al. “Wind power forecasting uncertainty and unit commitment”. In: *Applied Energy* 88.11 (Nov. 2011), pp. 4014–4023.

[104] L Wang and Chanan Singh. “PSO-based multi-criteria optimum design of a grid-connected hybrid power system with multiple renewable sources of energy”. In: *IEEE Swarm Inetlligence Symposium.* 2007.

[105] Louis L Whitcomb. “Underwater robotics: Out of the research laboratory and into the field”. In: *Robotics and Automation, 2000. Proceedings. ICRA’00. IEEE International Conference on.* Vol. 1. IEEE. 2000, pp. 709–716. DOI: `10.1109/ROBOT.2000.844135`.

[106] L T Wong and W K Chow. “Solar radiation model”. In: *Applied Energy* (2001).

[107] Jingda Wu et al. “Continuous reinforcement learning of energy management with deep Q network for a power split hybrid electric bus”. In: *Applied Energy* 222 (July 2018), pp. 799–811.

[108] Weidong Xiao and William G Dunford. “A modified adaptive hill climbing MPPT method for photovoltaic power systems”. In: *PESC Record - IEEE Annual Power Electronics Specialists Conference.* The University of British Columbia, Vancouver, Canada. IEEE, Nov. 2004, pp. 1957–1963.

[109] Hongxing Yang et al. “A novel optimization sizing model for hybrid solar-wind power generation system”. In: *Solar energy* 81.1 (2007), pp. 76–84. DOI: `10.1016/j.solener.2006.06.010`.

[110] Hongxing Yang et al. "Optimal sizing method for stand-alone hybrid solar–wind system with LPSP technology by using genetic algorithm". In: *Solar energy* 82.4 (2008), pp. 354–367. DOI: `10.1016/j.solener.2007.08.005`.

[111] A A El-Zeftawy et al. "Optimal planning of wind—diesel generation units in an isolated area". In: *PNAS* (1991).

[112] Chong wei Zheng and Jing Pan. "Assessment of the global ocean wind energy resource". In: *Renewable and Sustainable Energy Reviews* 33.C (May 2014), pp. 382–391.

[113] W Zhou et al. "Current status of research on optimum sizing of stand-alone hybrid solar–wind power generation systems". In: *Applied Energy* 87.2 (2010), pp. 380–389.